On the Evolution and Properties of AGB stars

Martin Groenewegen

R. J. TAKENS

On the Evolution and Properties of AGB stars

Over de evolutie en eigenschappen van AGB sterren

(Met een samenvatting in het Nederlands)

Academisch Proefschrift

**ter verkrijging van de graad van doctor
aan de Universiteit van Amsterdam,
op gezag van de Rector Magnificus
prof. dr. P.W.M. de Meijer,
in het openbaar te verdedigen in de Aula der Universiteit
(Oude Lutherse Kerk, ingang Singel 411, hoek Spui)
op 28 september 1993 te 13.30 uur**

door

Martin Arnold Theodoor Groenewegen

geboren te Ede

Sterrenkundig Instituut 'Anton Pannekoek', Amsterdam

promotiecommissie:

promotor:	prof. dr. T. de Jong
overige leden:	prof. dr. E.P.J. van den Heuvel
	prof. dr. H.J.G.L.M. Lamers
	prof. dr. J. van Paradijs
	prof. dr. S.R. Pottasch
	prof. dr. P.S. Thé
	dr. L.B.F.M. Waters

Contents

Chapter 1

Introduction

The research described in this thesis concerns the evolution and properties of stars on the Thermal-Pulsing Asymptotic Giant Branch (TP-AGB, usually simply denoted by AGB). This is a short-lived phase at the end of the active life of stars with initial masses between $\sim$1 $M_\odot$ and $\sim$8 $M_\odot$. Scaled to human proportions it would be the last month in a 100 year life time. After the AGB, (most) stars evolve to Planetary Nebulae (PNe) and eventually end as White Dwarfs (WDs). Although short-lived, the AGB phase gives rise to interesting phenomena related to several aspects of astronomy.

1 The evolution of AGB stars

Before reaching the AGB, a star goes through the phases of core hydrogen burning, shell hydrogen burning and core helium burning which are described in any textbook on stellar evolution (e.g. Kippenhahn & Weigert 1990).
After exhausting helium in the core, the star enters the Early-AGB phase (E-AGB) where the energy production is provided by helium shell burning. The duration of the E-AGB depends on the mass and composition of the star, and is typically 10^7 yrs for a 1 $M_\odot$ star (see e.g. Vassiliadis & Wood 1992). In due course the hydrogen burning shell is re-ignited and the star enters the TP-AGB phase, where the energy production takes place alternately in a hydrogen burning and a helium burning shell. For most of the time the hydrogen burning shell provides the energy. Hydrogen is converted into helium which is added to the helium shell which is located below the hydrogen shell. At some point the temperature and density in the helium shell become so high that the energy production of the triple-α process (3 ^{4}He $\rightarrow$ ^{12}C) exceeds the outflow rate of energy and a thermonuclear runaway occurs. This event is called a Thermal Pulse (TP) or a helium shell flash.
Most of the energy released by a TP is used to expand the star. The hydrogen burning shell is pushed outwards to cooler layers and is extinguished. The energy production is mainly provided by helium shell burning which now occurs at a much lower rate than during the TP. In due course, the star reaches approximately its pre-flash size and the hydrogen burning shell takes over from helium burning again. The time between two consecutive TPs is called the interpulse period. When the total energy output of the star is considered as a function of time and relative to the pre-flash value, the luminosity is increased by about 0.5 magnitudes for about 1% of the interpulse period after a TP, then the luminosity drops by about 0.8 magnitudes below the pre-flash luminosity for about 20% of the interpulse period and finally the star asymptotically reaches the pre-flash luminosity during the remaining 80% of the interpulse period (e.g. Boothroyd & Sackmann 1988a).
From evolutionary calculations it follows that important quantities like the interpulse period and

the luminosity during hydrogen shell burning primarily depend on the core mass[1] (these relations were originally presented in Paczyński 1970, 1975; see later work by e.g. Boothroyd & Sackmann 1988b, c).

2 What makes an AGB star interesting?

2.1 Nucleosynthesis

One interesting aspect of AGB evolution is the so-called 'third dredge-up' phenomenon[2]. This refers to the mixing of nucleosynthesis products, formed after a TP, or during the previous inter-pulse period, into the convective envelope. The main products which are mixed into the envelope are the result of incomplete helium burning (^{4}He, ^{12}C) and the s-process. The s-process refers to the slow neutron capture onto heavy elements (cf. Gallino 1988, Gallino et al. 1990, Busso et al. 1992). The most important s-processed elements which are used in quantitative studies are strontium, yttrium, zirconium, niobium, technetium (the 'light' elements) and barium, lanthanum, cerium, neodymium (the 'heavy' elements).
The addition of carbon to the envelope leads to an enhancement of the C/O ratio. This can lead to the formation of S-stars (with $0.8 \lesssim$C/O < 1) and carbon stars (with C/O ≥ 1). Historically, S-stars and C-stars are not defined by their C/O ratio but rather by spectroscopic criteria. Normal M-giants show TiO bands in their optical spectrum, S-stars are characterised by ZrO and LaO bands and carbon stars show strong C_2 bands. Abundance analyses in recent years have shown that the sequence M - MS - S - C is a sequence of increasing C/O ratio and increasing abundance of s-process elements (cf. Smith & Lambert 1990). Qualitatively the principle of dredge-up is well understood although quantitatively there remain problems, in particular the formation of carbon stars and the neutron source in the s-process.
In the early 80's deep surveys of carbon stars in the Large Magellanic Cloud (LMC) became available and Iben (1981) confronted these observations with the theoretical models available at that time. The models predicted carbon-star formation in massive stars at luminosities of $M_{\rm bol} \approx -6$, while the observations showed there were few carbon stars at such high luminosity and most had $-4 \lesssim M_{\rm bol} \lesssim -5$. The 'carbon star mystery' was born. Subsequent calculations managed to predict carbon stars at lower luminosities (see Lattanzio 1988) but still there remained a discrepancy. Chapter 8 discusses this issue.
A parallel problem is the source of the neutrons in the s-process. Two reactions have been considered: ^{22}Ne(α, n)^{25}Mg and ^{13}C(α, n)^{16}O (see the discussion in Lattanzio 1993). The former reaction can only occur in massive stars ($\gtrsim 7$ M$_\odot$) where the temperature is high enough. Observations indicate that the enhancement of the s-processed elements occurs in lower mass stars. Furthermore, enhancement of the ^{25}Mg isotope relative to the ^{24}Mg isotope is not seen. Recently Jorissen et al. (1992) discovered that the fluorine abundance correlates with C/O. This is a final objection to the operation of the ^{22}Ne reaction in the majority of AGB stars, since the fluorine is obviously not destroyed by ^{19}F(α, p)^{22}Ne, a reaction which is 20 times faster than the ^{22}Ne(α, n)^{25}Mg reaction. The ^{13}C-reaction, by virtue of elimination, must be the provider of neutrons for the s-process in the majority of AGB stars, although it has, up to now, only been shown to

[1] The core mass is usually defined as the mass inside the radius where the hydrogen abundance is half of that at the stellar surface. The core consists primarily of carbon and oxygen.

[2] The dredge-up process in AGB stars is referred to as the *third* dredge-up. The first dredge-up occurs for all stars on the Red Giant Branch (RGB) as the star develops a deep convective envelope which mixes mass layers, where during the previous main-sequence evolution hydrogen burning took place, into the outer envelope. The second dredge-up occurs for stars more massive than $\sim$5 M$_\odot$ at the end of core helium burning.

occur in evolutionary calculations for low metallicity and small envelope masses (see Lattanzio 1993). With the presently favoured new opacities (Rogers & Iglesias 1992) this may be overcome.

2.2 The formation of dust and molecules

AGB stars generally have large mass loss rates, from $\sim 10^{-7}$ to $\sim 10^{-4}$ $M_{\odot}$/yr, compared to $\sim 10^{-14}$ $M_{\odot}$/yr for the Sun. In the cool circumstellar envelopes around AGB stars, dust grains will form when the temperature is below ~1500 K. These dust grains absorb optical radiation which is re-emitted in the near- and far-infrared. That dust formation is an important characteristic of AGB stars has become clear with the advent of infrared astronomy, most particular with the IRAS satellite which observed about 250 000 sources (including many AGB stars) over 95% of the sky in at least one of four photometric bands at 12, 25, 60 and 100 μm.
Dust grains do not emit featureless continua but have spectral features. Silicates, typical for oxygen-rich stars, show features near 9.7 and 19 μm due to the stretching and bending modes of solid Si-O bonds, respectively. In stars with a low mass loss rate both features are in emission. For high mass loss rates the 9.7 μm feature goes into absorption while for extreme mass loss rates ($\gtrsim 10^{-4}$ $M_{\odot}$/yr) both the 9.7 μm and the 19 μm feature are in absorption. Silicon carbide, typical for carbon-rich stars, displays an emission feature near 11.3 μm. The silicate and silicon carbide dust features occur in the spectral region covered by the Dutch LRS (Low Resolution Spectrograph) instrument on board IRAS and assisted in the classification of M-, S- and C-stars in cases that no optical spectrum is available (for references see Jourdain de Muizon 1992). A total of about 6400 LRS spectra have now been published (LRS-atlas, JISWG 1986; Volk & Cohen 1989, 1990, Volk et al. 1991). Chapters 5 to 7 of this thesis deal with the dust emission around carbon stars.
Besides dust grains, molecules form in the circumstellar envelope. Because the CO molecule is very stable the chemistry is driven by the excess of carbon or oxygen atoms in the case the C/O ratio is larger or smaller than 1, respectively. The most important molecules are (between parentheses the number of stars detected up to 1991, taken from Olofsson 1992): CO (~200) and HCN (~100) in carbon stars, and CO (~170), H_2O (~200, maser emission), SiO (~45 thermal emission, ~200 maser emission) and OH (>1500 maser emission) in oxygen-rich stars. With a model to calculate the excitation of the molecules in the circumstellar envelope it is possible to derive mass loss rates and abundances from observed rotational line emission profiles (see Chapter 2 for such a model and references to earlier work).

2.3 Variability

Most AGB stars turn out to be variable on a time scale of 100 to 1000 days. Based on the amplitude and periodicity of the *optical* light curve they are designated Mira's, Semi-regulars and Irregulars (see the General Catalog of Variable Stars, Kholopov et al. 1985; sometimes the term Long Period Variables (LPVs) is used). Recent studies by Kerschbaum & Hron (1992) and Jura & Kleinmann (1992a, b) give space densities and scaleheights of LPVs. They confirm earlier work on the kinematics of variable stars (cf. Feast 1988) that the oxygen-rich Miras with periods less than ~300 days have a scaleheight of ~500 pc, much larger than the scaleheight of the other M-, S- and C-variables (~200-300 pc). Since most Miras with P $\lesssim$300 days do not show the radioactive s-process element technetium (Little et al. 1987) this probably means that the Miras with short periods are low mass stars which do not experience the third dredge-up.
As mentioned in the previous paragraph there are AGB stars which are very weak or invisible in the optical due to dust obscuration. Recently, periods of extreme mass losing AGB stars have

been derived by monitoring the *infrared* light curves (Jones et al. 1990, Le Bertre 1992, 1993). For OH/IR stars[3] periods (and distances) can be derived by monitoring the OH-emission using the phase-lag method (van Langevelde 1992).

Observationally, the mass loss rate of LPVs is correlated with their pulsation period (Schild 1989, Whitelock 1990, Wood 1990). This has led to theoretical models that take into account pulsations and radiation pressure on dust grains (see Bowen & Willson 1991) and even the formation and growth of dust (see Fleischer et al. 1992 and Höfner & Dorfi 1992 and references therein) to explain the observed mass loss rates.

The mass loss rate of AGB stars may vary on several distinct time scales. First of all, on a time scale of hundreds of days due to pulsation. Secondly, Bedijn (1987) proposed that the mass loss rate increases with evolution time along the AGB (a time scale of several 10^5 years), culminating into a 'superwind' at the tip of the AGB. Finally, the mass loss rate is related to thermal pulse cycle (a time scale of a few 10^4 years). Observational evidence for this last phenomenon comes from the observations of oxygen-rich and carbon stars with detached shells (Willems & de Jong 1988, Olofsson et al. 1990, Zijlstra et al. 1992).

The mixing of products of nucleosynthesis to the envelope of AGB stars combined with a high mass loss rate and dust formation results in an enrichment of the Galactic interstellar medium (ISM) in both gas and dust. It turns out that low- and intermediate-mass stars (1-8 $M_\odot$) are important contributors of carbon (25%), nitrogen (50%) and helium (50%) to the ISM (cf. van den Hoek et al. 1993). This implies that the present-day abundances in the ISM are determined partly by the ejecta of all AGB stars which have died during the evolution of the Galaxy. Modelling the chemical evolution of galaxies therefore indirectly constrains the effects of mass loss and nucleosynthesis in AGB stars.

3 Carbon stars *not* on the TP-AGB

Carbon-rich stars exist which have effective temperatures and luminosities which indicate that they are not on the TP-AGB.

First of all, there are carbon-rich objects in the evolutionary phase after the AGB. They are the carbon-rich PNe (in the Galaxy about 60% of the PNe are carbon-rich; Zuckerman & Aller 1986) and some RV Tau stars, which are considered to be post-AGB stars (For recent work see e.g. Jura 1986, Alcolea & Bujarrabal 1991, Shenton et al. 1992, Slijkhuis 1993). Carbon-rich objects in the evolutionary phase after the AGB are expected since for initial masses $\lesssim$8 $M_\odot$ nucleosynthesis ends on the AGB (may be some stars experience a late thermal pulse in the post-AGB phase) and apart from radioactive decay no abundance changes with respect to the AGB phase are expected.

More mysteriously, carbon-stars are known at luminosities below the TP-AGB, the so-called early R-stars (spectral type earlier than R5). They are hot (T_{eff} = 4400-5000 K, compared to T_{eff} $\lesssim$3000 K for the N-type C-stars), have no enhanced s-process elements, C/O $\approx$ 2 and $^{12}C/^{13}C \approx$ 4 (Dominy 1984). Unlike some stars to be discussed later they have a normal binary frequency (McClure 1988 and private communication).

Probably related to the early R-stars are the recently discovered carbon stars in the Galactic Bulge (Azzopardi et al. 1985, 1988, 1991). These carbon stars have absolute bolometric magnitudes in the range 0.25 $\lesssim M_{bol} \lesssim$-3 (Rich 1989, Westerlund et al. 1991). From spectropho-

[3]OH/IR stars are late M-stars which have a high mass loss rate leading to strong OH maser and infrared emission (te Lintel Hekkert 1990, van Langevelde 1992, Blommaert 1992). They have no or very faint optical counterparts.

tometric indices one derives that these stars generally have low $^{12}C/^{13}C$ ratios (Westerlund et al. 1991, Tyson & Rich 1991) similar to those found in R-stars. The main difference is probably the metallicity. While the R-stars have roughly solar metallicities (Dominy 1984) carbon stars in the Galactic bulge are probably metal rich (Azzopardi et al. 1988, Tyson & Rich 1991).
An unusual helium core flash (HeCF) has been suggested as the origin of the R-stars (Dominy 1984). Paczyński & Tremaine (1977) and Deupree & Wallace (1987) have shown that mixing of ^{12}C can occur, depending on the location of the HeCF and the degree of degeneracy of the flash. Consistent calculations of the HeCF taking into account e.g. core rotation are highly desirable. After the HeCF has formed an R-star the star probably evolves into an N-type carbon star (if mass loss at the HeCF or afterwards has not made the star to make a left-turn in the HR-diagram). That at least some R-stars probably evolve into N-stars has been inferred from observations in the LMC and SMC (Westerlund et al. 1992) which show that the N-type carbon stars with the lowest luminosities ($M_{bol} \approx -3$) are often enriched in ^{13}C.

Another scenario by which stars can be formed that have some characteristics of AGB stars but which themselves are not on the AGB, invokes binary evolution.
Consider a binary system where the primary has a mass in the range 1 - 8 $M_{\odot}$, and with an orbital separation such that the primary does not fills its Roche-lobe during the ascent of the RGB. The primary reaches the AGB and due to third dredge-up the C/O ratio and the abundance of the s-process elements are enhanced relative to the values in normal giants. Depending on the orbital separation mass is transferred to the secondary by a stellar wind or Roche-lobe overflow (RLOF). The abundances of carbon and the s-process elements in the secondary will now also be enhanced.
The primary evolves off the AGB and ends it active life as a WD. According to this evolutionary scenario for binary systems involving an AGB star, there should be binary stars of which one component has the chemical peculiarities similar to those in AGB stars, has a luminosity and effective temperature uncharacteristic of AGB stars, and have a WD companion. Classes of stars which are now thought to be the result of such evolution are: barium-stars, S-stars without the radioactive element technetium (see Chapter 4), CH-stars (and the CH-like and subgiant CH-stars) and carbon-dwarfs.

4 Thesis outline

In Chapter 2 a model is presented to calculate the molecular thermal emission in the expanding envelopes of AGB stars, consistently taking into account the kinetic temperature structure in the envelope. In Chapter 3 the model is applied to two OH/IR stars in order to derive mass loss rates from the observed CO(1-0) and CO(2-1) line profiles. For the OH/IR star with the smaller mass loss rate, I find that with the mass loss rate derived from infrared techniques the observed CO line profiles are well reproduced. For the OH/IR star with the large mass loss rate I find that with a constant mass loss rate the observed CO line profiles can not be reproduced. A model where the mass loss rate was lower in the past can fit the observations.
Chapter 4 concerns the S-stars. S-stars with and without Tc have been observed. The latter show enhanced s-process elements due to mass transfer. I show that the two classes can be separated (with high probability) based only on their infrared properties.
Chapters 5 to 7 deal with the dust shells around carbon stars. In Chapter 5, I present a dust radiative transfer model developed in particular to handle non-continuous mass loss rates. I discuss the likelihood of finding evidence for the presence of a mass loss rate law as proposed by Bedijn (1987) in the spectral energy distribution of oxygen-rich AGB stars. In Chapter 6

the star S Sct is discussed which is the only carbon star with a 60 μm excess that has been mapped in detail in CO, constraining the dust radiative transfer model. The mass loss rate in the different phases of the thermal pulse cycle is estimated. In Chapter 7, I discuss the dust shells of infrared carbon stars. The inner dust radius, the mass loss rate and the ratio of silicon carbide to amorphous carbon dust is determined in a sample of 21 stars.
Chapters 8 to 11 discuss the use of synthetic evolution models to study the conditions at which dredge-up and mass loss occur on the AGB. Chapter 8 introduces the synthetic evolution model and its application to carbon stars in the LMC. Chapter 9 discusses the best model found in Chapter 8 in relation to the observed abundances of PNe in the LMC. Chapter 10 discusses the influence of different mass loss rate laws. I show that a scaled version of the mass loss law proposed by Blöcker & Schönberner (1993) equally well fits the observational constraints as the Reimers law (1975) adopted in Chapters 8 and 9. Similarly, I show that this is not the case for the mass loss law proposed by Vassiliadis & Wood (1992). Chapter 11 discusses the LPVs in the LMC. The main conclusions are that most LPVs pulsate in the fundamental mode and that the AGB phase is not ended by most stars as LPVs.
Finally, in Chapter 12 an evolutionary scenario is presented for N-type carbon stars in the Galaxy. Stars with masses between $\sim$1.5 $M_{\odot}$ and $\sim$4 $M_{\odot}$ go through a carbon star phase. The average lifetime of the carbon star phase is $\sim 3\ 10^5$ yrs.

References

Alcolea J., Bujarrabal V., 1991, A&A 245, 499
Azzopardi M., Lequeux J., Rebeirot E., 1985, A&A 145, L4
Azzopardi M., Lequeux J., Rebeirot E., 1988, A&A 202, L27
Azzopardi M., Lequeux J., Rebeirot E., Westerlund B.E., 1991, A&AS 88, 265
Bedijn P.J., 1987, A&A 186, 136
Blöcker T., Schönberner D., 1993, in: IAU symposium 155 on Planetary Nebelae eds. R. Weinberger, A. Acker, Reidel, Dordrecht, in press
Blommaert J., 1992, Ph. D. thesis, University of Leiden
Boothroyd A.I., Sackmann I.-J., 1988a, ApJ 328, 632
Boothroyd A.I., Sackmann I.-J., 1988b, ApJ 328, 641
Boothroyd A.I., Sackmann I.-J., 1988c, ApJ 328, 653
Bowen G.H., Willson L.A., 1991, ApJ 375, L53
Busso M., Gallio R., Lambert D.L., Raiteri C.M., Smith V.V., 1992, ApJ 339, 218
Deupree R.G., Wallace R.K., 1987 ApJ 317, 724
Dominy J.F., 1984, ApJS 55, 27
Feast M.W., 1988, in: Evolution of peculiar red giant stars, eds. H.R. Johnson, B. Zuckerman, Cambridge UP, p. 26
Fleischer A.J., Gauger A., Sedlmayer E., 1992, A&A 266, 321
Gallino R., 1988, in: Evolution of peculiar red giant stars, eds. H.R. Johnson, B. Zuckerman, Cambridge UP, p. 176
Gallino R., Busso M., Picchio G., Raiteri C.M., 1990, in: From Miras to Planetary Nebulae, eds. M.O. Mennessier, A. Omont, Editions Frontieres, Gif-sur-Yvette, p. 329
Höfner S., Dorfi E.A., 1992, A&A 265, 207
Iben I., 1981, ApJ 246, 278
Joint IRAS Science Working Group, 1986, IRAS catalogs and atlases, Low Resolution Spectrograph (LRS), A&AS 65, 607

Jones T.J., et al., 1990, ApJS 74, 785
Jorissen A., Smith V.V., Lambert D.C., 1992, A&A 261, 164
Jourdain de Muizon M., 1992, in: Infrared astronomy with ISO, eds. Th. Encrenaz, M. Kessler, Nova science publishing inc., New York, p. 489
Jura M., 1986, ApJ 309, 732
Jura M., Kleinmann S.G., 1992a, ApJS 79, 105
Jura M., Kleinmann S.G., 1992b, ApJS 83, 329
Kerschbaum F., Hron J., 1992, A&A 263, 87
Kippenhahn R., Weigert A., 1990, Stellar structure and evolution, Springer, Berlin
Kholopov P.N., et. al., 1985, General catalog of variable stars, Nauka, Moscow
van Langevelde H.J., 1992, Ph. D. thesis, University of Leiden
Lattanzio J.C., 1988, in: Evolution of peculiar red giant stars, eds. H.R. Johnson, B. Zuckerman, Cambridge UP, p. 176
Lattanzio J.C., 1993, in: Planetary Nebulae, eds. R. Weinberger, A. Acker, Reidel, Dordrecht, in press
Le Bertre T., 1992, A&AS 94, 377
Le Bertre T., 1993, A&AS 97, 729
te Lintel Hekkert P., 1990, Ph. D. thesis, University of Leiden
Little S.J., Little-Marenin I.R., Bauer W.H., 1987, AJ 94, 981
McClure R.D., 1988, in: Evolution of peculiar red giant stars, eds. H.R. Johnson, B. Zuckerman, Cambridge UP, p. 196
Olofsson H., Eriksson K., Gustafsson B., Willson L.A., 1990, A&A 230, L13
Olofsson H., 1992, in: Mass loss on the AGB and beyond, ed. H. Schwartz, in press
Paczyński B., 1970, Acta Astron. 20, 47
Paczyński B., 1975, ApJ 202, 558
Paczyński B., Tremaine S.D., 1977, ApJ 216, 57
Reimers D., 1975, in: Problems in stellar atmospheres and envelopes, eds. B. Basheck et al., Springer, Berlin, p. 229
Rich R.M., 1989, in: The centre of the Galaxy, ed. M. Morris, Kluwer, Dordrecht, p. 63
Rogers F.J., Iglesias C.A., 1992, ApJS 79, 507
Schild H., 1989, MNRAS 240, 63
Shenton M., et al., 1992, A&A 262, 138
Slijkhuis S., 1993, A&A, submitted
Smith V.V., Lambert D.L., 1990, ApJS 72, 387
Tyson N.D., Rich R.M., 1991, ApJ 367, 547
Van den Hoek L.B., et al., 1993, A&A, in praparation
Vassiliadis E., Wood P.R., 1992, preprint
Volk K., Cohen M., 1989, AJ 98, 931
Volk K., Cohen M., 1990, AJ 100, 485
Volk K., Kwok S., Stencel R.E., Brugel E., 1991, ApJS 77, 607
Westerlund B.E., Lequeux J., Azzopardi M., Rebeirot E., 1991, A&A 244, 367
Westerlund B.E., Azzopardi M., Breysacher J., Rebeirot E., 1992, A&A 260, L4
Whitelock P.A., 1990, PASPC 11, 365
Willems F.J., de Jong T., 1988, A&A 196, 173
Wood P.R., 1990, in: From Miras to Planetary Nebulae, eds. M.O. Mennessier, A. Omont, Editions Frontieres, Gif-sur-Yvette, p. 67
Zijlstra A.A., Loup C., Waters L.B.F.M., de Jong T., 1992, A&A 265, L5
Zuckerman B., Aller L.H., 1986, ApJ 301, 772

Chapter 2

A revised model for circumstellar molecular emission

Abstract

A model is presented to calculate the line profiles of thermal emission of molecules in an expanding circumstellar envelope. Special attention is given to the heating and cooling mechanisms which determine the kinetic temperature of the gas. The constraints that the presence of dust put on the molecular emission model are discussed. The following processes are found to have an effect of more than 10% on the integrated intensities (relative to a standard model): cooling by ^{13}CO, cooling by H_2O, and the location of the inner boundary of the molecular shell. The model including all physical features predicts CO(6-5) intensities which are 25% larger and CO(1-0) intensities which are 10% smaller than those of the standard model. Photoelectric heating can be the dominant source of heating in the outer layers, thereby determining the CO(1-0) intensity, depending on the beam size of the telescope and the efficiency of the shielding of UV radiation by dust.

1 Introduction

Knowledge of the mass loss rate of AGB stars is crucial in understanding their evolution, because mass loss effectively determines the lifetime of a star on the AGB. The mass loss rate can be deduced from modelling the dust emission (e.g. Bedijn 1987, Schutte & Tielens 1989, Justtanont & Tielens 1992, Griffin 1993) or the molecular line emission. With regard to the latter, detailed models for individual stars have been proposed (IRC 10 216: Kwan & Hill 1977 (KH), Kwan & Linke 1982 (KL), Sahai 1987, Huggins et al. 1988, Truong-bach et al. 1991; U Cam: Sahai 1990; AFGL 2688: Truong-bach et al. 1990) or the convenient formula of Knapp & Morris (1985, KM) to calculate the mass loss rate has been widely used. Recently, Kastner (1992) presented an improved simple fit formula.
The KM-formula is based on the assumption that the kinetic temperature derived for the infrared carbon star IRC 10 216 holds in all cases. Recently it has been shown that the kinetic temperature structure can be very different from that in IRC 10 216 (Sahai 1990, Jura et al. 1988 (JKO), Kastner 1992). Evidently, the kinetic temperature is strongly coupled to the molecular excitation calculation.
In this paper the heating and cooling mechanisms and the assumptions involved in calculating the kinetic temperature and the influence of them on the line profiles are investigated. The constraints that the presence of dust puts on molecular models are discussed.
In Sect. 2 all necessary theoretical ingredients are presented. In Sect. 3 the different components involved in the heating and cooling calculations and their relation to the line profiles are investigated. The results are discussed in Sect. 4.

Table 1: The molecular constants

Molecule	μ_0 (D)	μ_{IR} (D)	B (MHz)	D (MHz)	ω (cm^{-1})
^{12}CO	0.11	0.09	57635.97	0.1835	2170
^{13}CO	0.11	0.09	55101.02	0.1677	2075
HCN	2.99	0.10	44315.98	0.0872	715

Note. In Sect. 3 a value of $\mu_{IR} = 0.10$ is adopted for CO, in accordance with the value adopted by KH. μ_0 and μ_{IR} are the molecular dipole moment and the vibrational matrix element, and ω is the frequency of the v = (0-1) transition.

2 Theory

2.1 The molecular excitation program

The model described by Morris et al. (1985) is used to calculate the level populations. The main assumptions are spherical symmetry and that the Sobolev approximation is valid (this presumes that the local linewidth is much smaller than the expansion velocity). The molecules are excited by: (1) collisions with H_2 molecules, (2) interaction with the 2.8 K background radiation, and (3) infrared radiation from a central blackbody of temperature T_{BB} and radius R_{BB} which leads to pumping from the v = 0 vibrational state into the v = 1 state.
The original model of Morris et al. was changed to incorporate the following effects:

1. In the original model the velocity law was used to calculate the radiation intensities in the vibrational and rotational lines but was not used in the density calculation. This was changed to give n(r) $\sim r^{-2}$ v^{-1} instead of the original n(r) $\sim r^{-2}$.

2. Helium is taken into account as a collision partner. The CO + He and HCN + He collisional cross sections are taken from Green & Chapman (1978) and Green & Thaddeus (1974), respectively. The abundance f_{He} = n(He)/n(H) is specified in the program.

3. In the original model the energy levels were calculated from E(J) = B J (J+1), where B is the rotational constant. Here, the second order term is included leading to E(J) = B J (J+1) − D (J (J+1))^2.

4. In the original model the temperature structure of the gas in the envelope is specified. The most important change to the Morris et al. model is that in the present calculations the temperature structure is calculated in a self-consistent manner (see the next section).

The main input parameters are: the mass loss rate, the velocity law, the distance to the star, the photospheric abundance of the molecule of interest, the inner and outer radius of the envelope and the temperature and radius of the central blackbody to calculate the infrared intensities.
The calculations are performed using 99 gridpoints in the radial distance. Twenty-five rotational levels in both the v = 0 and v = 1 vibrational state are included. The line profiles are calculated at 48 velocity points. The molecular constants used are listed in Table 1. In the case of HCN, hyperfine splitting is neglected in the calculations.

2.2 The thermal balance equation for the gas

The kinetic temperature of the gas is given by (Goldreich & Scoville 1976 (GS), JKO):

$$\frac{dT}{dr} = (2 - 2\,\gamma)\,(1 + 0.5\,\epsilon)\,\frac{T}{r} + \frac{\gamma - 1}{n(H_2)\,k\,v(r)\,(1 + 2\,f_{He})}\,(H - C) \tag{1}$$

where T is the gas temperature, γ the adiabatic index, $\epsilon = \frac{d \ln v}{d \ln r}$ the logarithmic velocity gradient, k the Boltzmann constant, H the total heating rate per unit volume and C the total cooling rate per unit volume.
Equation (1) can be simplified to:

$$\frac{dT}{dr} = -\beta \frac{T}{r} + f(r) \tag{2}$$

with as boundary condition $T(r_{inner}) = T_0$ and where β is essentially constant between two consecutive radial zones. The solution of Eq. (2) is:

$$T(r) = T_0 \left(\frac{r}{r_{inner}}\right)^{-\beta} + r^{-\beta} \int_{r_{inner}}^{r} f(x)\, x^{\beta}\, dx \tag{3}$$

The main heating processes are dust-gas collisions and the photoelectric effect on grains. Heating due to cosmic rays and to the temperature difference between the gas and the dust are also included.

2.2.1 The heating processes

The heating rate per unit volume by dust-gas collisions is given by (KH, GS):

$$H_{dg} = 0.5\, \rho\, v_{dr}^3\, n_d\, \sigma_d \tag{4}$$

where v_{dr} is the drift velocity of the dust w.r.t. the gas, n_d the dust grain number density and σ_d the dust cross section. This equation can be manipulated to give:

$$H_{dg} = 1.2254\, 10^{-40}\, n(H_2)^2\, \frac{\Psi\, (1 + 4\, f_{He})^2}{\rho_d\, a} \left(\frac{L\, Q\, v(r)}{\dot{M}}\right)^{3/2} \frac{1}{1 + \frac{v_{dr}}{v(r)}} \tag{5}$$

with the drift velocity in km s^{-1} given by:

$$v_{dr} = 1.4293\, 10^{-4} \left(\frac{L\, Q\, v(r)}{\dot{M}}\right)^{0.5} \tag{6}$$

where ρ_d is the dust grain density in gr cm^{-3}, a the grain size in μm, L the stellar luminosity in solar units, $\dot{M}$ the mass loss rate in $M_\odot$/yr, Q the effective absorption coefficient (defined in Eq. 18), v(r) the gas velocity in km s^{-1} and Ψ the dust-to-gas ratio. The term $1/(1+v_{dr}/v)$ was not included in the original KH result (see Sahai 1990).
The gas and the dust have different temperatures. Therefore, heat can be exchanged between the two species. This process is insignificant in the energy balance for the dust (see e.g. Elitzur 1982) but may be important for the gas. The heating rate of the gas per unit volume may be written as (Burke & Hollenbach 1983):

$$H_{\Delta T} = n_H\, n_d\, \sigma_d \left(\frac{8\, k\, T}{\pi\, m_H}\right)^{0.5} \alpha_c\, 2k\, (T_d - T) \tag{7}$$

where α_c is the accommodation coefficient and T_d the dust temperature. If all hydrogen is in molecular form (valid for T $\lesssim$1500 K) this equation can be written as:

$$H_{\Delta T} = 2.008\, 10^{-31}\, n(H_2)^2\, \frac{\Psi\, (1 + 4\, f_{He})}{\rho_d\, a}\, T^{0.5}\, (T_d - T)\, \alpha_c \tag{8}$$

The accommodation coefficient was determined by fitting the data in Fig. 4b of Burke & Hollenbach following the functional form in Hollenbach & McKee (1979):

$$\alpha_c = 0.35\, e^{-\sqrt{(T_d+T)/500}} + 0.1 \tag{9}$$

Note that when $T > T_d$, this process actually cools the gas.
The heating rate per unit volume by the photoelectric effect can be written as (see de Jong 1977, Tielens & Hollenbach 1985):

$$H_{pe} = 1.37\, 10^{-24}\, n(H_2)\,(1+4\, f_{\rm He})\,\frac{\Psi}{\rho_d\, a}\, G_0 \left(\frac{Y}{0.1}\right) e^{-\tau_{0.1}} \left[\frac{(1-x)^2}{x} + x_k\, \frac{x^2-1}{x^2}\right] \tag{10}$$

where $\tau_{0.1}$ is the dust optical depth from radius r to infinity at 0.1 μm, a is in micron, Y is the photoelectric yield of dust grains and G_0 is the UV flux in terms of the diffuse interstellar medium. The standard values Y = 0.1 and G_0 = 1 are used unless otherwise noted. The grain charge parameter x is given by:

$$x^3 + (x_k - x_d + \gamma)\, x^2 - \gamma = 0 \tag{11}$$

with x_k = kT/13.6 eV = 6.33 10^{-6} T and x_d = 0.442 for the standard photoelectric threshold energy (6 eV) and γ is given by:

$$\gamma = 2.910^{-5}\, G_0 \left(\frac{Y}{0.1}\right) \frac{T^{0.5}}{n_e}\, e^{-\tau_{0.1}} \tag{12}$$

where n_e is the electron density. The reaction CO $\rightarrow$ O + C $\rightarrow$ O + C^+ + e^- is the main provider of electrons. Mamon et al. (1988) show that the abundance of neutral carbon is always less than the CO or C^+ abundance, so it is assumed that $n_e = n_{H_2}\, f_{CO}\, (1-X_{CO})$, where X_{CO} (see Eq. 19) is the fraction of C atoms in CO ($X_{CO} \equiv 1$ at the inner radius).
The heating rate per unit volume by cosmic rays is given by (Goldsmith & Langer 1978):

$$H_{cr} = 6.4\, 10^{-28}\, n(H_2)\,(1+4\, f_{\rm He}) \tag{13}$$

The uncertainty in the numerical coefficient is roughly a factor of 2.

2.2.2 The cooling processes

The cooling term C in Eq. (1) comprises molecular cooling by ^{12}CO, ^{13}CO, HCN, H_2 and H_2O. Other species may be neglected. The cooling rate of ^{12}CO, ^{13}CO and HCN is calculated in the molecular excitation program from (Goldreich & Kwan 1974, de Jong et al. 1975):

$$C_{\rm mol} = n_{\rm mol} \sum_{J=1}^{\infty} (2J+1)\, A_{J,J-1}\, \beta_{J,J-1}\, E_{J,J-1} \left(n_J - \frac{n_{J-1} - n_J}{\exp(E_{J,J-1}/kT_{BG}) - 1}\right) \tag{14}$$

where $\beta_{J,J-1}$ is the escape probability of the rotational line radiation (see Castor 1970), $A_{J,J-1}$ the Einstein coefficient, $E_{J,J-1}$ the energy difference between levels J and J-1, n_J the fractional sub level population, $n_{\rm mol}$ the number of molecules per unit volume and T_{BG} the temperature of the cosmic background radiation.
The cooling rate by H_2 molecules, under the assumption of LTE, has been tabulated by Hartquist

et al. (1980). The cooling rate per unit volume in the temperature range 100-900 K is well described by:

$$C_{H_2} = n(H_2)\, 2.611\, 10^{-21}\, (T/1000)^{4.74} \tag{15}$$

The assumption of LTE is valid at densities $\gtrsim 10^6$ cm^{-3}. For a mass loss rate of $\sim 10^{-5}$ $M_\odot$/yr and an expansion velocity of $\sim$15 km s^{-1}, this occurs at distances $\lesssim 3\ 10^{15}$ cm, or near the inner radius. Based on Eq. (15) it is expected that cooling by H_2 molecules is only important at high temperatures, or small radii, where the condition of LTE is fulfilled. At larger radii the condition of LTE is not fulfilled but it is expected that cooling by H_2 is not important. Therefore the assumption to use Eq. (15) in the entire envelope is not critical.
It is beyond the scope of this paper to include the effects of H_2O cooling in a self-consistent manner. Therefore the results available in the literature are used. Goldreich & Scoville (1976) developed a simple model to calculate the cooling rate by H_2O molecules. A similar model was used by Tielens (1983). Goldreich & Scoville presented their formula only for the explicit case they considered. Furthermore, they made some "non-essential simplifying approximations", which are neither necessary nor completely valid in all cases. Therefore, the formalism to calculate the cooling rate by H_2O is re-derived for the general case in Appendix A.
An important quantity is the water abundance. The water abundance is determined by the photodecay chain $H_2O \rightarrow OH + H \rightarrow O + H + H$. Other oxygen containing molecules like SO, SO_2 or O_2 always remain trace species. From chemical equilibrium studies which plot the H_2O, OH and O abundance as a function of radial distance it is derived that oxygen is mainly atomic at radii larger than twice the radius where the OH abundance reaches its maximum (Nejad & Miller 1988, Nercessian et al. 1989). The same conclusion is drawn from calculations which explicitly study the OH density profile as a function of mass loss rate and expansion velocity (Huggins & Glassgold 1982, Netzer & Knapp 1987). If the radius at which the OH profile peaks is taken from Netzer & Knapp, and it is assumed that oxygen is atomic at twice that distance, the maximum radius at which H_2O cooling can be important is given by:

$$r^{\max}(H_2O) = 35\, (\dot{M}/10^{-5}\, M_\odot/yr)^{0.7}\, (v/15\, \mathrm{kms}^{-1})^{-0.4}\quad 10^{15}\, \mathrm{cm}. \tag{16}$$

The photospheric abundance of H_2O is determined by the carbon and oxygen supply available. During first dredge-up the carbon abundance is depleted to roughly two-thirds of the main-sequence value while the oxygen abundance remains unchanged with respect to the main-sequence values, which are assumed to be solar (H = 12.0, C = 8.60 and O = 8.93 on a logarithmic scale). If it is assumed that all C is locked up in CO and the remaining O is in water, typical CO and H_2O abundances are $f_{CO} = n(CO)/n(H_2) = 5.3\ 10^{-4}$ and $f_{H_2O} = n(H_2O)/n(H_2) = 1.2\ 10^{-3}$ when the star arrives on the AGB. On the AGB a star may add carbon to its envelope during third dredge-up after a thermal pulse. If a star has increased its C/O ratio to 0.7, the abundances change to $f_{CO} = 1.2\ 10^{-3}$ and $f_{H_2O} = 5.1\ 10^{-4}$. Since oxygen is partly depleted in the gas phase due to dust formation, the estimated water abundances are in fact upperlimits. The CO abundance is allowed to vary with radius (see Sect. 3.9). For simplicity we assume that the water abundance is constant between the inner radius and $r^{\max}(H_2O)$. The importance of water cooling is investigated in Sect. 3.6.

2.3 How does dust affect the molecular excitation model?

Dust radiative transfer (DRT) models have been used to fit the spectral energy distribution (SED) of AGB stars and to derive mass loss rates (e.g. Bedijn 1987, Schutte & Tielens 1989). In fact, the mass loss rate can only be inferred if other quantities like the dust-to-gas ratio and

the dust properties are known.
The quantity which is derived from fitting the SED is the dust optical depth:

$$\tau_\lambda = 5.405\ 10^8\ \frac{\dot{M}\ \Psi\ Q_\lambda/a}{r_c\ R_*\ v_d\ \rho_d} \tag{17}$$

where $\dot{M}$ is in $M_\odot$/yr, v_d the dust velocity in km s^{-1}, Ψ is the dust-to-gas ratio, Q_λ/a the dust absorption coefficient over the grain size in cm^{-1}, ρ_d the grain density in gr cm^{-3}, r_c the inner radius in stellar radii and R_* the stellar radius in solar units. The inner radius is determined by the temperature of the dust at the inner radius, T_c. The derivation of equation (17) assumes a constant dust velocity and mass loss rate. Near the dust condensation radius, which effectively determines the optical depth, the dust velocity is $v_d = v_{gas}(r_{condensation}) + v_{drift} \approx$ (0.8-0.9) $v_{gas}(\infty)$ + (1-4 km s^{-1}) $\approx v_{gas}(\infty)$ for typical parameter values. The assumption that the dust velocity equals the terminal velocity of the gas is correct to within 10%. Comparing the parameters in Eq. (17) with the dominant heating source (Eq. 5) shows that $\dot{M}, \Psi, \rho_d$, a and Q cannot be varied independently but always must fulfill Eq. (17). JKO and Sahai (1990) also used the infrared fluxes to constrain their models, but their treatment is approximate and only uses the far-infrared fluxes. This method uses a fit to the entire SED.
The effective absorption efficiency Q (Eq. 5-6) is calculated following Sahai (1990):

$$Q = \frac{\int F_\lambda\ Q_\lambda\ d\lambda}{\int F_\lambda\ d\lambda} \tag{18}$$

where F_λ is the emerging flux from the central star and the dust shell. In principle Q depends on the radius since F_λ is continuously changed by the dust emission but this is only important near the inner radius where the dust temperature changes rapidly. The molecular emission originates from several tens to hundreds of stellar radii where F_λ is almost independent of the radial distance.
Radiative pumping of molecules is provided by thermal emission from hot dust close to the star. In molecular emission models this is represented by a blackbody of temperature T_{BB} and radius R_{BB}. These quantities can be estimated from the DRT-models. At each gridpoint in the DRT-model the blackbody temperature of the radiation field can be determined. It is then possible to obtain a realistic estimate of T_{BB} and R_{BB}. Finally, DRT-models provide $\tau_{0.1}$, which is needed to calculate the photoelectric heating (Eq. 10) and the dust temperature profile which is needed in the heating rate due to the gas-dust temperature difference (Eq. 7).

3 The relation between gas kinetic temperature and line profiles

In this section the components involved in calculating the gas kinetic temperature are investigated. The CO line profiles are calculated. The model of KH for IRC 10 216 will be the reference case. The aim is not to re-investigate IRC 10 216 but the KH results are the best documented regarding heating- and cooling rates and temperature structure.
The parameters in the KH model are: luminosity L = 21 000 $L_\odot$, distance D = 200 pc, mass loss rate $\dot{M} = 2\ 10^{-5}\ M_\odot$/yr, dust-to-gas ratio $\Psi = 0.01$, grain radius a = 0.1 μm, grain density ρ_d = 1 gr cm^{-3}, absorption efficiency Q = 0.013. For the effective temperature a value of T_{eff} = 2300 K is assumed (Ridgway & Keady 1988).
The inner boundary condition is T = 350 K at 2 10^{15} cm. The adiabatic index is $\gamma = 5/3$. The CO abundance is $f_{CO} = 8\ 10^{-4}$ and is constant between $r_{inner} = 2\ 10^{15}$ and $r_{outer} = 5\ 10^{17}$ cm. The velocity law is $v(r) = 16.0\ (1 - \frac{4 10^{14} cm}{r})^{0.5}$ km s^{-1}, but in the heating and cooling calculations KH assumed v = constant = 16.0 km s^{-1} and neglected the drift velocity (see Eq. 5).

Cooling by H_2, ^{13}CO and HCN is neglected and there is no Helium or H_2O present. Heating by the photoelectric effect, cosmic rays and the temperature difference between the gas and the dust is neglected. The central blackbody for calculating the infrared excitation is a 650 K blackbody of radius 6 10^{14} cm for CO and a 300 K, 3 10^{15} cm blackbody for HCN. The CO + H_2 and HCN + H_2 collision rates are taken from Green & Thaddeus (1974, 1976). KH did not explicitly state how they extrapolated the CO cross sections; I used the fit by de Jong et al. (1975).
The results of this standard case regarding the temperature structure and the CO(1-0), CO(2-1) and CO(3-2) profiles are shown in Fig. 1a. The profiles have been calculated for a 30m telescope (HPBW = 23" at 115 GHz, corresponding to a linear radius of 3.4 10^{16} cm at 200 pc). For the standard case I find a heating rate (neglecting the drift velocity in Eq. 5) per H_2 molecule of 7.5 10^{-26} erg s^{-1} and a cooling rate of 5.1 10^{-26} erg s^{-1} at 1 10^{17} cm. KH find 7.4 10^{-26} and 4.6 10^{-26} erg s^{-1}, respectively. The gas temperature and CO(1-0) excitation temperature in the model are 9.73 and 8.39 K at 1 10^{17} cm, 4.92 and 2.86 K at 4 10^{17} cm. KH find 9.8 K, 8.1 K and 5.0 K, 2.8 K, respectively. The model results agree excellently with KH, the small differences are probably due to numerical details in the two codes.
In the following subsections the influence of several assumptions on the temperature structure and the CO line profiles is investigated. In Table 2 the changes in the integrated intensity ($\int T\, dv$) relative to the standard case are tabulated for the lowest six transitions of ^{12}CO. In Figs. 1-4 the temperature structure and line profiles are shown for selected models.

Table 2: The integrated intensity of ^{12}CO

	Integrated intensity and relative change (in %)					
Model	J = 1-0	2-1	3-2	4-3	5-4	6-5
1 Standard KH case (in K km s^{-1})	417	876	1220	1490	1705	1875
2 v(r) and drift velocity consistent	−4	−7	−8	−9	−10	−10
3 Photoelectric heating $r_{0.1} = 2.3\ 10^{17}$cm/r	0	0	0	0	0	0
4 Cosmic ray heating	0	0	0	0	0	0
5 Heating due to gas-dust temperature difference	2	5	8	9	10	10
6 Cooling due to H_2	0	0	0	0	0	0
7 Cooling by H_2O included, $f_{H_2O} = 5\ 10^{-4}$	−4	−11	−15	−17	−18	−20
8 Cooling by H_2O included, $f_{H_2O} = 1.2\ 10^{-3}$	−5	−10	−13	−14	−15	−16
9 Cooling by ^{13}CO and HCN included	−4	−7	−9	−10	−11	−11
10 Helium, $f_{He} = 0.1$	−7	1	5	6	7	7
11 Outer radius set by photodissociation	0	0	0	0	0	0
12 Inner boundary T=1000 K at 5 R_*, γ=5/3	1	4	10	21	37	59
13 As model 12, $\gamma = 7/5$ when T > 350 K	1	4	10	22	39	62
14 L = 5250 $L_\odot$, d = 100 pc	−41	−42	−40	−37	−36	−35
15 L = 47250 $L_\odot$, d = 300 pc	−2	11	22	29	33	37
16 Mass loss times 2, dust opacity times 0.5	−34	−42	−41	−41	−40	−38
17 Mass loss times 0.5, dust opacity times 2	−11	12	35	51	61	67
18 combined model	−10	−2	6	13	20	27

The combined model includes: an inner radius at 4.2 10^{14} cm with T = 850 K, $\gamma = 7/5$ when T > 350 K, the outer radius determined by photodissociation, the photoelectric effect included, an helium abundance of n(He)/n(H) = 0.1, cooling by H_2, ^{13}CO and HCN included, velocity law and drift velocity included in the heating calculation as well as heating by cosmic rays and due to the gas-dust temperature difference. Standard values for the mass loss rate, distance and dust opacity are used.

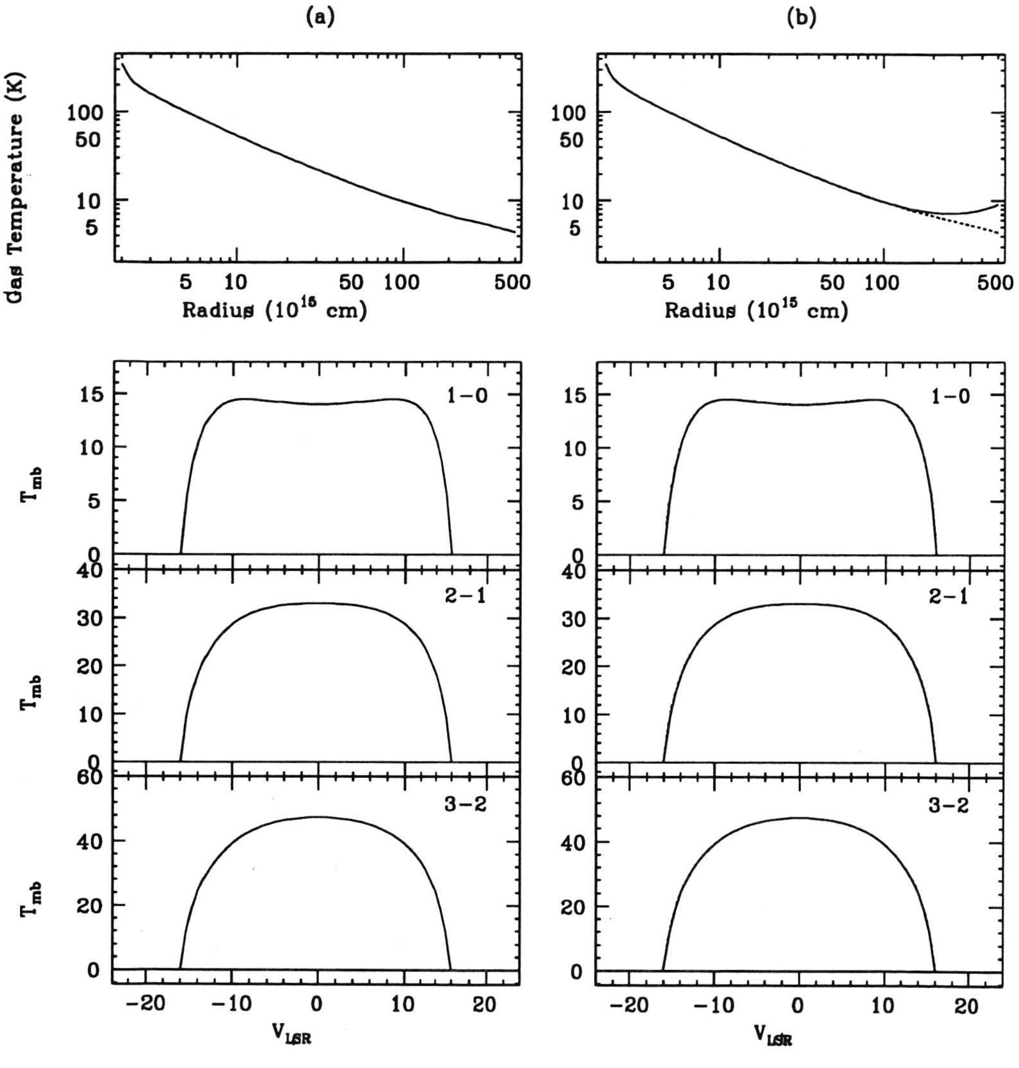

Figure 1: The temperature structure and CO line profiles for, (a) the standard Kwan & Hill (KH) case, and (b) when photoelectric heating is included. There is no change in the line profiles, only in the temperature structure. In panel (b) the standard KH case is represented by the dotted line. All profiles are calculated for a 30m telescope.

3.1 The velocity law and drift velocity

KH assumed v(r) = constant and neglected a term of the order $1/(1 + v_{dr}/v)$ in the heating calculation. This results in an overestimate of the heating rate (Eq. 5). When the velocity law and the drift velocity are properly taken into account, lower temperatures and less emission are expected. The intensities are reduced by 5-10%.

3.2 Heating by the photoelectric effect

When UV radiation can penetrate the outer layers of the envelope the photoelectric effect on grains can become important. The heating rate is given by Eqs. 10-12. Since KH assumed a constant CO abundance, the electron density would be zero and there would be no photoelectric effect ($\gamma \rightarrow \infty$, $x \rightarrow 1$, $H_{pe} \rightarrow 0$). In order to get an estimate of the heating rate a value of $x = 0.7$ was assumed (Eq. 10). This gives an heating rate similar to the one adopted by KL and Truong-Bach et al. (1990). The parameter $\tau_{0.1}$ was estimated from Ridgway & Keady (1988) who derived an dust optical depth of 5.5 at 2 μm and an inner dust radius of 5 R_*. Extrapolating the optical depth to 0.1 μm using the absorption efficiency of amorphous carbon (Rouleau & Martin 1991) which is appropriate for IRC 10 216 (Martin & Rogers 1987, Orofino et al. 1990, Griffin 1990), leads to an optical depth of 730 at the inner dust radius, or $\tau_{0.1} = 2.3\ 10^{17}$ cm/r. This calculation neglects scattering. When scattering is important, which depends on the grain size, the optical depth at 0.1 μm will be larger. The line profiles and temperature structure are shown in Fig. 1b, which clearly illustrates the heating in the outer layers. *In this particular case*, photoelectric heating has a negligible effect on the line intensities because the beam size ($3.4\ 10^{16}$ cm) is smaller than the region where the temperature is increased ($>2.3\ 10^{17}$ cm). The ^{12}CO(1-0) integrated intensity is raised by 0.1%.

The photoelectric effect is a potentially important heating mechanism in the outer layers, but the effect on the (1-0) profile depends on the telescope beam size relative to the region where the UV radiation can effectively penetrate, which in turn depends on the uncertain contribution of scattering to the dust opacity at UV wavelengths.

3.3 Heating by cosmic rays

This effect is totally negligible in this case. The temperature at the outer radius is raised by only 0.3 K compared to the standard case. The (1-0) integrated intensity is raised by 0.1%.

3.4 Heating by the gas-dust temperature difference

To estimate the effect of this process (Eq. 7), a dust temperature profile has to be adopted. From Griffin (1990) it is derived that for IRC 10 216 $T_d = 530\ (r/10^{15}\ \mathrm{cm})^{-0.413}$ is a good approximation. The effect is non-negligible. The intensities are raised by up to 10 percent. The ratio of the heating rates $H_{\Delta T}/H_{dg}$ is 0.18 at the inner radius and 0.04 at 10^{17} cm.

3.5 Cooling by H_2

Cooling by H_2 turns out to be negligible at the temperatures considered in the KH case (T < 350 K). The CO(6-5) integrated intensity is decreased by 0.2%. Since the cooling rate is a strong function of the T (see Eq. 15), it is expected that cooling by H_2 molecules may become important at higher temperatures.

3.6 Cooling by H_2O

In the case of oxygen-rich envelopes, H_2O cooling in the inner part of the envelope will be important. We included H_2O cooling following the recipe outlined in Appendix A. From Eq. (16) it follows that $r^{max}(H_2O) = 55.4\ 10^{15}$ cm. Models are calculated for abundances $f_{H_2O} = 5.0\ 10^{-4}$ and $1.2\ 10^{-3}$. The profiles are shown in Fig. 2a. The reduction in integrated intensity is substantial, up to 20% for the 6-5 transition. The reduction in the (1-0) line profile is much smaller, partly because all oxygen is in atomic form at the radii where the (1-0) emission arises. Most interestingly, the reduction in intensities is less for the larger water abundance. This can be understood in terms how water cooling is treated (see Appendix A). The amount of water

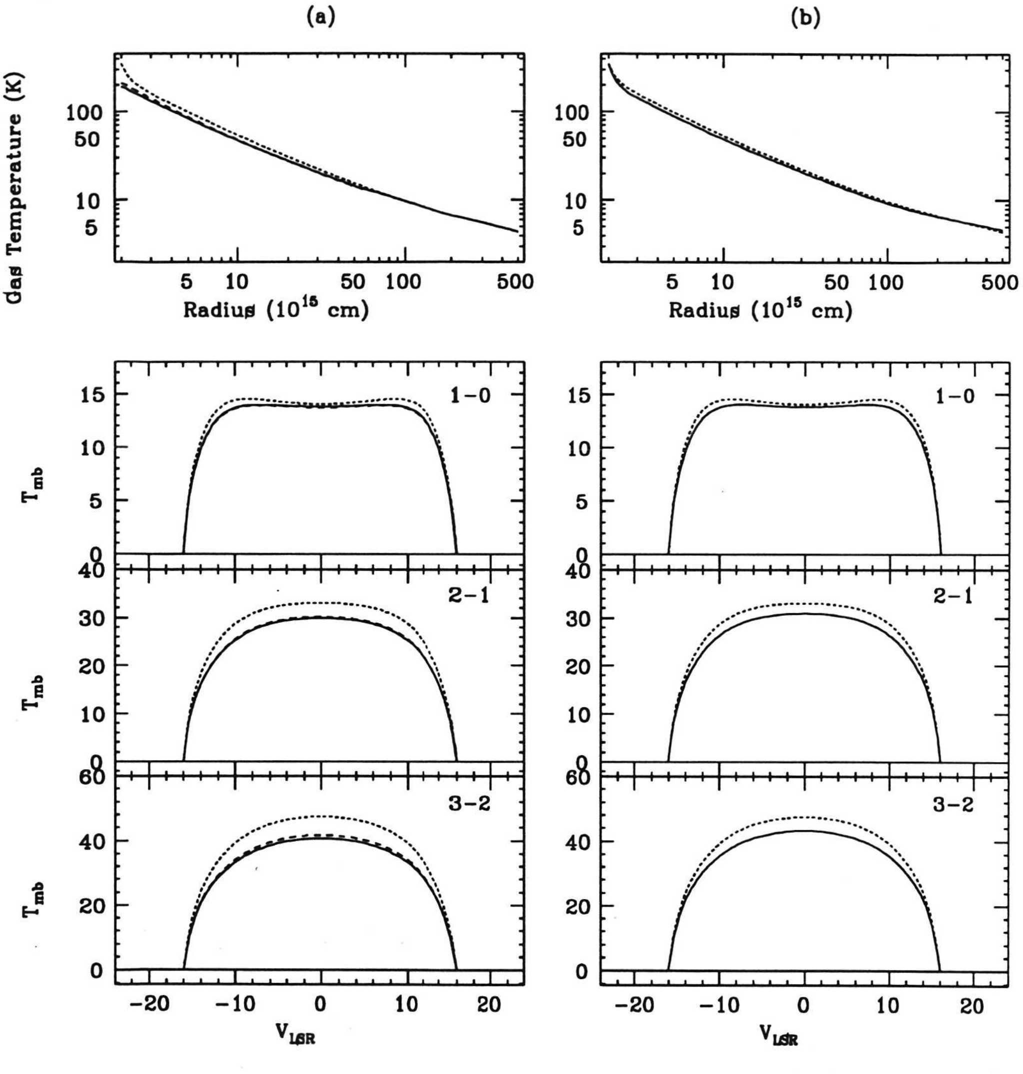

Figure 2: The temperature structure and CO line profiles when, (a) water cooling is included with an abundance f_{H_2O} = 5 10^{-4} (solid line) and f_{H_2O} = 1.2 10^{-3} (dashed line), and (b) cooling by ^{13}CO and HCN is included. The dotted line indicates the standard KH case.

cooling depends on the product of the number density of water molecules and the difference between the gas temperature and the excitation temperature of the water molecules. For large water abundances collisions tend to make both temperatures equal, so that with increasing water abundance the reduction in the integrated CO line intensities reaches a maximum. From some test calculations it follows that the lowest CO line intensities are found for 3 10^{-4} $\lesssim f_{H_2O} \lesssim$8 10^{-4}, depending on the transition. For f_{H_2O} = 5 10^{-4}, the ratio of the H_2O to the CO cooling rate is ~64% at the inner radius, ~36% at 10^{16} cm and ~15% at $r^{max}(H_2O)$. The excitation temperature of the water molecules is about 2 K below the gas temperature.

3.7 Cooling by ^{13}CO and HCN

Cooling by ^{13}CO can be expected to be more important than H_2O cooling because the photodissociation radius of ^{13}CO is within 10% equal to that of ^{12}CO (Mamon et al. 1988). Therefore cooling by ^{13}CO will be important in the entire envelope and not, like water cooling, be limited to the inner envelope. In the following calculations an isotopic ratio ^{12}CO/^{13}CO = 35 ($f_{^{13}CO}$ = 2.29 10^{-5}) and f_{HCN} = 1.0 10^{-5} are assumed. For simplicity, the outer radius for HCN is also taken to be 5 10^{17} cm[1]. The ^{12}CO line profiles, when ^{13}CO and HCN cooling are included, are shown in Fig. 2b. The emission is decreased by 4% (J = 1-0) to 11% (J = 6-5).
Although the abundance of the relevant species is ^{12}CO : ^{13}CO : HCN = 96.0 : 2.8 : 1.2, the contribution of the cooling rates is 81.2 : 8.1 : 10.7 at 2 10^{15} cm, 81.2 : 11.8 : 7.0 at 1 10^{16} cm and 89.4 : 8.8 : 1.8 at 1 10^{17} cm. This clearly demonstrates that ^{13}CO and HCN are more important coolants than indicated by their relative abundances. This is due to the fact that ^{12}CO is optically thick and line radiation can not escape. The ^{13}CO lines are optically thin. When ^{12}CO is optically thin (low $\dot{M}$, low f_{CO}) it is expected that the relative cooling rates are similar to the abundance ratios. This suggests that ^{13}CO cooling is a non-negligible coolant in the envelopes of J-type carbon stars, where ^{12}C/^{13}C $\approx$ 5-10.

3.8 Helium

All other parameters being equal, the presence of Helium will increase the CO line intensities. The heating rate will remain the same, but the cooling rate will decrease since the CO number density is less. The profiles are shown in Fig. 3a for f_{He} = 0.1. The intensities are increased up to 7%. The change in lineshape is due to the increase in the emission region relative to the beam size of the telescope.

3.9 The outer radius and photodissociation

KH assumed a constant CO abundance and outer radius. In reality, CO will be dissociated by the interstellar UV field and the CO abundance will decrease outward. Mamon et al. (1988) have investigated this effect and found that the CO abundance, relative to the value close to the star, can be approximated as:

$$X_{CO} = e^{-ln(2)\,(r/r_{1/2})^{\alpha}} \tag{19}$$

where $r_{1/2}$ and α depend on $\dot{M}$ and v and are tabulated by Mamon et al. (1988). For the KH-case they are $r_{1/2}$ = 3.5 10^{17} cm and α = 2.9. The outer radius is set at the radius where the relative CO abundance drops to 1%, or r_{outer} = 6.7 10^{17} cm. *In this particular case*, the change in the line profiles is negligible because the beamsize is much smaller than $r_{1/2}$.

3.10 Dust opacity and mass loss rate

Following the equation for the heating rate (Eq. 5) and the constraint put by DRT-models (Eq. 17) the largest change in the profiles can be expected by changing $\dot{M}$ and the dust opacity Q. Keeping $\dot{M}$Q constant (cf. Eq. 17), $\dot{M}$ = 4 10^{-5} $M_\odot$/yr, Q = 0.0065 and $\dot{M}$ = 1 10^{-5} $M_\odot$/yr, Q = 0.026 are considered. The profiles are shown in Fig. 3b. Not only are the intensities changed due to the difference in heating, also the profiles are changed due to the change in the ratio of the beam size to the size of the emission region.
For both $\dot{M}$ = 1 10^{-5} and 4 10^{-5} $M_\odot$/yr the CO(1-0) emission is less than for 2 10^{-5} $M_\odot$/yr. As noted by Kastner (1992), the relation $T_{mb} \sim \dot{M}$ of the KM-formula breaks down for high

[1] Observations of IRC 10 216 show that HCN is present to at least 22" or 6.6 10^{16} cm (Bieging et al. 1984).

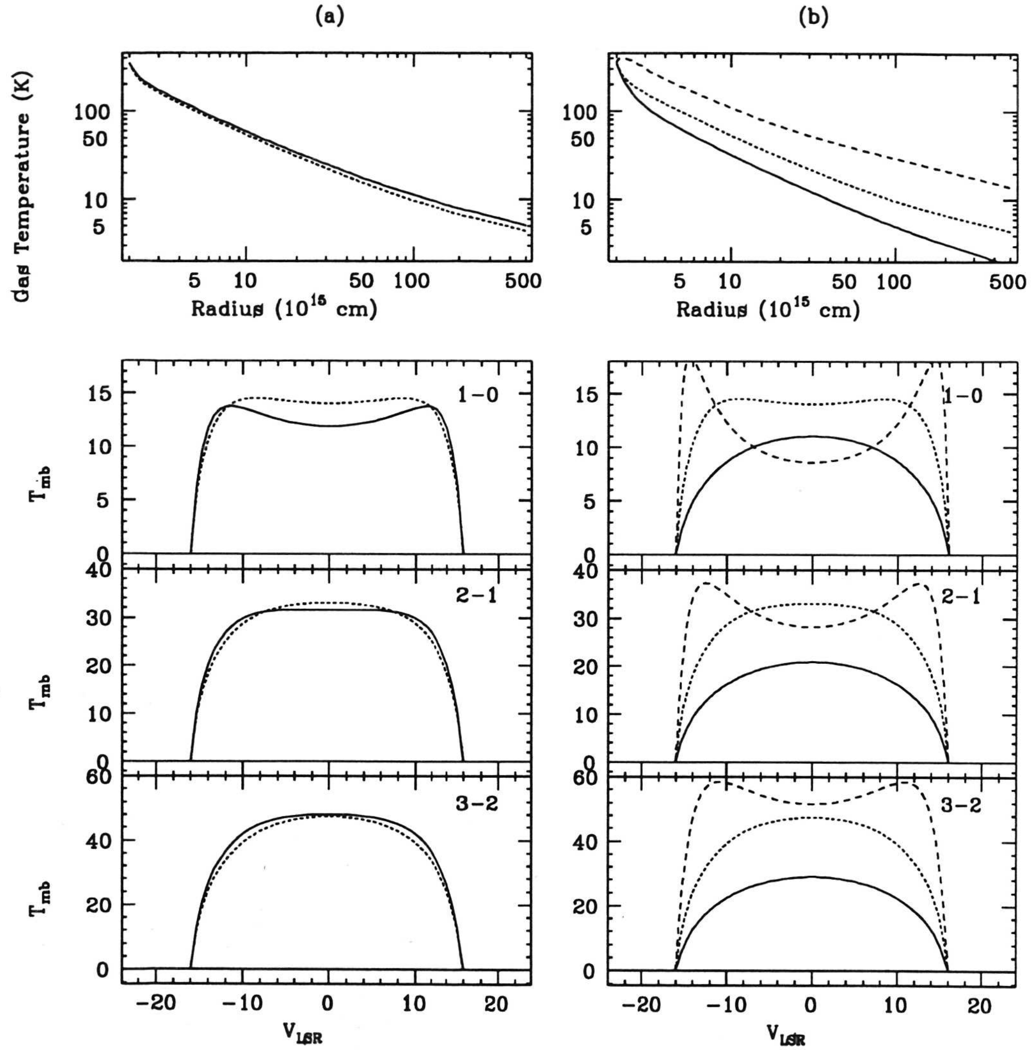

Figure 3: The temperature structure and CO line profiles when, (a) an Helium abundance $f_{He} = 0.1$ is included, and (b) the mass loss rate and absorption efficiency are changed: $\dot{M} = 4\ 10^{-5}\ M_\odot/yr$, $Q = 0.0065$ (solid line) or $\dot{M} = 1\ 10^{-5}\ M_\odot/yr$, $Q = 0.026$ (dashed line). The dotted line is the standard KH case.

mass loss rates. For mass loss rates above a certain value, the decrease in heating rate is more important than the increase in the CO number density, if the mass loss rate is increased beyond this critical value.

3.11 The inner boundary and the adiabatic index

The influence of the inner boundary condition on the temperature and the line profiles has not been properly investigated. KH assumed T = 350 K at 2 10^{15} cm, JKO assumed 4000 K at 3 10^{15} cm. Sahai (1990) points out that to take the radiative excitation into account properly, one needs to start the calculations at a few 10^{14} cm. Ideally one would use the central star as the inner boundary condition but this is not feasible. Shocks may have dissociated the molecules and ionized the hydrogen (Hinkle et al. 1982). From CO observations of χ Cyg there seems to be a stationary inner layer of ~800 K at ~10 R_* (Hinkle et al. 1982). A natural boundary condition seems to be the dust condensation radius since at this point the gas-dust heating process becomes effective.

For the standard KH case a model is calculated with the inner boundary condition modified to T = 1000 K at $r_{\rm inner} = 5\ R_* = 3.2\ 10^{14}$ cm. In the velocity law ($v \sim (1 - c/r)^{0.5}$) the constant c is reduced from 4 10^{14} cm (see Sect. 3.0) to 3 10^{14} cm to make this inner boundary possible. As could be expected, the emission from the higher transitions is significantly increased (up to 60% for the J = 6-5 transition).

An additional complication is that due to rotational excitation of H_2, the adiabatic index becomes less than 5/3 when T $\gtrsim$300-1000 K (GS, JKO). To simulate this effect the same boundary condition as above, but with $\gamma = 7/5$ when T > 350 K was assumed. The profiles are shown in Fig. 4a (dashed line). The effect of the change in adiabatic index is small (~3%) even at the high transitions.

3.12 Putting it all together: the combined model

The combined effect of the parameters discussed in Sect. 3.1-3.11 is investigated now. The standard value of the mass loss rate, distance and opacity are adopted. The velocity law and drift velocity are taken into account in the heating calculations, photoelectric heating is included with $\tau_{0.1} = 2.3\ 10^{17}$cm/r, heating by cosmic rays and the gas-dust temperature difference is included, photodissociation of ^{12}CO and ^{13}CO is included (Eq. 19) with $r_{1/2} = 3.5\ 10^{17}$ cm, $\alpha = 2.9$ for both species (for simplicity the same values are used for HCN), cooling by H_2, ^{13}CO and HCN is included ($f_{^{13}CO} = 2.29\ 10^{-5}$, $f_{HCN} = 1.00\ 10^{-5}$), Helium is included ($f_{He} = 0.1$) and the inner boundary is at $r_{\rm inner} = 4.2\ 10^{14}$ cm. In Sect 3.11 a temperature at the inner boundary of 1000 K was used. This value was probably too low as the temperature immediately rises for larger radii (Fig. 4a). In the combined model the temperature at the inner radius is varied to give a smooth temperature profile near the inner radius. This results in an inner temperature of 850 K. The adiabatic index is $\gamma = 7/5$ when T > 350 K and $\gamma = 5/3$ when T < 350 K.

The resulting temperature structure and profiles are shown in Fig. 4b. Relative to the standard KH case, the J = 1-0 and 2-1 intensities are reduced by up to 10% while the higher transitions (J = 5-4, 6-5) are increased by 20-25%. For completeness, the ^{13}CO and HCN profiles and intensities for the standard KH case and the combined model are given in Fig. 5 and Table 3. The ^{13}CO intensities are reduced by ~25% and the HCN(1-0) line by ~15%.

Table 3: The integrated intensity of ^{13}CO and HCN

		Integrated intensity (K km s^{-1})			
Model		^{13}CO(1-0)	^{13}CO(2-1)	^{13}CO(3-2)	HCN(1-0)
1	Standard KH case	34.0	112	195	181
18	combined model	25.8	85.9	151	158
	relative change	–24%	–23%	–23%	–13%

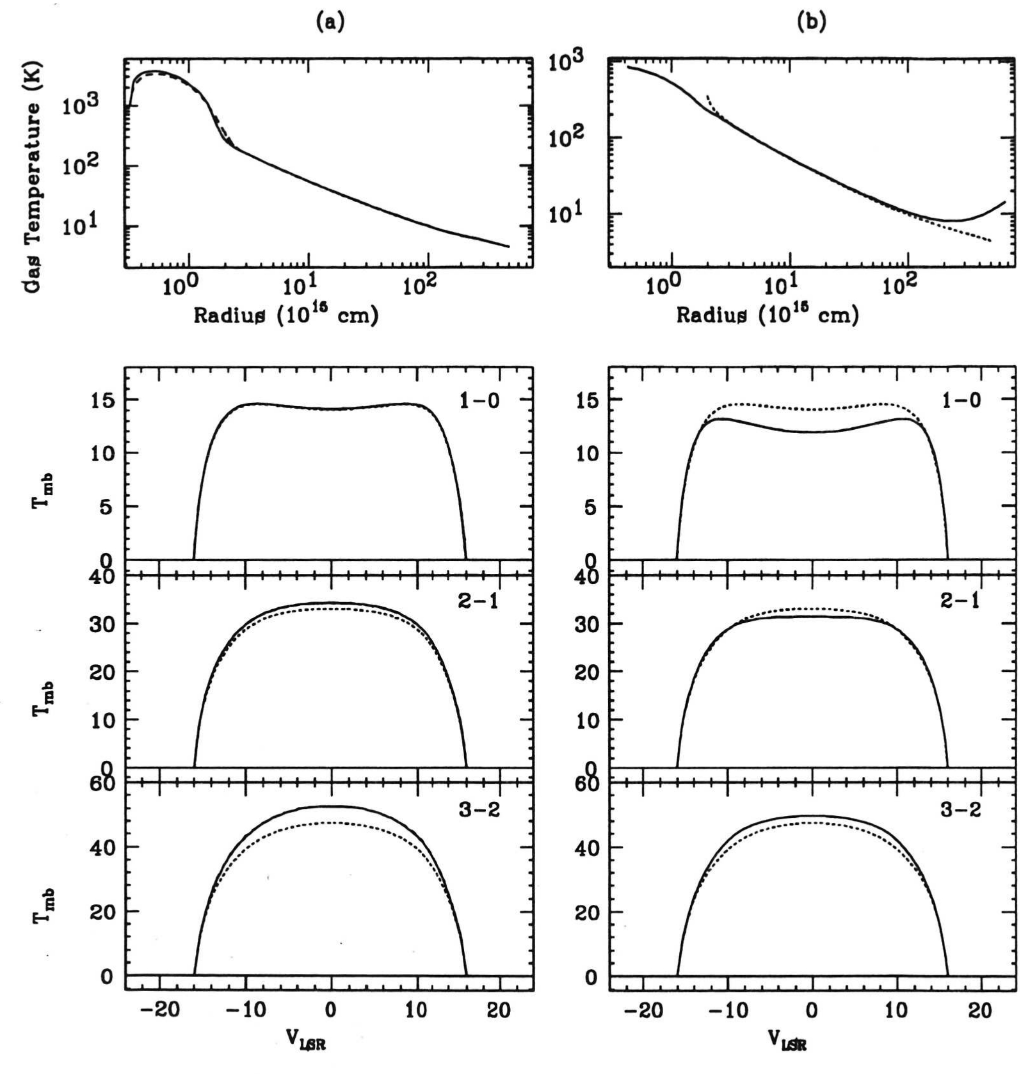

Figure 4: The temperature structure and CO line profiles when, (a) the inner boundary is T = 1000 K at 3.2 10^{14} cm with $\gamma = 5/3$ for all temperatures (solid line) and (b) the 'combined' model including all physics (see Sect. 3.12 for all details). The dotted line is the standard KH case.

4 Discussion

A model is presented to calculate the line profiles of molecules in the expanding shell around a central star. The temperature structure is calculated in a self-consistent manner. Previous models (e.g. KH or Sahai 1990) usually only considered heating due to dust-gas collisions and cooling due to ^{12}CO (and adiabatic cooling). Here, also additional heating and cooling processes are considered. It is found that ^{13}CO and HCN can be important coolants in carbon stars. The model can also be applied to oxygen-rich stars, since water cooling has been included in an approximate manner. Photoelectric heating can be the dominant source of heating in the outer

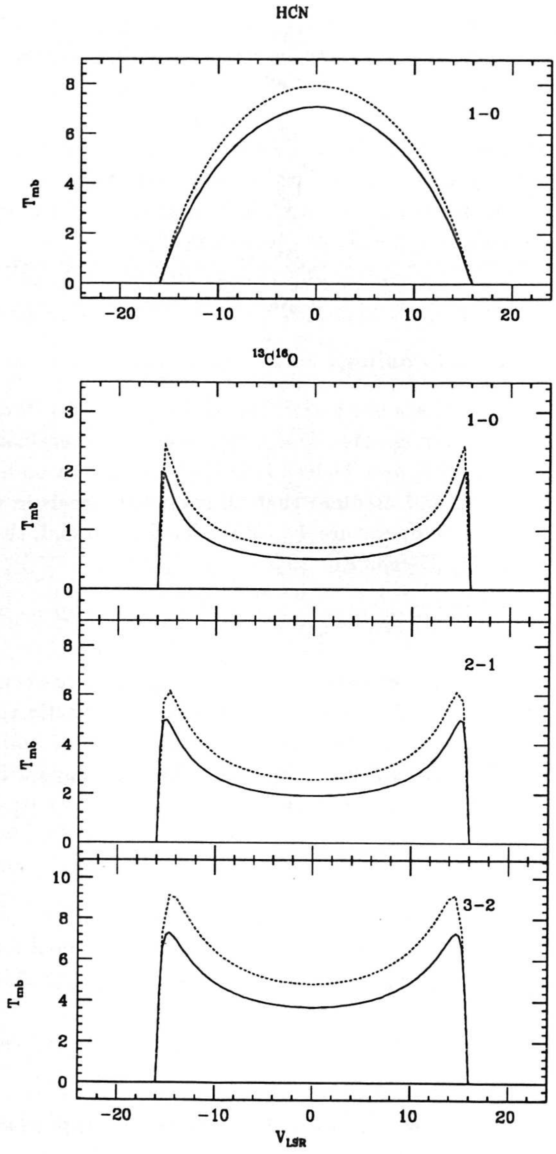

Figure 5: The HCN and ^{13}CO line profiles for the combined model (solid line) and the standard KH case (dotted line).

layers, thereby determining the CO(1-0) intensity, depending on the beam size of the telescope and the efficiency of the shielding of UV radiation by dust. For IRC 10 216 the effects of several physical modifications to the standard KH model are investigated. The final model, including all physics, predicts integrated intensities which are 25% larger for the CO(6-5) transition and 10% smaller for the CO(1-0) transition. The changes for the low ^{13}CO transitions are $\sim$25% and for the HCN(1-0) transition about 15%. The accuracy of observed line profiles is usually limited by calibration uncertainties (about 10%). This means that the physical effects discussed in Sect.

3.1-3.11 have to be included in theoretical models for an accurate comparison with observations. The combination of simultaneously fitting the spectral energy distribution and the molecular line emission is potentially the most accurate method to determine the mass loss rate in AGB stars.

Acknowledgements. I thank Mark Morris for providing a copy of his numerical code and subsequent support and Xander Tielens for his comments on the treatment of water cooling and the photoelectric effect, and for his interest in this project. Teije de Jong and René Oudmaijer are thanked for valuable comments on the manuscript.

Appendix A: H_2O rotational cooling

I re-derive the equations to calculate the excitation temperature of a H_2O molecule and present the equation to calculate the cooling rate. This treatment is a generalization of the description by Goldreich & Scoville (1976, GS) and Tielens (1983). The calculation is based on the classical treatment of the H_2O molecule and assumes that all rotational levels in the ground vibrational state have the same excitation temperature T_x. With T_x determined, the cooling rate per unit volume is given by (GS Eq. 11, Tielens Eq. 15):

$$C_{H_2O} = n_{H_2}\,(1+\sqrt{2}\,f_{He})\,n_{H_2O}\ <\sigma\,v>\ h\nu\,\left(e^{-h\nu/kT}-e^{-h\nu/kT_x}\right) \tag{A1}$$

where n_{H_2} and n_{H_2O} are the number densities of the respective molecules, f_{He} is the Helium abundance relative to hydrogen and $<\sigma\ v>$ is the H_2-H_2O inelastic collisional rate constant which is set to $<\sigma\ v> = 2.0\ 10^{-11}\ T^{1/2}\ cm^3 s^{-1}$ (GS). The He-H_2O collisional rate is assumed to be a factor $\sqrt{2}$ lower due to the difference in mass. The frequency ν is the classical value of the rotational frequency of an H_2O molecule whose rotational energy is $3kT_x/2$, or:

$$\nu = \nu_0\, T_x^{1/2} \tag{A2}$$

In the derivation of the excitation temperature I closely follow GS. The idealised water molecule has three scalar levels, two rotational levels in the ground vibrational state and one rotational level in the excited vibrational state. The rate equations are given by (GS Eq. A1):

$$\begin{aligned}
\frac{d\,n_1}{d\,t} &= \beta_{21}A_{21}n_2 + (A_{31}+B_{31}J_{13})n_3 - B_{13}J_{13}n_1 - C[n_1\ \exp(-h\nu_{21}/kT) - n_2]\\
\frac{d\,n_2}{d\,t} &= -\beta_{21}A_{21}n_2 + (A_{32}+B_{32}J_{23})n_3 - B_{23}J_{23}n_2 + C[n_1\ \exp(-h\nu_{21}/kT) - n_2]\\
\frac{d\,n_3}{d\,t} &= B_{13}J_{13}n_1 + B_{23}J_{23}n_2 - (A_{31}+B_{31}J_{13}+A_{32}+B_{32}J_{23})n_3\\
n_1 &+ n_2 + n_3 = n
\end{aligned} \tag{A3}$$

where $C = <\sigma\ v>\ n_{H_2}\ (1+\sqrt{2}\ f_{He})$. The molecular levels are numbered 1, 2 and 3 in order of increasing energy. The net radiative decay rate is given by $\beta_{21}\ A_{21}$, where A_{21} is the spontaneous decay rate of level 2, and β_{21} is the probability that a photon escapes without further interaction. GS verified that the rotational transitions are optically thick and using the Sobolev approximation (Castor 1970), the term $\beta_{21}\ A_{21}$ is given by (GS Eq. A5):

$$\beta_{21}\ A_{21} = \frac{16\,\pi\,v(r)}{3\,r\,\lambda_{21}^3\,(n_1-n_2)}\,(1+0.5\epsilon) \tag{A4}$$

where $\epsilon = \frac{d \ln v}{d \ln r}$. The profile averaged mean intensity for an optically thick line is given by (Castor 1970, GS Eq. A8):

$$J_{ij} = \epsilon \, W \, B_{\nu_{ij}}(T_e) \tag{A5}$$

where $B_{\nu_{ij}}(T_e)$ is the Planck function for a temperature T_e and W is the dilution factor $W = 0.5\,(1 - (1 - (R_e/r)^2)^{0.5})$. GS used the effective temperature and stellar radius for T_e and R_e, respectively. In other words, they neglected the influence of dust. The proper values for T_e and R_e are therefore T_{BB} and R_{BB}. Only in the case of low mass loss rates T_{BB} and R_{BB} will equal T_{eff} and R_*.

From the condition $dn_3/dt = 0$, assuming $A_{31} = A_{32}$ and defining $\frac{n_2}{n_1} \equiv e^{-h\,\nu_{21}/k\,T_x}$, the following relation is derived:

$$\frac{n_3}{n_2} = \frac{1}{\frac{2}{\epsilon W} + \frac{1}{e^{h\nu_{31}/kT_e}-1} + \frac{1}{e^{h\nu_{32}/kT_e}-1}} \left(\frac{e^{h\nu_{21}/kT_x}}{e^{h\nu_{31}/kT_e}-1} + \frac{1}{e^{h\nu_{32}/kT_e}-1} \right) \tag{A6}$$

Substituting Eq. (A6) in $\frac{1}{n_2}\frac{d\,n_1}{d\,t} = 0$ results in:

$$C \left(\exp(\frac{h\,\nu_{21}}{k}\,(\frac{1}{T_x} - \frac{1}{T})) - 1 \right) = \beta_{21}\, A_{21} +$$

$$\epsilon\, W\, A_{31} \left(\frac{1}{2 + \frac{\epsilon W}{e^{h\nu_{31}/kT_e}-1} + \frac{\epsilon W}{e^{h\nu_{32}/kT_e}-1}} \right) \left(\frac{1}{e^{h\nu_{32}/kT_e}-1} - \frac{e^{h\nu_{21}/kT_x}}{e^{h\nu_{31}/kT_e}-1} \right) \tag{A7}$$

It can be verified that if $h\nu_{21}/kT_x \ll 1$, $h\nu_{21}/kT \ll 1$, $h\nu_{21}/kT_e \ll 1$, $h\nu_{32}/kT_e \gg 1$ and $h\nu_{31}/kT_e \gg 1$ are fulfilled, Eq. (A7) simplifies to Eq. (A15) of GS, except for a factor 1/2 which seems to be missing in the last term of Eq. (A15) in GS.

If the excitation temperature derived from Eq. (A7) is to approximate the excitation temperature of the rotational levels of real water molecules, the values of ν_{21} and n (Eq. A3) must be chosen with some care. The appropriate value for n is given by (GS):

$$n = \frac{2\,(2\,J+1)}{Z_{rot}}\, n_{H_2O} \tag{A8}$$

where the rotational quantum number J and the partition function Z_{rot} are given by GS (Eq. A10-A12) and Tielens (Eq. A1-A2). They can be expressed as:

$$J = -0.5 + \sqrt{0.25 + j_0\, T_x} \tag{A9}$$

$$Z_{rot} = z_0\, T_x^{3/2} \tag{A10}$$

The frequency ν_{21} is given by Eq. (A2). The constants[2] are $\nu_0 = 2.54\ 10^{11}$ Hz, $j_0 = 7.39\ 10^{-2}$, $z_0 = 8.38\ 10^{-3}$. For the frequency $\nu_{31} = 1.13\ 10^{14}$ Hz is assumed, corresponding to the strong transition at 2.66 μm (GS). The frequencies are related through $\nu_{32} = \nu_{31} - \nu_{21}$. The Einstein coefficient equals $A_{31} = 34\ s^{-1}$ (GS). Substituting Eq. (A4) in Eq. (A7), using Eqs. (A2, A8, A9, A10) and the continuity equation results in:

$$2.0\ 10^{-11}\, T^{0.5}\, n_{H_2}\, (1 + \sqrt{2}\, f_{He}) \left(\exp(\frac{h\,\nu_{21}}{k}\,(\frac{1}{T_x} - \frac{1}{T})) - 1 \right) =$$

[2]Note that in some equations in GS the factor h should read $\hbar$ and that the quoted moments of inertia are a factor 2π too high, although the quoted values for j_0 and z_0 are correct. The value for ν_0 seems to be a factor 2 too low in GS. The values for j_0, z_0 and ν_0 are based on the more recent values of $I_1 = 1.004\ 10^{-40}$, $I_2 = 1.928\ 10^{-40}$ and $I_3 = 3.017\ 10^{-40}$ gr cm^2. Furthermore, GS make the approximation $M/\hbar = J$ while the correct expression is $M/\hbar = \sqrt{J(J+1)}$. This is why the value for j_0 approximately is the square of the value quoted by GS.

$$\frac{16\pi}{6} z_0 \left(\frac{\nu_0}{c}\right)^3 v(r)\,(1+0.5\epsilon)\,\frac{T_x^3}{\sqrt{1+4\,j_0\,T_x}} \left(\frac{1+e^{-h\,\nu_{21}/k\,T_x}+\frac{n_3}{n_2}}{1-e^{-h\,\nu_{21}/k\,T_x}}\right) /(r\, f_{H_2O}\, n_{H_2})$$
$$+\,\epsilon\, W\, A_{31} \left(\frac{1}{2+\frac{\epsilon W}{e^{h\nu_{31}/kT_e}-1}+\frac{\epsilon W}{e^{h\nu_{32}/kT_e}-1}}\right) \left(\frac{1}{e^{h\nu_{32}/kT_e}-1}-\frac{e^{h\nu_{21}/kT_x}}{e^{h\nu_{31}/kT_e}-1}\right) \quad \text{(A11)}$$

where n_{H_2} is the number density of H_2 molecules at radius r. For a given mass loss rate, velocity law, effective temperature, water abundance and gas temperature, Eq. (A11) can be solved for T_x at any radius r. Having determined T_x, the water cooling rate is determined from Eq. (A1).

References

Bedijn P.J., 1987, A&A 186, 136
Bieging J.H, Chapman B., Welch W.J., 1984, ApJ 285, 656
Burke J.R., Hollenbach D.J., 1983, ApJ 265, 223
Castor J.I., 1970, MNRAS 149, 111
Elitzur M., 1982, ApJ 262, 189
Goldreich P., Kwan J., 1974, ApJ 189, 444
Goldreich P., Scoville N., 1976, ApJ 205, 144 (GS)
Goldsmith P.F., Langer W.D., 1978, ApJ 222, 881
Green S., Chapman S., 1978, ApJS 37, 169
Green S., Thaddeus P., 1974, ApJ 191, 653
Green S., Thaddeus P., 1976, ApJ 205, 766
Griffin I.P., 1990, MNRAS 247, 591
Griffin I.P., 1993, MNRAS 260, 831
Hartquist T.W., Oppenheimer M., Dalgarno A., 1980, ApJ 236, 182
Hinkle K.H., Hall D.N.B., Ridgway S.T., 1982, ApJ 252, 697
Hollenbach D.J., McKee C.F., 1979, ApJS 41, 555
Huggins P.J., Glassgold A.E., 1982, AJ 87, 1828
Huggins P.J., Olofsson H., Johansson L.E.B., 1988, ApJ 332, 1009
de Jong T., Chu S.I., Dalgarno A., 1975, ApJ 199, 69
de Jong T., 1977, A&A 55, 137
Jura M., Kahane C., Omont A., 1988, A&A 201, 80 (JKO)
Justtanont K., Tielens A.G.G.M., 1992, ApJ 389, 400
Kastner J.H., 1992, ApJ 401, 337
Knapp G.R., Morris M., 1985, ApJ 292, 640
Kwan J., Hill F., 1977, ApJ 215, 781 (KH)
Kwan J., Linke R.A., 1982, ApJ 254, 587 (KL)
Mamon M., Glassgold A.E., Huggins P.J., 1988, ApJ 328, 797
Martin P.G., Rogers C, 1987, ApJ 322, 374
Morris M., Lucas R., Omont A., 1985, A&A 142, 107
Nejad L.A.M., Miller T.J., 1988, MNRAS 230, 79
Nercessian E., Guilloteau S., Omont A., Benayoun J.J., 1989, A&A 210, 225
Netzer N., Knapp G.R., 1987, ApJ 323, 734
Orofino V., Colangeli L., Bussoletti E., Blanco A., Fonti S., 1990, A&A 231, 105
Ridgway S.T., Keady J.J., 1988, ApJ 326, 843
Rouleau F., Martin P.G., 1991, ApJ 377, 526
Sahai R., 1987, ApJ 318, 809

Sahai R., 1990, ApJ 362, 652
Schutte W.A., Tielens A.G.G.M., 1989, ApJ 343, 369
Tielens A.G.G.M., 1983, ApJ 271, 702
Tielens A.G.G.M., Hollenbach D., 1985, ApJ 291, 722
Truong-Bach, Morris D., Nguyen-Q-Rieu, Deguchi S., 1990, A&A 230, 431
Truong-Bach, Morris D., Nguyen-Q-Rieu, 1991, A&A 249, 435

Chapter 3

The mass loss rates of OH/IR 32.8–0.3 and 44.8–2.3

Abstract

In a previous paper a model was presented to calculate the thermal emission of molecules around a central star. The model includes a self-consistent determination of the gas kinetic temperature, photoelectric heating, cooling by water molecules and the constraints that the presence of dust has on the molecular excitation.

The model is applied to the CO(1-0) and CO(2-1) observations of the OH/IR stars OH32.8–0.3 and OH44.8–2.3 (abbreviated to OH32.8 and OH44.8). Both come from the sample observed by Heske et al. (1990) who noted that in the less extreme OH/IR stars (like OH44.8) the mass loss rate derived from infrared properties agrees reasonably well with that estimated from the CO emission but that in extreme OH/IR stars (like OH32.8) the mass loss rate derived from the infrared is an order of magnitude larger than that derived from CO emission.

For a dust opacity at 60 μm of 228 $cm^2 gr^{-1}$ the best model for OH44.8 has the following parameters: $\dot{M} = 9.0\ 10^{-6}\ M_{\odot}/yr$, dust-to-gas ratio $\Psi = 0.0035$ and mean dust grain size $a = 0.14$ μm. The derived mass loss rate is insensitive to the adopted opacity. The results are relatively insensitive to any model assumptions.

For OH32.8 no model is found that fits the observed line profiles for a constant mass loss rate throughout the envelope. For a grain size of $a = 0.125\ \mu m$, an opacity of 228 $cm^2 gr^{-1}$ (following the result for OH44.8) and a mass loss history in which the mass loss rate drops by a factor of 10 for radial distances larger than a critical distance R_c, the following model reproduces the observed intensities: (present-day) $\dot{M} = 2.0\ 10^{-5}\ M_{\odot}/yr$, $\Psi = 0.015$ with $R_c \approx 1.3\ 10^{17}$ cm. Models with $\dot{M} \gtrsim 4.0\ 10^{-5}\ M_{\odot}/yr$ can not be made to fit the observations, models with $\dot{M} < 2.0$ $10^{-5}\ M_{\odot}/yr$ probably can, but result in higher dust-to-gas ratios ($\Psi \sim \dot{M}^{-1}$).

The distinction made by Heske et al. (1990) between moderate OH/IR stars (like OH44.8) and extreme OH/IR stars (like OH32.8) can be understood as follows: the CO shell in the extreme OH/IR stars is so large that the outer part samples a previous phase of lower mass loss, several 10^3 yrs ago.

1 Introduction

Heske et al. (1990) noted that the mass loss rates as derived from the infrared properties of stars and from the Knapp & Morris (1985, KM) formula for their CO emission do not agree for extreme OH/IR stars. Since Other authors (Sahai 1990, Jura et al. 1988 (JKO), Kastner 1992) have shown that the kinetic temperature structure can be very different from that in IRC 10 216, a possible explanation is that the gas kinetic temperature in these stars is very different from the temperature structure in IRC 10 216, on which KM based their mass loss formula. Evidently, the kinetic temperature is strongly coupled to the molecular excitation.

In this paper a recent model to calculate the thermal emission of molecules (Groenewegen 1993a,

Chapter 2) is applied to two OH/IR stars. In this model all relevant heating and cooling mechanisms are included to calculate the gas kinetic temperature in a consistent manner. The constraints that the presence of dust has on the molecular excitation is included.
In Sect. 2 the model is briefly described. In Sect. 3 a dust radiative transfer model and the molecular emission model are applied to OH32.8–0.3 and OH44.8–2.3. The results are discussed in Sect. 4.

2 The Model

The model is explained in full detail in Chapter 2. Here, only the main features are outlined. The model described by Morris et al. (1985) is used to calculate the level populations. The main assumptions are spherical symmetry and the use of the Sobolev approximation (valid when the local linewidth is much smaller than the expansion velocity). The CO molecules are excited by: (1) collisions with H_2 molecules, (2) interaction with the 2.8 K background radiation, and (3) infrared radiation from a central blackbody of temperature T_{BB} and radius R_{BB}. The calculations are performed using 99 gridpoints in the radial distance. Twenty-five rotational levels in the v = 0 and v = 1 vibrational states each are included. The line profiles are calculated at 48 velocity points.
The most important change with respect to the Morris et al. model is the inclusion of a self-consistent calculation of the kinetic temperature. The main heating processes are dust-gas collisions and the photoelectric effect on grains (in the outer part of the envelope). Heating due to cosmic rays and the temperature difference between the gas and the dust are also included in the model, but are less important. For reference, the main heating rate due to dust-gas collisions can be written as (Chapter 2):

$$H_{dg} = 1.2254\, 10^{-40}\, n(H_2)^2\, \frac{\Psi\, (1+4\, f_{\rm He})^2}{\rho_d\, a}\, \left(\frac{L\, Q\, v(r)}{\dot{M}}\right)^{3/2} \frac{1}{1+\frac{v_{dr}}{v(r)}}, \tag{1}$$

with the drift velocity in km s^{-1} given by:

$$v_{dr} = 1.4293\, 10^{-4}\, \left(\frac{L\, Q\, v(r)}{\dot{M}}\right)^{0.5} \tag{2}$$

where ρ_d is the dust grain density in gr cm^{-3}, a the grain size in μm, L the stellar luminosity in solar units, $\dot{M}$ the mass loss rate in $M_\odot$/yr, Q the effective absorption coefficient (defined in Eq. 18 of Chapter 2), v(r) the gas velocity in km s^{-1} and Ψ the dust-to-gas ratio.
In the model adiabatic cooling is included as well as molecular cooling by ^{12}CO, ^{13}CO, HCN, H_2 and H_2O. Other species may be neglected. The water cooling rate is calculated from a generalization of the treatment developed by Goldreich & Scoville (1976).
The presence of dust constrains the molecular emission model. By fitting the spectral energy distribution (SED) using a dust radiative transfer (DRT) model one can determine the dust optical depth:

$$\tau_\lambda = 5.405\, 10^8\, \frac{\dot{M}\, \Psi\, Q_\lambda/a}{r_c\, R_*\, v_d\, \rho_d} \tag{3}$$

where $\dot{M}$ is the mass loss rate in $M_\odot$/yr, v_d the dust velocity in km s^{-1}, Ψ is the dust-to-gas ratio, Q_λ/a the dust absorption coefficient over de grain size in cm^{-1}, ρ_d the grain density in gr cm^{-3}, r_c the inner radius in stellar radii and R_* the stellar radius in solar units. The inner radius is determined by the temperature of the dust at the inner radius, T_c. Comparing the parameters in Eq. (3) with the dominant heating rate of Eq. (1) shows that $\dot{M}, \Psi, \rho_d, a, Q$ can not be varied independently but always must fulfill Eq. (3). JKO and Sahai (1990) also used the infrared fluxes to constrain their models, but their treatment is approximate, and only uses the far-infrared fluxes. In our model a fit to the entire SED is used.

Radiative pumping of molecules is provided by thermal emission from hot dust close to the star. In molecular models this is represented by a blackbody of temperature T_{BB} and radius R_{BB}. These quantities can be estimated from the DRT-models. At each gridpoint in the DRT-model the blackbody temperature of the radiation field can be determined. It is then possible to obtain a realistic estimate of T_{BB} and R_{BB}. Finally, DRT-models provide $\tau_{0.1}$ (the dust optical depth at 0.1 μm), which is needed to calculate the photoelectric heating rate (Eq. 10 in Chapter 2) and the radial dust temperature profile which is needed for the heating rate due to the gas-dust temperature difference (Eq. 7 in Chapter 2).

3 OH 32.8–0.3 and OH 44.8–2.3

Heske et al. (1990) discussed two groups of OH/IR stars. Group 1 contains objects with relatively low mass loss rates ($\dot{M} \lesssim 10^{-5}$ $M_\odot$/yr). The mass loss rates derived from the CO lines and other methods agree within an order of magnitude. Group 2 stars have higher mass loss rates. The mass loss rates derived from the CO lines using the KM formula are systematically lower by more than an order of magnitude compared to other methods.

From both groups one star was chosen. Criteria for selection were the availability of a phase lag distance and infrared photometry. From group 1 we selected OH44.8–2.3, from group 2 OH32.8–0.3. Characteristics of both stars are given in Table 1. The distances are phase lag distances as quoted by Heske et al. The uncertainty is about 0.2 kpc. The expansion velocities are averages from the OH and CO expansion velocities as quoted by Heske et al. and are accurate to within 10%. Heske et al. determined the mass loss rate using different methods. The mass loss rates quoted in Table 1 are the geometric mean values of all determinations (except the CO determination) and agree with each other within a factor of 2. These mass loss rates will be the first guess in the DRT- and the molecular excitation calculations. For comparison, the mass loss rate based on the KM-formula for the CO lines give a value of 2.2 10^{-5} and 3.3 10^{-6} $M_\odot$/yr for OH32.8 and OH44.8, respectively (Heske et al.). The integrated intensities of the CO(1-0) and CO(2-1) lines are taken from Heske et al. as observed with the IRAM 30m telescope.

Table 1: Characteristics of OH32.8–0.3 and OH44.8–2.3

Star	D (kpc)	L ($L_\odot$)	P (days)	v_{exp} (km s^{-1})	$\dot{M}$ ($M_\odot$/yr)	$\int T\,dv$ (1-0) (K km s^{-1})	$\int T\,dv$ (2-1) (K km s^{-1})
OH 32.8–0.3	4.8	15800	1539	15.0	1.6 10^{-4}	$\lesssim 4$	14.0 ± 0.5
OH 44.8–2.3	1.2	3950	534	16.0	9.0 10^{-6}	13.9 ± 0.6	28.5 ± 0.6

3.1 The dust modelling

The dust radiative transfer model of Groenewegen (1993b) is used. In this model the radiative transfer equation and the equation of thermal equilibrium are solved simultaneously for the dust. The photometric data for OH32.8 is taken from the IRAS Point Source Catalog (only 12 and 25 μm bands available), Evans & Beckwith (1977), Werner et al. (1980) and Herman et al. (1984); for OH44.8 from the PSC (all four bands), Ney & Merrill (1980), Price & Murdock (1983) and

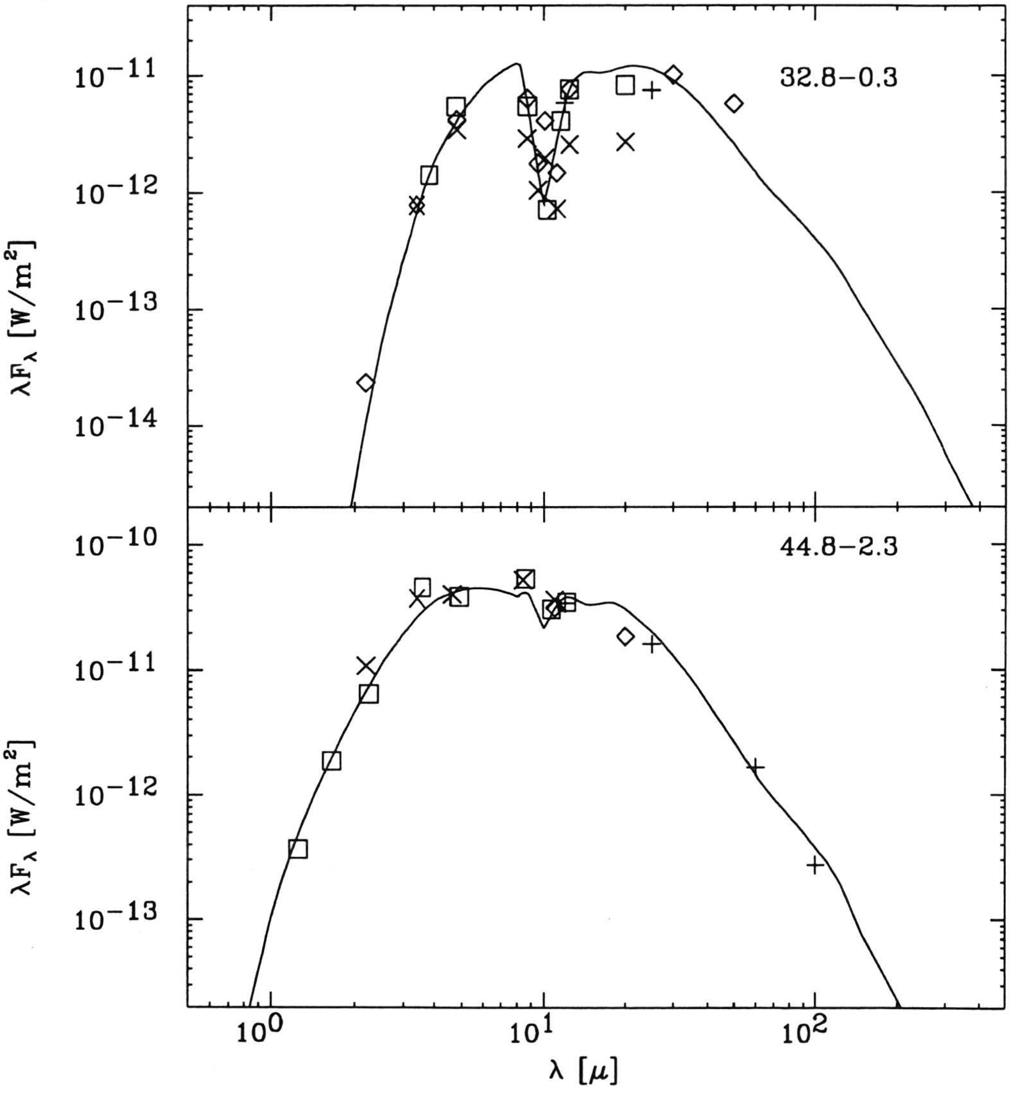

Figure 1: The best-fit radiative transfer model results for OH32.8 and OH44.8. Details are given in the text. The legend to the photometry is as follows. For OH32.8: + = IRAS PSC, X = Evans & Beckwith (1977), ◇ = Werner et al. (1980), □ = Herman et al. (1984). For OH44.8: + = IRAS PSC, X = Fix & Mutel (1984), ◇ = Price & Murdock (1983), □ = Ney & Merrill (1980).

Fix & Mutel (1984). Because both stars are highly variable (both have IRAS variability index 9) it is necessary to scale the fluxes to a common standard. Since all photometric data sets contain an observation between 10 and 13 μm, all data sets are scaled to the IRAS 12 μm band. The observed fluxes are corrected for interstellar extinction using Milne & Aller (1980)[1] and the interstellar extinction curve of Cardelli et al. (1988). The visual extinctions are 1.9

[1]The visual extinction is given by $A_V = 0.18\ (1 - \exp\ (-11.1\ D(\mathrm{kpc})\ \sin(|b|)))/\sin(|b|)$

Table 2: Parameters derived from the DRT-models

Star	τ_5	r_{inner}	Ψ	Q	$\tau_{0.1}$ r (cm)[1]	T_{BB} (K)	R_{BB} (cm)	v_{drift} (km s^{-1})
OH 32.8–0.3	4.51	8.75	0.0038	0.0136	9.19 10^{16}	430	3.0 10^{15}	0.64
OH 44.8–2.3	1.22	6.28	0.0070	0.0187	8.91 10^{15}	815	2.9 10^{14}	1.64

Note. (1) The optical depth at 0.1 μm does not include scattering. The correction factors to estimate the influence of scattering are listed in Sect. 4.1

and 8.4 magnitudes for OH44.8 and OH32.8 respectively. The total flux at Earth, corrected for extinction, is 2.2 10^{-11} and 8.9 10^{-11} W m^{-2} for OH32.8 and OH44.8. The uncertainty is about 10%. The luminosities at the assumed distances are listed in Table 1.

The following dust properties are assumed: grain radius a = 0.05 μm, grain density ρ_d = 2 gr cm^{-3}, condensation temperature T_c = 1000 K. The absorption efficiency is a combination of dirty silicate (Jones & Merrill 1976) at $\lambda < 8$ μm and the silicate feature of David & Papoular (1990) at longer wavelengths. The silicate feature of David & Papoular is used for it peaks at 10 μm, which is observed in the LRS spectra of both stars. Dirty silicate has the advantage of a high opacity in the near infrared, needed to fit the spectra of oxygen-rich stars in general (Jones & Merrill 1976, Schutte & Tielens 1988). For the adopted Q_λ, the values of Q_λ/a at 1, 5, 10 and 60 μm are 12050, 2410, 16676, 304 cm^{-1}, respectively, corresponding to opacities $\kappa_\lambda = (3\ Q_\lambda/4\ a\ \rho)$ of 4520, 900, 6250, 114 $cm^2 gr^{-1}$, respectively.

In Fig. 1 the best fits to the spectra are shown. The optical depths at 5 μm are 4.5 and 1.2 for OH32.8 and OH44.8, respectively, with an uncertainty of about 10%. The fit at $\lambda > 30$ μm for OH32.8 is rather poor. OH32.8 is located almost directly in the galactic plane, and contamination by cirrus is very likely. The CIRRUS-flags in the PSC catalog indicate that this is indeed the case. The PSC only lists upper limits for the IRAS 60 and 100 μm flux-densities. May be the observations of Werner et al. (1980) at 30 and 50 μm are also contaminated by cirrus.

OH44.8 has been observed at 1.3 mm by Walmsley et al. (1991). The flux they measured was 4.8 ± 5.6 mJy (or a 3σ upper limit of 21.6 mJy) corresponding to (8.5 ± 9.9) 10^{-21} W/m^2/μm (or < 3.8 10^{-20} W/m^2/μm). The predicted flux at 1.3 mm is 3.4 10^{-21} W/m^2/μm, consistent with the upper limit. The effective temperatures of the underlying central stars can not be determined from the DRT modelling. The canonical value of 2500 K is adopted for both stars. From Eq. (3) it is derived that the dust-to-gas ratios are 0.0038 and 0.0070 for OH32.8 and OH44.8 respectively[2].

For the molecular program the optical depth at 0.1 μm, the flux-weighted absorption efficiency and the temperature and radius of the blackbody emitting at 4.6 μm (the wavelength of the CO v=(0-1) vibrational transition) are needed. These parameters, together with the inner radius of the dust shell (in stellar radii), the drift velocity and the dust-to-gas ratio are listed in Table 2. The extrapolation of the optical depth from 5 to 0.1 μm assumes no scattering. An estimate of the influence of scattering may be obtained from Draine (1987) for astronomical silicate which should be indicative for our adopted Q_λ as well. The values of $Q^{extinction}/Q^{absorption}$ at 0.1 μm are 1.90, 2.10, 2.21, 2.27, 2.31 and 2.35 for a = 0.05, 0.1, 0.15, 0.2, 0.25 and 0.30 μm, respectively. These are the values by which $\tau_{0.1}$ in Table 2 has to be multiplied to estimate $\tau_{0.1}$ including scattering.

[2]The exact choice of T_{eff} does not affect the dust-to-gas ratio. For OH32.8 it was verified that for T_{eff} = 2000 K the dust-to-gas ratio would change to Ψ = 0.0036.

For radii smaller than R_{BB}, I assume an undiluted blackbody of temperature $T_{BB}(r)$. I fitted a function of the form:

$$\log T_{BB}(r) = a + b \log(r/r_c) + c (\log(r/r_c))^2 \tag{4}$$

to the data of the DRT-modelling and find a = 3.081, b = –0.735, c = 0.557 for OH44.8 and a = 3.024, b = –0.966, c = 0.593 for OH32.8, respectively. The value of T_{BB} and R_{BB} listed in Table 2 correspond to the temperature and radius where the optical depth at 4.6 μm becomes $\sim$2/3. For the dust temperature as a function of radius I fitted the same functional dependence as Eq. (4) and find a = 3.000 (T_c = 1000 K assumed for both stars), b = –0.678, c = 0.076, and b = –0.696, c = 0.063 for OH44.8 and OH32.8 respectively.

3.2 The CO modelling

I first discuss the standard CO model and then comment on each star individually.

3.2.1 The standard CO model

The molecular program includes all physical features of the 'combined model' presented in Sect. 3.11 of Chapter 2. The following parameters are assumed: the adiabatic index is $\gamma = 5/3$ when T < 350 K and 7/5 when T > 350 K, helium is present with abundance n(He)/n(H) = 0.1, the velocity law and drift velocity are included in the heating calculation. Heating by cosmic rays and due to the gas-dust temperature difference as well as H_2 cooling are included.
No HCN is assumed to be present. Although HCN has been detected in O-rich stars the abundances are low, typically two orders of magnitude less than in carbon stars (Lindqvist et al. 1992). The CO and H_2O abundances (relative to H_2) are set at $f_{CO} = 6\ 10^{-4}$ and $f_{H_2O} = 1.0\ 10^{-3}$. An isotopic ratio of $^{12}CO/^{13}CO$ = 25 is assumed, in between the value measured in red giants ($\approx$18, Harris et al. 1988) and non-J-type carbon stars ($\gtrsim$30, Lambert et al. 1986). Water cooling is important up to 2.4 10^{17} and 3.2 10^{16} cm in OH32.8 and OH44.8, respectively (Eq. 16 of Chapter 2).
The photoelectric effect on dust grains is included with an optical depth at 0.1 μm including the correction factor for scattering as outlined in Sect. 3.1. Photodissociation of ^{12}CO and ^{13}CO is included using the formalism of Mamon et al. (1988; Eq. 19 in Chapter 2). From Mamon et al. (1988) it is derived that $r_{1/2} = 1.475\ 10^{18}$ cm and $\alpha = 3.52$ for OH32.8 and $r_{1/2} = 2.20\ 10^{17}$ cm and $\alpha = 2.75$ for OH44.8, respectively, for the standard value of the mass loss rate in Table 1. The outer radius is set at the radius where the CO abundance drops to 0.1% of the value close to the star, or $r_{outer} = 2.8\ 10^{18}$ and 5.1 10^{17} cm, respectively.
The velocity law is taken as $v(r) = v_\infty\,(1 - \frac{\delta}{r})^\beta$, where v_∞ is listed in Table 1. Based on simple arguments (see e.g. Schutte & Tielens 1989) one can estimate that $\beta \approx 0.5$ and that the flow accelerates near the dust condensation temperature. I fixed β at 0.5 and determined δ from the condition that $v/v_\infty = 0.9$ at $r = 1.5\ r_c$. This results in $\delta = 1.16\ 10^{14}$ and 4.17 10^{13} cm in OH32.8 and OH44.8 respectively. The precise form of the velocity law is not important because CO is collisionally excited and radiative excitation is unimportant.
Contrary to the calculations in Chapter 2, I did not use the CO collisional cross sections of Green & Thaddeus (1974) but the more recent ones of Fowler & Launay (1985). For transitions or temperatures not listed by them I used an extrapolation formula, using the functional dependence of formula given by the de Jong et al. (1975) and determining the coefficients a(Δj) and b(Δj) (see de Jong et al. for details) by fitting the Fowler & Launay data.

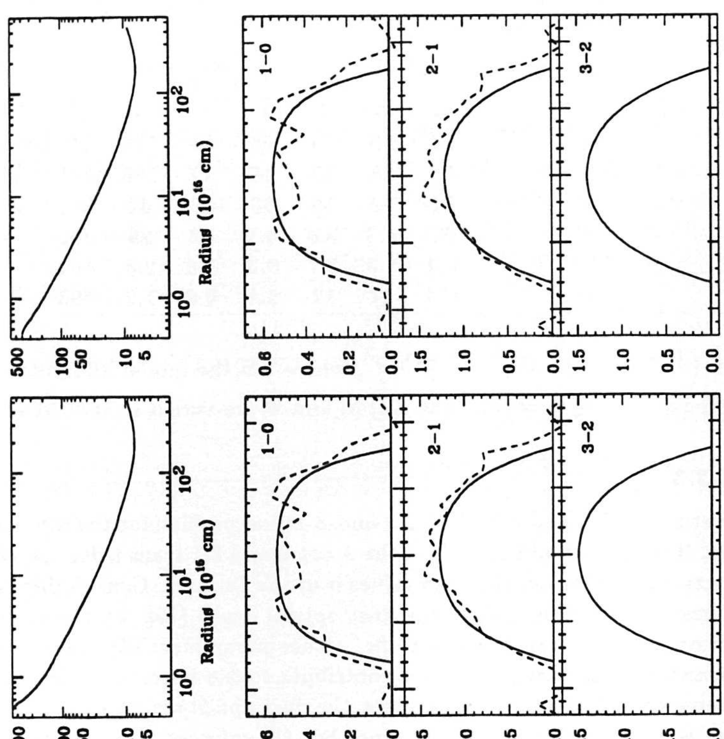

Figure 2: Temperature structure and line profiles for OH44.8–2.3. (a) model with $\dot{M} = 9.0\ 10^{-6}\ M_\odot/yr$, $\Psi = 0.0070$, Q = 0.019, $a = 0.05\ \mu m$ (= standard model), (b) model with $\dot{M} = 8.0\ 10^{-6}\ M_\odot/yr$, $\Psi = 0.0079$, Q = 0.094, $a = 0.25\ \mu m$ (= best model for $\kappa_{60} = 114\ cm^2gr^{-1}$), (c) model with $\dot{M} = 9.0\ 10^{-6}\ M_\odot/yr$, $\Psi = 0.0035$, Q = 0.105, $a = 0.14\ \mu m$ (= best model for $\kappa_{60} = 228\ cm^2gr^{-1}$). The observed J = 1-0 and 2-1 profiles (rms noises 0.07 and 0.11 K, respectively) are indicated by the dotted line. The observed profiles have been shifted by the system velocity with respect to the local standard of rest, quoted in Heske et al. (1990).

Table 3: OH 44.8-2.3: results of χ^2 calculations[1]

a (in 0.05 μm) (2)	$\dot{M}$ (in 10^{-6} $M_\odot$/yr) (3)						
	4	6	7	8	9	10	20
1	59	35	36	56	88	124	541
2	65	28	29	46	71	105	671
3	74	12	10	19	26	62	618
4	90	6.3	2.0	4.1	12	29	542
5	114	8.6	3.7	**0.3**	1.6	9.8	464
6	134	17	12	5.1	0.6	1.2	393

Notes. (1) $\chi^2 \equiv \left(\frac{I(1-0)-13.9}{0.6}\right)^2 + \left(\frac{I(2-1)-28.5}{0.6}\right)^2$, where I is the model integrated intensity. (2) Q and a are varied so that Q/a = constant. (3) $\dot{M}$ and Ψ are varied so that $\dot{M}\,\Psi$ = constant.

3.3 OH 44.8-2.3

The gas temperature profile and J = 1-0, 2-1 and 3-2 line profiles for the standard model are shown in Fig. 2a. The integrated intensity of the J = 1-0 and 2-1 transitions are 16.9 and 23.7 K km s^{-1}. The discrepancy with the observed values is at the 5σ level. Considering the parameters involved in the heating rate (Eq. 1) and the dust optical depth (Eq. 3), the parameters $\dot{M}$, Ψ, Q and a are varied to try to obtain a better fit. Other parameters like the velocity and grain density are relatively well known and do not contribute to the uncertainty in the heating rate. To limit all possible variations of the parameters, the dust opacity is kept constant, i.e. Q and a are varied by the same factor. Consequently, since Eq. (3) enforces $\dot{M}\,\Psi$ = constant, an increase in $\dot{M}$ has to be accompanied by a similar decrease in Ψ. If $\dot{M}$ is changed the parameters to describe the photodissociation of CO ($r_{1/2}$ and α) and the extent to which water cooling can be important are changed accordingly. Likewise the parameter $\tau_{0.1}$ is changed depending of the grain size (the correction for scattering). The parameter space is investigated and the result is in Table 3. The best model, shown in Fig. 2b, has the following parameters: $\dot{M}$ = 8.0 10^{-6} $M_\odot$/yr, Ψ = 7.8 10^{-3}, a = 0.25 μm and Q = 0.094. For mass loss rates in the range 7-10 10^{-6} $M_\odot$/yr a grain size can be found which fits the observations about equally well. The dust grain sizes found are generally large, $\gtrsim$0.20 μm, much larger than found in the interstellar medium or predicted in theoretical calculations (cf. Dominik et al. 1990).

The influence of some of the assumptions is now investigated. A major assumption is the value of the dust opacity, which is 114 cm^{2}gr^{-1} at 60 μm for the standard model (Sect. 3.1). This is lower than the values quoted by Jura (1986; 150 cm^{2}gr^{-1}) or Justtanont & Tielens (1992; 240 cm^{2}gr^{-1}). To investigate the influence of a higher opacity a new set of models was run for κ_{60} = 228 cm^{2}gr^{-1}. The results are collected in Table 4. The best model has $\dot{M}$ = 9.0 10^{-6} $M_\odot$/yr, Ψ = 3.5 10^{-3}, a = 0.14 μm and Q = 0.105 (shown in Fig. 2c). This model is in better agreement (has a lower χ^2) with the observations than the best model with the lower opacity. The dust grain sizes are significantly smaller, also in better agreement with observations. The mass loss rate is very similar to that in the low opacity case. The results are relatively insensitive to the uncertainties in the shielding of the UV radiation by dust ($\tau_{0.1}$), the strength of the diffuse UV radiation field (G) and the photoelectric yield (Y, see Eq. 10 of Chapter 2) or the cooling by water molecules (cf. Table 4). The line profiles in Figs. 2b, c are in good agreement with the observed ones, although both the expansion velocity and the system velocity may be slightly different from the values quoted in Heske et al. (1990).

Table 4: Additional models for OH 44.8-2.3[1]

$\dot{M}$ (in 10^{-6} $M_\odot$/yr)	a (in 0.05 μm)	$\tau_{0.1}$ r (in 8.91 10^{15} cm)	Remark	χ^2
9	2.8	2.15	best model	0.01
9	2.8	10	influence $\tau_{0.1}$	3.5
9	2.8	0.4	influence $\tau_{0.1}$	0.8
9	2.8	2.15	GY = 1/30	5.3
9	2.8	2.15	no water cooling	10.5

Notes. (1) For an opacity κ_{60} = 228 $cm^2 gr^{-1}$. $\dot{M}$, Q, a and Ψ are varied in such a way that Q/a = 0.748 μm^{-1} and $\dot{M}\Psi\ Q/a$ = constant. χ^2 is defined in Table 3.

3.4 OH 32.8-0.3

The gas temperature profile and line profiles for the standard model are shown in Fig. 3a. The integrated intensity of the J = 1-0 and 2-1 lines are 41.9 and 24.7 K km s^{-1}, in clear discord with the observations. Remarkable is that the (1-0) intensity is larger than the (2-1) intensity. This is entirely due to the influence of photoelectric heating in the outer part of the envelope (see Sect. 4).

The parameter space in $\dot{M}$, Ψ, Q and a is investigated in a similar way as for OH44.8 but no satisfactory model could be found. For parameter combinations for which the (2-1) intensity is near the observed value, the (1-0) intensity always remains too high. Changes in the CO or H_2O abundance, or in the dust opacity have no effect. Interstellar contamination could be a problem (cf. Heske et al. 1990) but should have affected both the (1-0) and (2-1) observations in a similar way. I am forced to conclude that one of the fundamental model assumptions (spherical symmetry and a constant mass loss rate) is incorrect. OH32.8 has not been mapped in CO, but mapping of other oxygen-rich stars shows that the deviations from spherical symmetry are small (Bujarrabal & Alcolea 1991). OH32.8 has been mapped in OH (Herman et al. 1985) showing that the envelope is fairly symmetric up to ~8 10^{16} cm.

To investigate a lower mass loss rate in the past, the specific case of Q = 0.068 and a = 0.125 μm is considered, following the results for OH44.8 (κ_{60} = 228 cm^2 gr^{-1}). Based on the observation that for some carbon-stars and oxygen-rich stars the mass loss rate seems to be related to thermal-pulses (Willems & de Jong 1988, Zijlstra et al. 1992), it is assumed that the mass loss rate is a factor f = 10 below the present-day mass loss rate for distances larger than a critical distance R_c.

The models which are best in agreement with the observations are collected in Table 5 and Figs. 3b and 3c. Only models with present-day mass loss rates $\lesssim$4.0 10^{-5} $M_\odot$/yr are in agreement with observations. Models with present-day mass loss rates <2.0 10^{-5} $M_\odot$/yr probably can also be made to agree with observations but result in dust-to-gas ratios which are larger than 0.015. Table 5 shows that the result that the mass loss rate was lower in the past by a factor of f does not depend very sensitively on the assumed value of f, the opacity or the grain size. The shape of the (2-1) line profile for the $\dot{M}$ = 2 10^{-5} $M_\odot$/yr model (Fig. 3c) is in better agreement with the observed one than that for the $\dot{M}$ = 4 10^{-5} $M_\odot$/yr model (Fig. 3b). Fig. 3 shows that J = 3-2 observations may be helpful in further constraining the mass loss history.

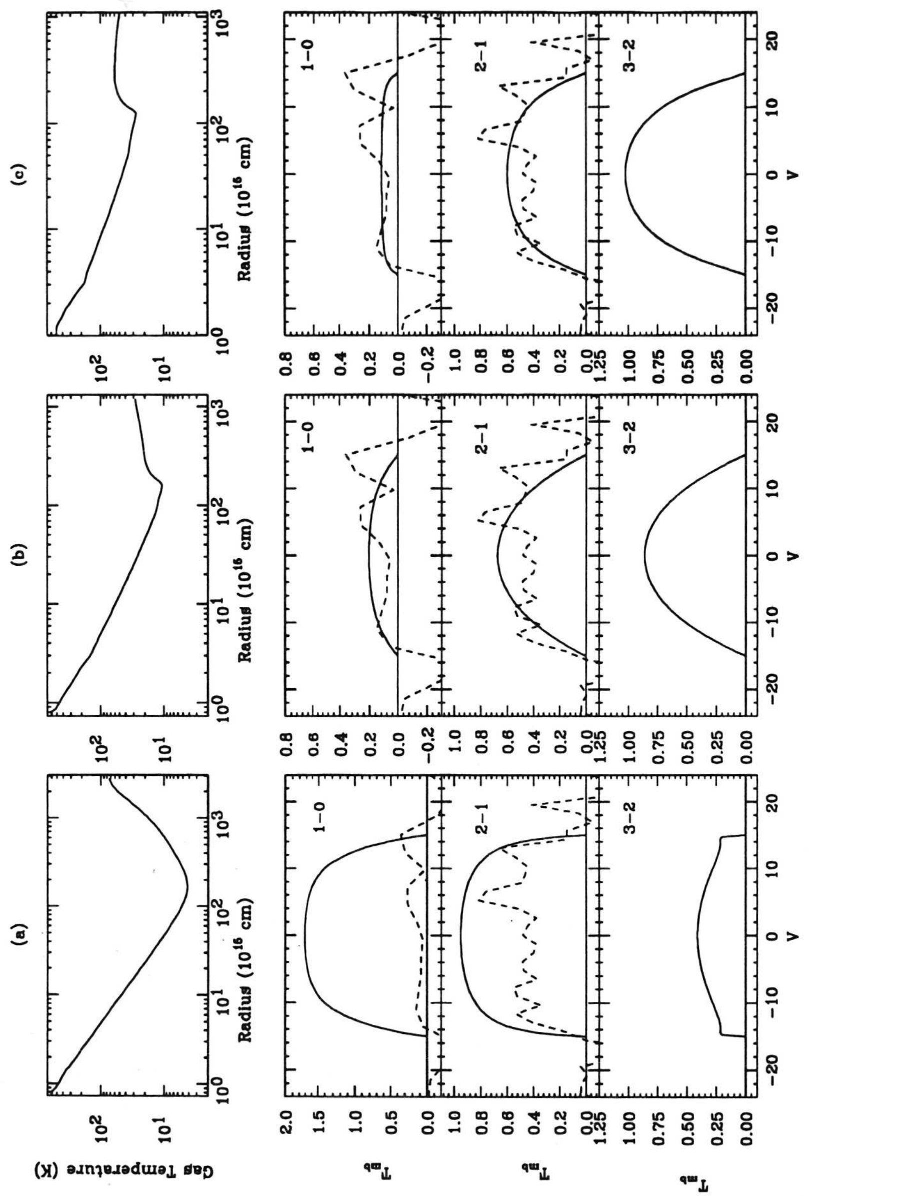

Figure 3: Temperature structure and line profiles for OH32.8–0.3. (a) model with $\dot{M}$ = 1.6 10^{-4} $M_\odot$/yr, Ψ = 0.0038 , Q = 0.0136, a = 0.05 μm (= standard model), (b) model with present-day $\dot{M}$ = 4.0 10^{-5} $M_\odot$/yr and $\dot{M}$ = 4.0 10^{-6} $M_\odot$/yr for r > 1.6 10^{17} cm, Ψ = 0.0076 , Q = 0.068, a = 0.125 μm, (c) model with present-day $\dot{M}$ = 2.0 10^{-5} $M_\odot$/yr and $\dot{M}$ = 2.0 10^{-6} $M_\odot$/yr for r > 1.3 10^{17} cm, Ψ = 0.0152 , Q = 0.068, a = 0.125 μm. The observed J = 1-0 and 2-1 profiles (rms noises 0.05 and 0.10 K, respectively) are indicated by the dotted line. The observed profiles have been shifted by the system velocity with respect to the local standard of rest quoted in Heske et al. (1990).
The upturn in the temperature structure of the gas in the top panel of (b) and (c) at ~10^{17} cm is due to the mass loss history.

Table 5: Models for OH 32.8-0.3

$\dot{M}$ (10^{-5} $M_\odot$/yr)	Ψ (in 0.0038)	Q (in 0.0136)	a (in 0.05 μm)	R_c (10^{17} cm)	f	I(1-0)	I(2-1)	I(3-2)
						(in K km s^{-1})		
2	4	5	2.5	1.3	10	3.1	14.0	22.9
2	4	2	1.0	1.7	10	3.9	14.0	19.4
2	8	2	2.0	1.7	10	3.9	14.0	19.4
4	2	5	2.5	1.6	10	4.5	13.9	17.8
4	2	5	2.5	1.6	100	4.3	13.7	17.7
4	2	5	2.5	1.6	5	5.1	14.3	17.9
4	2	5	2.5	1.5	5	5.0	14.0	17.7
4	4	2	2.0	2.3	10	5.9	14.0	14.5

Note. Columns 1, 5 and 6 are related as follows. For OH32.8 the following mass loss history is considered. For radial distances smaller than R_c, the mass loss rate is given by the value in column 1; for distances larger than R_c the mass loss rate is a factor of f lower than the value listed in column 1.

4 Discussion

In some of the models for OH32.8 the integrated intensity (I) in the (1-0) line is larger than in the (2-1) line. This is due to the photoelectric effect and an interplay of several length scales: the beam size of the telescope in the (1-0) transition at the distance of the star ($R_{\rm beam}$), the distance where photoelectric heating begins to dominate the other heating processes ($R_{\rm UV}$; corresponding to $\tau_{0.1}$ $\lesssim$0.1-0.2) and the size of the CO envelope ($r_{1/2}$). The situation that I(1-0) > I(2-1) can only occur if $R_{\rm beam} > R_{\rm UV}$ and $r_{1/2} > R_{\rm UV}$ (this is a necessary but not a sufficient condition). The catalog of Loup et al. (1993) contains CO(1-0) and CO(2-1) data for about 125 stars. Only 5 convincing examples with I(1-0) > I(2-1) are contained in this catalog. From observations at IRAM and SEST of 22 (carbon-) stars not in Loup's catalog (or with either only the (1-0) or (2-1) transition listed; Groenewegen et al., in preparation) one additional example was discovered. So, in about 4% of the sources the two conditions derived above for I(1-0) > I(2-1) to occur are met. Of the six stars, two are carbon stars (IRAS 08074–3615, S Sct), one is a S-star (S Cas), one is a supergiant (TV Gem), one is a planetary nebula (BD 30 3069) and one is OH/IR 30.7–27.1. For S Sct (a carbon star with a detached shell) and the planetary nebula it is obvious that they have extended CO shells where photoelectric heating could indeed raise the temperature in the outer layers. The papers reporting the CO observations were checked. The authors only noted that the (2-1) transition is "not sufficiently excited" (Olofsson et al. 1990) or is "unusually low compared to (1-0)" (Heske et al. 1990), without referring to the possibility of an extra heating source in the outer most parts of the CO shell.

For OH32.8 evidence is presented for a lower mass loss rate in the past. The radius at which the mass loss rate becomes smaller is found to be $\sim$1.5 10^{17} cm, corresponding to a time scale of 3 10^3 yrs. The possibility to reconstruct the mass loss history in the CO shell depends on the time interval elapsed since the mass loss rate obtained its present value (c.q. the corresponding distance R_c), the beam size ($R_{\rm beam}$) and the extent of the CO envelope ($r_{1/2}$). The mass loss history is notable in the CO emission if $R_c < R_{\rm beam}$ and $R_c < r_{1/2} \sim \dot{M}^{0.6}$ (Mamon et al. 1988). This explains the segregation between the two groups of OH/IR stars discussed by Heske et al. (1990). Only the CO shells around the extreme OH/IR stars are large enough to contain information on the mass loss history.

The details of the mass loss history remain uncertain. In this paper a mass loss history related to thermal-pulses is adopted. Other mass loss histories probably can also fit the observations.

It would be worthwhile to re-observe the sample of Heske et al. (1990) and also obtain (3-2) observations. Observations of the higher transitions would constrain the present-day mass loss rate.
If the mass loss rate were related to the phase in the thermal-pulse cycle then the present-day mass loss rate should be identified with the phase of quiescent H-burning, and the lower mass loss rate with that during the luminosity dip. The fact that apparently in most extreme OH/IR stars the mass loss rate has been lower in the past history (if it is assumed that in other extreme OH/IR stars the low CO (1-0) emission is also due to a mass loss history effect) indicates that the duration of the quiescent H-burning phase can not be much longer than the 3 10^3 yrs derived for OH32.8. The interpulse period is roughly 20% longer than the duration of the quiescent H-burning phase. An interpulse period of 5 10^3 yrs corresponds to a core mass of $M_c \approx 0.9$ $M_\odot$ (Boothroyd & Sackmann 1988), indicating a higher than average initial mass for the progenitors of the extreme OH/IR stars. The luminosity (and indirectly the pulsation period) of OH32.8 is consistent with this.

Acknowledgements. I thank Thierry Forveille for providing the observed profiles of OH32.8 and OH44.8 and Teije de Jong for valuable comments on the manuscript.

References

Boothroyd A.I., Sackmann I.-J., 1988, ApJ 328, 653
Bujarrabal V., Alcolea V., 1991, A&A 251, 536
Cardelli J.A., Clayton G.C., Mathis J.S., 1988, ApJ 345, 245
David P., Papoular R., 1990, A&A 237, 425
Dominik C., Gail H.-P., Sedlmayer E., Winters J.M., 1990, A&A 240, 365
Draine B.T., 1987, Princeton Observatory Preprint 213, 1
Evans N.J., Beckwith S., 1977, ApJ 217, 729
Fix J.D., Mutel R.L., 1984, AJ 89, 406
Flower D.R., Launay J.M., 1985, MNRAS 214, 271
Goldreich P., Scoville N., 1976, ApJ 205, 144 (GS)
Green S., Thaddeus P., 1974, ApJ 191, 653
Groenewegen M.A.T., 1993a, Chapter 2, Ph.D. thesis, University of Amsterdam (paper I)
Groenewegen M.A.T., 1993b, Chapter 5, Ph.D. thesis, University of Amsterdam
Harris M.J., Lambert D.L., Smith V.V., 1988, ApJ 325, 768
Herman J., Baud B., Habing H.J., Winnberg A., 1985, A&A 143, 122
Herman J., Isaacman R., Sargent A., Habing H.J., 1984, A&A 139, 71
Heske A., Forfeille T., Omont A., van der Veen W.E.C.J., Habing H.J., 1990, A&A 239, 173
Jones T.W., Merrill K.M., 1976, ApJ 209, 509
de Jong T., Chu S.I., Dalgarno A., 1975, ApJ 199, 69
Jura M., 1986, ApJ 303, 327
Jura M., Kahane C., Omont A., 1988, A&A 201, 80 (JKO)
Justtanont K., Tielens A.G.G.M., 1992, ApJ 389, 400
Kastner J.H., 1992, ApJ 401, 337
Knapp G.R., Morris M., 1985, ApJ 292, 640
Lambert D.L, Gustafsson B., Eriksson K, Hinkle K.H., 1986, ApJS 62, 373
Lindqvist M., Olofsson H., Winneberg A., Nyman L.-A., 1992, A&A 263, 183
Loup C., Forveille T., Omont A., Paul J.F., 1993, A&AS 99, 291
Mamon M., Glassgold A.E., Huggins P.J., 1988, ApJ 328, 797

Milne D.K., Aller L.H., 1980, AJ 85, 17
Morris M., Lucas R., Omont A., 1985, A&A 142, 107
Ney E.P., Merrill K.M., 1980, The AFGL catalog, AFGL-TR-80-0050
Olofsson H., Carlstrom U., Eriksson K., Gustafsson B., Willson, L.A., 1990, A&A 230, L13
Price S.D., Murdock T.L, 1983, The revised AFGL catalog, AFGL-TR-83-0161
Sahai R., 1990, ApJ 362, 652
Schutte W.A., Tielens A.G.G.M., 1989, ApJ 343, 369
Walmsley C.M., et al., 1991, A&A 248, 555
Werner M.W., et al., 1980, ApJ 239, 540
Willems F.J., de Jong T., 1988, A&A 196, 173
Zijlstra A.A., Loup C., Waters L.B.F.M., de Jong T., 1992, A&A 265, L5

Chapter 4

On the infrared properties of S-stars with and without technetium

Abstract

There exist S-stars with and without technetium in their spectra. The S-stars with technetium are considered to be thermal pulsing AGB stars, while the S-stars without technetium are usually thought to be giants which acquired their s-process material from a (presently unseen white dwarf) companion. I investigate the possibility of discriminating between S-stars with ("intrinsic" S-stars) and without ("extrinsic" S-stars) technetium solely on the basis of their infrared properties. I find that intrinsic S-stars have a circumstellar envelope, while the infrared properties of extrinsic S-stars are consistent with (warm) stellar blackbodies with no or very little circumstellar material. This is reflected in the IRAS PSC fluxes, the LRS spectra and V – [12] color of the intrinsic and extrinsic S-stars. I find that S-stars with $S_{25} > 0.30\ S_{12}$ are intrinsic S-stars, stars with $0.25\ S_{12} < S_{25} < 0.30\ S_{12}$ can both be intrinsic or extrinsic S-stars and stars with $S_{25} < 0.25\ S_{12}$ are extrinsic S-stars. The LRS spectra of the extrinsic S-stars closely follow a $F_\nu \sim \lambda^{-2}$ law, indicative of a (warm) stellar blackbody. The LRS spectra of the intrinsic S-stars either show emission features near 10 and 19 μm or are featureless and characterised by cool blackbody temperatures. I find that 96% of S-stars with V – [12] > 7.0 are intrinsic and all S-stars with V – [12] ≤ 5.0 are extrinsic. S-stars with intermediate V – [12] color can belong to both groups. The infrared properties of the intrinsic and extrinsic S-stars are consistent with the evolutionary phase envisioned for both groups. I estimate that between 50 and 70% of S-stars in an optically complete sample are extrinsic S-stars.

1 Introduction

Traditionally S-stars are thought to be an intermediate phase of AGB evolution between M-stars and C-stars. The S-stars are characterised by nearly equal carbon and oxygen abundance in the photosphere and enhancement of the s-process elements relative to iron. Spectroscopically they are classified by means of the ZrO and LaO bands in the visual part of the spectrum. In recent years it has become clear that this picture has to be revised.

The unstable isotope ^{99}Tc, which is produced in the s-process during third dredge-up on the AGB, has a half life of $\tau_{1/2} = 2\ 10^5$ yr for T $\lesssim 10^8$ K, decreasing to $\tau_{1/2} = 1$ yr at T = 3.5 10^8 K (Schatz 1983). Detailed studies of the s-process indicate that the more rapid decay of Tc at higher temperatures is offset by an enhanced production rate due to a higher neutron flux (Mathews et al. 1986) leaving the Tc abundance almost unaltered. In the power down phase after a thermal pulse Tc is therefore mixed into the envelope. Because the interpulse period between two consecutive thermal pulses of $\lesssim 10^5$ yr (for core masses of $\gtrsim 0.58\ M_\odot$, Boothroyd & Sackmann 1988) is shorter than the Tc half life, it is expected that Tc shows up in all thermal pulsing AGB stars.

It was therefore surprising that ~40% of stars of spectral type MS and S (I will refer to both classes simply as S-stars) do not show Tc in their spectra (Little et al. 1987, Smith & Lambert 1988). Iben & Renzini (1983) put forward the idea that the S-stars without Tc are evolved Barium stars, which are G and K giants without Tc but with enhanced s-process elements. The discovery that the Barium stars are spectroscopic binaries (McClure et al. 1980, McClure 1983, Jorissen & Mayor 1988, McClure & Woodsworth 1990) has led to the scenario that Barium stars are the result of mass transfer from an AGB star (now a white dwarf (WD)) to a less evolved companion (now the Barium star). If the S-stars without Tc are evolved Barium stars they too must be spectroscopic binaries. The extrinsic S-stars which have been observed for binarity are indeed member of WD containing binary systems (Jorissen & Mayor 1988, 1992, Brown et al. 1990). Although the reverse is difficult to prove, radial velocity measurements, observations of the He I line at 1.083 μm (Brown et al. 1990) and IUE data (Smith & Lambert 1987, Johnson et al. 1992) are consistent with the proposition that intrinsic S-stars are not members of a WD containing binary system.

Of the about 1300 S-stars known in the Galaxy only 60 or so have been observed for the presence of Tc. Since the fraction of extrinsic S-stars is substantial it would be important to be able to separate extrinsic and intrinsic S-stars by means of another (indirect) criterion. Since the extrinsic S-stars are supposed to be less luminous, hot and probably have low mass loss rates while the intrinsic S-stars are luminous, cool AGB stars, surrounded by a circumstellar shell, the infrared characteristics of both classes of S-stars may be very different.

In this paper I investigate the infrared properties of the intrinsic and extrinsic S-stars. I define the sample in Sect. 2. The IRAS color-color diagram and the V − [12] color are discussed in Sect. 3. The LRS spectra are discussed in Sect. 4. I conclude in Sect. 5.

2 The sample

All stars classified as MS or S and observed for the presence of Tc were selected from Little et al. (1987) and Smith & Lambert (1988, 1990 hereafter SL88 and SL90). The 39 stars with Tc and the 30 stars without Tc were cross correlated with the S-star catalog of Stephenson (1984) and it turned out that 12 stars were not listed there. For those 12 stars the spectral types listed in the literature were more closely examined. Stars with Tc that subsequently were excluded are: HR 4647 (classified as M4 III by Hoffleit 1982, as M4/5 by Houck 1988 and as M4S by SL88. The star shows no enhanced s-process elements, SL90), R Hya (classified as M7 IIIe by Hoffleit 1982, as M6.5e by Keenan et al. 1974, as M6/7 by Houck 1988 and as M6e-M9eS by the general catalog of variable stars (GCVS, Kholopov et al. 1985)) and Z Sgr (classified as M5e by Keenan et al. 1974 and as M4e-M9(Se) in the GCVS). Stars without Tc that were excluded are: HR 2508 (classified as M1 Ib-IIa by Hoffleit 1982 and as M2 IIabS by Bidelman 1980. This star shows no enhanced s-process elements, Smith & Lambert 1986), RT Aql (Keenan et al. 1974 observe no ZrO and classify it as M7. The star is listed as M6e-M8e(S) in the GCVS) and X Cet (classified as M3e by Keenan et al. 1974 and as M2e(S)-M6e in the GCVS).

The final sample consists of 27 stars without Tc and 36 stars with Tc. They are listed in Tables 1 (intrinsic S-stars) and 2 (extrinsic S-stars), where the number in Stephenson's catalog, the HR/HD/BD number, the variable star name and the spectral type (from Stephenson 1984, Hoffleit 1982 or the GCVS) are given.

There are two stars in the sample which deserve some further attention. They are o^1 Ori and DY Gem. Omicron Ori has Tc in its spectrum (Little et al 1987, SL88, Vanture et al. 1991) but has a WD companion (Ake & Johnson 1988). Ake & Johnson conclude that the cooling time of the WD is far in excess of the Tc half life so that o^1 Ori may be an evolved Barium star which

has reached the TP-AGB (Brown et al. 1990) or is a case of parallel evolution of two stars, one of which is now a WD and the other an AGB-star (Ake & Johnson).
DY Gem has no Tc in its spectrum (SL90) but has all characteristics of a true TP-AGB star. From SL90 I derive that 89% (8/9) of the intrinsic S-stars have C/O $\geq$ 0.49, while 67% (10/15) of the extrinsic S-stars have C/O $\leq$ 0.47. The C/O ratio of 0.88 and the $^{12}C/^{13}C$ ratio of 30 $\pm$ 7 (SL90) in DY Gem are probably the result of nucleosynthesis in DY Gem and not from material accreted from a companion. I was informed by V. Smith (private communication) not to put too much weight on the 'non detection' of Tc in DY Gem since the spectrum was complicated and difficult to measure.
Other stars in the sample which have known WD companions are the extrinsic S-stars HR 363, HR 1105, HD 35155, V613 Mon and HD 191226 (Hoffleit 1982, Griffin 1984, Jorissen & Mayor 1992, Johnson et al. 1992). In the intrinsic S-stars HD 1760, RS Cnc, ST Her, HR 6702, HR 8062 and HR 8714 no WD companion has been detected (Smith & Lambert 1987, Johnson et al. 1992). Three stars in the sample have main sequence companions: HR 8815, HD 191589 and π^1 Gru.
The 63 stars were correlated on position with the point source catalog (PSC, JISWG 1986). All stars were detected by IRAS except HD 199799 and HR 8062 which are in a part of the sky not surveyed by IRAS. In Tables 1 and 2 the not-color-corrected fluxes at 12, 25 and 60 μm flux are listed. From the LRS atlas (JISWG 1986) and the additional work of Volk & Cohen (1989) and Volk et al. (1991) the LRS classification is listed.

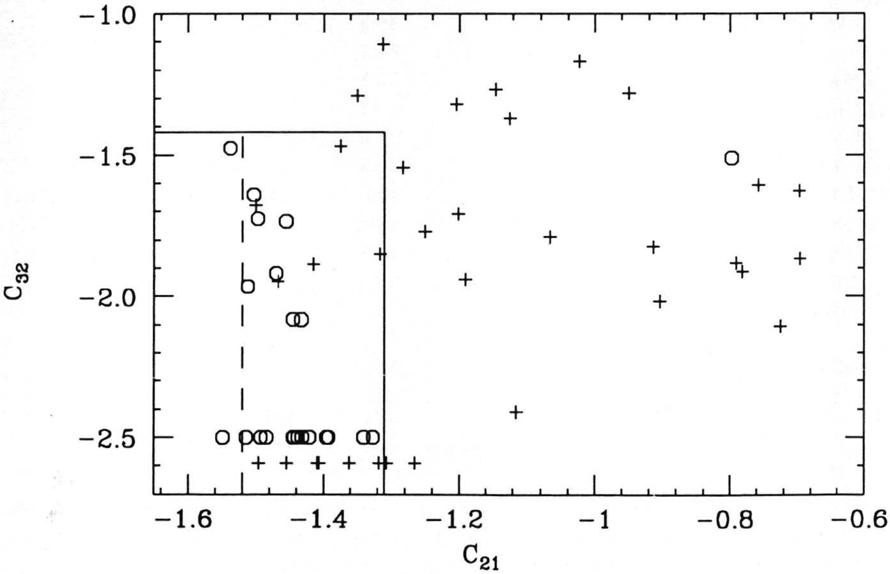

Figure 1: The IRAS color-color diagram. Plotted are the S-stars with Tc (+) and without Tc (O). The stars without 60 μm flux are plotted at C_{32} = -2.59 and -2.50 respectively. The intrinsic S-stars are located at $C_{21} > -1.31$ and $C_{32} > -1.42$. Stars with $-1.52 < C_{21} < -1.31$ and $C_{32} < -1.42$ can belong to both groups. Stars with $C_{21} < -1.52$ are extrinsic. These areas are indicated. The star located at $C_{21} \approx -0.8$, $C_{32} \approx -1.5$ is DY Gem.

Table 1: The S-stars with Tc

S	HD/HR/BD	name	sp. type	S_{12} (Jy)	S_{25} (Jy)	S_{60} (Jy)[1]	LRS [2]
8	HD 1760	T Cet	M5-6S	198	55.8	14.4	16
9	HD 1967	R And	S5-7	327	168	24.2	E
12	HD 4350	U Cas	S5/3	8.38	2.49		01
49	HD 14028	W And	S7/1	167	72.1	13.5	22
89	BD 23 654		S	24.4	7.30	2.63	S
103	HD 29147	T Cam	S6/5	41.3	11.9	3.63	17
114	HR 1556	o^1 Ori	M3S	85.4	21.4	4.57	18
116	BD 48 1187	TV Aur	S5/6	12.9	4.25	1.26	
149	HD 37536	NO Aur	M2S	43.5	22.9	5.12	43
307	HD 53791	R Gem	S5/5	21.6	7.52	2.34	16
312	HD 54587	AA Cam	M5S	14.5	6.06	1.86	
347	HD 58521	Y Lyn	M6S	122	64.2	11.5	23
403	HD 63334	T Gem	S4/4	3.73	1.02		
		V Gem	M4.5S	9.24	3.31	0.36:	
411	HD 63733		S4/3	2.20	0.66		
422	HD 64332	NQ Pup	S5/2	7.02	1.84		
589	HR 3639	RS Cnc	M6S	480	209	32.6	22
803	HD 110813	S UMa	S3/6	4.23	1.40	0.29:	
866	HD 131169	S Lup	Se	7.78	2.22		
903	HD 142143	ST Her	M6.5S	199	97.1	16.7	41
	BD 15 3063	S Her	M5S	34.3	11.5	1.92	17
	HR 6702	OP Her	M5 IIbS	54.1	17.1	3.35	17
1053	HD 170970		S3/1	5.08	1.39		
1070	HD 172804	V679 Oph	S5/6	4.43	1.21		
1099	HD 177175	V915 Aql	S5/2	11.0	3.36	0.81:	
1117	HD 180196	T Sgr	S5/6	40.3	14.3	4.04	F
1150	HD 185456	R Cyg	S6/6	105	52.2	12.0	22
1165	HR 7564	χ Cyg	S7/1.5	1690	459	80.7	E
1188	HD 190629	AA Cyg	S6/3	40.0	15.5	5.27	31
1226	HD 195763	Z Del	S4/2	3.11	0.97		
1254	HD 199799		MS	[3]			
	HR 8062		S4/1	[3]			
1292	HD 211610	X Aqr	S6,3	11.5	4.31	0.83:	
1294	HR 8521	π^1 Gru	S5,7	909	437	77.3	42
1315	HR 8714	HR Peg	S4/1	27.6	7.15	1.19	S
1346	HD 224960	W Cet	S5-7/1.5-3	13.3	3.96	0.72	16

Notes. (1) A (:) means a flux of moderate quality, no entry means only an upperlimit is listed in the PSC; (2) The letters F, S, E are used in the classification scheme of Volk & Cohen 1989 and Volk et al. 1991. The counterparts in the usual LRS classification are: F = 10-16, S = 17-19, E = 2n; (3) In a region of the sky not observed by IRAS.

3 The IRAS color-color diagram

In Fig. 1 the $C_{21} = 2.5 \log(S_{25}/S_{12})$ versus $C_{32} = 2.5 \log(S_{60}/S_{25})$ color-color diagram for the extrinsic (O) and intrinsic S-stars (+) is plotted. The stars without 60 μm flux are plotted at constant $C_{32} = -2.50$ and -2.59 respectively. There is a clear correlation: all S-stars with S_{25} >

Table 2: The S-stars without Tc

S	HD/HR/BD	name	sp. type	S_{12} (Jy)	S_{25} (Jy)	S_{60} (Jy)[1]	LRS
22	HD 6409		M2wkS	5.64	1.50		
26	HR 363		S3/2	11.5	3.01	0.61:	
79	HR 1105	BD Cam	S4/2	41.0	10.8	1.59	18
133	HD 35155		S4,1	7.98	2.01	0.41	16
231	BD 14 1350	DY Gem	S8,5	21.7	10.4	2.59	42
260	HD 49368	V613 Mon	S3/2	4.31	1.09		
382	HR 2967	NZ Gem	M3S	25.2	6.50	1.11	18
494	HD 70276	V Cnc	S3/6e	8.41	2.02		
566	BD 06 263		M3S	0.97			
	HR 4088	DE Leo	M3 IIIabS	14.29	3.58	0.79	01
712	BD -10 3156		M3S	0.88			
722	HD 96360		M3[Swk]	3.18	0.84		
829	BD -2 3726		M1wkS	1.01			
926	BD 57 1671		M2S	2.38	0.62		
937	BD -13 4495		M2S	8.21	2.09		19
938	BD -18 4320		Swk	12.20	2.96	0.76	31
1023	HD 165774		S4,6	2.24	0.66		
1031	BD 16 3426		M4wkS	5.59	1.51		
	HR 7442	V1743 Peg	M4.5 IIIaS	26.0	6.95	1.02	17
1173	BD -18 5539		S2*3	1.27			
1178	HD 189581		S4*2	3.44	1.00		
1192	HD 191226		M1S-M3SIIIa	4.36	1.08		
1194	HD 191589		S	2.20	0.61		
1301	BD -11 5880		M4S	3.89	1.04		
1304	BD 33 4573		Swk	1.52	0.42		
1322	HR 8815	GZ Peg	M4S	80.9	20.1	3.29	18

Notes. (1) A (:) means a flux of moderate quality, no entry means only an upperlimit is listed in the PSC.

0.30 S_{12} ($C_{21} > -1.31$) are intrinsic S-stars. The region $C_{21} < -1.31$ is populated by both intrinsic and extrinsic S-stars. Furthermore there are no extrinsic S-stars with $S_{60} > 0.27\ S_{25}$ and the two stars with $C_{21} < -1.52$ are extrinsic.

This conclusion is consistent with the idea that mass loss in extrinsic S-stars is low: blackbodies with 2000 K $< T_{\rm eff} <$ 10 000 K are located at $-1.41 < C_{21} < -1.56$ and $-1.88 < C_{32} - 1.88$. The only exception to this conclusion is DY Gem which was discussed in Sect. 2.

If the intrinsic and extrinsic S-stars have very different infrared properties this should also be reflected in the V – [12] color. In Fig. 2 a histogram of the V – [12] color for the intrinsic and extrinsic S-stars is presented. The V magnitudes are taken from Stephenson (1984) or, if not listed there, from Hoffleit (1982) or the GCVS[1]. There is a clear correlation: S-stars with V – [12] > 7 are intrinsic and S-stars with V – [12] $\leq$ 5 are extrinsic. S-stars with intermediate colors can belong to both groups. The exceptions are DY Gem and V Cnc both with V – [12] = 8.7. DY Gem is probably a TP-AGB star, as discussed in Sect. 2. V Cnc is a Mira and it V magnitude varies between 7.5 and 13.9 (GCVS). It is listed in the SAO catalog as a star of V = 7.1. If V = 7.1 then V CnC has V – [12] = 5.8.

[1]For stars in the GCVS the mean visual magnitude is taken, consistent with the entries in Stephenson's catalog.

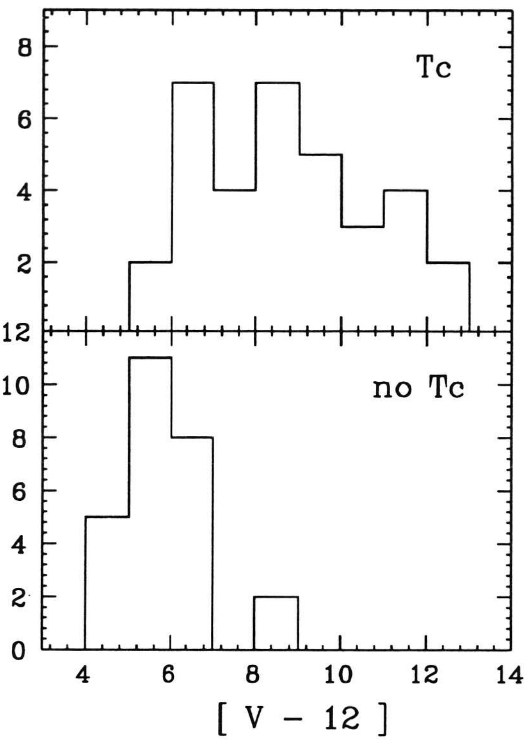

Figure 2: The histogram of V – [12] color for the intrinsic and extrinsic S-stars. The extrinsic S-stars at V – [12] = 8.7 are DY Gem and V Cnc.

The lack of extrinsic S-stars with V – [12] > 7 is not due to observational bias. Plotting the distributions of V and [12] separately shows that the distribution of V is about equal for the intrinsic and extrinsic stars (although the 5 faintest sources are intrinsic S-stars). The distribution of the 12 μm magnitudes shows that the intrinsic S-stars have in general higher 12 μm fluxes than the extrinsic S-stars.

4 The LRS spectrum

In Tables 1 and 2 the LRS classification is listed. It is well known that this classification scheme is not very reliable, requiring visual inspection of the LRS spectrum for correct classification. Furthermore, in the LRS atlas the spectra are plotted as λF_λ versus λ, while in a $\log F_\nu$ versus $\log \lambda$ plot spectral features stand out more clearly. Therefore the LRS spectra of the 25 stars listed in the LRS atlas were extracted. From a star without circumstellar shell it is expected that the flux comes from the photosphere which can be represented by the Rayleigh-Jeans tail ($F_\nu \sim \lambda^{-2}$) for high enough effective temperatures. In a $\log F_\nu$ versus $\log \lambda$ plot a slope of –2 is expected for hot stars without a circumstellar shell. In Figs. 3 and 4 the LRS spectra together with a line of slope –2 is plotted for the extrinsic (Fig. 3) and the intrinsic (Fig. 4) S-stars respectively. From Fig. 3 it is deduced that all intrinsic S-stars clearly follow the $F_\nu \sim \lambda^{-2}$ law in the LRS spectrum expected from hot stellar photospheres. The only exception is DY Gem, which was discussed in Sect. 2. From Fig. 4 it is clear that the intrinsic S-stars deviate significantly

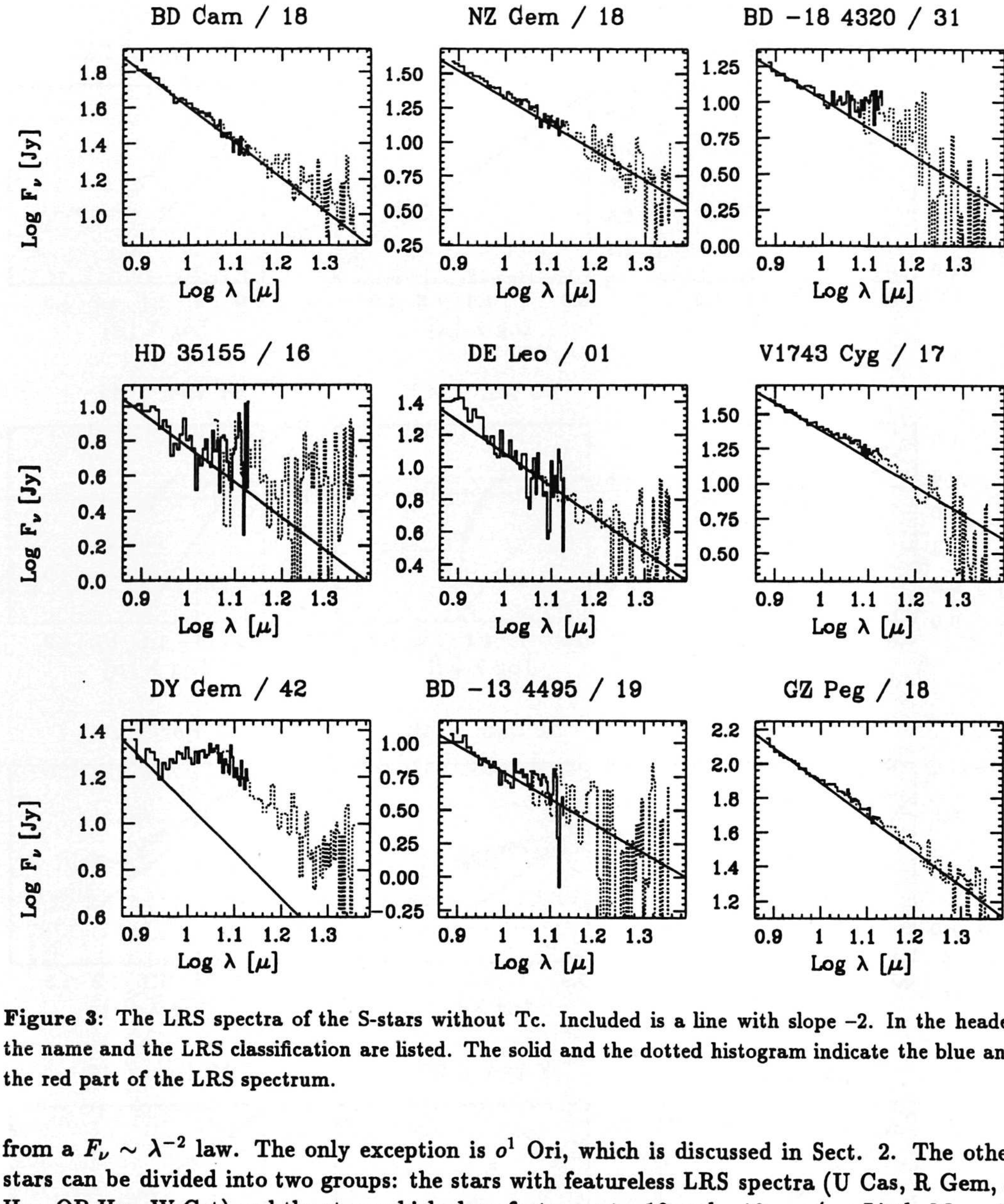

Figure 3: The LRS spectra of the S-stars without Tc. Included is a line with slope −2. In the header the name and the LRS classification are listed. The solid and the dotted histogram indicate the blue and the red part of the LRS spectrum.

from a $F_\nu \sim \lambda^{-2}$ law. The only exception is o^1 Ori, which is discussed in Sect. 2. The other stars can be divided into two groups: the stars with featureless LRS spectra (U Cas, R Gem, S Her, OP Her, W Cet) and the stars which show features at ~10 and ~19 μm (see Little-Marenin & Little 1988 for a thorough discussion on the features observed in the LRS spectra of S-stars). The four stars classified as 4n in the LRS atlas all show (weak) 18 μm emission.

The five additional stars (all intrinsic S-stars) not in the LRS atlas but listed in Volk & Cohen (1989) and Volk et al. (1991) are not plotted. R And, T Sgr and χ Cyg clearly show emission features near 10 and 19 μm. For BD 23 654 and HR Peg it is not possible to tell if there is excess flux relative to a λ^{-2} law from the usual $\log \lambda F_\lambda - \lambda$ plot.

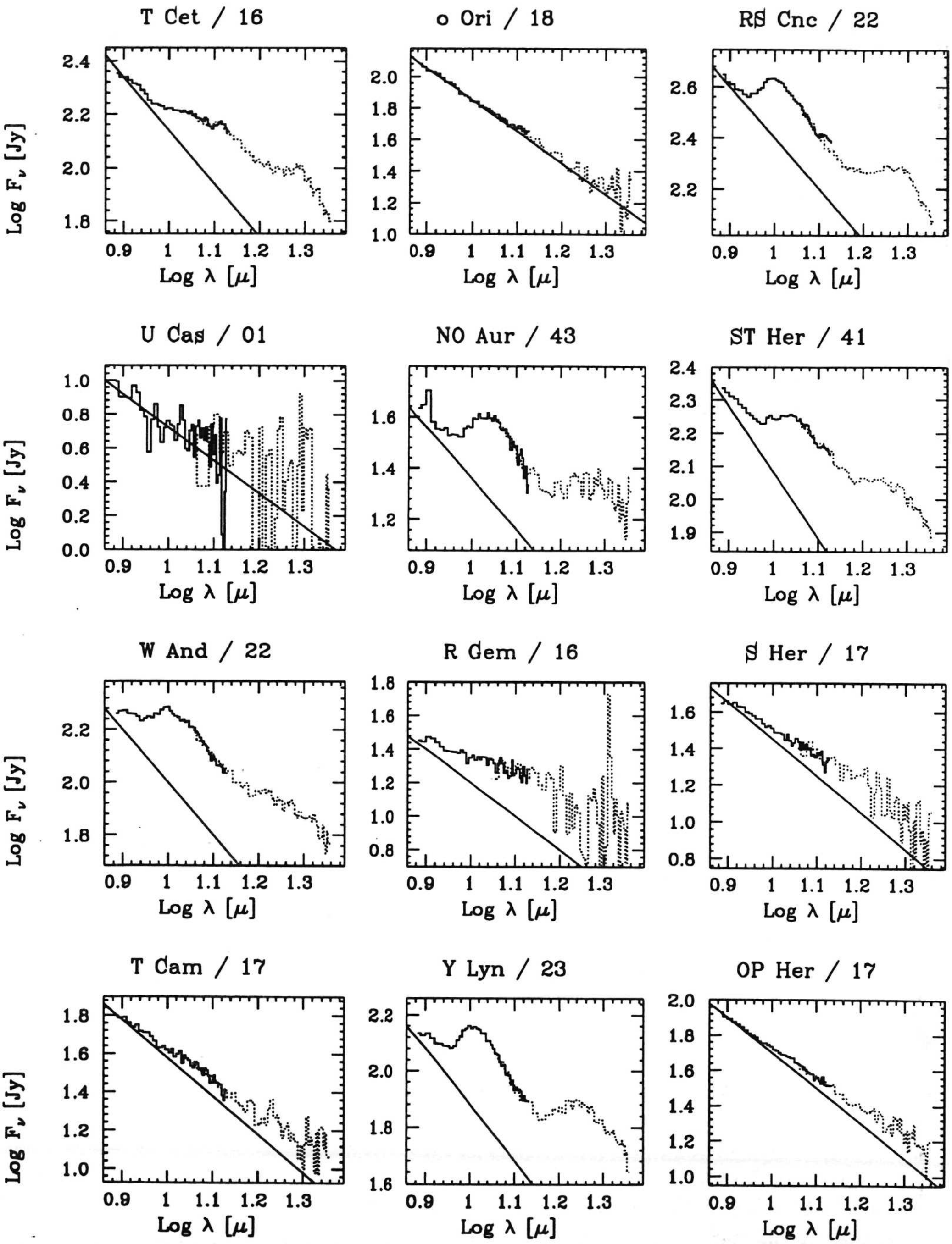

Figure 4: The LRS spectra of the S-stars with Tc. Included is a line with slope −2. In the header the name and the LRS classification are listed.

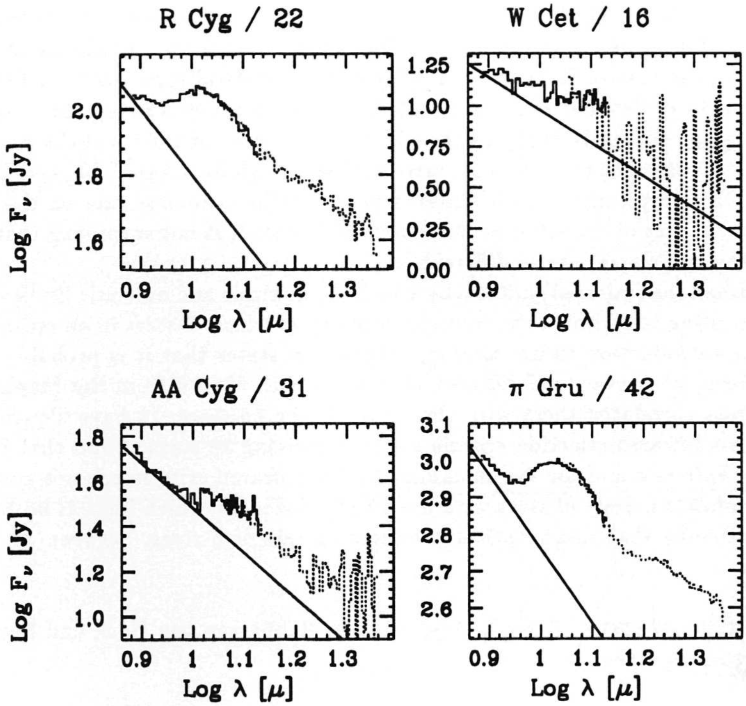

Figure 4: Continued

5 Conclusions

I show that on the basis of the IRAS PSC fluxes, the V−[12] color and the LRS spectra it is possible to classify a S-star, with high probability, as an intrinsic or an extrinsic S-star. This method uses the fact that extrinsic S-stars are less luminous (these stars have supposedly not reached the tip of the AGB), have higher effective temperatures and have a low mass loss rate, while the intrinsic S-stars are luminous cool, thermal-pulsing AGB stars with a substantial mass loss rate. This makes the infrared properties of both classes very different[2].

The criteria to discriminate between extrinsic and intrinsic stars can be summarized as follows:

1. S-stars with $V - [12] \leq 5$ are extrinsic, stars with $5 < V - [12] \leq 7$ can be intrinsic or extrinsic and ~96% of the S-stars with $V - [12] > 7$ are intrinsic.

2. S-stars with $C_{21} > -1.31$ or $C_{32} > -1.42$ are intrinsic S-stars. S-stars with $-1.52 < C_{21} < -1.31$ and $C_{32} < -1.42$ can belong to both groups. Stars with $C_{21} < -1.52$ are extrinsic.

3. When the LRS spectrum is plotted as $\log F_\nu$ versus $\log \lambda$ the extrinsic S-stars follow a line of slope -2. The intrinsic S-stars are characterised by featureless cool blackbodies or show the silicate emission features near 10 and 19 μm.

The conclusion that the extrinsic S-stars have little or no circumstellar material is consistent with the evolutionary scenario envisioned for these stars. The mass function of the extrinsic

[2]In a recent paper Jorissen et al. (1993) arrive at the same conclusion by considering the distribution of S(12 μm)/S(2.2 μm) and the $[K - 12]$, $[K - 25]$ color-color diagram.

S-stars is $Q = M_2^3/(M_1 + M_2)^3$ = 0.04-0.05 $M_\odot$ (Jorissen & Mayor 1992). For a WD companion of M_2 = 0.55-0.65 $M_\odot$ this puts the extrinsic S-stars at 1.2-1.7 $M_\odot$. If it is assumed that that the S-stars have $T_{eff} < 4000$ K to show ZrO (equivalent spectral type ≥M0) and using the new evolutionary tracks of Schaller et al. (1992) I find that for a Reimers law the mass loss rate is 2-10 10^{-9} $M_\odot$/yr on the RGB. If an extrinsic S-star is observed at the tip of the RGB (where the evolution is fastest though) the mass loss rate may be as high as ~3 10^{-8} $M_\odot$/yr. The mass loss rate on the AGB is typically 10-1000 times larger than the mass loss rate on the RGB. Given the evolutionary status of the intrinsic and extrinsic S-stars it is not surprising that the infrared properties of the two classes are so different.

Having established the (infrared) criteria by which the intrinsic and extrinsic S-stars can be separated it is interesting to estimate the contamination by extrinsic S-stars in an optically complete sample. In the introduction to his catalog, Stephenson states that it is probably complete up to V = 10. Being conservative, I selected all S-stars with V < 9 from the Stephenson (1984) catalog and cross correlated them with the PSC. Of the 66 stars, 13 have Tc and 23 have no Tc. I applied my infrared selection criteria to the remaining 30 stars. I find that 8 are intrinsic S-stars, 11 are extrinsic and for the remaining 11 the infrared criteria are not conclusive. The last category consists mainly of stars with low 12 μm fluxes for which there is no LRS spectrum available. I conclude that in an optical complete sample of S-stars, between 50 and 70% are extrinsic stars.

Acknowledgements. I thank Teije de Jong, Bobby van den Hoek and René Oudmaijer for a critical reading of the manuscript.

References

Ake T.B., Johnson H.R., 1988, ApJ 327, 214
Bidelman W.P., 1980, Publ. Warner and Swasey Obs. 2, 6
Boothroyd A.I., Sackmann I.-J., 1988, ApJ 328, 653
Brown J.A., et al., 1990, AJ 99, 1930
Griffin R.F., 1984, Observatory 104, 224
Hoffleit D., 1982, Bright star catalog, Yale university press
Houck N., 1988, Michigan catalog of two-dimensional spectral types for the HD stars, University of Michigan
Iben I., Renzini A., 1983, ARA&A 21, 271
Johnson H.R., Ake T.B., Ameen M.M., 1993, ApJ 402, 667
Joint IRAS Science Working Group, 1986, IRAS catalogs and atlases, Low Resolution Spectrograph (LRS), A&AS 65, 607
Joint IRAS Science Working Group, 1986, IRAS catalogs and atlases, Point Source Catalog (PSC), US Government Printing Office, Washington
Jorissen A., Mayor M., 1988, A&A 198, 187
Jorissen A., Mayor M., 1992, A&A 260, 115
Jorissen A., Frayer D.T., Johnson H.R., Mayor M., Smith V.V., 1993, A&A 271, 463
Keenan P.C., Garrison R.F., Deutsch A.J., 1974, ApJS 28, 271
Kholopov P.N., et al., General Catalog of Variable Stars, 1985, Nauka, Moscow
Little S.J., Little-Marenin I.R., Bauer W.H., 1987, AJ 94, 981
Little-Marenin I.R., Little S.J., 1988, ApJ 333, 305
Mathews G.J., Takahashi K., Ward R.A., Howard W.M., 1986, ApJ 302, 410
McClure R.D., Fletcher J.M., Nemec J.M., 1980, ApJ 238, L35

McClure R.D., 1983, ApJ 268, 264
McClure R.D., Woodsworth A.W., 1990, ApJ 352, 709
Scalo J.M., Miller G.E., 1981, ApJ 246, 251
Schaller G., Schaerer D., Meynet G., Maeder A., 1992, A&AS 96, 269
Schatz G., 1983, A&A 122, 327
Smith V.V., Lambert D.L., 1986, ApJ 311, 843
Smith V.V., Lambert D.L., 1987, AJ 94, 977
Smith V.V., Lambert D.L., 1988, ApJ 333, 219 (SL88)
Smith V.V., Lambert D.L., 1990, ApJS 72, 387 (SL90)
Stephenson C.B., 1984, Publ. Warner and Swasey Obs. 3, 1
Vanture A.D., Wallerstein G., Brown J.A., Bazan G., 1991, ApJ 381, 278
Volk K., Cohen M., 1989, AJ 98, 931
Volk K., Kwok S., Stencel R.E., Brugel E., 1991, ApJS 77, 607

Chapter 5

A new dust radiative transfer program

Abstract

A numerical code is presented to calculate the radiation transfer in a spherically symmetric dust shell around a central star. The dust temperature is derived from the condition of radiative equilibrium. The program allows for an arbitrary mass loss history. The model is tested and applied to the case of a mass loss rate increasing with time on the AGB following the mass loss law of Bedijn (1987). The far-infrared and sub-mm fluxes are especially sensitive to the effect of an increasing mass loss rate.
Given the uncertainty in the IRAS fluxes at 60 and 100 μm, which are usually used to constrain radiative transfer models, only increases in the mass loss rate of more than a factor of 2 over a time scale of 10^4 years are detectable. The sub-mm region is a more sensitive tracer of the mass loss history, but one has to take into account that sub-mm fluxes are usually measured with an instrument with a beam smaller than the region where the sub-mm emission originates. Another problem is that the far-infrared and sub-mm fluxes are also sensitive to the adopted absorption coefficient ($Q_\lambda \sim \lambda^{-\alpha}$). It is found that a change from α = 2.1 to 2.7 for $\lambda > 20$ μm has the same effect as the change from a constant mass loss rate to one which has increased by a factor of 10 over the past 10^4 years.

1 Introduction

The numerical problem of radiative transfer in circumstellar dust shells has been treated by many authors, e.g. Hummer & Rybicki (1971), Leung (1976), Taam & Schwartz (1976), Bedijn et al. (1978), Haisch (1979), Yorke (1980), Martin & Rogers (1984), Rogers & Martin (1984, 1986). The study of the dust shells around AGB stars based on these models are even more numerous, e.g. Jones & Merrill (1976), Rowan-Robinson (1980), Rowan-Robinson & Harris (1983a, b), Rowan-Robinson et al. (1986), Bedijn (1987), Martin & Rogers (1987), Schutte & Tielens (1989), Orofino et al. (1990), Griffin (1990), Justtanont & Tielens (1992) or Griffin (1993). The need for yet another radiative transfer code seems therefore hardly warranted. However, most, if not all, of the codes mentioned above allow only for a $1/r^2$ density distribution, at best a $1/r^\alpha$ distribution. In contrast, the mass loss rate of AGB stars is probably a function of time. This can be a graduate increase during the evolution on the AGB (see e.g. Bedijn 1987), or a more erratic behaviour related to thermal pulses (e.g. the carbon and M stars with a 60 μm excess, Willems & de Jong 1988, Zijlstra et al. 1992). The transition from the AGB to the post-AGB phase is yet another example of temporal behaviour of the mass loss rate that is not easily described by a $1/r^\alpha$ density distribution. The study of such phenomena requires a radiative transfer code where an explicit $\dot{M}(t)$ function may be specified.
In many numerical codes the inner radius of the dust shell is specified and then the corresponding dust temperature is calculated in the program. In the present model a more realistic approach is

adopted to specify the dust (condensation) temperature at the inner radius, and let the program determine the location of the inner radius.
The essence of the present radiative transfer code is not computational speed but rather flexibility in the choice of mass loss histories combined with a straightforward solution of the radiative transfer and the radiative equilibrium equation.
After developing the equations in Sect. 2, and testing the model in Sect. 3, an example of the influence of a non-constant mass loss rate on the spectral energy distribution is given in Sect. 4. The results are discussed in Sect. 5.

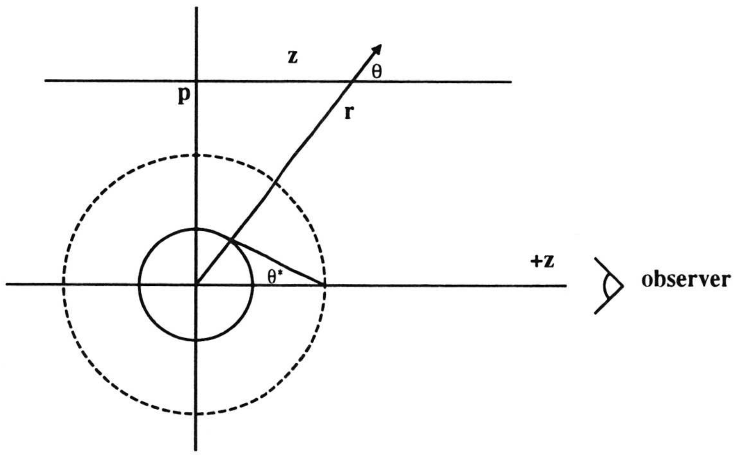

Figure 1: The geometry of the problem. Indicated are the radial coordinate, r, the impact parameter, p, the distance along the line of sight, z, and the angle θ. The angle the central star subtends from the inner dust radius is θ^*.

2 Basic equations

Consider the geometry in Fig. 1, with the radial coordinate, r, the impact parameter, p, and the distance along the line of sight, z, with the observer at $z = +\infty$. As usual we define $\mu = -\cos\theta$. The time-independent, non-relativistic radiative transfer equation along the line-of-sight may be written as:

$$\frac{dI_\lambda}{dz} = -\sigma^e I_\lambda + j_\lambda \tag{1}$$

where I is the specific intensity, σ^a, σ^s, σ^e ($\equiv \sigma^a + \sigma^s$) are the absorption, scattering and extinction coefficients and j_λ is the emissivity given by (in the case of isotropic and coherent scattering):

$$j_\lambda = \sigma^a B_\lambda + \sigma^s \frac{1}{2}\int_{-1}^{1} I_\lambda d\mu \tag{2}$$

where B_λ is the Planck function. The solution of Eq. (1) is:

$$I(z) = I_0\, e^{-\int_{z_0}^{z} \sigma^e dz'} + \int_{z_0}^{z} j(z')\, e^{-\int_{z'}^{z} \sigma^e dz''} dz' \tag{3}$$

When a grid in the z-direction exists ($z_{i+1} > z_i$), which is spaced closely enough to perform the integrations accurately by the trapezium-rule, Eq. (3) can be written as:

$$I(z_{i+1}) = I(z_i)e^{-\Delta\tau_{i+1}} + \frac{1}{2}(z_{i+1} - z_i)(j(z_{i+1}) + j(z_i)e^{-\Delta\tau_{i+1}}) \tag{4}$$

with

$$\Delta\tau_{i+1} = \frac{1}{2}(z_{i+1} - z_i)(\sigma^e_{i+1} + \sigma^e_i) \tag{5}$$

The intensity is solved in the inward (minus-z) direction, I^-, and the outward direction I^+. The boundary conditions are $I^- = 0$ at the outer radius ($z = +\infty$) and

$$\begin{aligned} I^+ &= I^- & p > R_* \\ I^+ &= B_\lambda(T_{eff})G_\lambda & p \leq R_* \end{aligned} \tag{6}$$

at $z = 0$. The central star is represented by a blackbody modified to allow for absorption features. For example, in Groenewegen et al. (1993) we consider the well known 3.1 μm feature observed in carbon stars and correspondingly chose the function G_λ to be:

$$G_\lambda = e^{-A\, e^{-\left(\frac{\lambda-\lambda_0}{\Delta\lambda}\right)^2}} \tag{7}$$

with $\lambda_0 = 3.1\ \mu m$. The emissivity depends on the dust temperature profile, which is determined from the condition of radiative equilibrium:

$$\int_0^\infty \sigma^a_\lambda\, B_\lambda(T_{dust})d\lambda = \int_0^\infty \sigma^a_\lambda\, J_\lambda d\lambda \tag{8}$$

In the numerical code, Eqs. (1), (2) and (8) are solved by an iterative method. To this end Eq. (8) is used in the following form (using $\sigma^a_\lambda = n(r)\,\pi\,a^2\,Q_\lambda$, where a is the grain size and Q_λ the absorption coefficient):

$$T^4_{dust}\,\frac{2k^4}{h^3c^2}\int_0^\infty Q_x\frac{x^3}{e^x - 1}\,dx = \int_0^\infty Q_\lambda\,\frac{1}{2}\int_{-1}^{\mu^i_*} I(\mu)\,d\mu\,d\lambda \tag{9}$$

$$+\frac{1-\mu^{i+1}_*}{1-\mu^i_*}\int_0^\infty Q_\lambda\,\frac{1}{2}\int_{\mu^i_*}^1 I(\mu)\,d\mu\,d\lambda$$

where μ^i_* is the cosine of the angle to the central star in the i-th iteration. This choice is convenient since it separates the integral over μ in two physically different regimes, namely rays that intersect the central star and rays that do not. In the absence of a dust shell, $\int_{-1}^{\mu^i_*} I(\mu)\,d\mu \equiv 0$ and $\int_{\mu^i_*}^1 I(\mu)\,d\mu = (1 - \mu^i_*)\,B_\lambda(T_{eff})$. When the iterative process has converged, μ^i_* is equal to μ^{i+1}_* and Eqs. (9) and (8) are identical.

When the intensity $I_\lambda(z,p)$ is determined, the flux at Earth is calculated from:

$$F_\lambda = \frac{2}{D^2}\int_0^\infty I_\lambda(z = +\infty, p)\,p\,e^{-\left(\frac{p-p_0}{\Delta p}\right)^2}\int_0^\pi e^{-2pp_0(1-\cos\phi)/(\Delta p)^2}d\phi\,dp \tag{10}$$

where D is the distance between the central star and the observer and where we assume that the flux at Earth is measured with an instrument with a Gaussian beam (FWHM = 1.6651Δp) centered at an offset p_0 from the central star.

In the code, grids in r, p, z, μ and λ need to be specified. These are not independent since $p^2 = r^2 - z^2 = r^2(1 - \mu^2)$. The main grid is in r. From the condition that the error using the trapezium-rule in Eq. (3) is small and from the fact that $\sigma \approx 1/r^2$, one may derive the following estimate for the step size in the radial grid ($h = r_{i+1} - r_i$):

$$h \sim \sqrt{\frac{r^3}{\tau(2+\tau/r)}} \tag{11}$$

where τ is the optical depth at some reference wavelength. In general the optical depth is given by:

$$\tau_\lambda = \int_{r_{inner}}^{r_{outer}} \pi a^2 Q_\lambda\, n(r)\, dr = 5.405\, 10^8 \frac{\dot{M}\, \Psi\, Q_\lambda/a}{R_\star\, v_\infty\, \rho_d\, r_c} \int_1^{r_{max}} \frac{R(x)}{x^2 w(x)}\, dx \tag{12}$$

where $x = r/r_c$, $\dot{M}(r) = \dot{M}\ R(x)$ and $v(r) = v_\infty\ w(x)$. The units are: the (present-day) mass loss rate at the inner radius $\dot{M}$ in $M_\odot$/yr, Ψ the dust-to-gas mass ratio, Q_λ/a in cm^{-1}, $R_\star$ in solar radii, v_∞ the terminal velocity of the circumstellar envelope in km s^{-1}, ρ_d the dust grain density in gr cm^{-3}, r_c the inner dust radius in stellar radii and r_{max} the outer radius in units of r_c. The normalised mass loss rate profile R(x) and the normalised velocity law w(x) should obey $R(1) = 1$ and $w(\infty) = 1$, respectively.

In Eq. (12) the radial coordinate r and the time t are related through:

$$t = \int_{R_\star}^{r} \frac{dr'}{v(r')} \tag{13}$$

With the grid in r determined, the grid in impact parameters is calculated. The grid points in p are the grid points in r with additional points in between chosen to give, approximately, an equidistant grid in μ. The number of impact parameters at $p < r_{inner}$, is a certain fraction (usually 20%) of the number of p-points between r_{inner} and r_{outer} and are chosen equidistant. The grid in wavelength consists of ~80 points between 0.1 and 1100 μm. In general there is no clear cut prescription how the various grids have to be chosen. From a computational point of view, the number of grid points should be as small as possible. On the other hand, the model results (dust condensation radius, dust temperature profile, spectral energy distribution) should not be dependent on the grid sizes.

In the code the following mass loss histories are considered. A mass loss rate increasing with time following Bedijn (1987):

$$\dot{M}(t) = \frac{\dot{M}_0}{(1 - t/t_0)^\alpha} \qquad (t < t_0) \tag{14}$$

and a decreasing mass loss rate:

$$\dot{M}(t) = \dot{M}_0\, e^{-t/t_0} + \dot{M}_\infty \tag{15}$$

Parameters to be specified are $\dot{M}_0$, $\dot{M}_\infty$, t_0, α and the time t at which the model has to be calculated.

In the program we allow for a velocity law of the form:

$$\frac{v(r)}{v_\infty} = w_0 + (1 - w_0)\left(1 - \frac{R_\star}{r}\right)^\beta \tag{16}$$

The following parameters are to be specified: stellar luminosity, effective temperature, grain size and density, dust-to-gas mass ratio and dust temperature at the inner radius (T_c), absorption and scattering efficiencies and the parameters in the mass loss history and the velocity law.

The solution of the radiative transfer and radiative equilibrium equations proceeds as follows. Suppose we have an initial estimate for the inner dust radius, $r_c^{(1)}$ and the dust temperature profile ($T_d^{(1)}(r)$). The initial guess for the intensity is $I^{(1)} \equiv 0$. For every wavelength point and impact parameter the radiative transfer equation is solved. In Eq. (3) the intensity enters at two locations: on the left hand side and in the scattering contribution to the emissivity. We use the estimate of I from the previous iteration ($I^{(i)}$) in the emissivity-term to calculate the new value of $I^{(i+1)}$. With $I^{(i+1)}$ determined we calculate $\int_{-1}^{\mu_*^i} I^{(i+1)}\, d\mu$ and $\int_{\mu_*^i}^{1} I^{(i+1)}\, d\mu$. We then calculate updated values for $r_c^{(i+1)}$ and $T_d^{(i+1)}(r)$ using Eq. (9). For the first radial grid point, which by definition is the inner dust radius, the temperature is fixed ($T_{dust} = T_c$). We solve Eq. (9) for $\mu_*^{(i+1)}$ and obtain an improved estimate for the inner radius $r_c^{(i+1)}$. For all other r-points we put $\mu_*^{(i+1)} = \mu_*^{(i)}$ in Eq. (9) and solve for T_{dust}. The iteration on r_c and $T_{dust}(r)$ is continued until they are determined with an relative accuracy of 10^{-4}. An optically thin model requires typically less than 5 iterations, the most optically thick models calculated in this paper require about 30 iterations. An additional verification on the model results is the conservation of total luminosity. Mathematically, this is equivalent to the condition of radiative equilibrium, but in practice it is an independent check.

Table 1: A comparison between the two radiative transfer codes

	$\tau_{9.5} = 0.1$		$\tau_{9.5} = 1.0$		$\tau_{9.5} = 1.0$ [a]	
	this work	RM	this work	RM	this work	RM
Inner radius (R_*)	5.230	5.232	5.663	5.663	5.893	5.892
Flux convergence (%)	0.26	0.21	0.50	0.16	0.61	0.11
12 μm flux (Jy)	22.4	22.3	112	111	117	116
25 μm flux (Jy)	8.3	8.0	65.6	62.6	68.3	65.4
60 μm flux (Jy)	1.26	1.20	10.3	9.6	10.7	10.1
100 μm flux (Jy)	0.33	0.33	2.6	2.5	2.7	2.6

	$\tau_{9.5} = 10.0$		$\tau_{9.5} = 50.0$	
	RM	this work	RM	this work
Inner radius (R_*)	7.84	7.86	11.9	12.1
Flux convergence (%)	0.19	0.00	0.07	0.06
12 μm flux (Jy)	205	206	113	112
25 μm flux (Jy)	409	401	807	802
60 μm flux (Jy)	119	113	645	636
100 μm flux (Jy)	32.3	31.0	220	212

Note. (a) Including isotropic scattering. Dust particle size is 0.1 μm and the mass loss rate is 7.08 10^{-7} $M_\odot$/yr.

3 Results

An an example, models are calculated assuming the following typical parameters for an AGB star: luminosity $L = 6000\ L_\odot$, $T_{eff} = 3000$ K. The star is set at an arbitrary distance of 1 kpc. We assume astronomical silicate (Draine & Lee 1984, Draine 1987) grains of radius $a = 0.1\ \mu m$ and density $\rho_d = 2$ gr cm^{-3} and a dust-to-gas ratio of 0.01. We assume a constant expansion

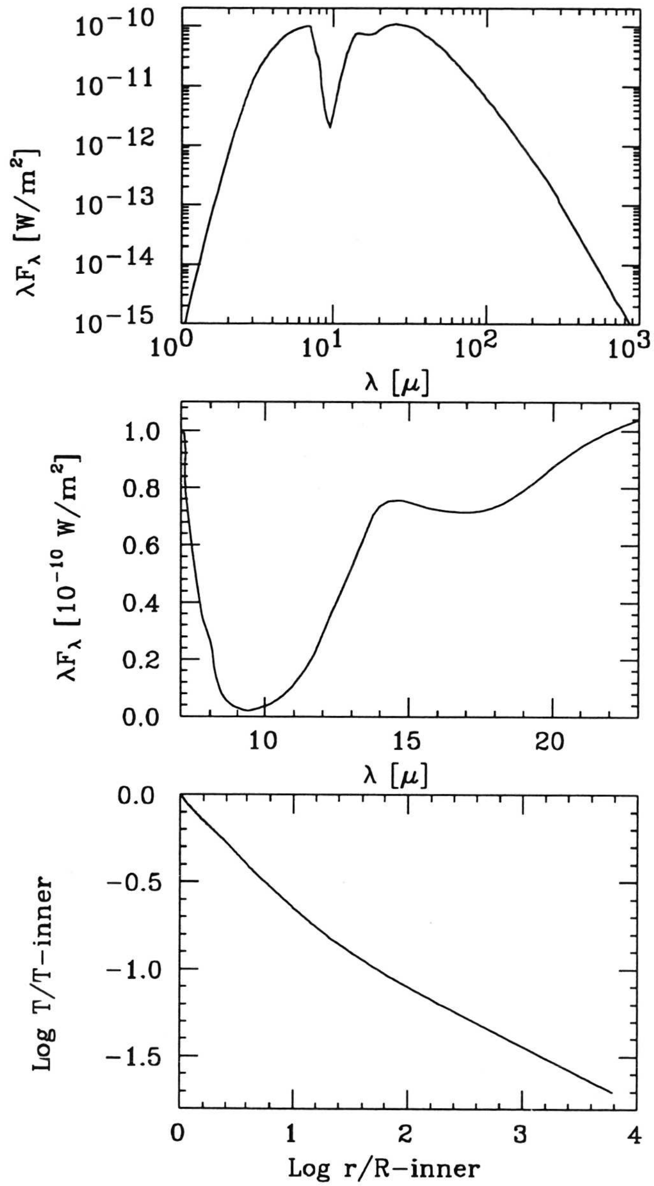

Figure 2: The spectral energy distribution (top panel), the LRS spectrum (middle panel) and dust temperature profile (bottom panel) for the model with $\tau_{9.5} = 50$.

velocity of 15 km s^{-1} and constant mass loss rates of $\dot{M} = 6.33\ 10^{-8}$, $6.81\ 10^{-7}$, $9.43\ 10^{-6}$, $7.13\ 10^{-5}$ $M_\odot$/yr corresponding to optical depths at the reference wavelength of 9.5 μm of 0.1, 1, 10 and 50. For the time being scattering is neglected. The dust temperature at the inner radius is assumed to be 1000 K and the outer radius is determined in the model by the condition that the dust temperature has dropped to 20 K. Beam effects are neglected. In Fig. 2 the spectral energy distribution, the LRS spectrum and the dust temperature profile are shown for the $\tau_{9.5}$

= 50 case.
We have tested our model against the code of Rogers & Martin (1984, 1986, hereafter RM-code). The results are listed in Table 1, where we compare the inner dust radius, the flux convergence and the IRAS fluxes for the 4 optical depths. The differences are a few percent at most. The differences in the spectral energy distribution, LRS spectrum and dust temperature profile are unnoticeably small.
To check our code and investigate the influence of scattering we included this effect in the $\tau_{9.5}$ = 1 model. It proved necessary to increase the mass loss rate to 7.08 10^{-7} $M_\odot$/yr to obtain $\tau_{9.5}$ = 1. The agreement between the two codes is again good. The cases with and without scattering are virtually identical (see Table 1). This implies that the influence of scattering introduces a negligible uncertainty (~4%) in the derived mass loss rate.

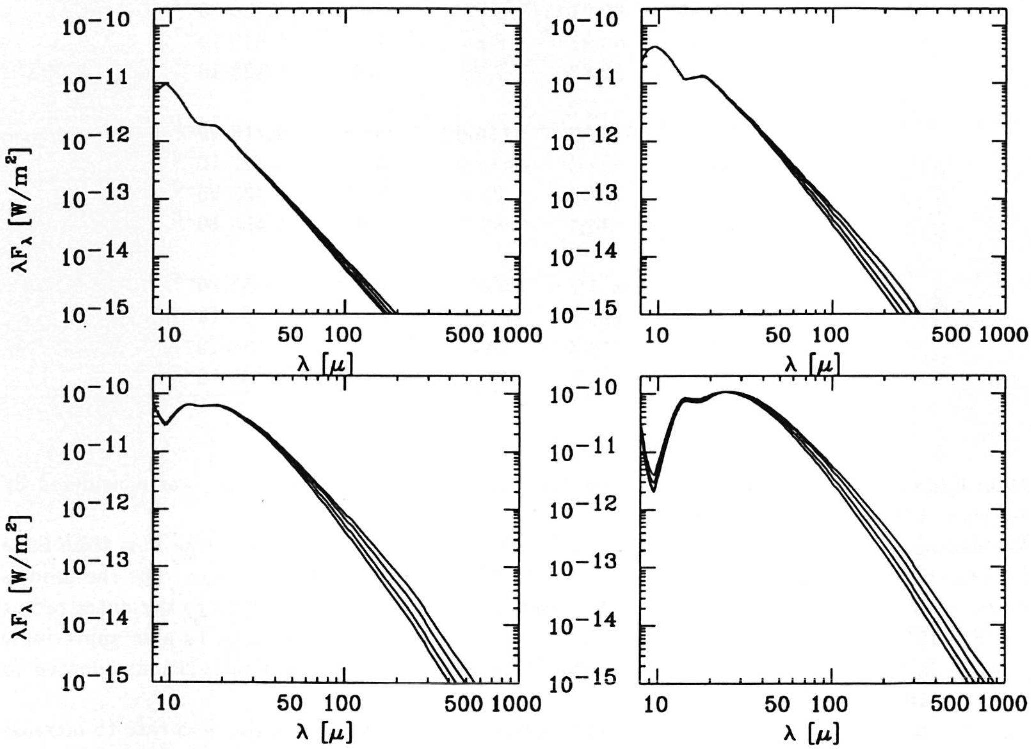

Figure 3: The influence of an increasing mass loss rate with time. The mass loss rate increases by a factor of f in 10^4 years, according to the mass loss history proposed by Bedijn (1987; see Eq. 17). The spectral energy distributions are for $\tau_{9.5}$ = 0.1 (upper left), 1 (upper right), 10, (lower left), 50 (lower right). Within each panel the four curves indicate f = 1, 2, 5, 10 from top to bottom.

4 Increasing mass loss rates on the AGB: observable or not ?

Our model has already been used extensively (Groenewegen & de Jong 1991, Slijkhuis & Groenewegen 1992, Groenewegen & de Jong 1992, Oudmaijer et al. 1993). In this section we predict the changes in the spectral energy distribution (SED) when the mass loss rate is continuously increasing on the AGB compared to the constant mass loss rate case. The case of a decreasing

Table 2: The effects of a decreasing mass loss rate on the IRAS fluxes

τ	f	S_{12} (Jy)	S_{25} (Jy)	S_{60} (Jy)	S_{100} (Jy)	$\dot{M}$ ($M_\odot$/yr)
0		8.7	2.2	0.38	0.12	0
0.1	1	22.43	8.34	1.26	0.33	$6.287\ 10^{-8}$
	2	22.43	8.31	1.21	0.30	$6.290\ 10^{-8}$
	5	22.39	8.19	1.13	0.26	$6.294\ 10^{-8}$
	10	22.31	8.00	1.04	0.23	$6.304\ 10^{-8}$
1	1	111.88	65.58	10.29	2.59	$6.806\ 10^{-7}$
	2	111.89	65.21	9.77	2.18	$6.809\ 10^{-7}$
	5	111.80	63.97	8.80	1.71	$6.815\ 10^{-7}$
	10	111.44	61.83	7.78	1.38	$6.828\ 10^{-7}$
10	1	205.0	407.6	116.6	31.6	$9.418\ 10^{-6}$
	2	206.4	405.5	110.5	26.5	$9.422\ 10^{-6}$
	5	209.5	397.9	98.8	20.7	$9.432\ 10^{-6}$
	10	213.9	384.3	86.7	16.4	$9.458\ 10^{-6}$
50	1	112.4	811.7	638.1	210.4	$7.155\ 10^{-5}$
	2	115.8	818.6	605.0	179.5	$7.164\ 10^{-5}$
	5	125.5	818.6	536.9	140.7	$7.184\ 10^{-5}$
	10	137.8	819.5	465.0	111.4	$7.207\ 10^{-5}$

mass loss rate, when the star moves from the AGB to the post-AGB phase, was considered by Slijkhuis & Groenewegen (1992).

We consider the mass loss rate of Eq. (14). The relevant time scales are the flow time scale through the envelope and the time scale on which the mass loss rate changes. For the models in the previous section the time for a dust particle to travel from the inner to the outer radius is ~3.5 10^4 yrs. The time scale on which the mass loss rate must change to give appreciable changes in the SED is therefore shorter than this and is in the present calculations adopted to be $\Delta t = 10^4$ yrs.

Suppose we want to calculate our model at time t_1, and to have the mass loss rate to increase by a factor of f over the past Δt years. The present-day mass loss rate is $\dot{M}_1$. Using Eq. (14) this gives:

$$\begin{aligned} \dot{M}_1 &= \frac{\dot{M}_0}{(1-t_1/t_0)^\alpha} \\ \dot{M}_1/f &= \frac{\dot{M}_0}{(1-(t_1-\Delta t)/t_0)^\alpha} \end{aligned} \tag{17}$$

from which follows:

$$\begin{aligned} t_0 &= t_1 + \frac{\Delta t}{f^{1/\alpha}-1} \\ \dot{M}_0 &= \dot{M}_1\, t_0^{-\alpha} \left(\frac{\Delta t}{f^{1/\alpha}-1}\right)^\alpha \end{aligned} \tag{18}$$

Values for α between 0.5 and 1 have been proposed in the literature (Baud & Habing 1983, Bedijn 1987, van der Veen 1989). In the following examples $\alpha = 0.75$ is used, expecting that the

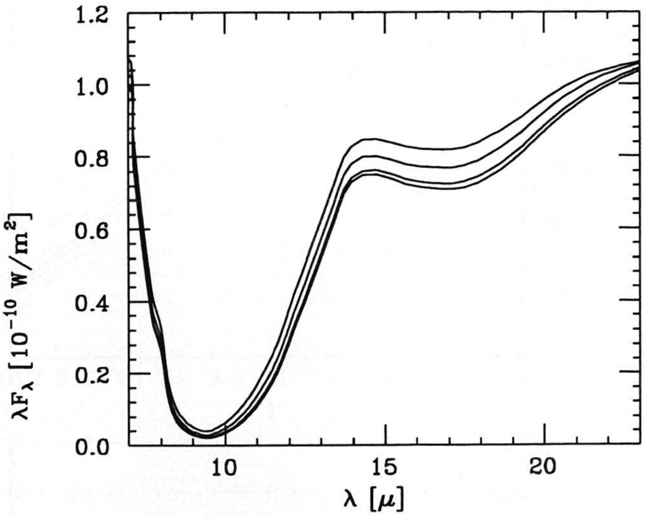

Figure 4: The LRS spectra for $\tau_{9.5}$ = 10.0 and f = 1, 2, 5, 10 from bottom to top.

results are qualitatively similar for α = 0.5 or 1.
We have calculated the SEDs for f = 1, 2, 5, 10 for the models with $\tau_{9.5}$ = 0.1, 1, 10, 50 without scattering. We used α = 0.75 and $\Delta t = 10^4$ yrs. The SEDs are shown in Fig. 3 and the predicted IRAS fluxes are listed in Table 2. It is clear that the effect of an increasing mass loss rate increases with f, $\tau_{9.5}$ and wavelength. Notice that the present-day mass loss rate is hardly affected. This suggests that the present-day mass loss rate is effectively determined by the spectrum up to ~10 μm where the hot dust, closest to the star, emits. The differences in the LRS spectra are only noticeable in the $\tau_{9.5}$ = 50 case which is shown in Fig. 4.
In Fig. 5 the quantity $Y \equiv (S_\lambda(\tau, f) - S_\lambda(\tau = 0)) \;/\; (S_\lambda(\tau, f = 1) - S_\lambda(\tau = 0))$ is plotted against f, for λ = 60 an 100 μm for the models in Table 2. There is a good correlation between the two quantities, independent of τ. This means that it is possible to estimate f even in the case a star has been modelled with a $1/r^2$-density law. Suppose the spectrum up to ~10 μm has been modelled to determine the mass loss rate and one notices that the predicted flux at 60 and 100 μm (corresponding to $S_\lambda(\tau, f = 1)$) is larger than the observed flux (corresponding to $S_\lambda(\tau, f)$). Estimate $S_\lambda(\tau = 0)$ from the model and calculate Y. One can then immediately find f from Fig. 5.
The observed spectrum longward of ~10 μm is not only determined by the mass loss history, but also by beam effects of the instrument and the absorption coefficient in the far-infrared. Usually, beam effects are neglected when a comparison is made with observations. In Chapter 6 we show that this is not justified in the case of detached shells. In Fig. 6 we show the $\tau_{9.5}$ = 10, f = 1 model with and without beam effects. At $\lambda < 7$ μm a Gaussian beam with a FWHM value of 20" (typical for near-IR observations) is assumed. Between 7 and 140 μm we use the spatial response of the IRAS detectors taken from the *Explanatory Supplement* (see Chapter 6 for details) and for longer wavelengths the beam of the JCMT telescope is assumed (typically 14" at 800 μm). The effects are important in the sub-mm region.
In previous studies (e.g. Rowan-Robinson et al. 1986, Justtanont & Tielens 1992) one usually adopted an absorption coefficient $Q_\lambda \sim \lambda^{-\alpha}$ for λ larger than some value (typically 20-30 μm) and determined α by fitting the IRAS 60 and 100 μm fluxes. Astronomical silicate has $\alpha \approx 2.06$

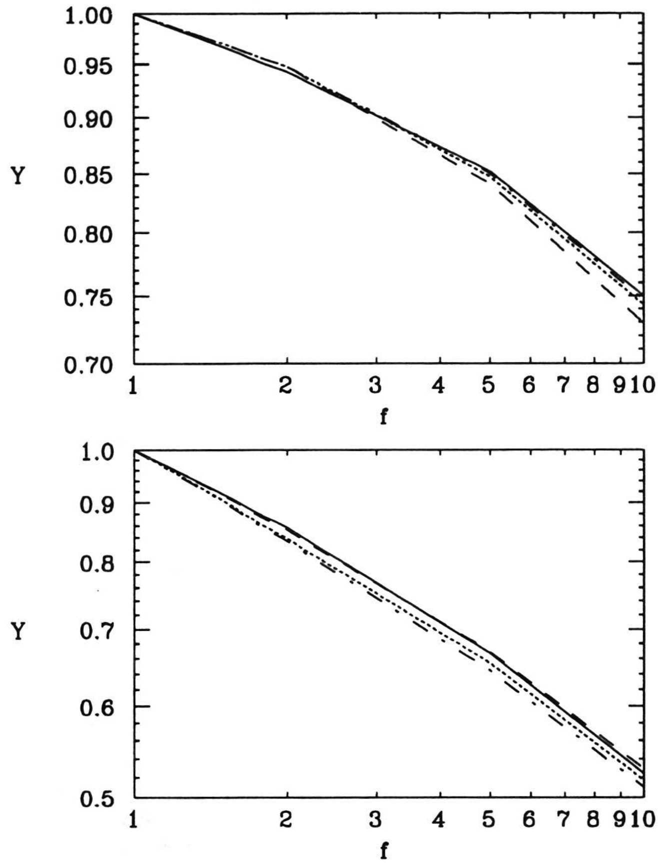

Figure 5: The ratio of fluxes Y (defined in the text) as a function of f for $\lambda = 60$ (top panel) and 100 μm (bottom panel). Indicated are $\tau_{9.5} = 0.1$ (solid), 1 (dot-dash), 10 (dotted), 50 (dashed).

for $\lambda > 20\,\mu m$. In Fig. 6 we show the $\tau_{9.5} = 10$, $f = 1$ model for astronomical silicate and for astronomical silicate with α= 2.2, 2.5, 2.7 for $\lambda > 20\,\mu m$. Comparing Figs. 3 and 6 shows that a steepening of the absorption coefficient has the same effect as an increasing mass loss rate.

5 Discussion

It was shown that an increase with time of the mass loss rate in an oxygen-rich AGB star produces observable signatures in its infrared energy distribution. For the typical case of $\dot{M} \approx 10^{-5}$ $M_\odot$/yr ($\tau_{9.5} = 10$) the 100 μm flux density for a mass loss rate increasing by a factor of 10 over 10^4 years is a factor of 2 lower than that for a constant mass loss rate. The difference at longer wavelengths is even larger (a factor of 5). The question is if these signatures would be recognised and attributed to a non-constant mass loss rate when a model is compared to real observations. Consider a comparison based on IRAS fluxes. Even for strong sources ($S_{12} > 100$ Jy) far from the galactic plane the flux uncertainty at 60 and 100 μm is seldom better than 15%. This means that mass loss increases of less than a factor of 2 over 10^4 years would be hard to detect based

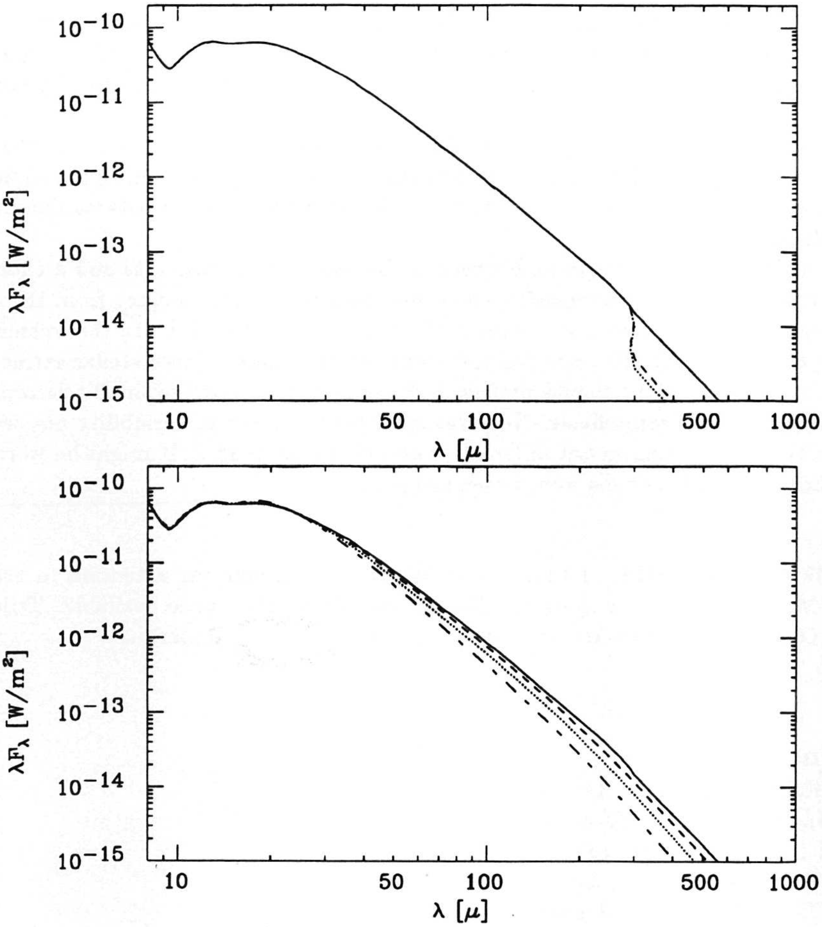

Figure 6: Top panel: the influence of beam effects on the SED for the $\tau_{9.5} = 10$ model. The solid curve indicates the standard model without beam effects. The dashed curve represents the model where we assumed a Gaussian beam with a FWHM of 20" up to 7 μm, the spatial response of the IRAS detectors between 7 and 140 μm and for longer wavelengths the response of the JCMT telescope. The 'instrument' is centered on-source. The dotted curve represent the model where the beam widths of the JCMT telescope are decreased by 1" and the 'instrument' is centered at 2" from the central position. Bottom panel: the influence of different absorption coefficients in the far-IR. Indicated are astronomical silicate (solid) and astronomical silicate with $Q_\lambda \sim \lambda^{-\alpha}$ (for λ >20 μm) with α = 2.2 (dashed), 2.5 (dotted), 2.7 (dashed-dotted).

on IRAS data.
The use of sub-mm observations is limited because of the sensitivity to beam effects. Furthermore, the flux measured may be an overestimate due to CO line emission at 867 and 1300 μm. In the case of IRC 10 216, Walmsley et al. (1991) estimate that the contribution of molecular line emission to the flux at 1.3 mm is 30%.
Most AGB sources are variables (Miras, Semi-regulars or Irregular). Periods are relatively well known from optical lightcurves for AGB stars that do not lose a lot of mass, but infrared

lightcurves for mass losing OH/IR and infrared carbon stars are less well known. Since the photometric data are usually taken at different epochs, and in the case of the IRAS data is simply an average over all observations, differences between the data and a model prediction can at least partly be attributed to variability.

It was shown that a steeper slope in the far-infrared absorption coefficient has the same effect as an increasing mass loss rate. Although the absorption and scattering properties of dust around AGB stars are uncertain one has to remember that the optical constants should obey the Kramers-Kronig relation.

It will prove difficult to discriminate between an increasing mass loss rate and a change in the far-IR dust properties. A pre-requisite would be simultaneous photometry from the optical to the mm region, preferably of a star with a thick shell, so as to minimize the influence of the underlying central star on the emerging spectrum and the effects of interstellar extinction. The far-IR and mm-observations should preferably be done with a relative small telescope to minimize the influence of beam effects. To investigate the influence of variability one would need to perform these measurements at different phases of the lightcurve. It might be worthwhile to perform such observations for a well chosen sample of stars.

Acknowledgements. I thank Rens Waters for drawing my attention to the work of Rogers & Martin, and Drs. Rogers and Martin for making their code available. Teije de Jong and René Oudmaijer are thanked for critical comments on the manuscript.

References

Baud B., Habing H.J., 1983, A&A 127, 73
Bedijn P.J., Habing H.J., de Jong T., 1977, A&A 69, 73
Bedijn P.J., 1987, A&A 186, 136
Draine B.T., Lee H.M., 1984, ApJ 285, 89
Draine B.T., 1987, Princeton Observatory Preprint 213, 1
Griffin I.P., 1990, MNRAS 247, 591
Griffin I.P., 1993, MNRAS 260, 831
Groenewegen M.A.T., de Jong T., 1991, ESO Messenger 66, 40
Groenewegen M.A.T., de Jong T., 1992, A&A 267, 410
Groenewegen M.A.T., de Jong T., Geballe T.R., 1993, in preparation
Haisch B.M., 1979, A&A 72, 161
Hummer D.G., Rybicki G.B., 1971, MNRAS 152, 1
Jones T.J., Merrill K.M., 1976, ApJ 209, 509
Justtanont K., Tielens, A.G.G.M., 1992, ApJ 389, 400
Leung C.M., 1976, JQSRT 16, 559
Martin P.G., Rogers C., 1984, ApJ 284, 317
Martin P.G., Rogers C., 1987, ApJ 322, 374
Orofino V., Colangeli L., Bussoletti E., Blanco A., Fonti S., 1990, A&A 231, 105
Oudmaijer R.D., et al., 1993, in preparation
Rogers C., Martin P.G., 1984, ApJ 284, 327
Rogers C., Martin P.G., 1986, ApJ 311, 800
Rowan-Robinson M., 1980, ApJS 44, 403
Rowan-Robinson M., Harris S., 1983a, MNRAS 202, 767

Rowan-Robinson M., Harris S., 1983b, MNRAS 202, 797
Rowan-Robinson M., Lock T.D., Walker D.W., Harris S., 1986, MNRAS 222, 273
Schutte W.A., Tielens A.G.G.M., 1989, ApJ 343, 369
Slijkhuis S., Groenewegen M.A.T., 1992, Ph.D. thesis, Chapter 6, University of Amsterdam
Taam R.E., Schwartz R., 1976, ApJ 204, 342
van der Veen W.E.C.J., 1989, A&A 210, 127
Walmsley C.M., et al., 1991, A&A 248, 555
Willems F.J., de Jong T., 1988, A&A 196, 173
Yorke H.W., 1980, A&A 86, 286
Zijlstra A.A., Loup C., Waters L.B.F.M., de Jong T., 1992, A&A 265, L5

Chapter 6

The circumstellar envelope of S Sct

Abstract

We fit the observed spectral energy distribution (SED) of S Sct. This star is the only carbon star with a 60 μm excess mapped in detail in CO. For a distance of 460 pc, corresponding to a luminosity of 7050 $L_\odot$, the CO data show that the present-day mass loss is low and that a phase of high mass loss ended about 9000 years ago. For the modelling of the SED we assume the following mass loss history: an initial mass loss rate ($\dot{M}_3$), followed by a phase of high mass loss ($\dot{M}_2$) lasting t_2 years, followed by a present-day mass loss rate ($\dot{M}_1$) lasting t_1 years. We consider both oxygen- and carbon-rich dust. The thickness of the CO shell implies a duration of the phase of high mass loss of between 350 and 1050 years. The observed SED allows values of t_2 up to 10^4 yrs for some combination of parameters, indicating that the width of the shell observed in CO and the dust emission may be different. From the SED we derive an effective stellar temperature of $T_{\rm eff} = 2700$ K and $\dot{M}_1 = 5.5\ 10^{-10}\ M_\odot$/yr. The parameters t_1, t_2, $\dot{M}_2$ and $\dot{M}_3$ are determined from the IRAS 60 and 100 μm flux densities. Both oxygen- and carbon-rich models can be constructed that fit the SED. A value of $\dot{M}_3 = 8\ 10^{-7}\ M_\odot$/yr is estimated under the assumption that the duration of the phase of high mass loss is 1050 yrs and ended 9000 yrs ago. The mass lost during one thermal pulse cycle is estimated to be $\sim$0.08 $M_\odot$. We predict that future (sub-)mm observations may resolve the question whether the dust which causes the 60 μm excess in some optical carbon stars is carbon-rich or oxygen-rich. Taking into account the finite beam width of the IRAS detectors, reduces the time for stars with detached shells to describe a loop in the IRAS color-color diagram by $\sim$30% compared to earlier calculations. The best estimate for the loop time is $\sim$1.0 10^4 years for oxygen-rich and $\sim$1.5 10^4 years for carbon-rich dust shells.

1 Introduction

The star S Sct belongs to the class of optically bright carbon stars with a 60 μm excess (Willems 1988). The chemical composition of the dust which causes this excess is still a matter of debate. Willems & de Jong (1988) suggested that these stars are formed after a thermal pulse has changed the previously oxygen-rich star into the present-day carbon star. The change in chemical composition of these stars could have caused the mass loss to drop and the oxygen-rich shell to expand and dilute, resulting in the 60 μm excess. This scenario has been criticized (see the discussion in Zuckerman & Maddalena 1989 and de Jong 1989), the main concern being that it is still unproven that the detached shell is indeed oxygen-rich. Recently, Zijlstra et al. (1992) showed that there are also M- and S-stars with a 60 μm excess. This implies that the drop in the mass loss rate probably takes place at some phase during most thermal pulses. Therefore, if a carbon star experiences another thermal pulse, which may also be accompanied by a temporary drop in the mass loss rate, the result could be a carbon star with a *carbon-rich* detached shell,

which would also result in a 60 μm excess.
S Sct is the only carbon star with a 60 μm excess which has been mapped in detail in the CO line by Olofsson et al. (1992, hereafter OCEG) and Yamamura et al. (1993, hereafter YOKID). They derived the inner radius and thickness of the detached shell and estimated the mass loss history.
The aim of this paper is twofold. First of all, we use a dust radiative transfer code to fit the observed spectral energy distribution (SED). The parameters derived from the CO-modelling will act as constraints to the model. We investigate the possibility of discriminating between an oxygen-rich and a carbon-rich detached shell. Secondly, based on these fits to S Sct we investigate the time for stars with detached shells to describe a loop in the IRAS color-color diagram and compare the results to the earlier work of Willems & de Jong (1988) and Chan & Kwok (1988).
In Sect. 2 the CO results are summarised. In Sect. 3 the observed SED is presented and in Sect. 4 the radiative transfer model is outlined. In Sect. 5 the SED of S Sct is fitted and the results are discussed in Sect. 6.

2 The CO results

OCEG have mapped S Sct with the SEST. They found that the CO is distributed nearly spherically symmetric but is probably clumped. The present-day mass loss rate is low and there is a geometrically thin (8") shell at 68" from the central star, expanding at 16.5 km s^{-1}. The mass in the shell is considerable ($\sim$0.04 M$_\odot$), implying a phase of high mass loss in the past.
From OCEG we derive the following expressions. The mass loss rate which produced the shell is:

$$\dot{M}_{shell} = 3.6\ 10^{-5}\ (d/460) \qquad M_\odot/yr \tag{1}$$

where d is the distance in pc. The uncertainty is a factor of 2.
The phase of high mass loss ceased

$$t = 9000\,(d/460) \qquad \text{years} \tag{2}$$

ago. This assumes an expansion velocity of 16.5 km s^{-1} and an inner radius of 68".
The geometrical extent (8") of the shell implies a duration of the high mass loss of:

$$\Delta t = 1050\,(d/460) \qquad \text{years.} \tag{3}$$

The present-day mass loss is:

$$\dot{M}_{present} = 2.3\ 10^{-8}\ (d/460)^2 \qquad M_\odot/yr, \tag{4}$$

with an uncertainty of a factor of 3. The present-day shell is expanding at roughly 5 km s^{-1}. Bergman et al. (1993) have modelled the CO data of OCEG in more detail. Their results do not differ significantly from the parameters derived by OCEG, which are used here.
After our work was completed we became aware of the results of YOKID. They observed the CO (1-0) line of S Sct with the Nobeyama telescope, which has a beam width of 16" compared to the 44" of the SEST. The spectra were fitted using a non-LTE molecular excitation code, taking into account chemical reactions and a self consistent temperature determination. The inner radius YOKID determine is within 2% of that of OCEG. They find expansion velocities of 16.5 and $\sim$7 km s^{-1}, in good agreement with OCEG. The main difference is that YOKID derive a shell width 1/3 of that of OCEG, corresponding to t_2 = 350 yrs in our model (see Sect. 5 and Eq. 3). In their modelling YOKID assume the CO to be uniformly distributed, while OCEG derive from their observations that the CO is clumped.

3 The observed spectral energy distribution

S Sct is a carbon star (number 4121 in Stephenson's 1989 catalog) with C/O = 1.07 and $^{12}C/^{13}C$ = 45 (Lambert et al. 1986). In Table 1 we present photometric data for S Sct collected from the literature. The observed flux densities are corrected for interstellar extinction adopting A_V = 0.79 and the interstellar extinction curve of Cardelli et al. (1988). The adopted value for A_V follows from the algorithm proposed by Milne & Aller (1980) and is consistent with the value of $0.6 \lesssim A_V \lesssim 0.9$ derived from Neckel & Klare (1980). The IRAS flux densities in Table 1 are color-corrected. The integrated flux at earth is 1.07 10^{-10} Wm^{-2}. For an assumed luminosity of 7050 $L_\odot$ (the observed mean luminosity of carbon stars in the LMC, Frogel 1980) S Sct is at 460 pc. In Sect. 5 the predicted model flux densities are directly compared to the observed IRAS flux densities in the PSC: $S_{12} = 58.3 \pm 7.8$ Jy, $S_{25} = 17.3 \pm 1.4$ Jy, $S_{60} = 9.3 \pm 1.1$ Jy and $S_{100} = 14.1 \pm 1.7$ Jy.
S Sct is classified as an SRb variable with a period of 148 days (Kholopov et al. 1985). The amplitude of the variability is small. The standard deviation in the Geneva photometric system (Rufener 1988) is only 0.13 mag in the V-band. The IRAS variability index is 0.
There is no LRS-spectrum in the LRS atlas (Joint IRAS Science Working Group 1986) but Volk & Cohen (1989) have extracted the spectrum from the LRS database. The spectrum is noisy but is essentially featureless and does not show the silicate or the silicon carbide feature. This implies a low present-day mass loss rate.

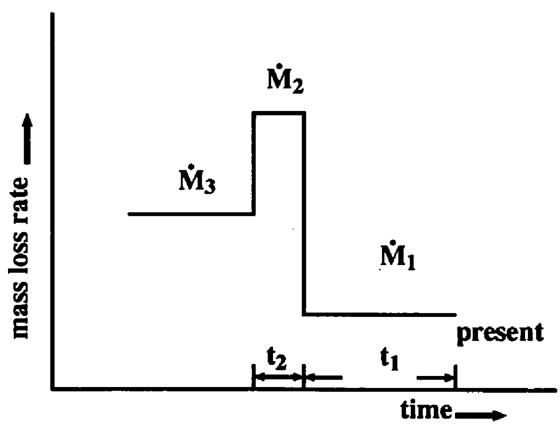

Figure 1: The adopted schematic mass loss history.

4 The dust radiative transfer model

The dust radiative transfer model of Groenewegen (1993) is used. This model was developed to handle non-r^{-2} density distributions. It simultaneously solves the radiative transfer equation and the thermal balance equation for the dust. The adopted mass loss history is schematically illustrated in Fig. 1. The central star is represented by a blackbody of temperature $T_{\rm eff}$. For the carbon-rich dust we assume amorphous carbon. The absorption coefficient is calculated from the optical constants listed in Rouleau & Martin (1991) for the AC1-amorphous carbon species. For the oxygen-rich dust we assume astronomical silicate (Draine & Lee 1984, Draine 1987). Condensation temperatures are 1500 and 1000 K, respectively. For both the carbon- and

Table 1: The observed fluxes of S Sct

Reference	λ [μm]	F_λ [$W/m^2/\mu m$]	Reference	λ [μm]	F_λ [$W/m^2/\mu m$]
Rufener (1988)	0.346	6.39 (−15)	Walker (1980)	1.25	5.00 (−10)
	0.402	8.48 (−13)		1.65	3.88 (−10)
	0.448	3.65 (−12)		2.20	2.41 (−10)
	0.540	4.51 (−11)		3.5	6.73 (−11)
	0.549	6.11 (−11)			
	0.581	8.29 (−11)	Hackwell (1972)	2.3	2.50 (−10)
				3.5	9.37 (−11)
Walker (1979)	0.360	8.52 (−14)		4.8	1.52 (−11)
	0.440	5.56 (−12)		8.6	2.40 (−11)
	0.550	6.39 (−11)		10.8	2.44 (−12)
	0.640	1.40 (−10)			
	0.790	2.71 (−10)	Gillet et al. (1971)	3.5	5.91 (−11)
				4.9	1.13 (−11)
Šleivytė (1987)	0.405	3.4 (−13)		8.4	2.81 (−12)
	0.466	9.3 (−12)		11.0	1.27 (−12)
	0.516	3.03 (−11)			
	0.544	5.04 (−11)	Ney & Merrill (1980)	3.5	5.91 (−11)
	0.655	1.70 (−10)		4.9	1.14 (−11)
				8.4	3.37 (−12)
Noguchi et al. (1981)	1.00	4.91 (−10)		11.2	1.10 (−12)
	1.25	4.80 (−10)			
	1.65	4.14 (−10)	Price & Murdock (1983)	4.2	3.95 (−11)
	2.25	2.40 (−11)		11.0	1.90 (−12)
	3.12	7.78 (−11)			
	3.70	6.74 (−11)	IRAS PSC	12	9.76 (−13)
			color-corrected	25	5.99 (−14)
				60	8.39 (−15)
				100	4.23 (−15)

oxygen-rich dust we assume a dust-to-gas ratio of $\Psi = 0.01$, a grain radius a $= 0.03$ μm and a grain density $\rho = 2.0$ g cm^{-3}. The expansion velocity in phase 2 is 16.5 km s^{-1}. For convenience we assume the same expansion velocity in phases 1 and 3. This seems inconsistent with the observed present-day (phase 1) velocity of about 5 km s^{-1}, which implies that there maybe a gap between the expanding shell and the matter currently expelled with a lower velocity. The density distribution may therefore be more complicated than sketched in Fig. 1. We verified that the neglect of the possible gap has negligible influence on the predicted flux densities (less than 0.015 Jy).

It is conceivable that the expansion velocity in phase 3 were less than 16.5 km s^{-1}. In that case the expanding shell would have swept up matter. This effect is negligible since the amount of matter swept up in 10 000 years is $\sim$2 10^{-3} $M_\odot$ (for a mass loss rate and an expansion velocity in phase 3 of 10^{-7} $M_\odot$/yr and 5 km s^{-1} respectively) which is much smaller than the mass in the shell ($\sim$0.04 $M_\odot$). The outer radius is determined in the model by a dust temperature of 20 K and scattering is neglected.

A feature which is usually neglected in radiative transfer calculations is the finite beam size of the IRAS detectors. In a star not surrounded by a detached shell this effect is probably not very important but considering that the emission of S Sct arises from dust at 1′ from the star this effect could be significant. The information on the spatial response of the IRAS detectors was taken from Table II.C.3, Table IV.A.1 and Fig. IV.A.3 of the *Explanatory Supplement* (Joint IRAS Science Working Group 1986). The 12 and 25 μm beams are taken to be rectangular with FWHM values of 60" in the in-scan direction for both detectors. The 60 and 100 μm beams are taken to be Gaussian with in-scan FWHM values of 120" and 220" respectively. For $\lambda > 140$ μm we assume a Gaussian beam with FWHM = 18.5". This approximates the beam size of the JCMT telescope at mm-wavelengths and allows us to estimate (Sect. 6) the flux which would be measured by the UKT 14 instrument (Duncan et al. 1990).

In the models the calculated flux is convolved with the spectral response (Table II.C.5 of the *Explanatory Supplement*) to compare the predicted fluxes directly to the fluxes listed in the PSC. A model is found to be in agreement with observations if the predicted flux densities are within the flux uncertainty of the observed flux densities.

For an easy interpretation of the model results it is useful to derive some analytical relations for the dust emission in the case that the emission is optically thin at all wavelengths. In the optically thin case and with an absorption coefficient $Q_\lambda \sim \lambda^{-p}$ the inner radius of the dust shell varies like $r_c \sim (T_{\rm eff}/T_c)^{\frac{4+p}{2}}$, where T_c is the (condensation) temperature at the inner radius. For carbon-rich dust we find from our models:

$$r_c\ (\text{in } R_*) = 2.313 \ \left(\frac{T_{eff}}{2700}\,\frac{1500}{T_c}\right)^{2.45} \tag{5}$$

The exponent is very close to the expected value of 2.5 for carbon-rich dust (p = 1). The emission (per unit wavelength) at infrared wavelengths is given by:

$$S(\lambda) = S_*(\lambda) + \Delta S(\lambda) \tag{6}$$

where S_* is the contribution from the central star and ΔS represents the dust emission. The stellar contribution can be written as:

$$S_*(\lambda) = \frac{B_\lambda(T_{eff})}{T_{eff}^4}\,\frac{L}{4\,\sigma d^2} \tag{7}$$

where L is the luminosity of the star and σ is the Stefan-Boltzmann constant. In the optically thin case the dust emission in the shell is given by (Sopka et al. 1985):

$$\Delta S(\lambda) = \frac{\pi a^2 Q_\lambda}{4\pi\ d^2}\int_{r_{inner}}^{r_{outer}} B_\lambda[T(r)]\,n(r)\,4\,\pi r^2\,dr \tag{8}$$

where n(r) is the dust grain number density and T(r) the dust temperature profile. The optical depth is defined as:

$$\tau_\lambda = \int_{r_c}^{\infty} \pi a^2\,Q_\lambda\,n(r)\,dr = \frac{3\,\dot{M}\,\Psi\,Q_\lambda/a}{16\,\pi\,r_c\,R_*\,v\,\rho} \tag{9}$$

where Ψ is the dust-to-gas ratio, a the grain radius, ρ the grain density, r_c the inner radius in units of stellar radii and R_* the stellar radius in cm. The last equality in Eq. (9) assumes a $1/r^2$ density distribution. Equation (8), with the help of Eq. (9) can be written as:

$$\Delta S(\lambda) = \tau_\lambda\,\frac{(r_c R_*)^2}{d^2}\,\left(\frac{\lambda\,k\,T_c}{h\,c}\right)^{\frac{4+p}{2}}\,\frac{h\,c^2\,(4+p)}{\lambda^5}\int_{\frac{hc}{\lambda k T_c}}^{\infty}\frac{y^{1+p/2}}{\exp(y)-1}\,dy \tag{10}$$

The integral is only weakly dependent on T_c. For example, when p = 2 and $\lambda = 12$ μm the integral changes by 8.5% when T_c is varied from 1500 to 1000 K. At longer wavelengths the T_c dependence of the integral is even less.

Table 2: Results for a carbon-rich detached shell

t_1 (yr)	t_2 (yr)	$\dot{M}_2$ ($M_\odot$/yr)	$\dot{M}_3$ ($M_\odot$/yr)	S_{60} (Jy)	S_{100} (Jy)
9000	350	$5.24\ 10^{-5}$	$5.24\ 10^{-7}$	9.28	12.74
9000	1050	$1.94\ 10^{-5}$	$1.94\ 10^{-7}$	9.28	12.80
9000	3050	$9.51\ 10^{-6}$	$9.51\ 10^{-8}$	9.28	14.12
9000	14050	$5.00\ 10^{-6}$	$5.00\ 10^{-8}$	8.32	15.78
9730	350	$7.34\ 10^{-5}$	$7.34\ 10^{-7}$	9.28	14.11
9735	1050	$2.69\ 10^{-5}$	$2.69\ 10^{-7}$	9.28	14.11
9000	1050	$1.65\ 10^{-5}$	$1.3\ 10^{-6}$	9.28	14.11
11000	1050	$2.4\ 10^{-5}$	$2.4\ 10^{-7}$	6.50	9.88

5 Results

5.1 The effective temperature and the present-day mass loss

The effective temperature and the present-day mass loss can be constrained without considering the 60 and 100 μm fluxes. For example, an effective temperature less than 2500 K can be excluded because this results in $S_*(25) > 18.7$ Jy. When $T_{\rm eff}$ is increased beyond 2500 K the stellar flux decreases at infrared wavelengths and there is increasing room for dust emission. For high effective temperatures the spectrum peaks at shorter wavelengths which for $T_{\rm eff} \gtrsim 3000$ K is no longer in agreement with the observed SED. We determined the effective temperature and the present-day mass loss rate by fitting the SED up to 25 μm. It turns out that it is not possible to fit the UV part of the spectrum ($\lambda < 0.5\ \mu m$) for any reasonable effective temperature. This is probably due to the blackbody approximation for the stellar flux which does not take into account the effect of molecular absorption bands. An effective temperature of 2700 K gives a good fit from 0.5 to 25 μm. Lambert et al. (1986) quote $T_{\rm eff} = 2895$ K based on the infrared-flux method[1].

The present-day mass loss rate is determined by fitting the 12 and 25 μm points. For carbon-rich dust and a mass loss rate of $\dot{M}_1 = 5.5\ 10^{-10}\ M_\odot$/yr the model has 12 and 25 μm fluxes of 66.9 and 17.3 Jy, in excellent agreement with observations. The present-day mass loss rate we derive is considerably less than that estimated from the CO. It is unclear how to explain this. As mentioned in Sect. 3 the LRS spectrum is photospheric showing no dust emission features. Maybe the estimate from the CO is too high. OCEG have derived the present-day mass loss rate from the Knapp & Morris (1985) formula which is based on the kinetic temperature of IRC 10 216. This most certainly is not applicable in the case of S Sct. For our model we adopt an effective temperature of $T_{\rm eff} = 2700$ K and a present-day mass loss rate of $5.5\ 10^{-10}\ M_\odot$/yr which results in $S_*(60) = 2.88$ Jy and $S_*(100) = 0.87$ Jy when folded with the IRAS spectral response.

[1] In the YOKID paper an effective temperature of 2350 K is assumed in their radiative transfer model. Although their calculated spectrum nicely fits the few data points in their plot, such a low effective temperature can be excluded on the basis of the larger observational data set listed in Table 1.

Table 3: Results for an oxygen-rich detached shell

t_1 (yr)	t_2 (yr)	$\dot{M}_2$ ($M_\odot$/yr)	$\dot{M}_3$ ($M_\odot$/yr)	S_{60} (Jy)	S_{100} (Jy)
9000	350	25.6 10^{-5}	25.6 10^{-7}	8.84	15.80
9000	1050	10.7 10^{-5}	10.7 10^{-7}	8.69	15.78
9000	2450	5.30 10^{-5}	5.30 10^{-7}	8.28	15.79
7750	350	1.72 10^{-4}	1.72 10^{-6}	9.28	14.11
7620	1050	7.00 10^{-5}	7.00 10^{-7}	9.28	14.12
8800	1050	6.0 10^{-5}	6.0 10^{-7}	6.50	9.88

5.2 The mass loss history

The far-infrared fluxes are determined by the parameters t_1, t_2, $\dot{M}_2$ and $\dot{M}_3$. We calculated several models to illustrate the influence of the parameters. Results for carbon-rich and oxygen-rich detached shells are collected in Tables 2 and 3. Based on the analysis of the CO observations (Sect. 2) the value of t_1 is initially fixed at 9000 years and the mass loss rate in phase 3 is arbitrarily set at 1% of $\dot{M}_2$. For the duration t_2 of mass loss phase 2 we adopt different values: 350 yrs (see YOKID), 1050 yrs (see OCEG), 3050 yrs (the best fit) and 14050 yrs (the maximum value allowed by the IRAS data) for the carbon-rich shell. For the oxygen-rich shell values of t_2 = 350, 1050 and 2450 yrs are considered. For t_2 =350 and 1050 yrs we determined the value of t_1 that best fits the IRAS 60 and 100 μm fluxes and found $t_1 \approx 9700$ for the carbon-rich and $\approx$7700 yrs for the oxygen-rich shell. For $t_2 = 1050$ the range in t_1 and $\dot{M}_2$ allowed by the IRAS data is 8000 - 11500 yrs and 1.7 - 4.2 10^{-5} $M_\odot$/yr for the carbon-rich shell and 6000 - 9500 yrs and 3.8 - 12 10^{-5} $M_\odot$/yr for the oxygen-rich shell, respectively. For the carbon-rich model with $t_1 = 9000$ and $t_2 = 1050$ we investigated the influence of the ratio $\dot{M}_2/\dot{M}_3$. A best fit is found for a ratio of $\sim$13. No fit is found for the oxygen-rich shell. An example of the fits is shown in Fig. 2 for the carbon-rich model with $t_1 = 9735$ and $t_2 = 1050$ yrs. The results are further discussed in Sect. 6.

Our conclusion may be affected by cirrus since S Sct is located at only 3 degrees below the galactic equator. The PSC lists a CIRR-2 index of 5, suggesting that up to 30% of the 100 μm flux may be due to cirrus, although Egan & Leung (1991) concluded that cirrus is not a major factor in determining the 60/100 color in carbon stars. To investigate the possible influence of cirrus contamination we assume that the true flux from S Sct at 60 and 100 μm is 70% of the flux listed in the PSC. With the help of Eqs. (6) and (10) and the stellar fluxes listed in Sect. 3 a new set of best-fitting parameters can be estimated (last entry in Tables 2 and 3). Cirrus contamination does not alter our conclusion that both oxygen-rich and carbon-rich models are consistent with the IRAS data. However, the best fitting oxygen-rich model is in better agreement with the IRAS data than the best-fitting carbon-rich model.

In the models, specific values are adopted for the expansion velocity, the dust condensation temperature, the effective temperature and the distance (c.q. luminosity). To indicate how the derived mass loss rates and time scales depend on these parameters we use the equations in Sect. 4. The dependence on the distance and the expansion velocity is like $t \sim d/v$ and $\dot{M} \sim v\ d$ (cf. Eq. 9). We next investigate the dependence on the condensation temperature and the effective temperature. From Eqs. (5), (9) and (10) it follows that $\Delta S \sim f(T_c)\ T_{\rm eff}^{0.5}$, where $f(T_c)$ denotes the integral in Eq. (10). Since $f(T_c)$ is only weakly dependent on the condensation temperature,

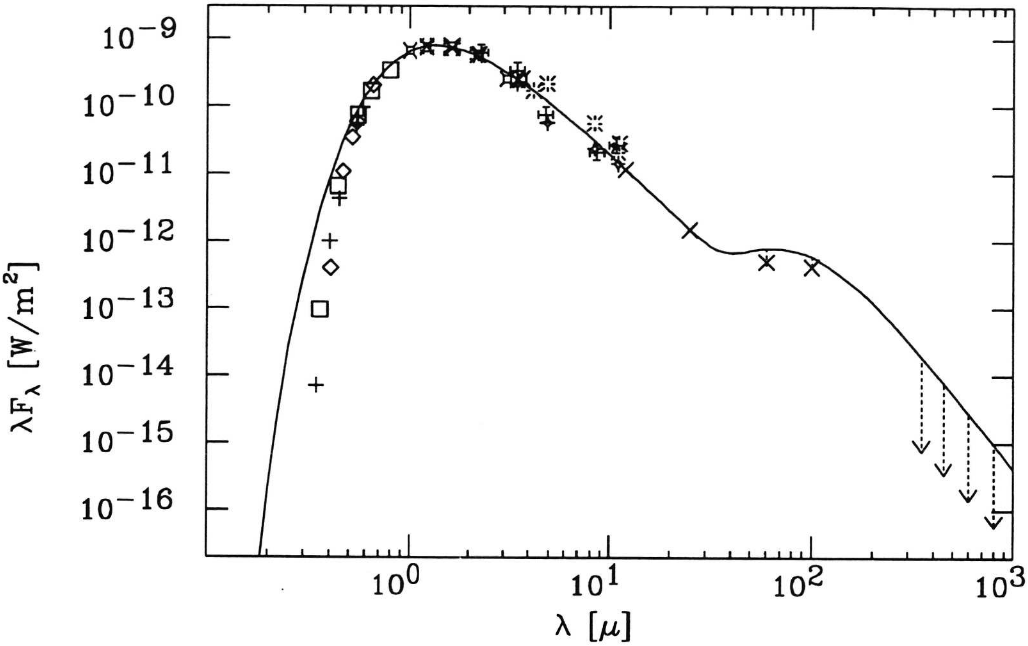

Figure 2: The observed spectral energy distribution of S Sct compared to the carbon-rich model with t_1 = 9735 yrs and t_2 = 1050 yrs. The effective temperature and present-day mass loss rate are 2700 K and 5.5 10^{-10} $M_\odot$/yr, respectively. The symbols indicate different sources of photometry (see Table 1): X = IRAS, + = Rufener (1988), ◇ = Šleivytė (1987), □ = Walker (1979), ✧ = Gillet et al. (1971), ⌑ = Noguchi et al. (1981), ⁜ = Hackwell (1972), ⁂ = Walker (1980), * = Ney & Merrill (1980) and Price & Murdock (1983). The solid line is the model without beam effects. The dashed line with arrows indicate the beam effect of IRAS observations (at 60 and 100 μm) and the JCMT (at 350, 450, 600 and 800 μm). The beam effect at (sub-) mm wavelengths is so large that only the central star is observed.

the dependence of the mass loss rates and time scales on T_c is weak. The effect of the effective temperature is more complicated, since both the stellar and the dust contribution are changed. When the effective temperature is increased, the stellar flux at infrared wavelengths is decreased while the dust emission is increased. From comparison with a model with T_{eff} = 2800 K we find that the effects of the stellar and the dust contribution nearly cancel.

6 Discussion and conclusion

Although the models for oxygen- and carbon-rich shells in Tables 2 and 3 are formally in agreement with the observed SED, the best carbon-rich model is in better agreement with the IRAS data then the best oxygen-rich model. We find t_1 = 9735 yrs, $\dot{M}_2$ = 2.7 10^{-5} $M_\odot$/yr for the carbon-rich model and t_1 = 7620 yrs, $\dot{M}_2$ = 7.0 10^{-5} $M_\odot$/yr for the oxygen-rich model. The values derived from the CO observations are t_1 = 9000 yrs and $\dot{M}_2$ = 3.6 10^{-5} $M_\odot$/yr. The mass loss rates are uncertain to a factor of ~5 due to uncertainties in the dust-to-gas ratio and the absolute value of Q_λ but the time scales are determined accurately. Since the expansion velocity is known the major uncertainty is in the adopted luminosity. The lifetimes scale like $\sqrt{L}$.
Since the CO shell in the high mass loss phase may be partially or largely destroyed by photodis-

Table 4: Predicted KAO and JCMT flux densities at 100, 850 and 1100 μm

grain type	t_1 (yr)	t_2 (yr)	JCMT on source 850 μm (mJy)	JCMT on source 1100 μm (mJy)	JCMT off source 850 μm (mJy)	JCMT off source 1100 μm (mJy)	KAO on source 100 μm (Jy)
carbon	9000	1050	13.2	7.6	2.20	0.91	1.36
carbon	9000	14050	13.4	7.7	2.37	1.08	1.29
carbon	9735	1050	13.3	7.7	2.89	1.31	1.35
oxygen	9000	1050	12.3	7.1	1.14	0.40	1.46
oxygen	9000	2450	12.3	7.1	1.29	0.45	1.41
oxygen	7620	1050	12.3	7.1	0.29	0.099	1.56

sociation the dust shell may be much ticker than the CO shell. The duration of the high mass loss phase is constrained by the infrared observations. For $t_1 = 9000$ yrs we find that $t_2 = 2450$ and 14050 yrs are just compatible with the IRAS observations in the case of an oxygen- and a carbon-rich shell, respectively.

Suppose that a negligible amount of the CO associated with phase 2 has been dissociated. This implies that the value of t_2 derived from the CO observations is the true duration of the phase of high mass loss. A lifetime of 1050 years for phase 2 is consistent with theoretical estimates which indicate that the duration of the increase in luminosity after a TP is about 1% of the interpulse time. Recent calculations by Vassiliadis & Wood (1992) show that the interpulse period is between 5 10^4 and 10^5 years. This implies theoretical values for t_2 of 500 to 1000 years. Using the CO data as constraint allows an estimate for the mass loss rate in phase 3. With t_1 and t_2 fixed at 9000 and 1050 years we determined $\dot{M}_2$ and $\dot{M}_3$ that best fit the IRAS data (see Table 2). The derived value of $\dot{M}_3$ scales with v_3. The value of v_3 is not known but is very likely to be in between the observed expansion velocities in phases 1 ($v_1 \approx 5$ km s^{-1}) and 2 ($v_2 = 16.5$ km s^{-1}). If $v_3 = 10$ km s^{-1} then $\dot{M}_3 = 8\ 10^{-7}$ $M_\odot$/yr. For an oxygen-rich shell no satisfactory model exists.

With values for the mass loss rates during the different phases of the thermal pulse cycle one can estimate the total mass lost. The observed duration of the thermal pulse (associated with the phase of high mass loss) of 1050 years suggest that the interpulse period is 10^5 years (see Vassiliadis & Wood 1992). An appropriate lifetime for the luminosity dip is then $\sim$2 10^4 years. The mass lost during the thermal pulse is 1050 yrs $\star$ 1.65 10^{-5} $M_\odot$/yr $\approx$ 0.02 $M_\odot$. The mass lost during the luminosity dip is very small 2 10^4 yrs $\star$ 2.3 10^{-8} $M_\odot$/yr $\approx$ 4 10^{-4} $M_\odot$. The mass lost during the quiescent H-shell burning phase is 8 10^4 yrs $\star$ 8 10^{-7} $M_\odot$/yr $\approx$ 0.06 $M_\odot$. This shows that most mass is lost in the quiescent phase. The total mass lost over one pulse cycle is 0.08 $M_\odot$. The average mass loss rate over the pulse cycle is about 8 10^{-7} $M_\odot$/yr. The mass lost in the phase of high mass loss derived from our dust modelling is a factor of 2 lower than that deduced from the CO. Considering the factor of 2 uncertainty in the CO result and the factor of 5 uncertainty in our result the two values are consistent.

Could future sub-mm continuum observations distinguish between a carbon-rich and an oxygen-rich shell? For selected models we calculate the flux-densities expected for the UKT 14 instrument at the JCMT at 850 and 1100 μm. A Gaussian beam with a FWHM value of 18.5" is assumed. Both the on-source flux density and the flux density at 72" (i.e. 68" inner radius plus half the shell width) from the central star are determined. The predicted flux densities are listed in Table 4. The on-source flux densities are higher than the off-source flux densities but the differences

Table 5: The time to reach $C_{32} = -1.55$ after the mass loss stops

grain type	beam effect	t (yrs)	grain type	beam effect	t (yrs)
oxygen	with	12 400	carbon	with	16 100
oxygen	without	16 400	carbon	without	23 300

between the different models are too small to be observationally significant. The beam of the JCMT is much smaller then the inner radius of the shell so only the central star is measured. It is better to observe the circumstellar shell directly. Not only have the carbon-rich models higher off-source flux densities than the oxygen-rich models, the spectral index ($S_\nu \sim \lambda^{-\alpha}$, with $\alpha \approx$ 3 for the carbon-rich models and $\alpha \approx 4$ for the oxygen-rich models) is significantly different. Unfortunately, the predicted flux densities are too low to be measured accurately enough with the UKT14 instrument[2]. The flux densities will be within reach of the next generation of JCMT instruments, e.g. the Sub-millimeter Common User Bolometer Array (SCUBA).

Hawkins (1992) has measured the on-source 100 μm flux density of S Sct onboard the Kuiper Airborne Observatory with a FWHM = 30" beam. He finds a 3σ upper limit of 3 Jy. In the last column of Table 4 we predict the on-source 100 μm flux density for different models for a 30" beam. We find $S_{100} < 1.6$ Jy, consistent with Hawkins upper limit.

Having determined the parameters characterizing the present status of S Sct, we are able to calculate the evolution of the spectral energy distribution. This is done for carbon-rich and oxygen-rich shells, and with and without the effect of the finite IRAS beams. The latter makes a comparison possible with the calculations of Willems & de Jong (1988) and Chan & Kwok (1988) who did not include beam effects. The beam effect is shown in Fig. 2 where we plot the best-fitting carbon-rich model (with $t_1 = 9735$ yrs and $t_2 = 1050$ yrs) and the effect of the IRAS and JCMT beam.

We calculated the evolution in the IRAS color-color diagram for the carbon rich model with $t_1 = 9735$, $t_2 = 1050$ yrs and the oxygen-rich model with $t_1 = 7620$, $t_2 = 1050$ yrs. In Table 5 we list for the different models the times to reach $C_{32} = 2.5 \log(S_{60}/S_{25}) = -1.55$ which approximately separates groups II and III in Groenewegen et al. (1992). The lifetime depends on distance and expansion velocity like d/v. We conclude that the beam effect reduces the time scale to loop through the IRAS color-color diagram by 25-30%.

Acknowledgements. We thank Fred Baas (JACH) for carrying out the JCMT observations.

References

Bergman P., Carlström U., Olofsson H., 1993, A&A 268, 685
Cardelli J.A., Clayton G.C., Mathis J.S., 1989, ApJ 345, 245
Chan S.J., Kwok S., 1988, ApJ 334, 362
Draine B.T., Lee H.M., 1984, ApJ 285, 89
Draine B.T., 1987, Princeton Observatory Preprint, 213, 1

[2]The shell position of S Sct was observed on 29 and 31 october 1992 during a JCMT service observing run with the UKT 14 instrument. Upper limits of 25 mJy at 800 μm and 200 mJy at 450 μm were obtained.

Duncan W.D., Robson E.I., Ade P.A.R., Griffin M.J., Sandell G., 1990, MNRAS 243, 126
Egan M.P., Leung C.M., 1991, ApJ 383, 314
Frogel J.A., Persson S.E., Cohen J.G., 1980, ApJ 239, 495
Gillett F.C., Merrill K.M., Stein W.A., 1971, ApJ 164, 83
Groenewegen M.A.T., 1993, Chapter 5, Ph.D. thesis, University of Amsterdam
Groenewegen M.A.T., de Jong T., van der Bliek N.S., Slijkhuis S., Willems F.J., 1992, A&A 253, 150
Hackwell J.A., 1972, A&A 21, 239
Hawkins G., 1992, in: Mass loss on the AGB and beyond, ed. H. Schwarz, in press
Joint IRAS Science Working Group, 1986, IRAS catalogs and atlases, Low Resolution Spectrograph (LRS), A&AS 65, 607
Joint IRAS Science Working Group, 1986, IRAS catalogs and atlases, Point Source Catalog (PSC), US Government Printing Office, Washington
Joint IRAS Science Working Group, 1986, IRAS catalogs and atlases, Explanatory Supplement, US Government Printing Office, Washington
de Jong, T., 1989, A&A 223, L23
Kholopov P.N., et al., 1985, General catalog of variable stars, Nauka, Moscow
Knapp G.R., Morris M., 1985, ApJ 292, 640
Lambert D.L., Gustafsson B., Eriksson K., Hinkle K.H., 1986, ApJS 62, 373
Milne D.K., Aller L.H., 1980, AJ 85, 17
Neckel Th., Klare G., 1980, A&AS 42, 251
Ney E.P., Merrill K.M., 1980, The AFGL catalog, AFGL-TR-80-0050
Noguchi K., et al., 1981, PASJ 33, 373
Olofsson H., Carlström U., Eriksson K., Gustafsson B., 1992, A&A 253, L17 (OCEG)
Price S.D., Murdock T.L., 1983, The revised AFGL infrared sky survey catalog, AFGL-TR-83-0161
Rouleau F., Martin P.G., 1991, ApJ 377, 526
Rufener F., 1988, Catalog of stars measured in the Geneva photometric system, 4th edition, Observatoire de Geneva
Šleivytė J., 1987, Vilnius Astr. Obs. Bull. 77, 33
Sopka R.J., et al., 1985, ApJ 294, 242
Stephenson C.B., 1989, Publ. Warner and Swasey Obs., 3, 55
Vassiliadis E., Wood P.R., 1992, preprint
Volk K., Cohen M., 1989, AJ 98, 931
Walker A.R., 1979, South African Astron. Obs. Circ., Vol 1, No 4, 112
Walker A.R., 1980, MNRAS 190, 543
Willems F.J., 1988, A&A 203, 51
Willems F.J., de Jong T., 1988, A&A 196, 173
Yamamura I., Onaka T., Kamijo F., Izumiura H., Deguchi S., 1993, PASJ, in press
Zijlstra A.A., Loup C., Waters L.B.F.M., de Jong T., 1992, A&A 265, L5
Zuckerman B., Maddalena R.J., 1989, A&A 223, L20

Chapter 7

Dust shells around infrared carbon stars

Abstract

The spectral energy distributions (SEDs) and LRS spectra of 21 infrared carbon stars are fitted using a dust radiative transfer model. The parameters derived are the temperature of the dust at the inner radius (T_c), the mass loss rate and the ratio of silicon carbide (SiC) to amorphous carbon dust (AMC). Mass loss rates between a few 10^{-6} and 1.3 10^{-4} $M_\odot$/yr are found. The SiC/AMC ratio and T_c are found to decrease with increasing S_{25}/S_{12} ratio. The former correlation may be due to an increasing C/O ratio. The latter correlation may be due to the fact that dust growth continues until the density is too low. For increasing mass loss rates this leads to increasing inner radii and hence to a decrease of T_c.
The standard model with a constant mass loss rate and amorphous carbon dust (with $Q_\lambda \sim \lambda^{-\beta}$; $\beta = 1$ for $\lambda > 30$ μm) predicts too much flux at 60 and 100 μm compared to the observations. The discrepancy increases with the S_{25}/S_{12} ratio. This indicates that either $\beta > 1$ and/or that the mass loss rate has been lower in the past. Mass loss histories as proposed by Bedijn (1987) and related to thermal pulses are considered. An increase in the mass loss rate by a factor of 3-30 over the past 10^4 yrs or β's in the range 1.2-1.9 both fit the observed IRAS 60 and 100 μm flux-densities. Based on six stars where sub-mm data is available there may be evidence for a phase of high mass loss in a distant past. If the mass loss history is related to thermal pulses then three distinct phases of mass loss can be identified from the SED.
Theoretically one expects that β decreases or remains constant as the dust continuum temperature decreases. This fact would point to the mass loss histories rather than a steeper slope of the absorption coefficient to explain the observed 60 and 100 μm flux-densities. Both mass loss histories predict sub-mm fluxes in better agreement with observations than a high value for β. If $\beta = 1$ for the most extreme carbon stars (those with $S_{25} \approx S_{12}$) then a mass loss history related to thermal pulses is preferred to the Bedijn-type mass loss history.
The correlation between the duration of the present-day high mass loss phase and the S_{25}/S_{12} ratio and between the SiC/AMC ratio and the S_{25}/S_{12} ratio can be understood if (on average) an increase in the S_{25}/S_{12} ratio implies an increase in progenitor mass.

1 Introduction

One of the characteristics of AGB stars is their large mass loss rate. In the cool circumstellar envelope dust grains form which absorb optical radiation and re-emit it in the infrared. Previous studies of dust shells around AGB stars either concentrated on oxygen-rich Mira's and OH/IR stars (e.g. Rowan-Robinson & Harris 1983a, Bedijn 1987, Schutte & Tielens 1989, Justtanont & Tielens 1992, Griffin 1993) or on the well-known carbon star IRC 10 216 (e.g. Mitchell & Robinson 1980, Martin & Rogers 1987, Le Bertre 1987, Orofino et al. 1990, Griffin 1990). Rowan-Robinson & Harris (1983b) considered a sample of 44 carbon stars but no IRAS and

LRS data were available at the time. Rowan-Robinson et al. (1986) fitted the spectral energy distributions (SEDs) of five carbon stars but fixed the dust temperature at the inner radius at 1000 K, and assumed a dust absorption law of $\sim\lambda^{-1}$ for all wavelengths without considering the presence of silicon carbide (which has a feature near 11.3 μm). Le Bertre (1988) fitted three carbon stars. Chan & Kwok (1990) fitted (SEDs) of 145 carbon stars with an LRS classification of 4n (indicating silicon carbide emission), and they therefore missed some carbon stars with weak silicon carbide emission and some extreme carbon stars which have an LRS = 2n classification. They fixed the dust temperature at the inner radius at 1500 K and only included silicon carbide dust in their model.

In this paper an attempt will be made to study is some detail questions regarding the mass loss rate, mass loss history, dust formation and strength of the silicon carbide feature. To this end fits are made to the spectral energy distributions (SEDs) and LRS spectra of 21 infrared carbon stars. The dust radiative transfer model used, allows for time-dependent mass loss rates. The dust temperature at the inner radius and the amount of silicon carbide to amorphous carbon dust are treated as free parameters. Recently acquired broad-band data at optical (Groenewegen & de Jong 1993a), near-infrared and sub-mm wavelengths (Groenewegen et al. 1993a), and 2-4 μm spectra (Groenewegen et al. 1993b) supplemented with data available in the literature are used to constrain the radiative transfer models. Preliminary results for three carbon stars were presented by Groenewegen & de Jong (1991).

In Sect. 2 the radiative transfer model is introduced. In Sect. 3 the fits to the SEDs and LRS spectra are presented and the results are discussed in Sect. 4.

2 The model

The radiative transfer model of Groenewegen (1993) is used. This model was developed to handle non-r^{-2} density distributions in spherical dust shells. It simultaneously solves the radiative transfer equation and the thermal balance equation for the dust.

The SED is determined by the dust optical depth, defined by:

$$\tau_\lambda = \int_{r_{inner}}^{r_{outer}} \pi a^2 Q_\lambda \, n(r) \, dr = 5.405 \, 10^8 \, \frac{\dot{M} \; \Psi \; Q_\lambda/a}{R_\star \; v_\infty \; \rho_d \; r_c} \int_1^{x_{max}} \frac{R(x)}{x^2} \, dx \tag{1}$$

where $x = r/r_c$ and $\dot{M}(r) = \dot{M}\, R(x)$. The units are: the (present-day) mass loss rate at the inner radius $\dot{M}$ in $M_\odot$/yr, Ψ the dust-to-gas mass ratio, Q_λ/a the absorption coefficient of the dust over the grain radius in cm^{-1}, $R_\star$ in solar radii, v_∞ the terminal velocity of the circumstellar envelope in km s^{-1}, ρ_d the dust grain density in gr cm^{-3}, r_c the inner dust radius in stellar radii and x_{max} the outer radius in units of r_c. The normalised mass loss rate profile R(x) should obey R(1) = 1. The velocity law is assumed to be constant in this paper. A dust-to-gas ratio of Ψ = 0.005, grain radius a = 0.1 μm and grain density ρ_d = 2.0 g cm^{-3} are adopted. The outer radius is determined in the model by a dust temperature of 20 K, and scattering is neglected (Le Bertre 1988). The main parameters in the model are the dust temperature at the inner radius (T_c), the optical depth at some reference wavelength and the ratio of silicon carbide to amorphous carbon dust. The inner dust radius (r_c) and the temperature at the inner radius (T_c) are uniquely related through the condition of radiative equilibrium. In Sect. 3 the mass loss rate is assumed to be constant, in Sect. 4 a time-dependent mass loss rate is considered.

The central star is represented by a blackbody modified to allow for the characteristic absorption feature in carbon stars at 3.1 μm:

$$B_\lambda(T_{eff}) \exp\left(-A \, e^{-\left(\frac{\lambda-\lambda_0}{\Delta\lambda}\right)^2}\right) \tag{2}$$

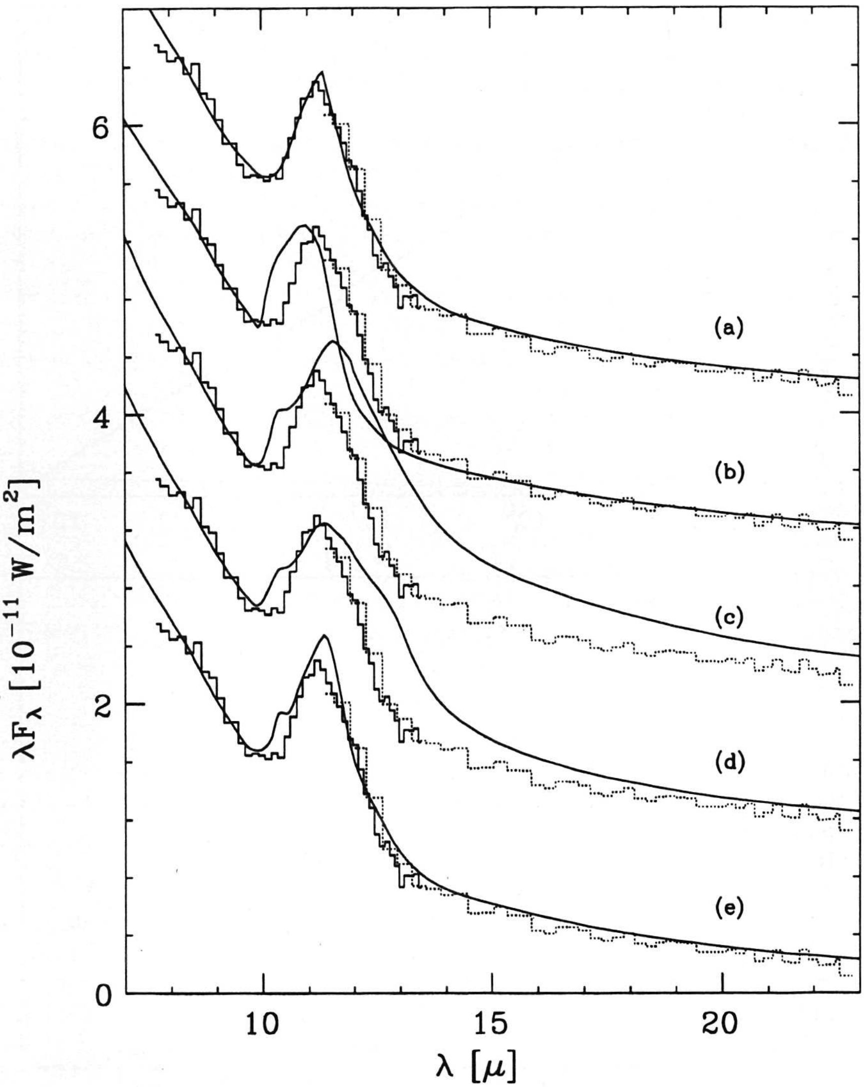

Figure 1: The LRS spectrum of IRAS 17172−4020 fitted with different species of dust containing x% silicon carbide and (100−x)% amorphous carbon. From top to bottom: (a) α-SiC (x = 10), (b) β-SiC (x = 15) , (c) SiCN (x = 15), (d) SiC1200 (x = 10) and (e) SiC600 (x = 10). The offset between each spectrum is one fluxunit. Spectrum (e) has no offset.

with λ_0 = 3.1 μm. This novelty is introduced to be able to directly fit the observed 2-4 μm spectra of some stars. Following Groenewegen et al. (1993b) A = 4.605 and $\Delta\lambda$ = 0.075 μm are adopted. A value of A = 4.605 means that in a star without a circumstellar shell the flux in the feature at 3.1 μm is 1% of the continuum. The effective temperatures and luminosities of Galactic carbon stars are poorly known. Canonical values of $T_{\rm eff}$ = 2500 K and L = 7050 $L_\odot$ are adopted throughout this paper (the mean luminosity of carbon stars in the LMC, Frogel et al. 1981). This implies $R_\star$ = 447 $R_\odot$.

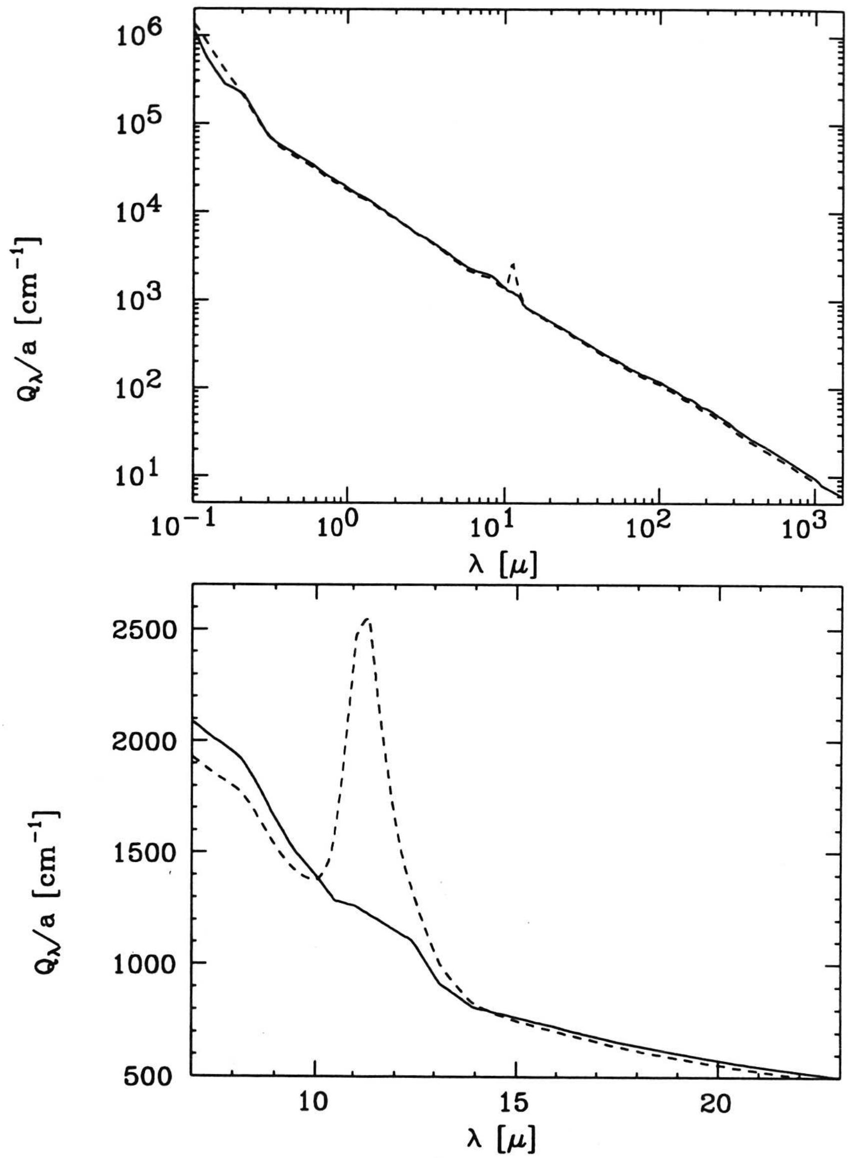

Figure 2: The absorption coefficient of pure amorphous carbon dust (solid line) and a mixture of 90% amorphous carbon and 10% silicon carbide dust (dashed line).

For the dust properties a combination of amorphous carbon (AMC) grains and silicon carbide (SiC) grains is assumed. For simplicity, one condensation temperature is used. In principle, SiC and AMC can have different temperature profiles but to take this into account requires two additional free parameters (a second condensation temperature and a dust-to-gas ratio). Since the abundance of SiC is found to be small, the simplification of the temperature profile is justified. In Eq. (1) the value of (Q_λ/a) is calculated from $(Q_\lambda/a) = x\ (Q_\lambda/a)^{\mathrm{SiC}} + (1-x)\ (Q_\lambda/a)^{\mathrm{AMC}}$ where x ($\in [0,1]$) is determined by the fit to the LRS spectrum. The absorption coefficient for AMC is calculated from the optical constants listed in Rouleau & Martin (1991) for their AC1-species. Absorption coefficients for several forms of SiC have been listed in the literature. Species considered here are SiC1200, SiC600, SiCN, β-SiC (all from Borghesi et al. 1985) and α-SiC (Pégourié 1988)[1]. To determine the best suitable choice some test runs were made fitting the SED and LRS spectrum of the star with the strongest SiC feature in the LRS atlas, namely IRAS 17172–4020 (LRS classification 46). Figure 1 shows that α-SiC (Pégourié 1988) gives the best result. The absorption coefficient of α-SiC is adopted for silicon carbide from now on. Figure 2 shows the absorption coefficient Q_λ for pure AMC and for a mix (by mass) of 90% AMC and 10% SiC for the wavelength region 0.1 - 1000 μm. Chan & Kwok (1990) concluded that the empirical opacity function they derived resembles that of β-SiC and suggested an evolution from α-SiC to β-SiC when a star evolves from an optical to an infrared carbon star. Unfortunately they did not publish any detailed fits to the LRS spectra of the stars in their sample. Our results show that excellent fits to most of the LRS spectra can be obtained with α-SiC (cf. Figs. 3-23). Only is the cases of IRAS 20396+4757 (Fig. 5) and IRAS 03229+4721 (Fig. 6) there maybe evidence for the presence of β-SiC. Previously, Baron et al. (1987) and Papoular (1988) also favoured α-SiC to explain the SiC feature.

In some stars to be discussed later a 30 μm emission feature has been observed (AFGL 489, 3068, 3116), in another (AFGL 2632) such a feature is absent (Forrest et al. 1981, Goebel & Moseley 1985). The 30 μm feature is not taken into account. The 30 μm feature may contribute up to ~30% of the IRAS 25 μm flux-density and up to ~10% of the IRAS 60 μm flux-density.

Usually, beam effects are neglected in dust radiative transfer calculations. For $\lambda < 7$ μm and between 150 $\mu m < \lambda <$ 300 μm a typical beam of 20" is assumed. Between 7 $\mu m < \lambda <$ 150 μm the beam effects of the IRAS detectors is taken into account. The information on the spatial response of the IRAS detectors is taken from Table II.C.3, Table IV.A.1 and Fig. IV.A.3 of the *Explanatory Supplement* (Joint IRAS Science Working Group 1986). The beams of the 12 and 25 μm bands are taken to be rectangular with FWHM values of 60" in the in-scan direction for both detectors. The beams of the 60 and 100 μm bands are taken to be Gaussian with in-scan FWHM (full width half maximum) values of 120" and 220" respectively. For $\lambda >$ 300 μm the beam width of the JCMT telescope is assumed. This allows a direct comparison with the observed sub-mm flux-densities in some of the program stars. The influence of beam effects is illustrated in Fig. 12 for AFGL 3116. The influence on the near-infrared and IRAS flux-densities is small. The main change is in the far-IR and mm-region.

In the models the calculated flux-density is convolved with the spectral response (Table II.C.5 of the *Explanatory Supplement*) to compare the predicted flux-densities directly to the flux-densities listed in the Point Source Catalog.

3 Fitting the SEDs

In Table 1 some general parameters are listed of the stars that are fitted. All are listed in Groenewegen et al. (1992; hereafter paper I), except IRAS 02345+5422 which is a group V star that has a 12 μm flux-density of 33 Jy, below the limiting flux-density of 100 Jy considered in paper I. The stars have been selected for the availability of as many flux determinations over as large a wavelength region as possible.

Table 1 lists the IRAS-name and AFGL number, the galactic coordinates, the C_{21} ratio (defined

[1]For SiC1200, SiC600, SiCN and β-SiC the absorption coefficients in the range 2.5 to 40 μm are taken from Borghesi et al. (1985) applying matrix correction factors of $h = 0.46$ and $\Delta\lambda = -0.3$ (see their Table 4). For $\lambda > 40\,\mu m$ the results of Blanco et al. (1991) are used for these species, scaled to 40 μm. For $\lambda < 2.5\,\mu m$ the values of Pégourié (1988) are used. For α-SiC (Pégourié 1988) the data points beyond 250 μm are extrapolated using $Q_\lambda \sim \lambda^{-2.0}$, based on the last two data points listed by him.

Table 1: The program stars

IRAS-name	AFGL	l	b	C_{21}	group[1]	A_V mag	v_∞ [2] km/s	P [3] days	photometry[4]
11318−7256	4133	297.3	−11.2	−1.182	III	0.6	30.0		10, 11
14484−6152		316.6	−2.5	−1.138	IV	1.2	20.4		6, 9, 10
20396+4757	2632	86.5	3.8	−1.133	III	1.0	13.0	421 (1)	2, 8, 10, 14
03229+4721	489	148.2	−7.6	−1.076	III	0.9	16.5	535 (1)	2, 4, 10, 14, 17
07217−1246		228.1	1.2	−1.003	IV	1.9	28.5		6, 9, 10
15194−5115		325.5	4.7	−0.921	III	0.7	25.0	580 (3)	5, 10, 15, 19
07098−2012	1085	233.3	−4.8	−0.872	IV	1.0	23.8	725 (3)	9, 10, 15
16545−4214		343.5	0.3	−0.833	III	1.0	15.0:		9, 10, 12
06342+0328	971	208.2	−1.7	−0.796	IV	1.7	9.0	653 (3)	8, 9, 10, 12, 15
23320+4316	3116	108.5	−17.1	−0.777	III	0.5	14.5	620 (2)	3, 8, 10, 13, 14, 17
19321+2757	2417	62.6	4.0	−0.703	III	1.4	25.0	625 (2)	8, 10, 13, 20
09116−2439	5254	252.8	16.2	−0.667	IV	0.6	13.0		6, 7, 10
13477−6532	4183	309.0	−3.6	−0.389	IV	1.8	19.0		10
06012+0328	865	200.8	−7.0	−0.379	IV	1.2	16.5	696 (3)	10, 13, 15
19594+4047	2494	76.5	5.6	−0.286	IV	1.1	21.0	783 (2)	1, 10, 11, 13, 18
08074−3615		253.5	−1.8	−0.239	IV	2.6	19.0		10, 11
02345+5422	5076	138.1	−5.1	0.062	V	1.8	15.0:		11
08171−2134	5250	242.2	8.1	0.084	V	1.2	16.0		10
23166+1655	3068	93.6	−32.2	0.101	V	0.3	15.3	696 (3)	10, 11, 13, 15, 16, 21
21318+5631	5625	98.2	3.7	0.211	V	1.9	17.0		10
15471−5644		325.6	−2.2	0.382	V	2.8	15.0:		10

Notes. (1) Group designation of Groenewegen et al. (1992). (2) When no value could be found in the literature a value of 15.0 km s^{-1} has been assumed. These entries are flagged by a semicolon. (3) Between parentheses the references for the pulsation period: 1 = GCVS (Kholopov et al. 1985), 2 = Jones et al. (1990), 3 = Le Bertre (1992). (4) References for the photometry used in Sect. 3: 1 = Alknis (1980), 2 = Bergeat et al. (1976), 3 = Cohen & Kuhi (1977), 4 = Dyck et al. (1974), 5 = Epchtein et al. (1987), 6 = Epchtein et al. (1990), 7 = Fouqué et al. (1992), 8 = Grasdalen et al. (1983), 9 = Groenewegen & de Jong (1993a), 10 = Groenewegen et al. (1993a), 11 = Groenewegen et al. (1993b), 12 = Guglielmo et al. (1993), 13 = Jones et al. (1990), 14 = Kholopov et al. (1985), 15 = Le Bertre (1992), 16 = Lebofsky & Rieke (1977), 17 = Lockwood (1974), 18 = Low et al. (1976), 19 = Meadows et al. (1987), 20 = Noguchi et al. (1981), 21 = Sopka et al. (1985). In addition the IRAS flux-densities and the LRS spectra, corrected according to Cohen et al. (1992), are used.

as 2.5 log(S_{25}/S_{12}); the stars are listed in order of increasing C_{21}), the group designation of paper I, the interstellar extinction in the V-band (see below), the terminal velocity of the envelope (see below), the pulsation period either from optical or infrared lightcurves and finally the references to the photometry used to construct the spectral energy distributions (SEDs). The interstellar extinction at V is estimated from the extinction maps of Neckel & Klare (1980), which list observed values of A_V as a function of galactic coordinates and distance, and the Parenago (1940) model for the interstellar extinction (see paper I for the exact form). For the distance the value in Table 2 is used. Both estimates for A_V usually agree and the average value is quoted in Table 1. The terminal velocities can be accurately determined from millimeter observations. The values in Table 1 are taken from the CO and HCN catalog of Loup et al. (1993) or from Groenewegen et al. (in preparation).

Table 2: The fit parameters

IRAS-name	T_c (K)	$\dot{M}$ ($M_\odot$/yr)	r_{inner} (R_*)	SiC/AMC	d (kpc)	$\tau_{11.33}$	$\tau_{0.5}$	remarks
11318−7256	1500	4.0 10^{-6}	2.3	0.07	0.67	0.37	6.49	
14484−6152	1100	1.8 10^{-5}	5.6	0.05	0.91	0.90	18.2	
20396+4757	1200	2.7 10^{-6}	3.9	0.06	0.55	0.33	6.12	
	1200	2.4 10^{-6}	2.2	0.06	0.53	0.33	6.12	T_{eff} = 2000 K
03229+4721	1000	6.0 10^{-6}	6.1	0.06	0.72	0.37	6.86	
07217−1246	1100	1.4 10^{-5}	5.2	0.03	1.79	0.48	11.3	
15194−5115	1100	1.4 10^{-5}	5.2	0.03	0.50	0.52	12.5	
07098−2012	1000	5.5 10^{-6}	6.2	0.05	1.07	0.39	7.91	
16545−4214	1300	2.7 10^{-6}	3.2	0.03	0.11	0.27	6.50	
06342+0328	1100	6.5 10^{-6}	5.4	0.05	1.15	0.76	15.4	
23320+4316	900	1.5 10^{-5}	8.5	0.03	0.68	0.60	14.2	
19321+2757	900	1.2 10^{-5}	7.9	0.03	0.87	0.30	7.14	
09116−2439	1100	1.9 10^{-5}	6.1	0.05	0.84	1.38	27.8	
13477−6532	800	3.8 10^{-5}	11.7	0.05	1.81	0.98	19.8	
06012+0328	800	4.5 10^{-5}	11.8	0.02	1.24	0.82	21.4	
19594+4047	900	3.3 10^{-5}	8.9	0.05	1.05	1.00	20.3	
08074−3615	650	9.1 10^{-5}	19.8	0	2.11	0.90	28.9	
02345+5422	650	7.5 10^{-5}	19.9	0	3.99	0.93	30.0	
08171−2134	700	1.3 10^{-4}	18.3	0	2.42	1.65	53.3	
23166+1655	650	1.0 10^{-4}	20.5	0	0.93	1.19	38.1	
	650	9.1 10^{-5}	11.9	0	0.90	1.19	38.1	T_{eff} = 2000 K
21318+5631	700	1.1 10^{-4}	17.7	0	1.47	1.36	43.7	
15471−5644	700	8.5 10^{-5}	17.4	0	1.73	1.21	38.9	

The fitting procedure is as follows. Typically four values for the dust temperature at the inner radius (T_c) are chosen. The mass loss rate (assumed constant) is varied to fit the SED. The distance is determined by demanding that the predicted and observed IRAS 25 μm flux-density agree. The SiC feature is fitted by changing the (mass) ratio SiC/AMC. This last step is straightforward since the strength of the SiC feature turns out to scale linearly with the adopted SiC/AMC ratio. In choosing the best value for T_c equal weight is given to the fits of the SED and the LRS spectrum. If necessary, the above mentioned steps are repeated for the final choice of T_c. The value of the mass loss rate and T_c can both be estimated to within 10%. The best-fitting models are shown in Figs. 3 to 23 (at the end of the chapter) and the corresponding model parameters are listed in Table 2.

The observed SEDs plotted in Figs. 3-23 have not been corrected for interstellar extinction. Reddening vectors are indicated in Figs. 3-23 for the shortest observed wavelength point based on the A_V's is Table 1 and the interstellar extinction curve of Cardelli et al. (1988). The correction for interstellar extinction is usually small compared to the variation in the SEDs due to variability.

Inspection of Figs. 3-23 shows that the quality of the fits to the SEDs and LRS spectra is high with only a few exceptions (08074–3615 and 08171–2134). In some of these cases the poor fit may be due to the fact that only one set of near-IR photometry is available, which makes it uncertain how to join the IRAS data with the near-IR data. When near-IR photometry at minimum and maximum light is available it is possible to estimate the effective phase which the

IRAS observations represent.

The fits to the 2-4 μm spectra ranges from poor (e.g. 11318–7256) to excellent (e.g. 13477–6532). In the stars where there is disagreement the predicted strength of the 3.1 μm feature is always too small. This is not due to an underestimate of the strength of the 3.1 μm feature in the central star as this was already adopted to be strong (cf. Eq. 2). The discrepancy may point to an additional contribution of circumstellar 3.1 μm absorption (see the discussion in Groenewegen et al. 1993b). Part of the discrepancy may is some cases also be due to the difference in phase between the different observations. It would be interesting to monitor the 2-4 μm region during a pulsation period in a few stars to investigate how large the changes in the continuum and the 3.1 μm feature are. In the cases that no observed 2-4 μm spectra are available, the line profiles are a prediction of the expected strength.

The derived mass loss rates are subject to the following systematic effects. Following Eq. (1) the mass loss rate scales like $\sim R_* \, v_\infty/\kappa$. For a constant effective temperature, the derived mass loss rates (and distances) scale like $\sqrt{L}$. The opacity at 60 μm for the adopted absorption coefficient ($\kappa = 3\ Q/4\ a\ \rho_d$) is 68 cm^2gr^{-1}. This is about a factor of 2 lower than the usually quoted value of $\sim$160 cm^2gr^{-1} (see e.g. Jura 1986). Since the mass loss rate scales like $1/\kappa$, the values quoted in Table 2 may be systematically too high by a factor of 2.

The influence of the adopted effective temperature of the underlying central star on the SED is explicitly verified in the cases of AFGL 2632 and AFGL 3068, where a model with T_{eff} = 2000 K is run (see Table 2). The influence of the effective temperature is twofold. Firstly, there is a direct effect in the stellar contribution to the emerging flux. For most infrared stars (like AFGL 3068) this effect is negligible since the stellar flux is completely reprocessed in the dust shell. Secondly, the effective temperature influences the temperature distribution of the dust (through the equation of radiative equilibrium). To obtain an optical depth equal to that for the standard model with T_{eff} = 2500 K, the mass loss rates need to be changed by $\lesssim$10% and the distances need to be changed by $\lesssim$5%. The decrease in the V-magnitude for AFGL 2632 is 1.9, indicating that for optical carbon stars and carbon stars with optical thin envelopes the uncertainty in the adopted effective temperature affects the fit of the SED in the optical part of the spectrum. The main change compared to the standard model is in the inner dust radius which changes according to $r_{inner} \sim T_{eff}^{2.5}$ for amorphous carbon dust.

The ratio (by mass) of silicon carbide dust to amorphous determined is listed in Table 2. This ratio depends on the adopted absorption coefficients for SiC and AMC. Groenewegen & de Jong (1991), who used an opacity for AMC about 5 times higher than in the present study, found SiC/AMC = 0.4. Egan & Leung (1991) adopt SiC/AMC = 0.07 in their analysis of optical carbon stars without commenting on their particular choice. Egan & Leung use the same opacity for SiC and a similar one for AMC as in this study. The ratio they find for optical carbon stars agrees well with the ratio found in the least obscured stars in this sample.

4 Discussion and conclusion

In Fig. 24 the derived quantities T_c, the ratio of SiC to AMC and the mass loss rate are plotted as a function of C_{21}. The mass loss rate increases from a few 10^{-6} $M_\odot$/yr to $\sim$1 10^{-4} $M_\odot$/yr for the most extreme carbon stars. Both the temperature of the dust at the inner radius and the ratio SiC/AMC decrease with increasing C_{21}. The dust temperature at the inner radius is for most stars considerably below the canonical condensation temperature of carbon-rich dust. A similar effect was found by Onaka et al. (1989) from fitting dust shell models to the LRS spectra of about 100 optically-bright oxygen-rich Mira variables. They explained this in terms of variations in the location of dust formation related to stellar pulsation.

The assumption of an unique inner dust shell radius is an oversimplification of the dust formation

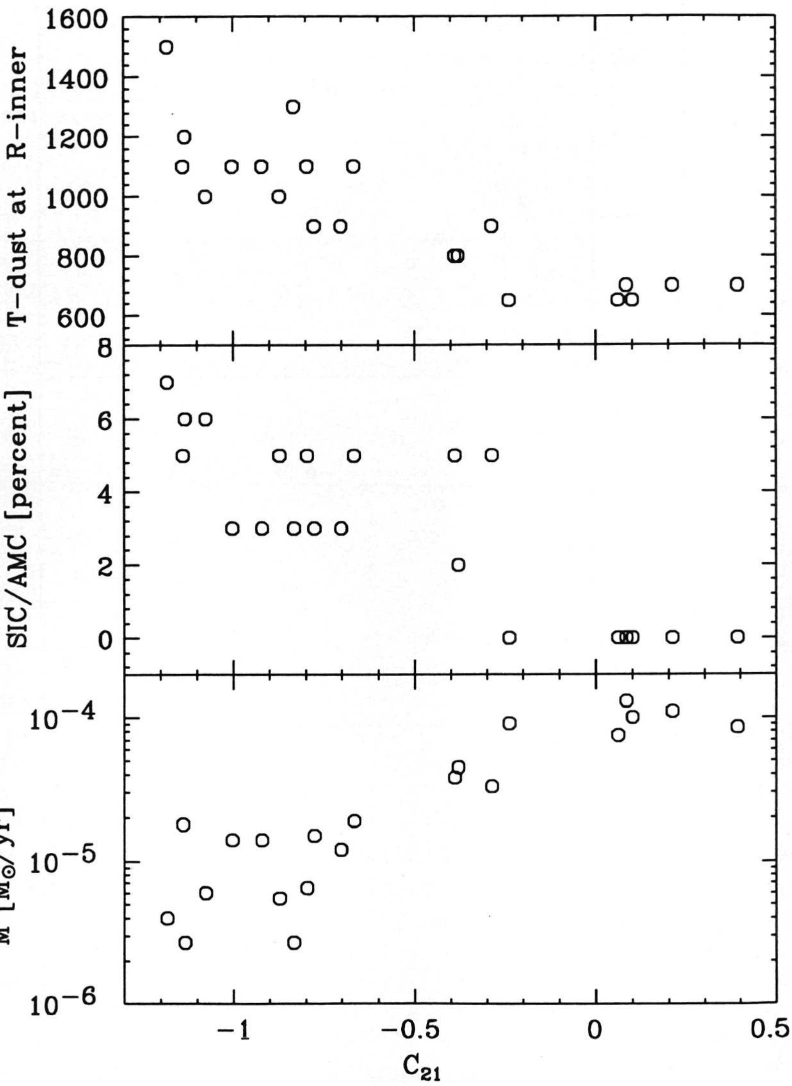

Figure 24: The dust temperature at the inner radius, the ratio of silicon carbide to amorphous carbon dust and the mass loss rate plotted versus $C_{21} = 2.5 \log(S_{25}/S_{12})$.

and growth process around long-period variables (LPVs). This has been studied theoretically by Fleischer et al. (1992) who show that the dust-to-gas ratio is a complicated function of radius, due to the periodic generation of shock waves. The derived inner dust radius should therefore be considered as the characteristic radius at which the dust formation has essentially been completed. While the mass loss rates differ by almost a factor of 50 in the sample, the density at the inner dust radius ($\rho_{\rm inner} \sim \dot{M}/v_{\infty}\ r^2_{\rm inner}$) varies by less than a factor of 4. This suggests that the density beyond a certain radius is too low for further dust formation. This radius effectively corresponds to the inner radius we derive. For larger mass loss rates (larger C_{21}) this critical density is reached at larger radii and hence at lower dust temperatures. This

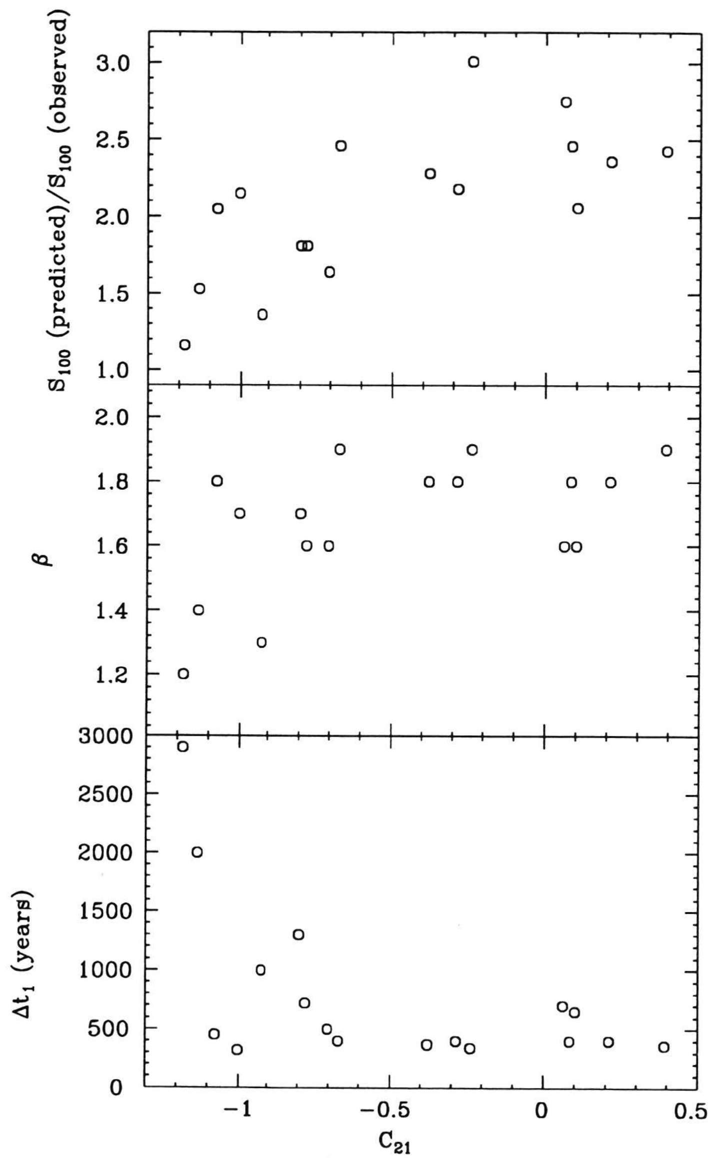

Figure 25: The ratio of the predicted and observed flux-densities at 100 μm as a function of C_{21} for the standard model with a constant mass loss rate and a wavelength dependence of the absorption coefficient ($Q_\lambda \sim \lambda^{-\beta}$ for $\lambda \gtrsim 30$ μm) of $\beta = 1$ (top panel). The observed IRAS 60 and 100 μm flux-densities can be fitted using either a larger value for β (middle panel) or a mass loss rate where the mass loss rate is lower by a factor of 30, Δt_1 years ago (bottom panel). Details are given in the text.

may explain the variation of T_c with C_{21} in the top panel of Fig. 24. One might envision the following dust formation scenario. Condensation probably starts near the normal condensation temperature (~1500K) fairly close to the star. The carbon (or SiC) dust grains that are formed are small and do not absorb (Tielens 1990) and therefore do not affect the observed SED. At

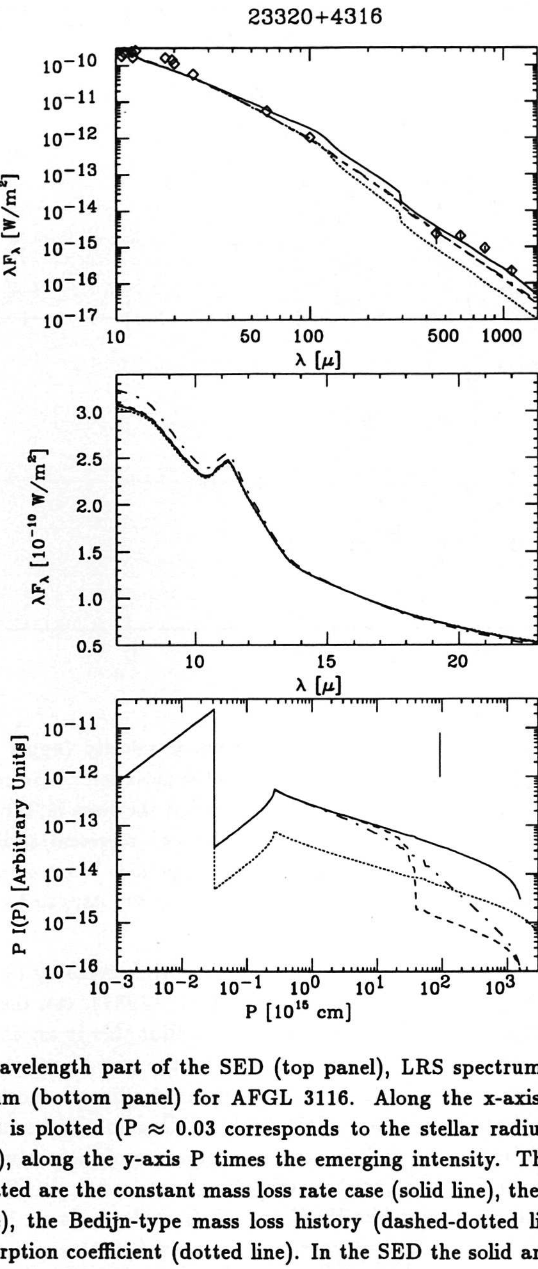

Figure 26: The long-wavelength part of the SED (top panel), LRS spectrum (middle panel) and the brightness curve at 1 mm (bottom panel) for AFGL 3116. Along the x-axis of the brightness curve the impact parameter P is plotted ($P \approx 0.03$ corresponds to the stellar radius, $P \approx 0.25$ corresponds to the inner dust radius), along the y-axis P times the emerging intensity. The flux is proportional to $\int_0^{P_{max}} I(P)P\,dP$. Indicated are the constant mass loss rate case (solid line), the thermal-pulse-type mass loss history (dashed line), the Bedijn-type mass loss history (dashed-dotted line) and a model with a steeper slope of the absorption coefficient (dotted line). In the SED the solid and the dashed-dotted line are indistinguishable. The parameters are given in the text and are chosen to fit the IRAS 60 and 100 μm flux-densities. The LRS spectra have been normalised at 16 μm. The line in the bottom panel at 9 10^{16} cm represents the beam size of the JCMT telescope at 1 mm.

larger radii the dust grains have become larger and now have typical absorption properties. The dust-to-gas ratio has increased. The process of dust growth continues until the density is too low for further dust formation.

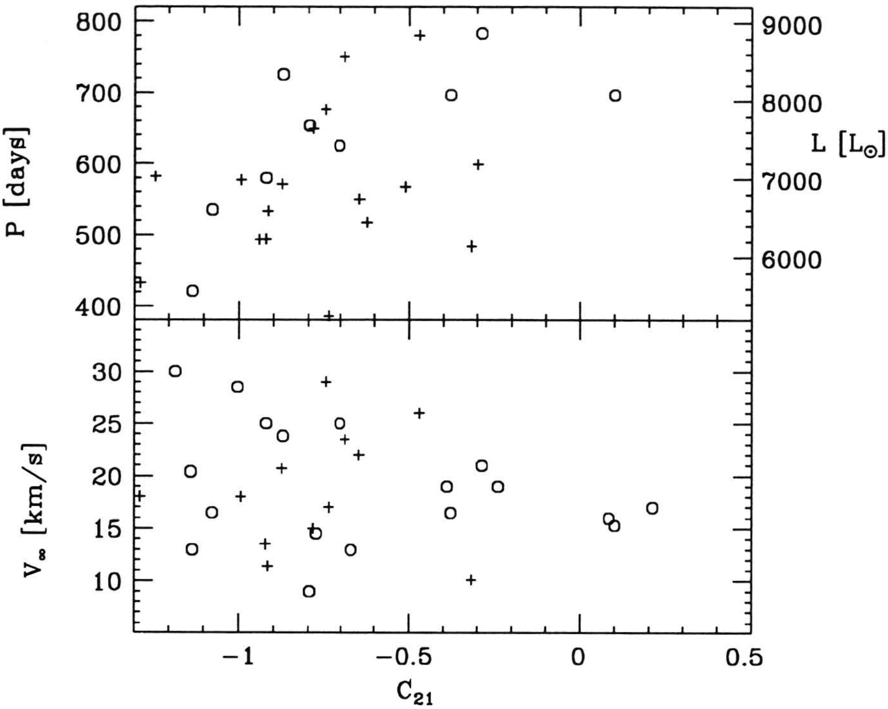

Figure 27: The pulsation period (top panel) and terminal velocity (upper panel) versus $C_{21} = 2.5 \log(S_{25}/S_{12})$ color. The right hand scale of the top panel is the pulsation period converted into a luminosity using the P-L-relation described in the text. The (o) represent the stars in Table 1 for which a pulsation period and well determined expansion velocity exist. The (+) represent additional carbon stars from Jones et al. (1990) and Le Bertre (1992) for which pulsation periods based on infrared light curves exist. The well-known carbon star IRC 10 216 has $C_{21} = -0.785$, P = 649 days and $v_\infty = 15.0$ km s^{-1}.

The decrease in strength of the silicon carbide feature with increasing optical depth (cf. Fig. 24 middle panel) had already been noticed by Baron et al. (1987), van der Bliek (1988), Chan & Kwok (1990), and in paper I. Here, it is demonstrated that this is an abundance effect and not an optical depth effect. Because silicon is depleted in the gas phase it has been inferred that practically all silicon is in grains (Sahai et al. 1984). Since silicon is not involved in any nuclear reactions, this suggests that the decrease of the SiC/AMC ratio is either a sequence of decreasing metallicity of the progenitor of the carbon star or a sequence of increasing C/O ratio. The latter possibility derives from the fact that, with nearly all oxygen tied up in CO, the number of carbon atoms to form dust (and molecules like HCN and C_nH_m) depends on (C/O–1). A sequence of decreasing metallicity is unlikely for two reasons. First, carbon stars are formed from stars $\gtrsim$1.5 $M_\odot$ (lifetime $\lesssim$3 Gyr). In such relatively young stars the metallicity is expected to be close to solar. Second, one might expect the dust-to-gas ratio to scale with the metallicity. If so, one would expect a decrease in the optical depth with decreasing metallicity (cf. Eq. 1). However, the sequence of decreasing SiC/AMC ratio is a sequence of increasing mass loss rate (i.e. optical depth). If the sequence of decreasing SiC/AMC ratio were indeed a sequence of increasing C/O ratio then one could argue that this would also be a sequence of increasing initial mass, since more massive stars are expected to experience more thermal pulses as carbon stars, resulting in

larger C/O ratios.
Danchi et al. (1990) found that in IRC 10 216 (with $C_{21} = -0.785$) dust forms at $\sim$3 R_* at temperatures 1200-1300 K. Figure 24 suggests that for $C_{21} = -0.785$, T_c lies in the range 900-1300 K. If $T_c = 1300$ K then $r_{inner} \approx 3.2$ R_* (cf. Table 2) in good agreement with observations. It would be interesting to perform interferometric observations for group V stars where inner radii of more than 10 stellar radii are predicted (if $T_{eff} = 2500$ K).
Inspecting Figs. 3-23 closely, reveals that the best-fitting models predict too much flux at 100 μm (and to a lesser extent also at 60 μm). The ratio of the predicted to the observed 100 μm flux-density is smallest (1.2) in 11318–7256 and largest (3.0) in 08074–3615. There may be a correlation with C_{21} (Fig. 25). There are two possible explanations. The wavelength dependence of the absorption coefficient ($Q_\lambda \sim \lambda^{-\beta}$) is steeper for $\lambda \gtrsim 30$ μm than adopted by me for the amorphous carbon dust species, and/or the mass loss rate has been lower in the past.
Two mass loss histories are considered. Bedijn (1987) proposed that the mass loss rate at the tip of the AGB varies like:

$$\dot{M}(t) = \frac{\dot{M}_0}{(1 - t/t_0)^\alpha} \qquad (t < t_0) \tag{3}$$

Suppose the mass loss rate has increased by a factor of f in the last Δt years and the present-day (time t_1) mass loss rate is $\dot{M}_1$. These parameters are related to $\dot{M}_0$ and t_0 as follows:

$$\begin{aligned} t_0 &= t_1 + \tfrac{\Delta t}{f^{1/\alpha} - 1} \\ \dot{M}_0 &= \dot{M}_1\, t_0^{-\alpha} \left(\tfrac{\Delta t}{f^{1/\alpha}-1}\right)^\alpha \end{aligned} \tag{4}$$

Values for α between 0.5 and 1 have been proposed in the literature (Baud & Habing 1983, Bedijn 1987, van der Veen 1989). In the following calculations $\alpha = 0.75$ is used, expecting that the results are qualitatively similar for $\alpha = 0.5$ or 1. The relevant time scales are the flow time scale through the envelope and $\dot{M}/\ddot{M}$. For the models in the previous section the time for a dust particle to travel from the inner to the outer radius is $\sim$3.5 10^4 yrs. The relevant time scale on which the mass loss rate must change to give appreciable changes in the SED is therefore shorter than this and in the present study adopted to be $\Delta t = 10^4$ yrs.
The observation that some AGB stars make loops in the IRAS color-color-diagram (Willems & de Jong 1988, Zijlstra et al. 1992) indicates that the mass loss rate depends on the phase in the thermal-pulse cycle (cf. Groenewegen & de Jong 1993b). The second mass loss history considered here is a sudden drop in the mass loss rate by a factor of f_1, Δt_1 years ago. Based on theoretical arguments a ratio of the mass loss rate in the quiescent H-burning phase to that in the luminosity dip is adopted of $f_1 = 30$.
For 17 stars in the sample, β ($Q_\lambda \sim \lambda^{-\beta}$ for $\lambda > 30$ μm), f (for the Bedijn-type mass loss history) and Δt_1 (for the thermal-pulse-type mass loss history) are determined by fitting the IRAS 60 and 100 μm flux-densities. For T_c the values in Table 2 are used. For some stars the present-day mass loss rate has been changed to give the same fit in the optical and NIR as for the constant mass loss rate case. The following range in values is found: $\beta = 1.2$-1.9, $f = 3$-30 and $\Delta t_1 =$ 340-2900 yrs.
Changing f_1 to 20 or ∞ introduces a 20% change in Δt_1. Not surprisingly, the highest values for β and f and the lowest values for Δt_1 are found for the stars where the constant mass loss rate case predicts the highest 100 μm flux-density compared to the observations (cf. Fig. 25).
The different models are illustrated in Fig. 26 for AFGL 3116, for which $\beta = 1.6$, $f = 11$ and $\Delta t_1 = 720$ yrs are derived. Since the absorption coefficient is changed only for $\lambda > 30$ μm there

is no change in the LRS spectrum. The fit at sub-mm wavelengths is noticeably worse than the two mass loss history models (see the brightness curve in the bottom panel of Fig. 26). This is found for all six stars where sub-mm data is available to make the comparison.

The difference between the two mass loss histories is that the Bedijn-type history also changes the emission close to the star. This is demonstrated in the brightness curve and in the LRS spectrum where the Bedijn-type mass loss history gives the steepest slope. For AFGL 3116, with $f = 11$, this effect is not so large but for the most extreme carbon stars (with $f \gtrsim 20$) the Bedijn-type mass loss history predicts LRS spectra which are steeper than observed. Another effect of the Bedijn-type mass loss history is that the present-day mass loss rate is higher than that for the thermal-pulse-type mass loss history and the constant mass loss rate case. For AFGL 3116 this is only a 3% effect, for the most extreme carbon stars this amounts to 20%.

A combination of a steeper slope in the absorption coefficient and a mass loss history is also possible. For $\beta = 1.3$, which would fit the 60 and 100 μm data of all moderate infrared carbon stars, I find $f = 5$ and $\Delta t_1 = 1600$ yrs, for AFGL 3116. In that case the Bedijn-type and the thermal-pulse-type mass loss history can equally well fit the observations.

With both the Bedijn mass loss history and the mass loss history related to thermal pulses the observed IRAS 60 and 100 μm flux-densities can be fitted. For all six stars where sub-mm data is available the observations in the sub-mm wavelength range lie above the model predictions (see Fig. 26 for AFGL 3116). There are several possibilities to explain this discrepancy: (1) there is a contribution of CO line emission to the sub-mm fluxes. For IRC 10 216 this contribution at 1.3 mm has been estimated to be 30% (Walmsley et al. 1991), (2) this is due to pulsational variability. This is unlikely, since the probability to observe six stars above the mean flux level is only $(\frac{1}{2})^6 = 1.6\%$, (3) it may point to a detached shell, due to a phase of high mass loss in a distant past. This would be incompatible with the Bedijn mass loss history in which mass loss on the AGB changes in a continuous way. In the case of the mass loss history related to thermal pulses it would point to three distinct phases of mass loss: a present-day phase of high mass loss, a phase of lower mass loss which ended Δt_1 years ago and a phase of high mass loss in a distant past, or (4) the sub-mm fluxes may sample a region where the circumstellar shell is slowed down by the interstellar medium, leading to a (relative) higher density and hence larger flux. The most powerful method to trace the density distribution of the dust is by mapping the circumstellar shell. This is illustrated in Fig. 26 where the Bedijn-type mass loss histoty and the mass loss history related to thermal pulses predict the same sub-mm fluxes (top panel) but have different brightness curves (bottom panel).

The value of Δt_1 represents the duration of the present-day high mass loss rate, associated with the phase of quiescent H-burning in the thermal pulse mass loss history. The fact that in Fig. 25 no stars are found with red C_{21} colors and S_{100}(predicted)/S_{100}(observed) $\lesssim 1.5$ implies that the derived values for Δt_1 are comparable to the *maximum* duration of the present phase of high mass loss. This implies interpulse periods of $\lesssim 10^3$ yrs and hence relative high core masses (i.e. initial masses). By default this implies on average lower core (and initial) masses for the bluer carbon stars with larger values for Δt_1. This then suggests that the reddest carbon stars have on average more massive progenitors than the blue infrared carbon stars.

The variation of β with C_{21} (cf. Fig. 25) could be interpreted, at first sight, as an increasing contribution of crystalline carbon (with $Q_\lambda \sim \lambda^{-2}$) relative to amorphous carbon (with $Q_\lambda \sim \lambda^{-1}$). Baron et al (1987) find evidence that the proportion of crystalline to amorphous carbon *increases* with increasing temperature of the dust continuum, in agreement with the theoretical expectation (Gail & Sedlmayer 1984). This would point to the mass loss history models rather than the steeper slope in the absorption coefficient as the correct model to explain the IRAS 60 and 100 μm flux-densities. The mass loss history models predict sub-mm fluxes in better agreement with

the observations than the model with the steeper absorption coefficient.
One point of discussion during the last few years has been whether the sequence of infrared carbon stars from low-to-high S_{25}/S_{12} ratio is a sequence in mass or in time (Habing 1990). In the discussion above both the decrease of the SiC/AMC ratio and the decrease in Δt_1 (c.q. the increase in f) with C_{21} can be taken as evidence for an increasing progenitor mass. In Fig. 27 the pulsation period and v_∞ are plotted versus C_{21}, quantities which may further assess this question. The pulsation period is a direct measure of the luminosity through the P-L relation. The relation used here is $M_{\rm bol} = 0.23 - 1.86 \log P$, based on the P-L-relation of Feast al. (1989) for carbon-rich Miras in the LMC and a distance modulus to the LMC of 18.50 (Panagia et al. 1991). There may be a systematic effect due to the metallicity difference between the Galaxy and the LMC, which is neglected here. There may be a weak correlation of P with C_{21} but the scatter is large. Some stars have a luminosity above the adopted mean of 7050 $L_\odot$.
A terminal velocity in excess of 17.5 km s^{-1} is generally viewed as indicative for a more massive star (e.g. Barnbaum et al. 1991). Figure 27 suggest that stars with $v_\infty \gtrsim 17.5$ km s^{-1} are confined to $C_{21} \lesssim -0.2$, while stars with lower terminal velocities are found over the whole range in color. The apparent anti-correlation between terminal velocity and infrared colors may be explained as follows. Habing et al. (1993) recently showed that for stellar winds driven by radiation pressure on dust grains, the expansion velocity as a function of $\dot{M}$ first increases, reaches a maximum and then decreases. Possibly the expansion velocities of the present sample represent the latter regime. An alternative scenario is the following. The terminal velocities are measured from CO(1-0) and CO(2-1) emission lines which are formed at several 10^{17} cm from the star. If the CO is associated with a *previous* phase of lower mass loss (= lower luminosity in the case of the thermal-pulsing mass loss history) then the CO outflow velocities are probably lower than the present-day outflow velocities. This phenomenon occurs e.g. in S Sct, an optical carbon star with a detached shell, where the present-day expansion velocity is $\sim$5 km s^{-1} while the shell expands with 16.5 km s^{-1} (Olofsson et al. 1992, Yamamura et al. 1993).

Acknowledgements. I thank A. Blanco for providing the extinction coefficients for several dust species and Teïje de Jong for valuable comments on the manuscript.

References

Alknis A., 1980, Investigations of the sun and red stars 11, 5
Barnbaum C., Kastner J.H., Zuckerman B., 1991, AJ 102, 289
Baron Y., de Muizon M., Papoular R., Pégourié B., 1987, A&A 186, 271
Baud B., Habing H.J., 1983, A&A 127, 73
Bedijn P.J., 1987, A&A 186, 136
Bergeat J., Sibille F., Lunel M., Jefevre J., 1976, A&A 52, 227
Blanco A., Fonti S., Rizzo F., 1991, Infrared Physics 31, 167
Borghesi A., Bussoletti E., Colangeli L., De Blasi C., 1985, A&A 153, 1
Cardelli J.A., Clayton G.C., Mathis J.S., 1989, ApJ 345, 245
Chan S.J., Kwok S., 1990, A&A 237, 354
Cohen M., Kuhi L.V., 1977, PASP 89, 829
Cohen M., Walker R.G., Witteborn F.C., 1992, AJ 104, 2030
Danchi W.C., Bester M., Degiaconi C.G., McCullough P.R., Townes C.H., 1990, ApJ 359, L59
Dyck H.M., Lockwood G.W., Capps R.W., 1974, ApJ 189, 89
Egan M.P., Leung C.M., 1991, ApJ 383, 314
Epchtein N., et al., 1987, A&AS 71, 39

Epchtein N., Le Bertre T., Lépine J.R.D., 1990, A&A 227, 82
Feast M.W., Glass I.S., Whitelock P.A., Catchpole R.M., 1989, MNRAS 241, 375
Fleischer A.J., Gauger A., Sedlmayr E., 1992, A&A 266, 321
Forrest W.J., Houck J.R., McCarthy J.F., 1981, ApJ 248, 195
Fouqué P., Le Bertre T., Epchtein N., Guglielmo F., Kerschbaum F., 1992, A&AS 93, 151
Frogel J.A., Cohen J.G., Persson S.E., Elias J.H., 1981, in: Physical Processes in Red Giants Stars, eds. I. Iben, A. Renzini, Reidel, Dordrecht, p. 159
Gail H.-P., Sedlmayer E., 1984, A&A 132, 163
Goebel J.H., Moseley S.H., 1985, ApJ 290, L35
Grasdalen G.L., Gehrz R.D., Hackwell J.A., Castelaz M., Gullixson C., 1983, ApJS 53, 413
Griffin I.P., 1990, MNRAS 247, 591
Griffin I.P., 1993, MNRAS 260, 831
Groenewegen M.A.T., 1993, Chapter 5, Ph.D. thesis, University of Amsterdam
Groenewegen M.A.T., de Jong T., 1991, ESO Messenger 66, 40
Groenewegen M.A.T., de Jong T., 1993a, A&AS, in press
Groenewegen M.A.T., de Jong T., 1993b, A&A, in press (Chapter 6)
Groenewegen M.A.T., de Jong T., Baas F., 1993a, A&AS, in press
Groenewegen M.A.T., de Jong T., Geballe T.R., 1993b, A&A, submitted
Groenewegen M.A.T., de Jong T., van der Bliek N.S., Slijkhuis S., Willems F.J., 1992, A&A 253, 150 (paper I)
Guglielmo F., et al., 1993, A&AS 99, 31
Habing H.J., 1990, in: From miras to planetary nebulae, eds. M.O. Mennessier, A. Omont, Editions Frontieres, Gif-sur-Yvette, p. 16
Habing H.J., Tignon J., Tielens A.G.G.M., 1993, in preparation
Joint IRAS Science Working Group, 1986, IRAS catalogs and atlases, Low Resolution Spectrograph (LRS), A&AS 65, 607
Joint IRAS Science Working Group, 1986, IRAS catalogs and atlases, Point Source Catalog (PSC), US Government Printing Office, Washington
Joint IRAS Science Working Group, 1986, IRAS catalogs and atlases, Explanatory Supplement, US Government Printing Office, Washington
Jones T.J., et al., 1990, ApJS 74, 785
Jura M., 1986, ApJ 303, 327
Justtanont K., Tielens, A.G.G.M., 1992, ApJ 389, 400
Kholopov P.N., et al., 1985, General Catalog of Variable Stars (GCVS), Nauka, Moscow
Le Bertre T., 1987, A&A 176, 107
Le Bertre T., 1988, A&A 203, 85
Le Bertre T., 1992, A&AS 94, 377
Lebofsky M.J., Rieke G.H., 1977, AJ 82, 646
Lockwood G.W., 1974, ApJ 192, 113
Loup C., Forveille T., Omont A., Paul J.F., 1993, A&AS 99, 231
Low F.J., Kurtz R.F., Vrba F.J., Rieke G.H., 1976, ApJ 206, L153
Martin P.G., Rogers C., 1987, ApJ 322, 374
Meadows P.J., Good A.R., Wolstencroft R.D., 1987, MNRAS 225, 43P
Mitchell R.M., Robinson G., 1980, MNRAS 190, 669
Neckel Th., Klare G., 1980, A&AS 42, 251
Noguchi K., et al., 1981, PASJ 33, 373
Olofsson H., Carlstrom U., Eriksson K., Gustafsson B., 1992, A&A 253, L17
Onaka T., de Jong T., Willems F.J., 1989, A&A 218, 169

Orofino V., Colangeli L., Bussoletti E., Blanco A., Fonti S., 1990, A&A 231, 105
Panagia N., Gilmozzi R., Macchetto F., Adorf H.-M., Kirshner R.P., 1991, ApJ 380, L23
Papoular R., 1988, A&A 204, 138
Parenago P.P., 1940, Astron. Zh. 17, 3
Pégourié B., 1988, A&A 194, 335
Rouleau F., Martin P.G., 1991, ApJ 377, 526
Rowan-Robinson M., Harris S., 1983a, MNRAS 202, 767
Rowan-Robinson M., Harris S., 1983b, MNRAS 202, 797
Rowan-Robinson M., Lock T.D., Walker D.W., Harris S., 1986, MNRAS 222, 273
Sahai R., Wootten A., Clegg R.E.S., 1984, ApJ 284, 144
Schutte W.A., Tielens A.G.G.M., 1989, ApJ 343, 369
Sopka R.J., et al., 1985, ApJ 294, 242
Tielens A.G.G.M., 1990, in: From miras to planetary nebulae, eds. M.O. Mennessier, A. Omont, Editions Frontieres, Gif-sur-Yvette, p. 186
van der Bliek N.S., 1988, M.Sc. thesis, University of Amsterdam
van der Veen W.E.C.J., 1989, A&A 210, 127
Walmsley C.M., et al., 1991, A&A 248, 555
Willems F.J., de Jong T., 1988, A&A 196, 173
Yamamura I., Onaka T., Kamijo F., Izumiura H., Deguchi S., 1993, PASJ, in press
Zijlstra A.A., Loup C., Waters L.B.F.M., de Jong T., 1992, A&A 265, L5

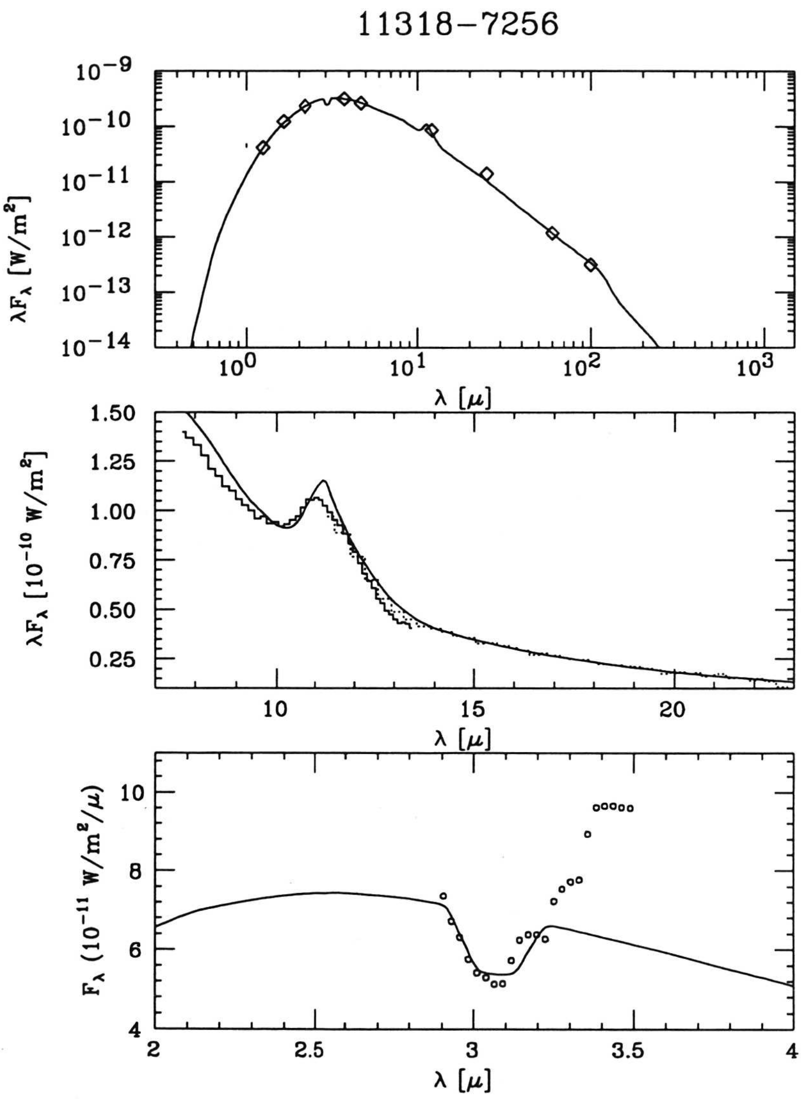

Figure 3: The fit to the SED, LRS spectrum and 2-4 μm region of IRAS 11318−7256. For the corresponding parameters see Table 2. The model is represented by the solid line, the observations by the symbols and the ragged lines. The sub-mm and the most uncertain optical and near-IR data points have errorbars. Observations at minimum and maximum light are connected. Upperlimits are indicated by a $\vee$. The line near 1 μm represents the reddening vector at the shortest observed wavelength point (see Table 1). The predicted LRS spectrum and 2-4 μm spectrum are scaled to the observations. The scaling factor f (in the sense that the plotted model flux equals the calculated model flux multiplied by f) is 1.075 for the LRS spectrum and 0.675 for the 2-4 μm spectrum.

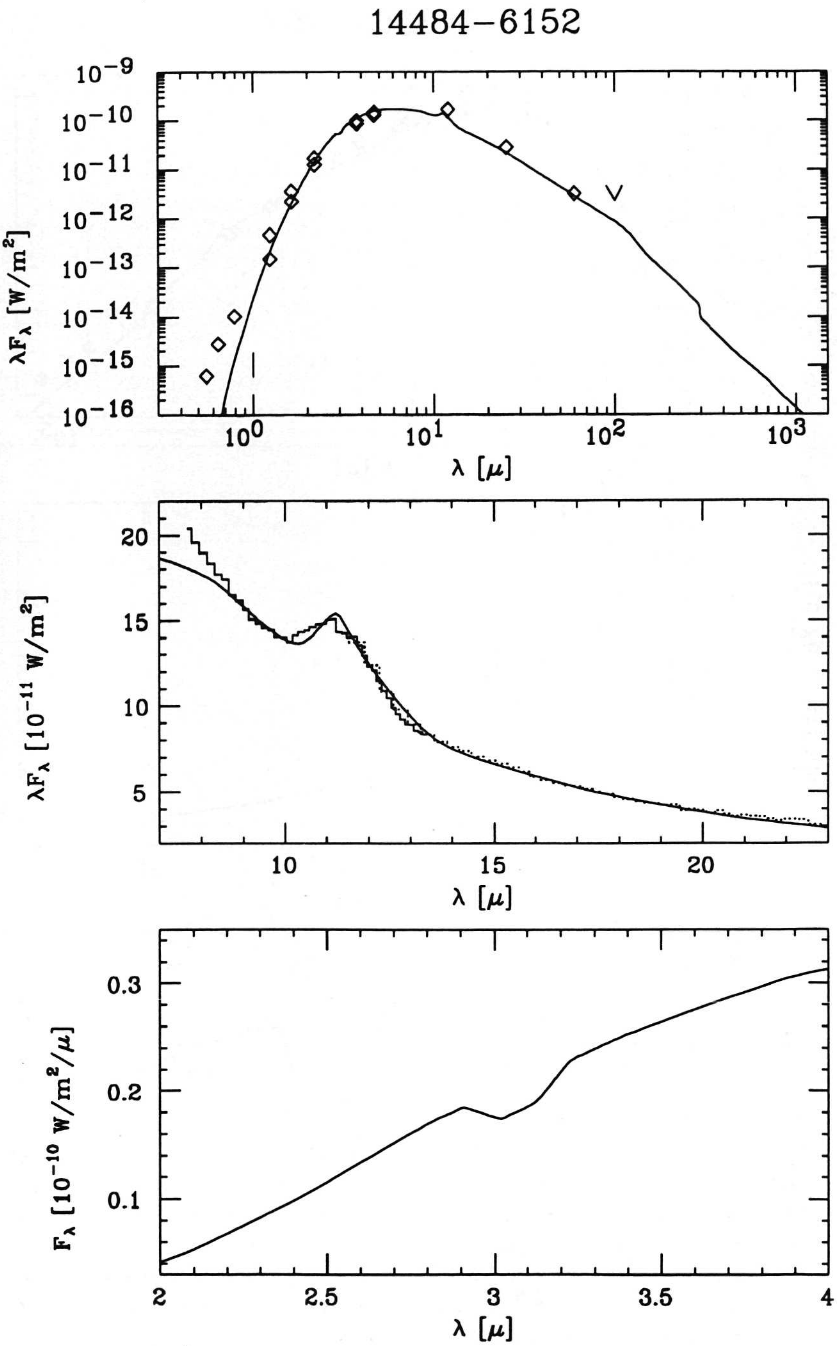

Figure 4: As Fig. 3 for IRAS 14484−6152. The scaling factor for the LRS spectrum is 1.104.

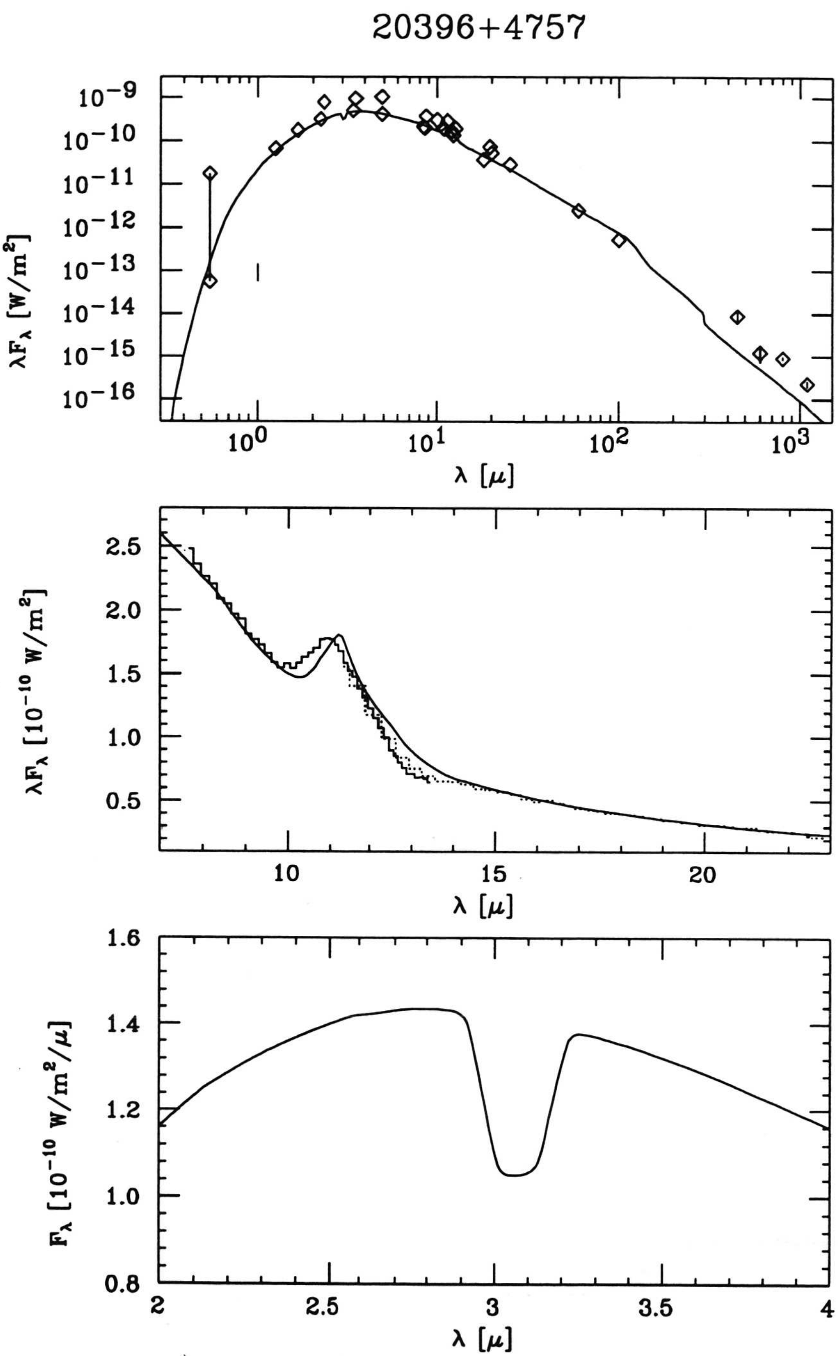

Figure 5: As Fig. 3 for IRAS 20396+4757. The scaling factor for the LRS spectrum is 0.888.

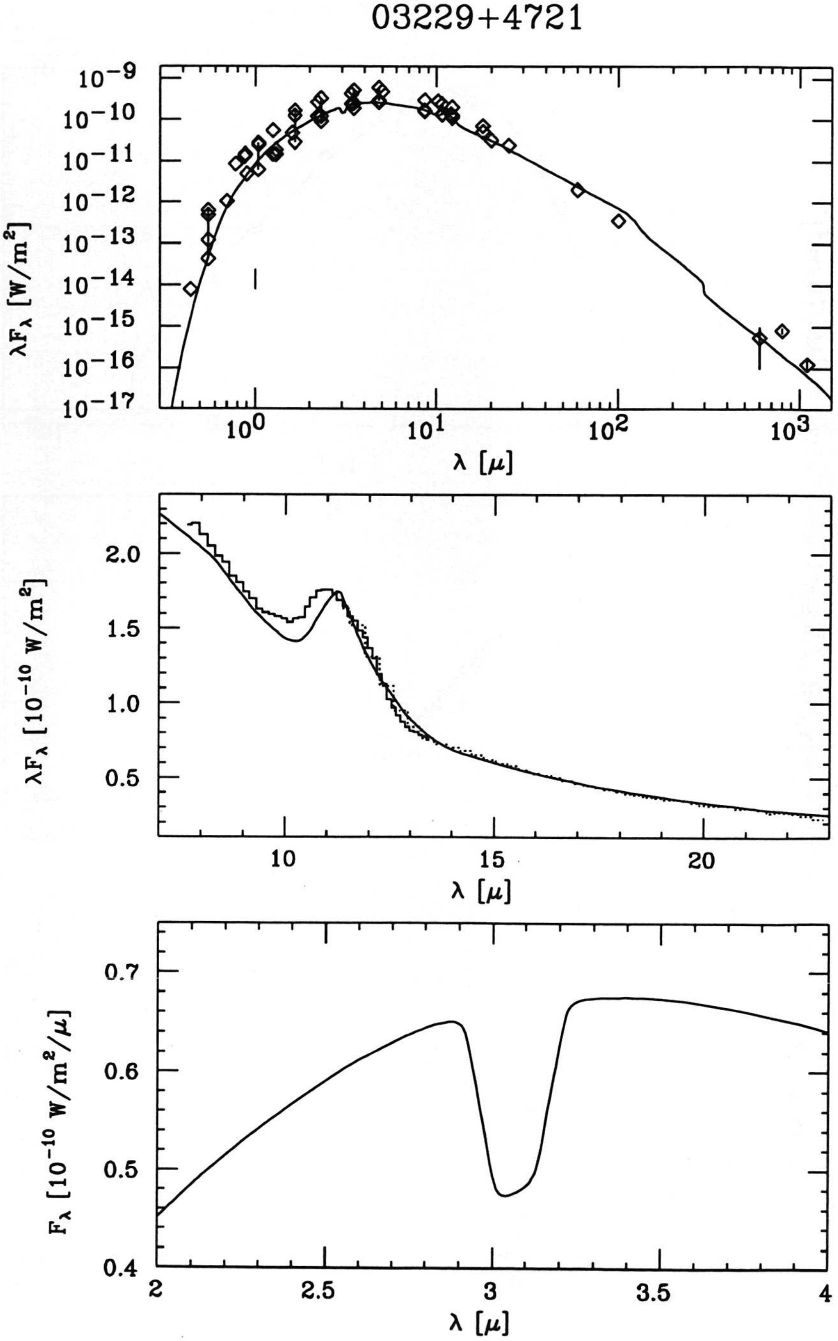

Figure 6: As Fig. 3 for IRAS 03229+4721. The scaling factor for the LRS spectrum is 1.097.

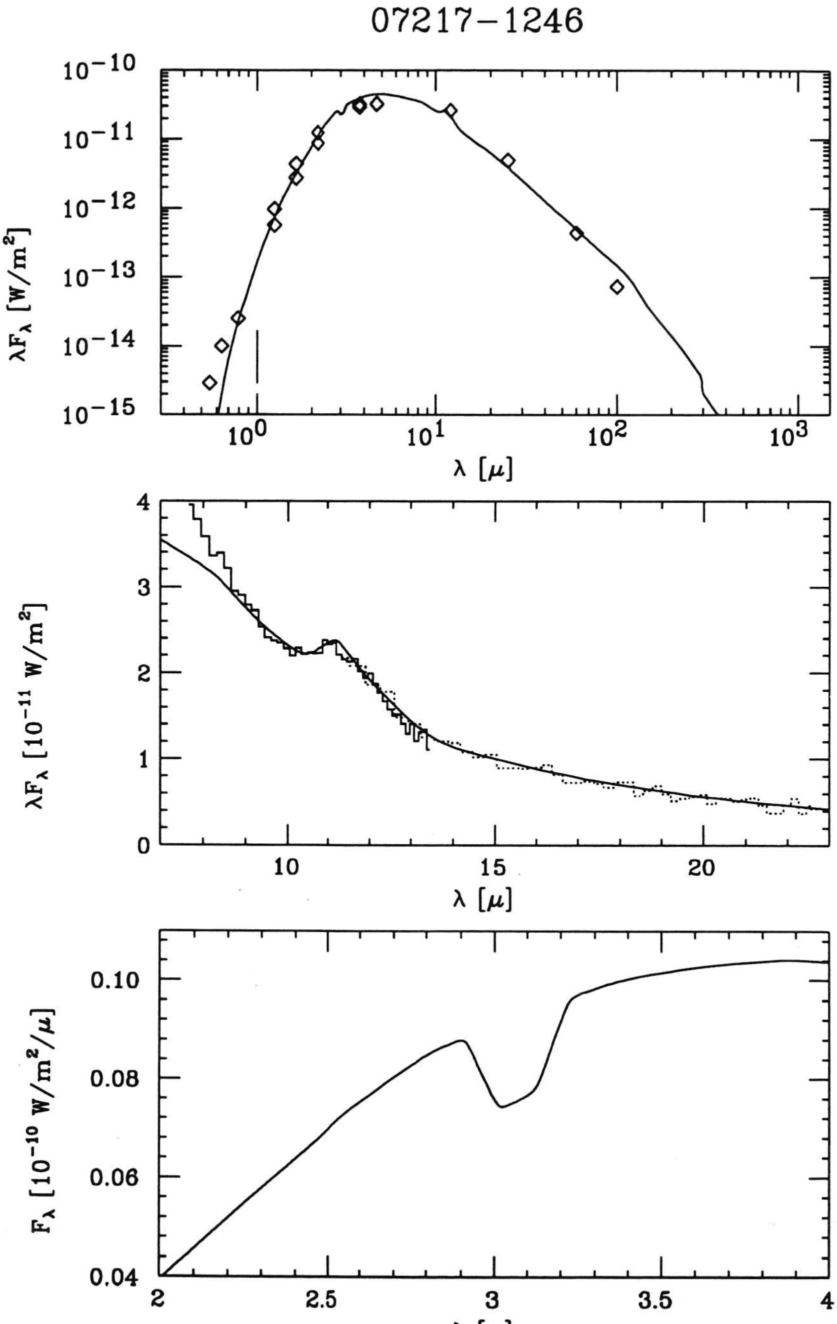

Figure 7: As Fig. 3 for IRAS 07217−1246. The scaling factor for the LRS spectrum is 0.906.

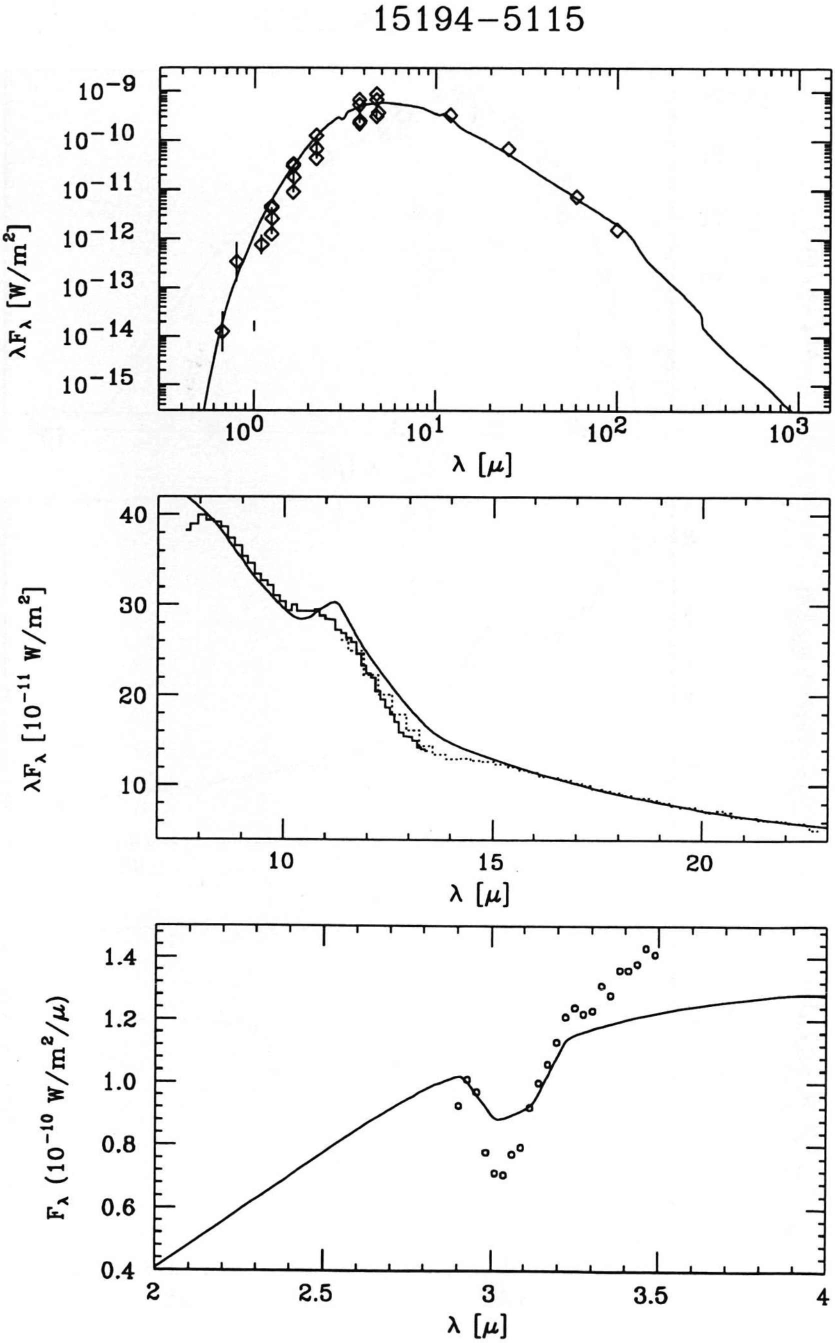

Figure 8: As Fig. 3 for IRAS 15194−5115. The scaling factor for the LRS spectrum is 0.86.

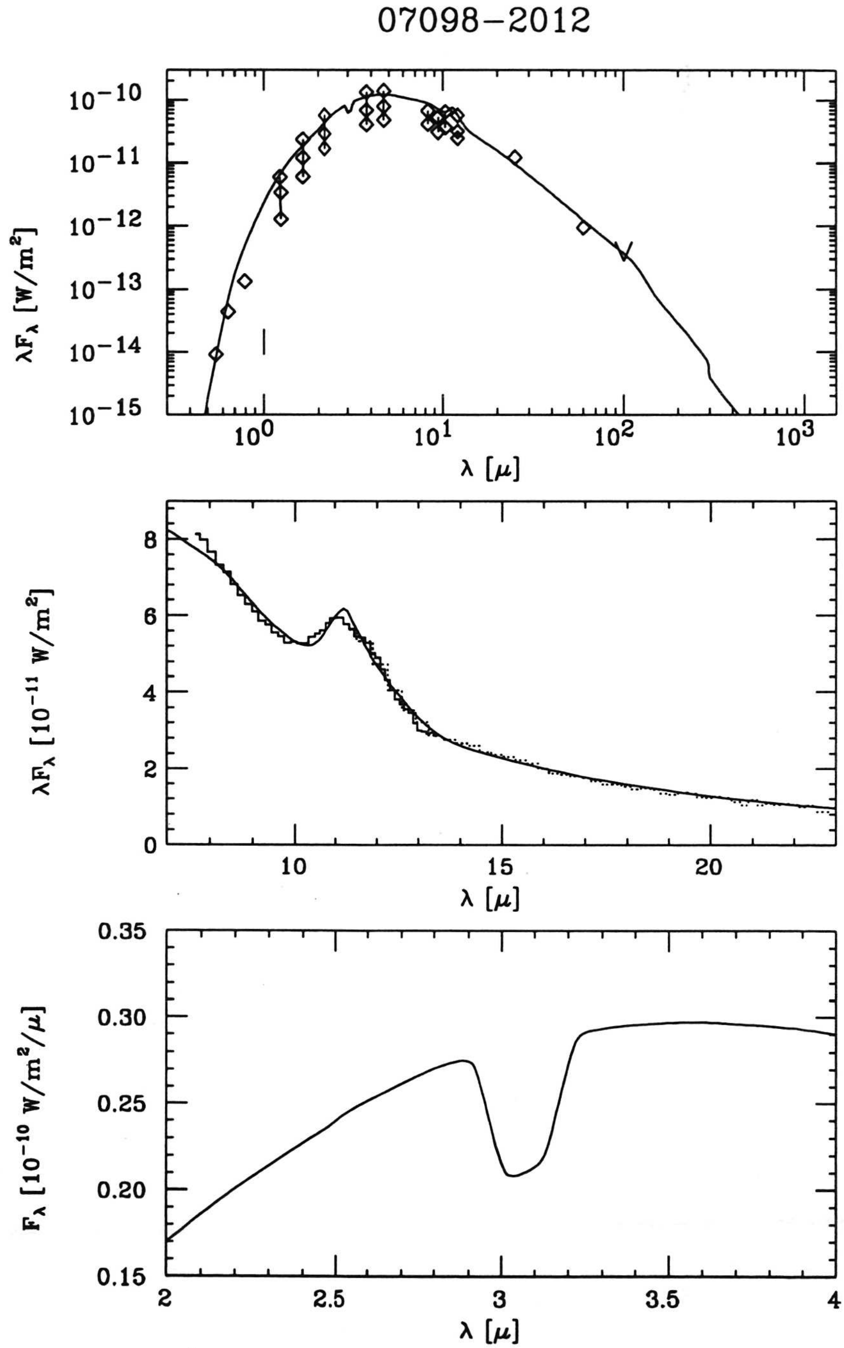

Figure 9: As Fig. 3 for IRAS 07098–2012. The scaling factor for the LRS spectrum is 0.821.

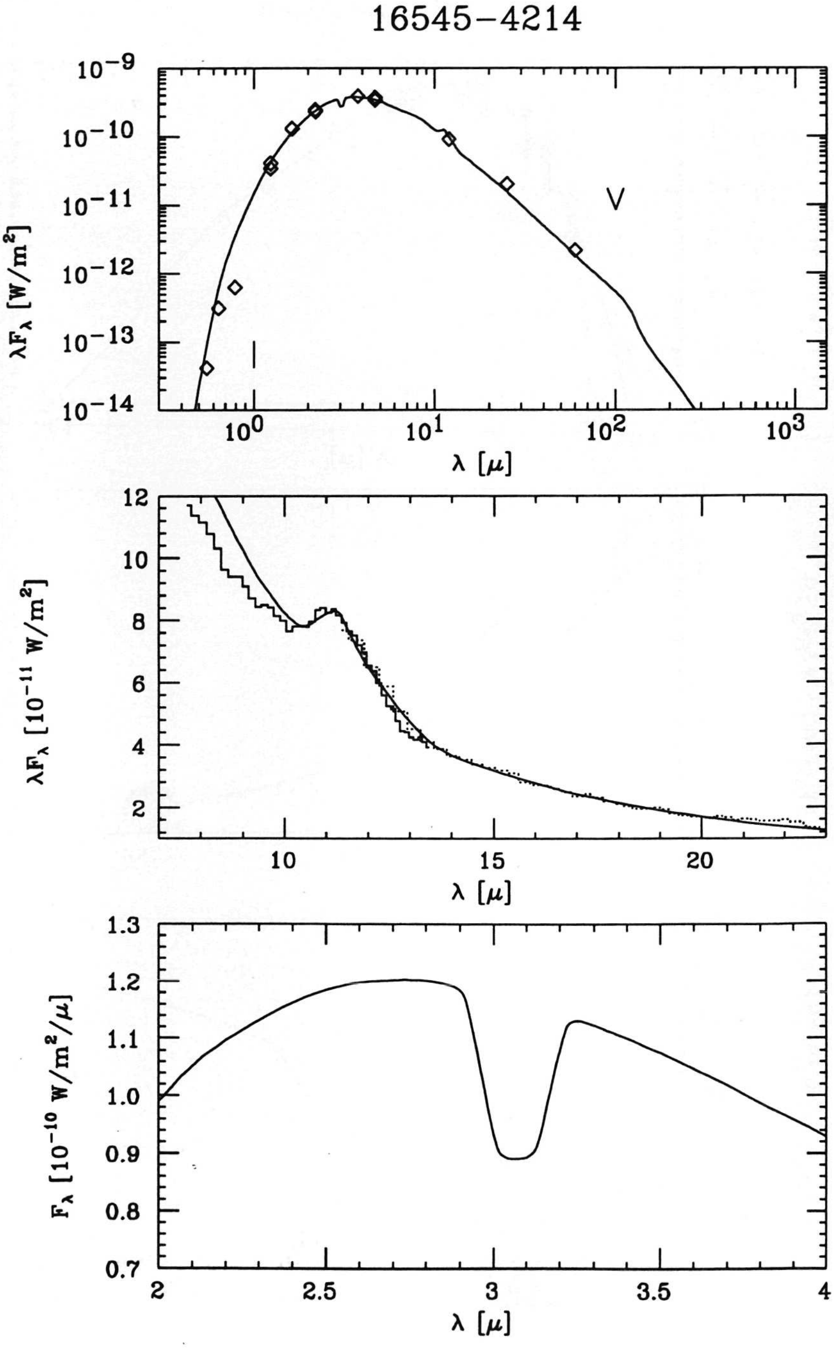

Figure 10: As Fig. 3 for IRAS 16545−4214. The scaling factor for the LRS spectrum is 0.665.

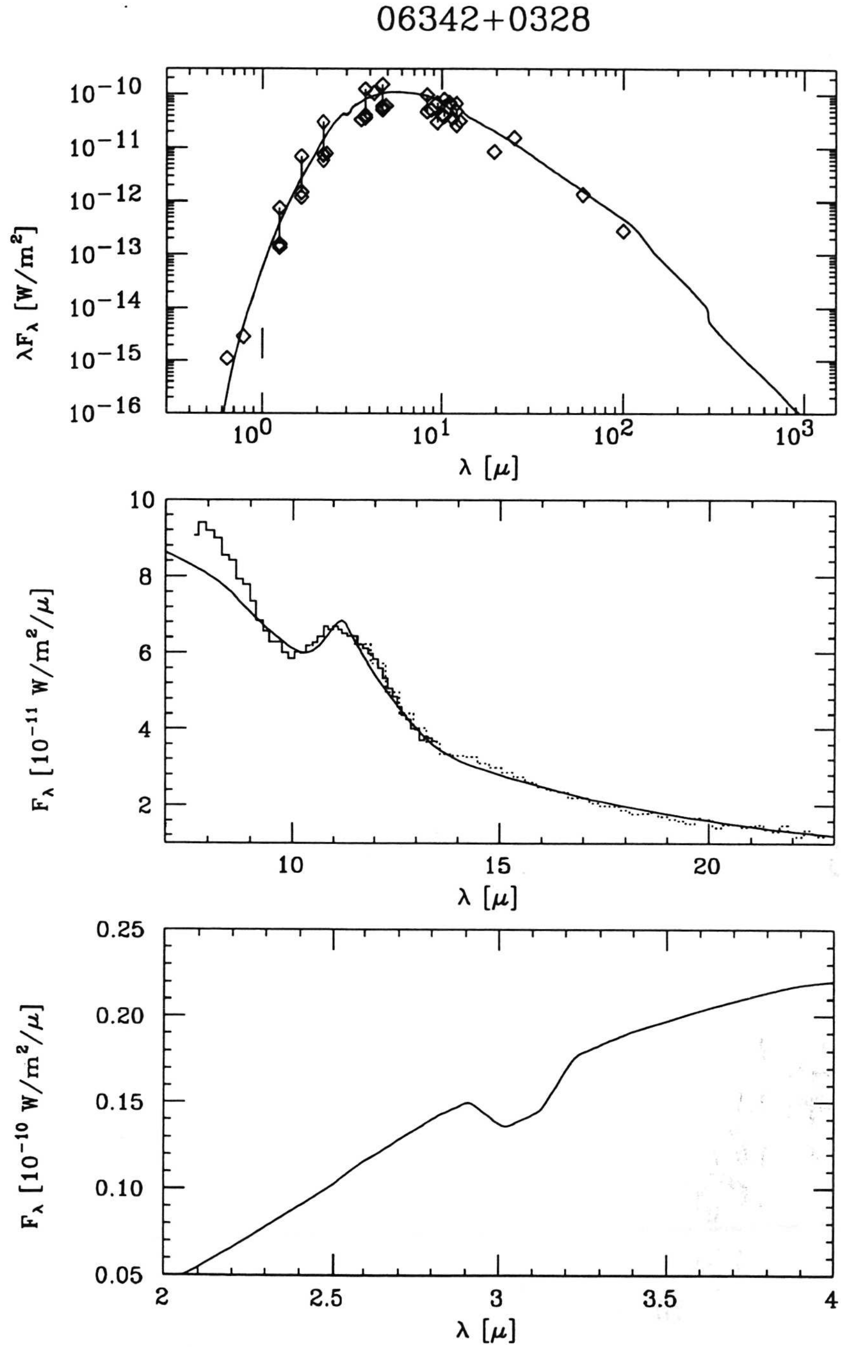

Figure 11: As Fig. 3 for IRAS 06342−0328. The scaling factor for the LRS spectrum is 0.837.

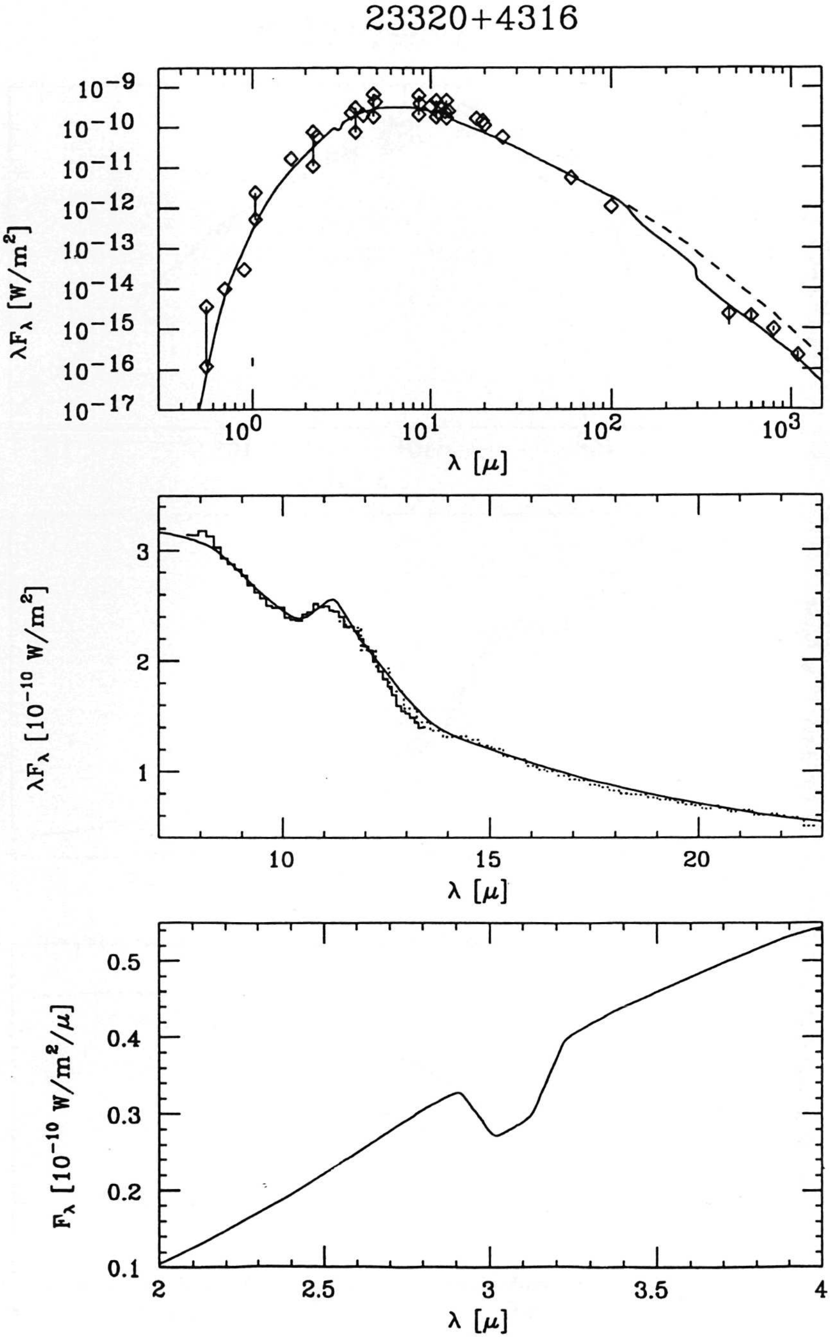

Figure 12: As Fig. 3 for IRAS 23320+4316. The scaling factor for the LRS spectrum is 1.00. The dashed line is the same model without beam effects.

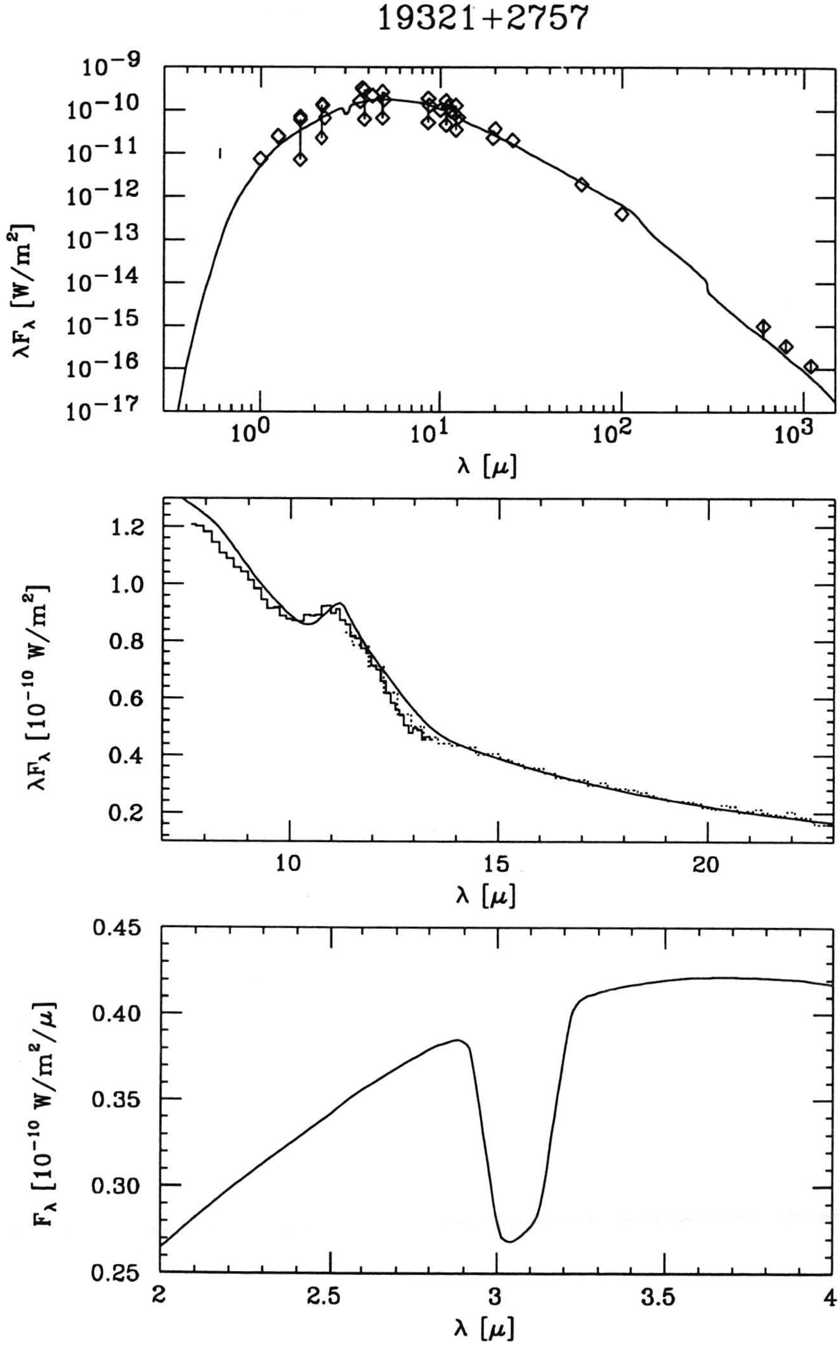

Figure 13: As Fig. 3 for IRAS 19321+2757. The scaling factor for the LRS spectrum is 0.85.

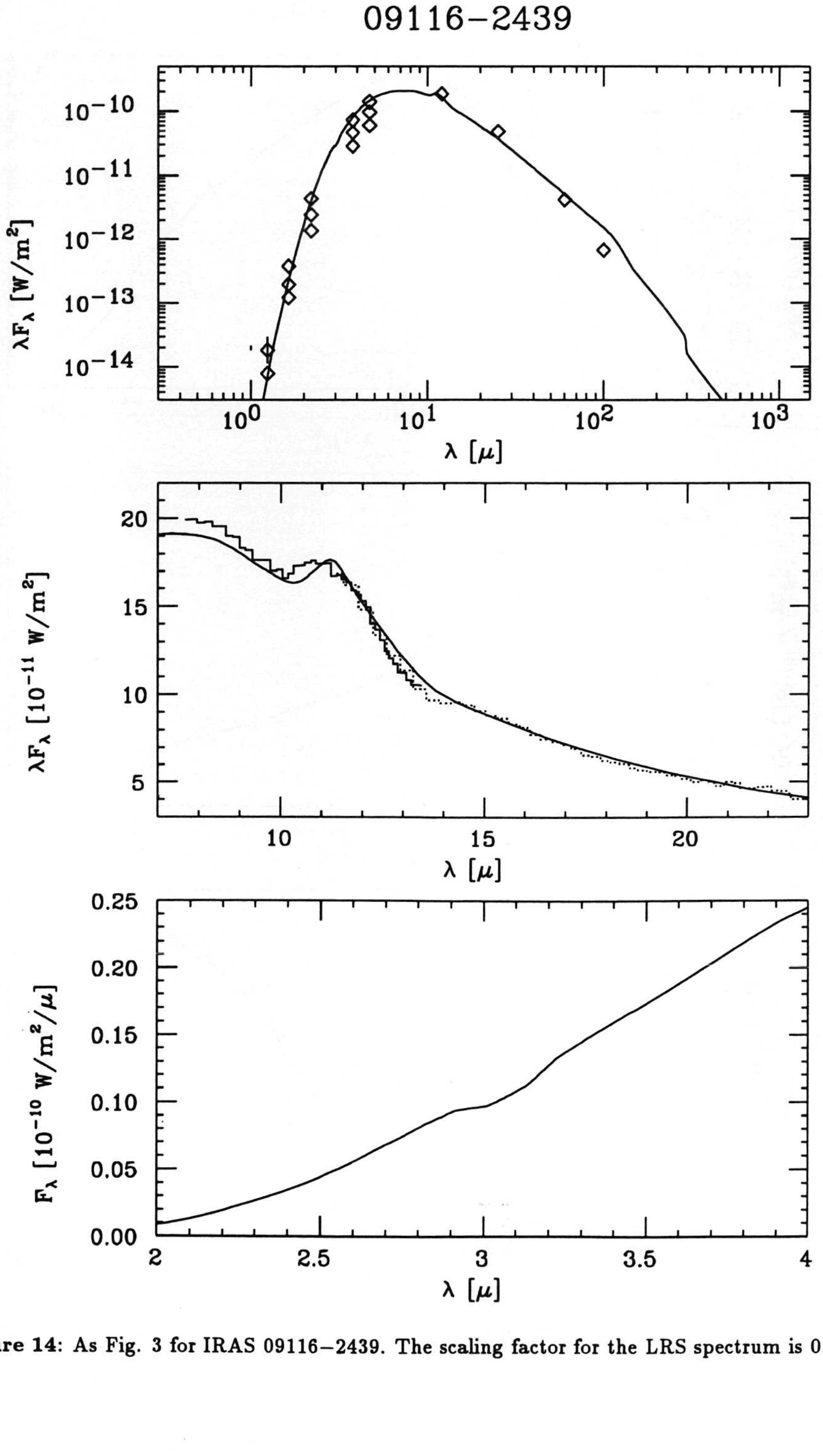

Figure 14: As Fig. 3 for IRAS 09116−2439. The scaling factor for the LRS spectrum is 0.928.

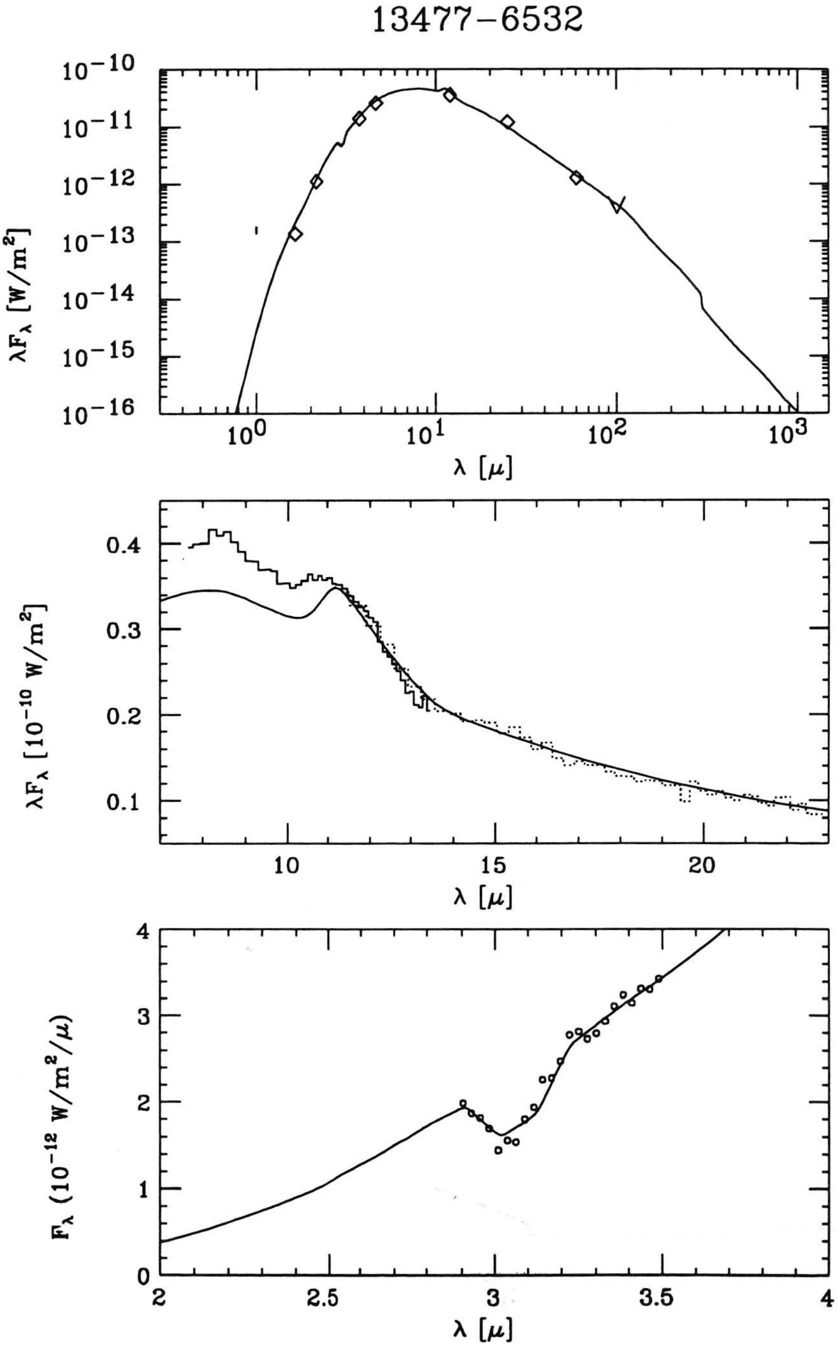

Figure 15: As Fig. 3 for IRAS 13477−6532. The scaling factor for the LRS spectrum is 1.097, for the 2-4 μm spectrum 0.758.

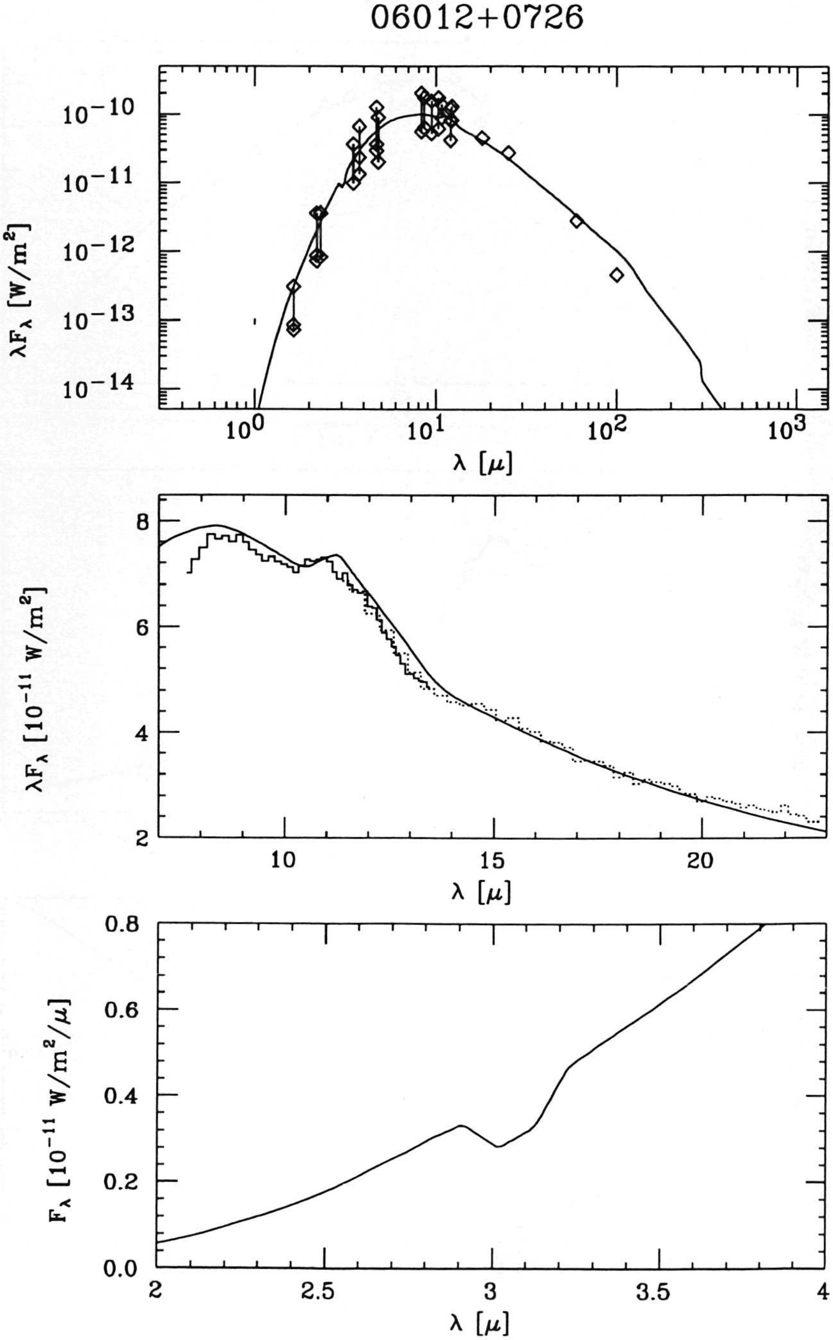

Figure 16: As Fig. 3 for IRAS 06012+0328. The scaling factor for the LRS spectrum is 0.800.

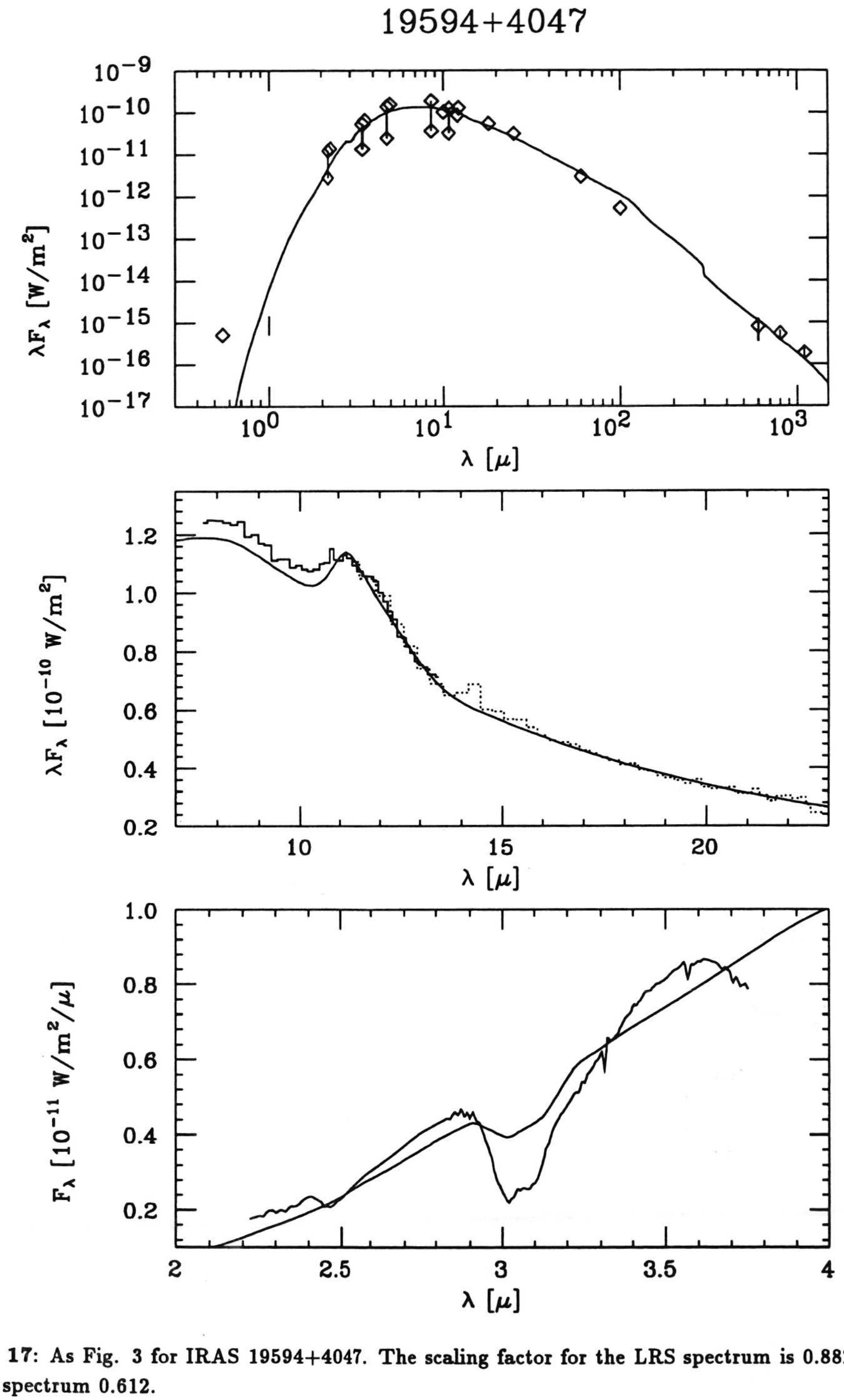

Figure 17: As Fig. 3 for IRAS 19594+4047. The scaling factor for the LRS spectrum is 0.882, for the 2-4 μm spectrum 0.612.

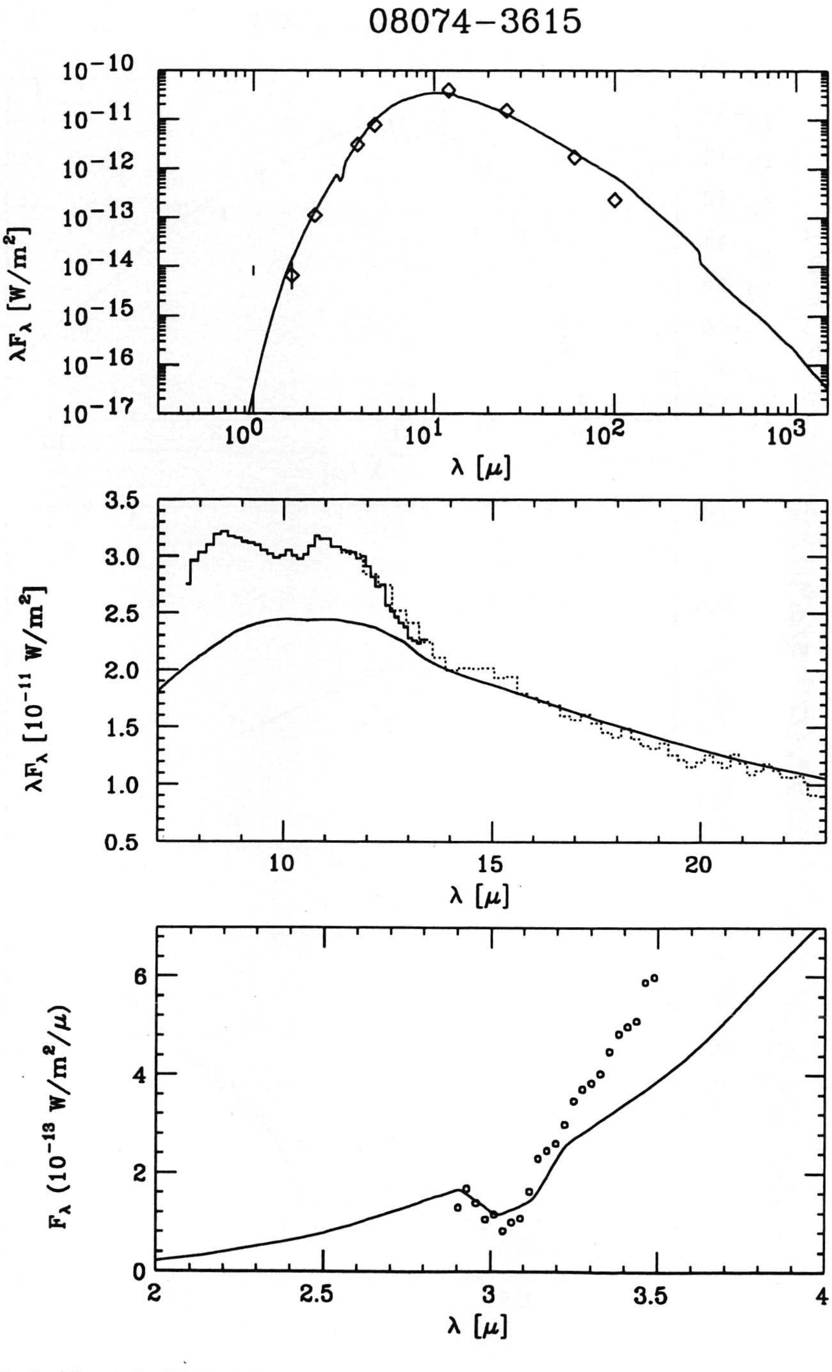

Figure 18: **As Fig. 3 for IRAS 08074−3615. The scaling factor for the LRS spectrum is 0.707, for the 2-4 μm spectrum 0.640.**

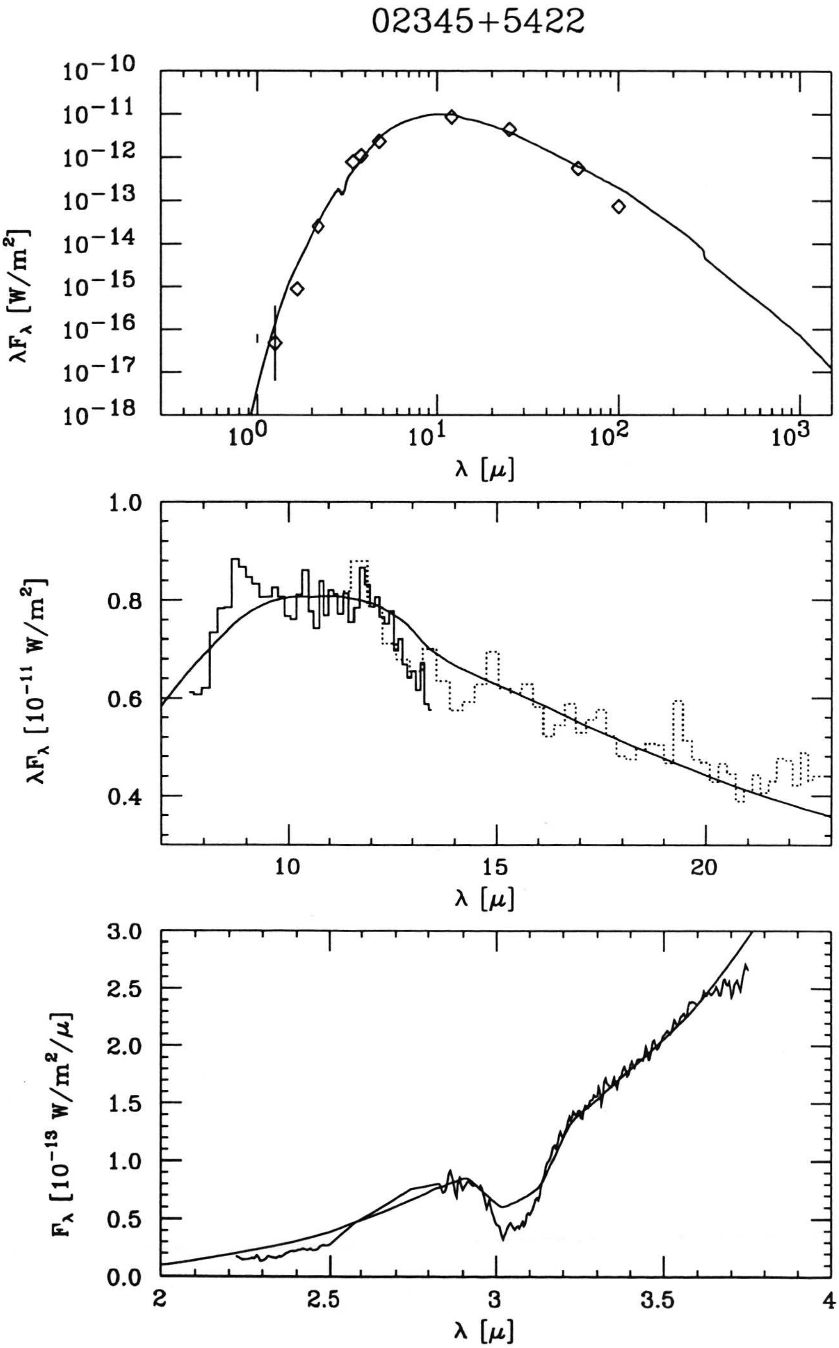

Figure 19: As Fig. 3 for IRAS 02345+5422. The scaling factor for the LRS spectrum is 0.833, for the 2-4 μm spectrum 1.357.

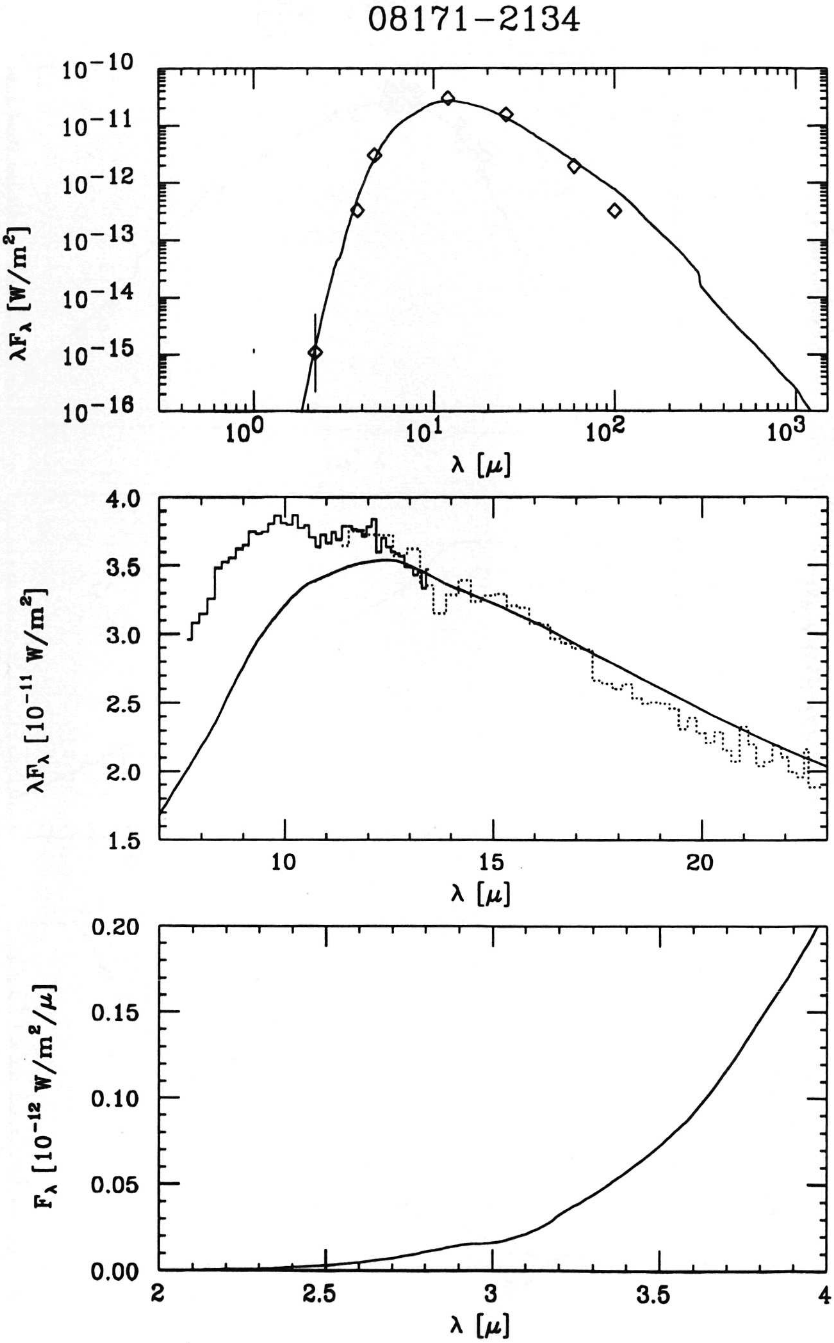

Figure 20: As Fig. 3 for IRAS 08171−2134. The scaling factor for the LRS spectrum is 1.314.

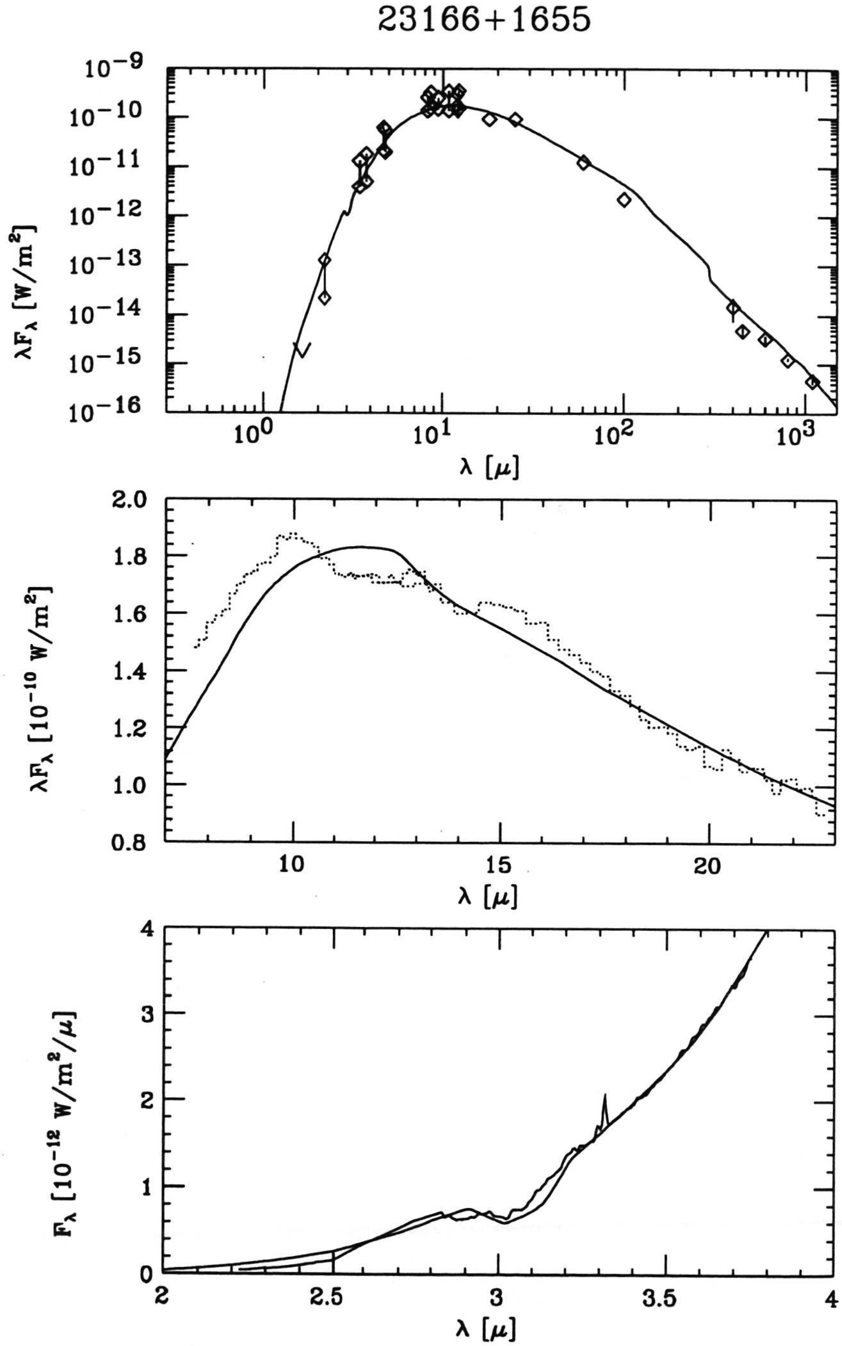

Figure 21: As Fig. 3 for IRAS 23166+1655. The scaling factor for the 2-4 μm spectrum is 1.79.

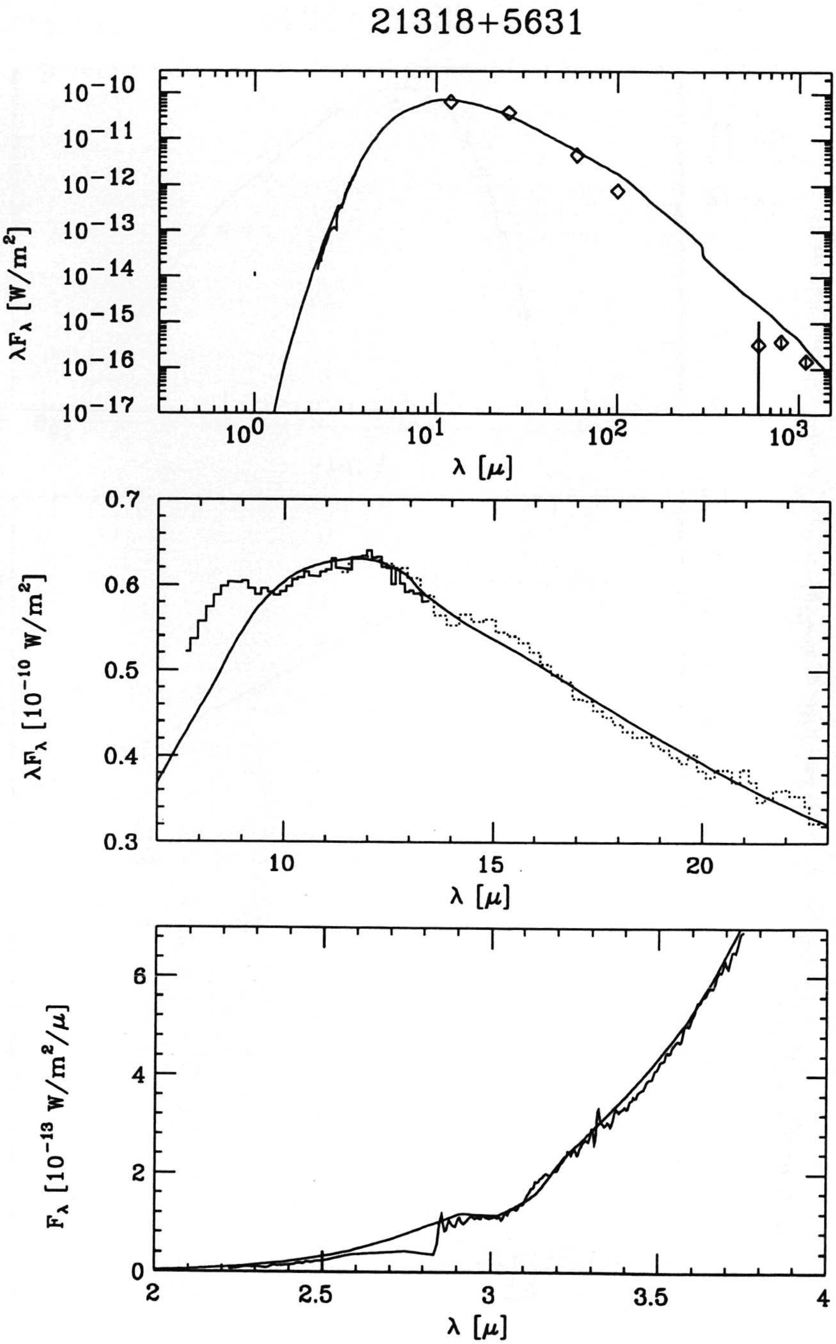

Figure 22: As Fig. 3 for IRAS 21318+5631. The scaling factor for the LRS spectrum is 0.86.

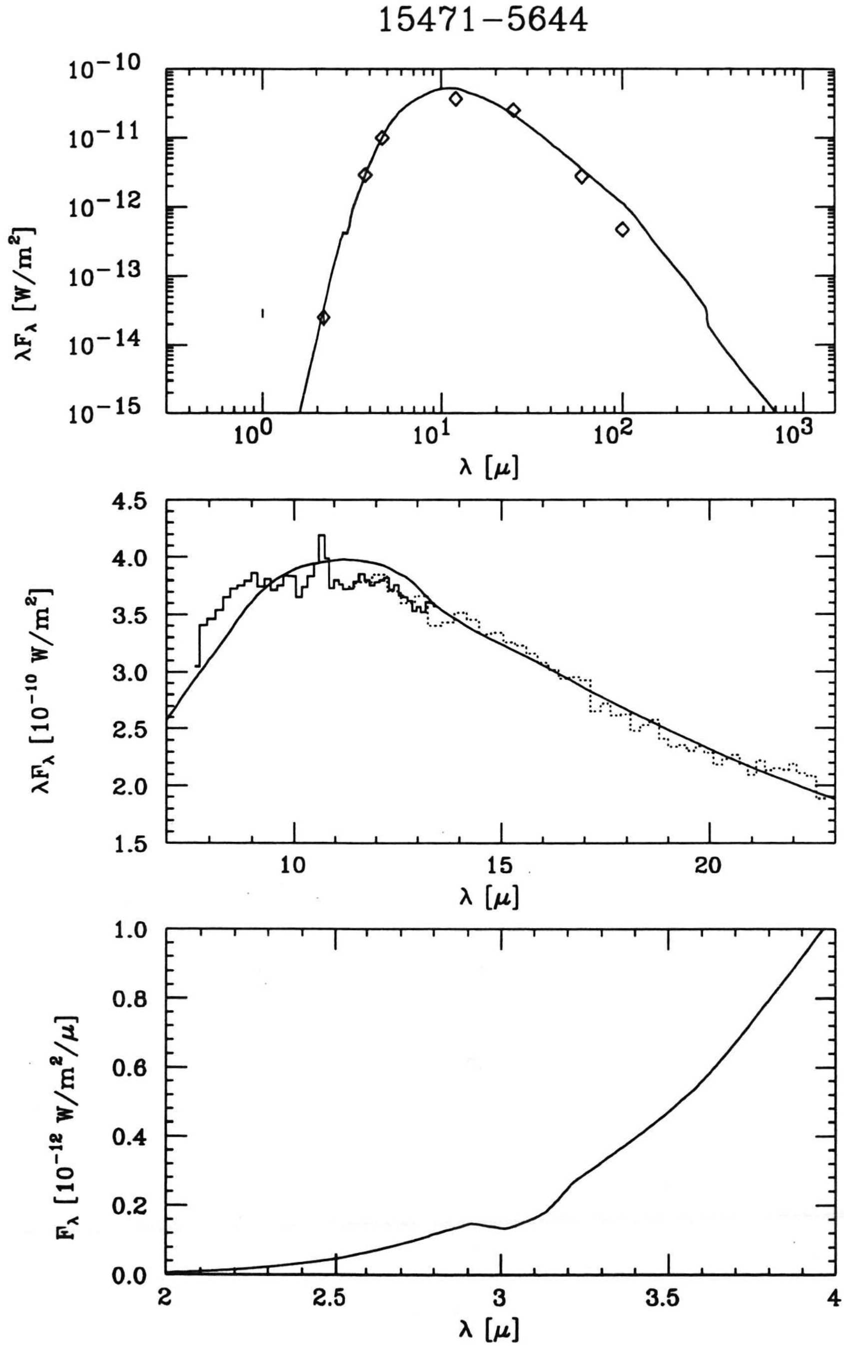

Figure 23: As Fig. 3 for IRAS 15471−5644. The scaling factor for the LRS spectrum is 0.759.

Chapter 8

Synthetic AGB evolution: I. A new model

Abstract

We have constructed a model to calculate in a synthetic way the evolution of stars on the asymptotic giant branch (AGB). The evolution is started at the first thermal pulse (TP) and is terminated when the envelope mass has been lost due to mass loss or when the core mass reaches the Chandrasekhar mass.
Our model is more realistic than previous synthetic evolution models in that more physics has been included. The variation of the luminosity during the interpulse period is taken into account as well as the fact that, initially, the first few pulses are not yet at full amplitude and that the luminosity is lower than given by the standard core mass-luminosity relations. Most of the relations used are metallicity dependent to be able to make a realistic comparison with stars of different metallicity. The effects of first, second and third dredge-up are taken into account. The effect of Hot Bottom Burning (HBB) is included in an approximate way. Mass loss on the AGB is included through a Reimers Law. We also include mass loss prior to the AGB.
The free parameters in our calculations are the minimum core mass for dredge-up (M_c^{min}), the third dredge-up efficiency (λ) and three mass loss scaling parameters ($\eta_{RGB}, \eta_{EAGB}, \eta_{AGB}$).
The model has been applied to the LMC using a recent determination of the age-metallicity and Star Formation Rate for the LMC. The observed carbon star luminosity function and the observed ratio of oxygen-rich to carbon-rich AGB stars in the LMC act as constraints to the model.
Several models are calculated to demonstrate the effects of the various parameters. A model with $M_c^{min} = 0.58$ $M_\odot$, $\lambda = 0.75$, $\eta_{RGB} = 0.86$, $\eta_{AGB} = \eta_{EAGB} = 5$, including HBB reproduces the observations best. It is possible that the amount of carbon formed after a TP is higher than the standard value of $X_{12} = 0.22$. As long as $\lambda X_{12} = 0.165$ the model fits the observations. It is difficult to discriminate between a higher X_{12} and a higher λ. Third dredge-up needs to be more efficient and must start at lower core masses than commonly predicted to account for the observed carbon star LF. It is suggested that evolutionary calculations have been performed with a mixing-length parameter which is too small.
The adopted mass loss rate coefficients correspond to a pre-AGB mass loss of 0.20 $M_\odot$ for a 1 $M_\odot$ and 1.8 $M_\odot$ for a 5 $M_\odot$ star. The low mass stars loose this on the RGB, the high mass stars in the core helium burning phase when they reach high luminosities before the TP-AGB. The Reimers coefficient on the AGB ($\eta_{AGB} = 5$) corresponds to a mass loss rate of 1.0 10^{-6} $M_\odot$/yr at the first TP for an initially 1 $M_\odot$ star with LMC abundances.
These high mass loss rates are necessary to fit the initial-final mass relation and the high luminosity tail of the carbon star LF. The lifetimes of the massive stars with these high mass loss rates are in good agreement with the observed number of massive AGB stars and their progenitors, the Cepheid variables. We suggest that the core mass at the first TP for massive stars has previously been overestimated because their evolution was calculated neglecting pre-AGB mass loss.

Observationally the distribution of ^{13}C-enriched carbon stars in the LMC is bimodal. There is a small number ($\sim$0.1%) of high-luminosity ($M_{bol} < -5$) J-type stars and a larger ($\sim$10%) number of low-luminosity ($M_{bol} > -4.75$) J-type stars. The difference in relative numbers as well as the gap in luminosity between the two distributions suggest a different evolutionary origin. The low-luminosity J-type stars may be related to the R-stars in the Galactic bulge which have luminosities between $0 \lesssim M_{bol} \lesssim 3$ indicating an origin at luminosities below the AGB.
The small number of high-luminosity J-type carbon stars can be explained by HBB. Given the uncertainty in the observed LF and our approximate treatment of HBB the agreement is good. We predict that about 1% of M and S stars are enriched in ^{13}C (and ^{14}N).
We considered the effect of 'obscuration', when stars loose so much mass that they become optically invisible. Based on V-band, I-band and IRAS data of Reid et al. (1990) and a radiative transfer model we find that at most 3% of all carbon stars brighter than $M_{bol} = -6$ could have been missed in optical surveys. Using our model we derive that the overall effect of obscuration of carbon stars is negligible ($\sim$0.1%).
The predicted average final mass (M_f = 0.59 $M_\odot$) is in good agreement with the observed value (0.60 $\pm$ 0.02 $M_\odot$). We predict for our LMC model that stars with initial masses larger than 1.2-1.4 $M_\odot$ turn into carbon stars directly and that stars initially more massive than about 1.5 $M_\odot$ pass through an intermediate S-star phase before becoming carbon stars. This is consistent with observations of carbon stars and S-stars in LMC clusters.
The predicted birth rate of AGB stars is found to be in agreement with the death rate of the Cepheids and the clump stars. The birth rate of planetary nebulae (PNe) is a factor of 2 lower than the death rate of AGB stars suggesting that low mass stars ($M \lesssim 1.1\ M_\odot$) may not become PNe.

1 Introduction

Stars in the main sequence mass range 0.9 $M_\odot \lesssim M_{ms} \lesssim 8\ M_\odot$ go through a double-shell burning phase, also referred to as the Asymptotic Giant Branch (hereafter simply AGB) phase, at the end of their life. In this phase carbon may be dredged up to the surface after a thermal pulse (TP), also referred to as a Helium shell flash, by convective dredge-up. By mixing additional carbon into the envelope a star can be transformed from a M-star phase (oxygen-rich), to a S-star phase (carbon about equal to oxygen) or a C-star phase (carbon outnumbering oxygen).
Although this general principle is well understood (see e.g. the review by Iben & Renzini 1983; hereafter IR) many problems remain. Progress in this field has been slow however because it is very (computer) time consuming to calculate an AGB-model using stellar evolution codes. For example, it takes about 2000 models to calculate one TP and the following interpulse period for one set of parameters. To explore the influence of metallicity or mass loss in this way is a formidable task. Finally, to calculate a consistent AGB-model one would have to evolve it from the main sequence to the red giant phase and to the AGB. A consistent set of models including the latest physics, with a sufficient narrow grid in stellar mass, metallicities and mass loss rates is not available and will probably not be available for some years to come.
To make progress in our understanding of stellar evolution on the AGB it is therefore useful to turn to 'synthetic' AGB-evolution. In synthetic evolution one uses empirical laws, derived from 'exact' model calculations, to calculate the evolution of an AGB star. The predicted results, e.g. final masses or luminosity functions (LFs) can than be compared to observations. This can provide information about quantities such as the mass loss rate on the AGB or the minimum core mass for dredge-up.
The first to use synthetic evolution models for the AGB were Iben & Truran (1978, hereafter

IT). They were primarily interested in the abundances of the s-process elements. The most well known study is probably that of Renzini & Voli (1981, hereafter RV). Their results were used to compare the theoretical luminosity function of carbon stars with the observed one in the LMC (Frogel et al. 1981, Richer 1981b) and to compare the predicted abundances in the ejecta of the AGB stars with the observed abundances in Planetary Nebulae (PNe) (see Clegg 1991 and references therein). RV also calculated the amount of matter returned to the Interstellar Medium (ISM) in the form of ^{4}He, ^{12}C, ^{13}C, ^{14}N, ^{16}O, which were used in Galactic chemical evolution models (e.g. Matteucci et al. 1989, Rocca-Volerange & Schaeffer 1990). Other studies employing synthetic evolution are Scalo & Miller (1979), Iben (1981), IR, Frantsman (1986), Bedijn (1988) and, more recently, de Jong (1990) and Bryan et al. (1990).
Except for the Bryan et al. study, the formulae used in these studies were mainly based on evolutionary AGB calculations for massive stars ($3 \lesssim M/M_\odot \lesssim 8$). These results were then extrapolated to less massive stars. This may not be (and indeed is not, as we will discuss later) valid. Another important aspect which was neglected in almost all studies so far, is the metallicity dependence of the evolutionary algorithms used. From observations of the Magellanic Clouds it was derived that the LF of carbon stars is probably different in the LMC and SMC. One of the explanations for this difference is the different metallicity in these systems (see e.g. Lequeux 1990).
In recent years several detailed studies of AGB evolution have been published which concentrate on low mass stars ($0.9 \lesssim M/M_\odot \lesssim 3$) and also investigate the metallicity dependence (e.g. Iben 1982; Boothroyd & Sackmann 1988a, b, c, d hereafter BS1, BS2, BS3, BS4; Lattanzio 1986, 1987a, b, 1989a, b, c and Hollowell 1987, 1988). With these new results it is possible to extend the empirical laws to lower masses as well as to include a metallicity dependence.
An important effect which was not included in most synthetic models is the variation of the luminosity during the flashcycle. During about 20% of the time following a TP the luminosity of the star is about 0.5 magnitude below its pre-flash value. This has significant implications for any theoretical LF since inclusion of this effect will create a significant (low-) luminosity tail in the LF.
Another important fact neglected in most synthetic evolution models so far is that during the first few pulses, when the TP's are not yet at full amplitude, the luminosity is lower than given by the canonical core mass-luminosity relations. This will also affect the low-luminosity tail of the LF.
The aim of this paper is to present a synthetic evolution model which includes physical effects like the ones described above, and also to include as much as possible the metallicity dependence of all relations used. In Sect. 2 we present the model and in Sect. 3 we apply it to the LMC with emphasis on a comparison with the observed LF of carbon stars in the LMC. The results are discussed in Sect. 4.

2 The Model

We start with describing the conditions of the star at the first TP. We proceed with the core mass-luminosity relation for full amplitude pulses, the core mass-interpulse period relation, the position of a star in the HR-diagram, the mass loss rate before and on the AGB, the effect of the luminosity variations during the flashcycle and finally the effects of the first, second and third dredge-up are discussed.

2.1 Conditions at the first Thermal Pulse

Since the evolution of an AGB star is governed by its core mass, the core mass at the first TP ($M_c(1)$) is the most important quantity for determining the initial condition of an AGB star. Since the luminosity of a star at the first TP is lower than the luminosity given by the core mass luminosity relation for full amplitude pulses (see below) a second important quantity is the luminosity at the first TP (L(1)).

2.1.1 The core mass at the first Thermal Pulse

For low mass stars ($M \leq 3\ M_\odot$) we use the formulae presented by Lattanzio (1989c). The core mass (in solar units) at the first TP for low mass stars is given by:

$$\begin{aligned} M_c(1) &= 0.53 - (1.3 + \log Z)(Y - 0.2) && Z \geq 0.01 \\ &= 0.524 + 0.58(Y - 0.2) + (0.025 - 20Z(Y - 0.2))M && 0.003 \leq Z \leq 0.01 \\ &= (0.394 + 0.3Y)\ \exp(M(0.1 + 0.3Y)) && Z \leq 0.003 \end{aligned} \tag{1}$$

where Y is the helium content and Z the metallicity at the first TP and M the (initial) mass in solar units.

For higher mass stars, i.e. stars massive enough to undergo the second dredge-up (see section 2.9.3) we use the formalism of RV as originally put forward by Becker & Iben (1979, 1980; hereafter BI1 and BI2). For completeness we will repeat them here.

Define $Z_1 = \log(Z/0.02)$, $Z_2 = Z - 0.02$, $Y_1 = \log(Y/0.28)$, $Y_2 = Y - 0.28$ were Z, Y are the main sequence values. The mass of the core just before the second dredge-up is given by:

$$M_c^B = AM + B \tag{2}$$

where

$$\begin{aligned} A &= 0.2954 + 0.0195Z_1 + 0.377Y_1 - 1.35Y_1^2 + 0.289Z_1Y_1 \\ B &= -0.500 - 30.6Z_2 - 412Z_2^2 - 1.43Y_2 + 29.3Y_2^2 - 204Z_2Y_2. \end{aligned} \tag{3}$$

The mass of the core just after the second dredge-up is given by:

$$M_c^A = CM + D \tag{4}$$

where

$$\begin{aligned} C &= 0.0526 + 0.754Z_2 + 54.4Z_2^2 + 0.222Y_2 - 1.07Y_2^2 + 5.53Z_2Y_2 \\ D &= 0.590 - 10.7Z_2 - 425Z_2^2 - 0.825Y_2 + 9.22Y_2^2 - 44.9Z_2Y_2 \end{aligned} \tag{5}$$

The lowest mass for which the second dredge-up will occur, M_{crit}, is determined from $M_c^B = M_c^A$ and is therefore given by:

$$M_{crit} = (B - D)/(C - A) \tag{6}$$

Therefore, for stars more massive than M_{crit}, the core mass at the first TP equals M_c^A. This assumes that there is no significant increase in the core mass between the second dredge-up and the first TP. This is indeed the case as can be verified by comparing Table 4 of BI1 (listing M_c^A) and Table 2 of BI2 (listing the true value of $M_c(1)$). The differences are of the order of 0.001 $M_\odot$. For stars in the range $3 < M/M_\odot < M_{crit}$ we interpolate linear in $M_c(1)$.

In Fig. 1 the core mass at the first TP is plotted as a function of initial mass for the composition

$Z = 0.02$, $Y = 0.28$ (solid line) and $Z = 0.001$, $Y = 0.24$ (dashed line). For comparison the values of $M_c(1)$ given by BS3 for $Z = 0.02$, $Y = 0.27$ (circles) and $Z = 0.001$, $Y = 0.24$ (plusses) and the recent results from Castellani et al. (1990) for $Z = 0.02$, $Y = 0.27$ (diamonds) are plotted. The dotted line represents the relation used by RV, irrespective of composition, for the low mass stars. In general there is good agreement for the massive stars. For the low mass stars, BS find somewhat lower initial core masses compared to Lattanzio.

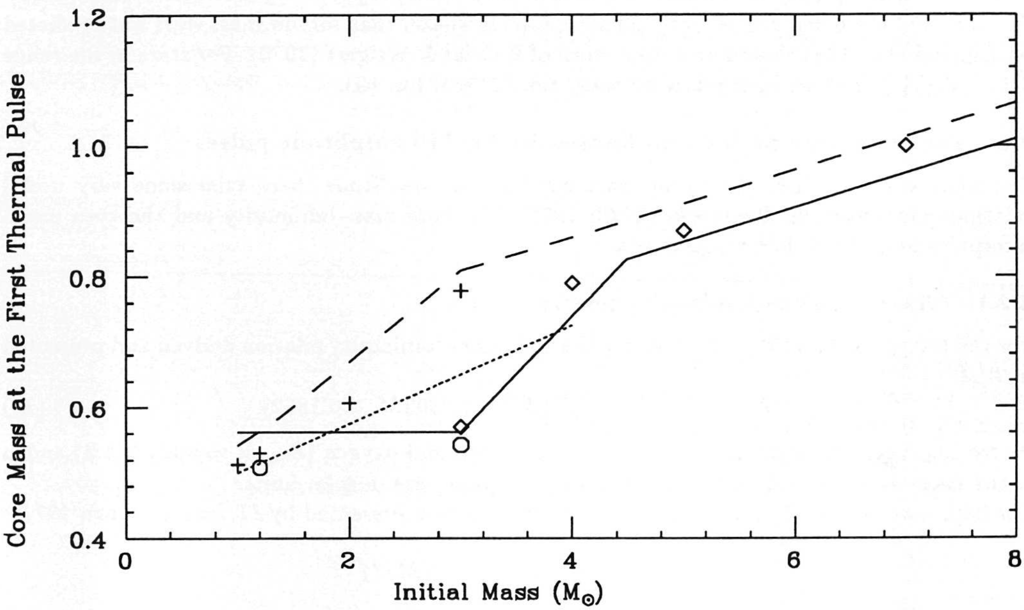

Figure 1: The core mass at the first thermal pulse, $M_c(1)$, derived from Eqs. (1) and (4) for the composition $Z = 0.02$, $Y = 0.28$ (solid line) and $Z = 0.001$, $Y = 0.24$ (dashed line). The standard pre-AGB mass loss rate of Sect. 2.6.1 is used to calculate $M_c(1)$. For comparison the results of BS3 for $Z = 0.02$, $Y = 0.27$ (circles) and $Z = 0.001$, $Y = 0.24$ (plusses) and of Castellani et al. (1990) for $Z = 0.02$, $Y = 0.27$ (diamonds) are also plotted. The dotted line represents the formula used by RV, irrespective of composition, for the low mass stars.

2.1.2 The luminosity at the first Thermal Pulse

For low mass stars ($M_c(1) \leq 0.8$) the luminosity (in solar units) at the first TP, L(1), is derived by fitting a straight line to data points in Fig. 4 of BS2:

$$\begin{aligned} L(1) &= 29000\,(M_c(1) - 0.5) + 1000 \qquad Z = 0.001 \\ &= 27200\,(M_c(1) - 0.5) + 1300 \qquad Z = 0.02 \end{aligned} \tag{7}$$

For other metallicities we interpolated in log Z.
For massive stars ($M_c(1) \geq 0.85$) we re-examined the original data presented by BI1 (their Table 2). Following the suggestion of BS2 that the composition dependence of the core mass-luminosity relation for full amplitude pulses for low mass stars scales with μ^3, where μ is the mean molecular weight:

$$\mu = \frac{4}{5X + 3 - Z} \tag{8}$$

we included a μ^α term in our fit to the BI data. Our result:

$$L(1) = 213180\,\mu^2\,(M_c(1) - 0.638) \tag{9}$$

gives a surprisingly good fit (within 5%) to all the datapoints, given the wide range of metallicities ($0.001 < Z < 0.03$) and helium contents ($0.20 < Y < 0.36$) considered by BI. The luminosities derived with Eq. (9) agree to within 5% with those recently reported by Castellani et al. (1990). The fact that the μ dependence for high mass stars is weaker than for low mass stars was predicted by Kippenhahn (1981) based on earlier work of Refsdal & Weigert (1970). For stars in the range $0.8 \leq M_c(1) \leq 0.85$ we interpolate between Eq. (7) and Eq. (9).

2.2 The interpulse period and luminosity for full amplitude pulses

For AGB stars in which the pulses have reached full amplitude there exist some very useful relations discovered by Paczynski (1970, 1975): the core mass-luminosity and the core mass-interpulse period relation, respectively.

2.2.1 The core mass-luminosity relation

For the low mass stars ($M_c < 0.7$) we use the core mass-luminosity relation derived and presented in BS2:

$$L = 238000\,\mu^3\,Z_{cno}^{0.04}\,(M_c^2 - 0.0305 M_c - 0.1802) \tag{10}$$

where Z_{cno} is the total abundance of carbon, nitrogen and oxygen (Z_{cno} is roughly 0.8 Z) and μ is the same as in Eq. (8). All luminosities in this paper are in solar units.
For high mass stars ($M_c > 0.95$) we modified the equation presented by IT (see also Iben 1977):

$$L \;=\; 63400\,(M_c - 0.44)(M/7)^{0.19}$$

in the following manner. Iben presented his formula for a mixing-length parameter $\alpha = l/H_p = 0.7$. BS2 argue that Iben's definition of α is different from the common one and his value corresponds to $\alpha \approx 1.3$ in most other models. But even this value for α is lower than presently felt to be the appropriate value, $\alpha \approx 1.9$ (Maeder & Meynet 1989). Iben reported an increase in luminosity by 15% if α is increased from 0.7 to 1.0. We took the luminosities at different core masses reported by Iben (1977) for his $M = 7\,M_\odot$ model and increased them by 15% to simulate the more appropriate value of α. We then fitted a straight line to it. We kept the mass dependence given by IT and introduced a composition dependence. For the composition dependence we assumed $L \sim \mu^2$, simply because this gave very good results for the L-$M_c(1)$ relation for massive stars (see Sect. 2.1.2). This assumption is not of any practical importance because μ changes only by 4% when Z is changed from 0.005 to 0.02 and Y is chosen according to Eq. (24). Our final result for the higher mass stars is:

$$L = 122585\,\mu^2\,(M_c - 0.46)\,M^{0.19} \tag{11}$$

For stars with $0.7 < M_c < 0.95$ we interpolate between Eq. (10) and (11).
Recent calculations by Blöcker & Schönberner (1991) seem to indicate that the standard core mass-luminosity relation may not be valid in the case of the massive stars. We have not taken this effect into account. Their results depend sensitively on the adopted mixing length parameter. Since they use the Cox & Steward (1970) opacities, their choice for the mixing length parameter is rather high ($\alpha = 2$). Furthermore, when the evolution of this model is continued, the luminosities fall on the standard core mass-luminosity relation again (Schönberner 1991).

In Fig. 2 the core mass-luminosity relations for both full amplitude pulses and at the first TP for both Z = 0.02 and 0.001 are shown. The helium abundance is calculated from Eq. (24) and the luminosity for the high core masses is calculated for M = 5 $M_\odot$. The difference in luminosity due to the difference in metallicity is about 0.4 in bolometric magnitude. Figure 2 shows that it is important to take into account that during the first few pulses the luminosity is below the value given for full amplitude pulses. The difference can amount to 0.8 magnitudes. For comparison the core mass-luminosity relation used by RV, irrespective of metallicity or pulse number, for a M = 3 $M_\odot$ and a M = 5 $M_\odot$ star, is also plotted.

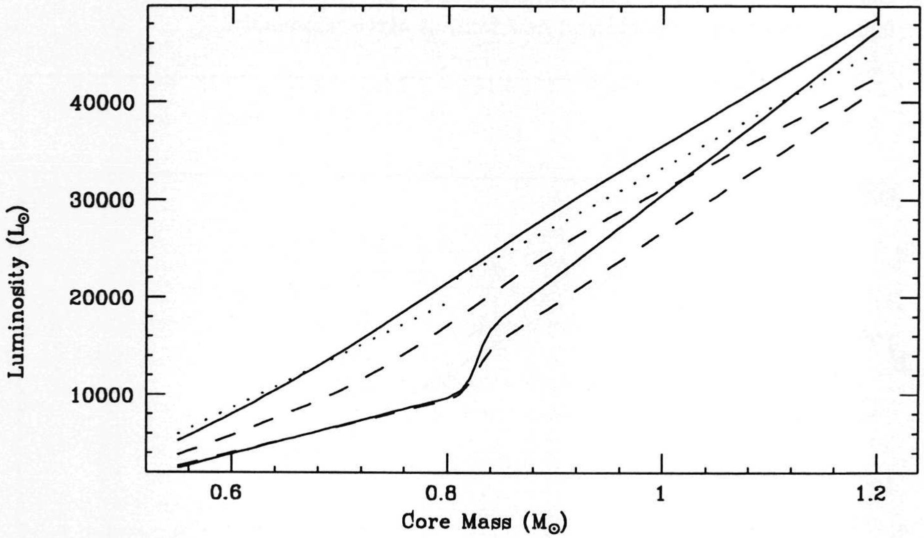

Figure 2: The core mass-luminosity relations for the first TP (lower solid and dashed curves) and for full amplitude pulses (upper solid and dashed curves) used in this work. Indicated are Z = 0.02 (solid line) and Z = 0.001 (dashed line). Note the difference between the luminosity at the first thermal pulse and for full amplitude pulses, especially for low core masses. For comparison, the dotted curve is the relation used by RV, irrespective of metallicity and pulse number. The lower part ($M_c \leq 0.8$ $M_\odot$) of this curve is calculated for a M = 3 $M_\odot$, the upper part for a M = 5 $M_\odot$ star. The wiggle in the relations for the luminosity at the first TP is due to the joining of Eq. (7) with Eq. (9).

2.2.2 The core mass-interpulse period relation

The timescale on which TPs occur is a function of core mass as was discovered by Paczynski (1975).
For all core masses we use the core mass-interpulse period relation presented in BS3:

$$\begin{aligned} \log\, t_{ip} &= 4.50\,(1.689 - M_c) \qquad Z = 0.02 \\ &= 4.95\,(1.644 - M_c) \qquad Z = 0.001 \end{aligned} \tag{12}$$

For other metallicities we interpolated in log t_{ip} using log Z as variable. The interpulse period is expressed in years. Both equations are derived for $M_c < 0.85$, but since Eq. (12a) is almost identical to the original Paczynski relation, log t_{ip} = 4.5 (1.678 − M_c), which is valid in the range 0.5 $\lesssim M_c \lesssim 1.4$ and for Z=0.03, it seems justified to extent Eq. (12a) to all core masses. For the low metallicity case there seems to be no data available regarding the M_c-t_{ip} relation for high mass stars, so we assume Eq. (12b) to be valid over the whole range of core masses. In actual computations this assumption will not play a significant role because high core masses are attained only by high mass stars which, in general, have a metallicity closer to Z = 0.02 than to Z = 0.001, even in the LMC.

In Fig. 3 the interpulse period is shown for Z = 0.02 and 0.001. For comparison the interpulse period relation derived from the formulae in RV for a 1 $M_\odot$ star with Z = 0.001 and a 5 $M_\odot$ star with Z = 0.02 (the dotted lines) are also shown. The differences with the formulae of BS are large for the lowest core masses. The formulae used by RV (taken from Iben 1977) were derived for $M_c \gtrsim 0.65$. In this region the old and new formula agree reasonably.

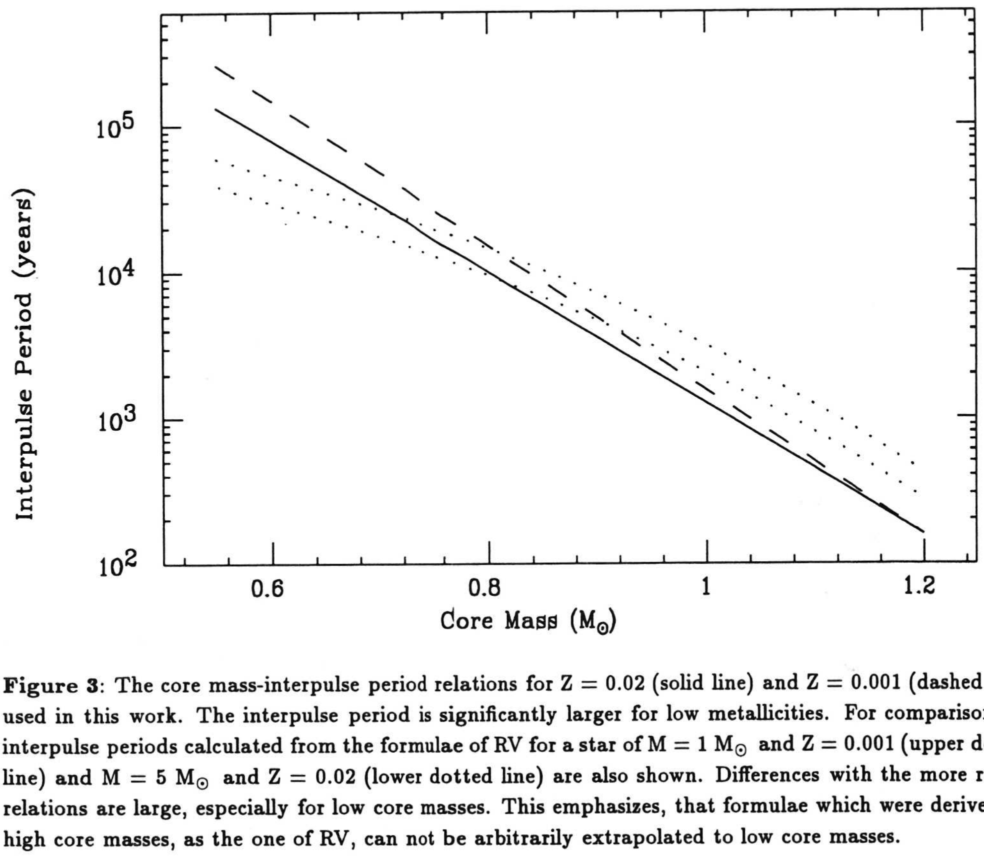

Figure 3: The core mass-interpulse period relations for Z = 0.02 (solid line) and Z = 0.001 (dashed line) used in this work. The interpulse period is significantly larger for low metallicities. For comparison the interpulse periods calculated from the formulae of RV for a star of M = 1 $M_\odot$ and Z = 0.001 (upper dotted line) and M = 5 $M_\odot$ and Z = 0.02 (lower dotted line) are also shown. Differences with the more recent relations are large, especially for low core masses. This emphasizes, that formulae which were derived for high core masses, as the one of RV, can not be arbitrarily extrapolated to low core masses.

2.3 From the first pulse to full amplitude pulses

It has been long known (see IR for references) that it takes some time before the TP reach full amplitude. During this period the equations presented in sections 2.2.1 and 2.2.2 are not applicable, without proper corrections. Since these corrections are necessary during approximately the first half dozen pulses they will mainly affect the low mass stars; a 1.5 $M_\odot$ star experiences about 50 TP, a 4 $M_\odot$ star about 1000 pulses during its AGB phase (RV).

2.3.1 Corrections to the core mass-luminosity relation

From the data presented in Fig. 4 of BS2 we deduce that it takes approximately 6 flashes before the luminosity at a given core mass lies on the core mass-luminosity relation for full amplitude pulses. This agrees with other calculations (e.g. Wood & Zarro 1981 and Lattanzio 1986).
We introduce a correction factor, f, depending upon the time already spent on the AGB, by which the luminosity, obtained from Eqs. (10) or (11), has to be multiplied to approximately get the true luminosity. For f a simple linear relation is assumed:

$$f = f_1 + (1 - f_1)\, t/\tau \qquad (t \leq \tau) \tag{13}$$

where t is the time spent on the AGB and τ is the time at which the TPs have reached full amplitude. We have taken τ to be 6 times the interpulse period at the first TP. For the first TP we have $f = f_1$, and so f_1 can be derived from:

$$f_1 = L(1)/L \tag{14}$$

Typical values for f_1 are 0.55 for a 1 $M_\odot$ star with Z = 0.005, and 0.67 for a 4.5 $M_\odot$ star with Z = 0.02.

2.3.2 Corrections to the core mass-interpulse period relation

From Fig. 11 in BS3 we derive that during the first few pulses the interpulse period is much shorter compared to the values given by the equations in 2.2.2. It seems that the star mimics a star of higher core mass.
In order to approximately get the correct interpulse period during the first six pulses we introduce a correction factor, ΔM_c, which has to be added to the true core mass to get an 'effective' core mass to be used in Eq. (12). The correction factors ΔM_c are given in Table 1.

Table 1: The correction factors ΔM_c for the interpulse period during the first six pulses

Pulse Number	ΔM_c	
N_p	Z = 0.02	Z = 0.001
1	0.09	0.06
2	0.065	0.01
3	0.04	0
4	0.03	0
5	0.02	0
6	0.01	0
≥ 7	0	0

2.4 The HR-diagram

To obtain the position of a star in the Herzsprung-Russell diagram we need to link the luminosity of a star to its effective temperature ($T_{\rm eff}$ in Kelvin).
We use the relations presented by Wood (1990) derived for oxygen-rich Miras:

$$\begin{aligned} \log T_{eff} &= (M_{bol} + 59.1 + 2.65 \log M)/15.7 - 0.12\ \log(Z/0.02) + \Delta \quad (M \leq 1.5) \\ &= (M_{bol} + 74.1 + 4.00 \log M)/20.0 - 0.10\ \log(Z/0.02) \qquad (M \geq 2.5) \end{aligned} \tag{15}$$

where $M_{bol} = -2.5 \log L + 4.72$ and Δ is a correction term which accounts for the fact that the effective temperature increases at the end of the AGB when the envelope mass becomes small. The Δ-term is calculated from Wood (1990):

$$\begin{aligned} \Delta &= 0 && x \geq 0.8 \\ &= 0.07\,(0.8 - x)^{2.54} && x < 0.8 \\ x &= M_{bol} + 7.0 - 1.2/M^{1.7} && \end{aligned} \tag{16}$$

For intermediate mass stars we interpolate in log T_{eff} using the mass M as variable. The zero point of these relations was determined by Wood from the assumption that the star o Ceti (Mira) with a period of 330 days, $Z = Z_{\odot}$ and $M_{bol} = -4.32$ has a mass of 1 $M_{\odot}$ and is pulsating in the fundamental mode. If o Ceti has a mass of 2 $M_{\odot}$ or is a first overtone pulsator the zero point in Eq. (15a) would be 57.1. This translates into a difference in T_{eff} of 15%.
The radius of the star (in solar units) is derived from:

$$R = \sqrt{\frac{L}{(T_{eff}/5770)^4}} \tag{17}$$

Equation (15) is, strictly speaking, only valid for oxygen-rich stars, but we also used it for carbon stars, lacking any better estimate. If the T_{eff}-L relation would be different for carbon stars this would merely affect the choice of the mass loss scaling parameter η_{AGB} (Sect. 2.6.2), through the dependence of the mass loss rate on the stellar radius and hence on the effective temperature.

2.5 The rate of evolution

Since hydrogen burning is the source of energy during most of the interpulse period the rate of evolution, i.e. the rate of core mass growth in $M_{\odot}$/yr is to a good approximation given by:

$$\frac{dM_c}{dt} = 9.555\;10^{-12}\;\frac{L_H}{X} \tag{18}$$

where X is the hydrogen abundance (by mass) in the envelope, L_H the luminosity provided by H-burning (in solar units) and the numerical factor includes the energy released from the burning of 1 gram of Hydrogen (6.4 10^{18} erg).
There is a small contribution from He-burning and gravitational energy to the total luminosity L, so that:

$$L = L_H + 2000(M/7)^{0.4}\,\exp(3.45(M_c - 0.96)) \tag{19}$$

This equation, derived for high mass ($M_c > 0.96$) stars, is taken from IT (see also RV) but we changed the exponent of the mass dependence from 0.19 to 0.4. This has no significant influence for high mass stars but gives better results when compared to the value given by Paczynski (1970) for a star with a core mass of 0.57 $M_{\odot}$. The correction to the total luminosity due to He-burning and gravitational energy is small: for a M = 7 $M_{\odot}$ star with $M_c = 0.96$ it is 6%, for a M = 1 $M_{\odot}$ star with $M_c = 0.6$ the correction term equals 4% of the total luminosity.

2.6 The mass loss process

The mass loss process on the AGB (but also prior to this phase) is an important, but unfortunately, a poorly understood phenomenon. The mass loss rate on the AGB has important consequences for the evolution of a star. It reduces the envelope mass more rapidly with the effect that (a) AGB evolution is terminated at a lower core mass, i.e. luminosity, (b) a star is more easily turned into a carbon star since less carbon needs to be dredged up and (c) it hampers the dredge-up process (Wood 1981).

The mass loss rate on the AGB has also important consequences with regard to the LF derived for e.g. carbon stars in extragalactic systems. With the advent of the IRAS satellite it has become clear that there exist many sources in our Galaxy (e.g. OH/IR sources or obscured carbon stars) which loose mass at such a rate ($> 10^{-5}$ $M_\odot$/yr) that they are optically very faint or even invisible. Their IR-signature (silicate emission or absorption, silicon carbide or amorphous carbon emission) is an important diagnostic to identify these sources as either oxygen- or carbon-rich. Since the identification of carbon stars in extragalactic systems is done using the C_2 bands at 4735 and 5165 Å or the CN bands at 7945, 8125, 8320 Å or V, R, I filters (see e.g. Lequeux 1990) these surveys could easily have missed carbon stars with optically thick dust shells. The IR surveys carried out so far (see e.g. Frogel & Richer 1983) did not go deep enough to detect these dust enshrouded stars, if they exist. Since stars with thick dust shells are usually associated with somewhat more luminous stars this implies that the LF presented for carbon stars (and also for M-stars) in extragalactic systems might be incomplete at the high luminosity end. To investigate the existence, and relative importance of obscured stars we calculated the LF of stars below and above a critical vale of the mass loss rate, $\dot{M}_{IR}$, to simulate optical visible and obscured stars. Details are given in Appendix C.

2.6.1 Mass loss up to the AGB

For low mass stars, i.e. stars which undergo the Helium Core Flash (HeCF), the most important phase prior to the AGB regarding mass loss is the Red Giant Branch (RGB). Several tenths of solar masses can be lost in this phase.

We parameterised the values of the mass loss on the RGB from the data presented in Fig. 8 of Sweigart et al. (1990). From this it is deduced that the amount of mass lost on the RGB, ΔM, is well represented by two straight lines:

$$\begin{aligned} \Delta M &= A_1 M + B_1 \quad && M < M_1 \\ &= A_2 M + B_2 && M_1 \leq M < M_2 \\ &= 0 && M \geq M_2 \end{aligned} \qquad (20)$$

M being the initial mass. The coefficients A_1, A_2, B_1, B_2 as well as M_1 and M_2 are listed in Table 2. We interpolate linearly in ΔM using Y and log Z as variables. The values given by Sweigart et al. (1990) are calculated for $\eta_{RGB} = 2/3$ (η_{RGB} being the coefficient in the Reimers law). For any other desired value of η_{RGB} one has to multiply the values calculated with Eq. (20) with an appropriate factor.

It is interesting to note that the amount of mass lost on the RGB increases with decreasing mass. This is due to two effects. Firstly, the luminosity at the tip of the RGB increases with decreasing mass in the mass range $M_1 \lesssim M \lesssim M_2$ (see e.g. Fig. 2 of Sweigart et al. 1990). Secondly, the time spent between the main sequence and the tip of the RGB increases with decreasing mass (see e.g. Sweigart et al. 1989). This means that $\Delta M \sim \dot{M}\, \Delta t \sim L\, \Delta t$ increases with decreasing mass.

For stars which do not pass through the HeCF the amount of matter lost on the RGB is negligible. For a 3 $M_\odot$ star (Z = 0.02, Y = 0.27) BS3 finds that $\Delta M = 0.003$ $M_\odot$, even for η_{RGB} = 1.4. So the fact that we assume $\Delta M = 0$ for $M \geq M_2$ is justified.

The most appropriate value of η_{RGB} can be derived from the observational constraint that population II stars on the Horizontal Branch must have lost approximately 0.2 $M_\odot$ on the RGB

(Rood 1972). Specifically, if we take Roods model for M3 that a M = 0.85 $M_\odot$ star with X = 0.75 and Z = 0.017 has lost 0.22 $M_\odot$ on the RGB, the appropriate value for η_{RGB} using the mass loss rates from the models of Sweigart et al. is η_{RGB} = 0.86. This will be our prime choice for η_{RGB} in our models.
Massive stars evolve up to high luminosities before they experience their first TP (see Fig. 2). If Reimers law is still applicable, massive stars can loose a considerable amount of mass before the first TP on the horizontal branch (HB) and Early-AGB. We parameterized the results of Maeder & Meynet (1989) for stars in the range 3 - 7 $M_\odot$ and find for the mass lost up to the first TP for the massive stars (in solar units):

$$\Delta M_{EAGB} = \eta_{EAGB}\, 0.056\, (M/3)^{3.7} \tag{21}$$

The subscript EAGB stands for early-AGB, although the mass is lost not only on the E-AGB but also on the latest phases of the HB. Maeder & Meynet (1989) use a Reimers law with η_{EAGB} = 0.5, but its not clear if this value is appropriate because the mass loss rates of stars that are on the E-AGB are unknown.

Table 2: The amount of mass loss on the RGB

Composition		A_1	B_1	M_1	A_2	B_2	M_2
Y = 0.2	Z = 0.004	−0.108	0.300	2.10	−0.292	0.689	2.36
	0.010	−0.106	0.317	2.20	−0.250	0.625	2.50
	0.040	−0.104	0.339	2.25	−0.160	0.465	2.91
Y = 0.3	Z = 0.004	−0.116	0.269	1.77	−0.224	0.467	2.08
	0.010	−0.124	0.306	1.85	−0.232	0.506	2.18
	0.040	−0.132	0.348	2.00	−0.168	0.420	2.50

The coefficients A_1, A_2, B_1, B_2, M_1, M_2 refer to Eq. (20).

2.6.2 Mass loss on the AGB

Mass loss on the AGB will be represented by Reimers (1975) law:

$$\dot{M} = \eta_{AGB}\, 4.0\, 10^{-13}\, \frac{L\, R}{M} \qquad\qquad M_\odot/yr \tag{22}$$

The luminosity L is not the quiescent luminosity but includes the effect of the luminosity variation during the flashcycle, i.e. the mass loss rate just after a TP is higher than at quiescence or in the luminosity dip. We do not include an explicit metallicity dependent term in the mass loss rate, as for example is suggested from the study of the mass loss rates of hot O-stars in the Galaxy and the Magellanic Clouds which seem to indicate $\dot{M} \sim Z^{0.5}$ (Kudritzki et al. 1987).
From IR's relation between η and the final mass it is derived that $\eta_{AGB} \gtrsim 3$ is needed to fit the observed initial-final mass relation in the Galaxy (see Weidemann & Koester 1983). Therefore the initial value in our model will be η_{AGB} = 3.

2.7 When to end the AGB evolution ?

Basically two approaches have been adopted to this question. The first approach is to end the AGB evolution with the instantaneous ejection of what is supposed to represent a Planetary

Nebula. This solution has been adopted by de Jong (1990), who assumed that 10% of the initial mass was ejected at the end of the AGB, as well as RV who assumed a core mass dependent relation (their Eq. (33)) which increases from 0.02 $M_\odot$ at $M_c = 0.5\ M_\odot$ to a maximum of 1.38 $M_\odot$ at $M_c = 1.33\ M_\odot$.
The second approach is to end the evolution on the AGB when the envelope mass is reduced below a critical value, when the star starts moving to the left in the HR diagram. This approach is adopted in this study and we used Iben's (1985) suggestion that the critical envelope mass, M_{end}, is given by:

$$M_{end} = 0.1\ \frac{dM_c}{dt}\ t_{ip} \tag{23}$$

For typical parameters this corresponds to $M_{end} = 7.9\ 10^{-4}\ M_\odot$ ($M_c = 0.6\ M_\odot$, $M = 1.5\ M_\odot$, $X = 0.7$, $Z = 0.02$) or $M_{end} = 9.4\ 10^{-6}\ M_\odot$ ($M_c = 1.2\ M_\odot$, $M = 7\ M_\odot$, $X = 0.7$, $Z = 0.02$). For lower metallicities, M_{end} increases due to the increase in the interpulse period. For the $M = 1.5\ M_\odot$ star e.g., $M_{end} = 1.3\ 10^{-3}\ M_\odot$ when $Z = 0.001$. These values agree within a factor two with the formula given by Iben (1985), the difference probably being due to differences in total mass and composition. The values of M_{end} derived here also agree with the values reported by Paczynski (1971), Schönberner (1983) and Blöcker & Schönberner (1990).

2.8 The flashcycle

The luminosity between two thermal pulses is not constant (as given by the equations in Sect. 2.2.1). It has been known for a long time (see e.g. IR) that for short periods of time the luminosity can be both higher and lower than the quiescent value.
From the data presented by BS1 as well as from Iben (1975), Sackmann (1980), Wood & Zarro (1981), Iben (1982) and Lattanzio (1986) the following (simplified) relations are derived.
Stars with $M_{env} \leq 2\ M_\odot$ have, for a brief moment directly following a TP, a luminosity higher than the quiescent value. The duration t_{flash} (in units of the interpulse period, not in years !) and the value $\Delta \log L_{flash}$ to be added to the logarithm of the quiescent luminosity to obtain the peak flash luminosity are given in Table 3. From BS1 these values are found to be slightly metallicity dependent.
More significant is the luminosity dip following this peak, or in the case of high mass stars directly following a TP. The duration, t_{dip} (relative to the interpulse period) and the extent of the luminosity dip $\Delta \log L_{dip}$ are given in Table 4. Both parameters depend on the envelope mass. Since large envelopes more easily absorb the changes taking place deep in the star, the duration and extent of the luminosity dip are smaller when the envelope mass is higher.
The shape of the luminosity flash and dip is assumed to be a rectangular profile.

Table 3: The peak luminosity and duration of the flash for stars with $M_{env} \leq 2\ M_\odot$

Z	t_{flash}	$\Delta \log L_{flash}$
$Z \leq 0.001$	0.008	0.3
$0.001 < Z \leq 0.02$	0.01	0.25
$Z > 0.02$	0.015	0.2

t_{flash} is relative to the interpulse period.

Table 4: The extent of the luminosity dip and its duration

M_{env}	t_{dip}	$\Delta \log L_{dip}$
$M_{env} \leq 0.05$	0.4	−0.4
$0.05 < M_{env} \leq 0.5$	0.3	−0.3
$0.5 < M_{env} \leq 1.5$	0.25	−0.25
$M_{env} > 1.5$	0.2	−0.2

t_{dip} is relative to the interpulse period.

2.9 First, second and third dredge-up

One of the fascinating aspects of AGB evolution is the possibility of forming carbon-rich stars by the dredge-up of carbon from the carbon-rich pocket formed after the helium shell flash. This process is generally referred to as third dredge-up.
Before reaching this interesting phase, the main sequence composition has changed during the first dredge-up (experienced by all stars on the RGB) and the second dredge-up (experienced by stars with $M > M_{crit}$; see Sect 2.2.1) occurring on the E-AGB.
In the following sections our treatment of first, second and third dredge-up is described.

2.9.1 The initial composition

The main sequence composition is determined in the following way. The parameter to be specified is the metallicity Z. The helium abundance is calculated from:

$$Y = Y_0 + \frac{\Delta Y}{\Delta Z} Z \tag{24}$$

The hydrogen content is calculated from X = 1 − Y − Z. We assumed a primordial helium abundance Y_0 of 0.231 (Steigman et al. 1989). For the Galaxy values between 1.7 and 5 are quoted for $\frac{\Delta Y}{\Delta Z}$ (Steigman 1985, Pagel et al. 1986). For the LMC and SMC there seem to be no independent estimates. Based on the observed abundances in HII regions and field F-type supergiants in the LMC and SMC (Russell & Dopita 1990) we derive that $\frac{\Delta Y}{\Delta Z} = 2.5$ describes the present day abundances well in both LMC and SMC. Since this value is within the quoted range for the Galaxy we will use $\frac{\Delta Y}{\Delta Z} = 2.5$ for Galaxy, LMC and SMC alike.
Following Anders & Grevesse (1989) and Grevesse (1991) the main sequence abundances of carbon, nitrogen and oxygen are chosen as:

$$\begin{aligned} Z_{cno} &= 0.791Z \\ ^{12}C &= 0.2384Z_{cno} \\ ^{13}C &= 0.0029Z_{cno} \\ ^{14}N &= 0.0707Z_{cno} \\ ^{16}O &= 0.6880Z_{cno} \end{aligned} \tag{25}$$

This implies an initial value $^{12}C/^{13}C = 89$ (all abundances are mass fractions, all ratios will be number ratios, unless otherwise specified). Equation (25) is based on relative solar abundances. Abundance analyses of field stars in the LMC and SMC (Spite & Spite 1991a, 1991b, Barbuy et al. 1991) generally give near solar relative abundances so that Eq. (25) can be used with some confidence for Galaxy, LMC and SMC alike.

2.9.2 The first dredge-up

The first dredge-up occurs when the convective envelope moves inwards as a star becomes a red giant for the first time. The convective motion dredges up material which was previously located near the hydrogen burning shell. Helium and CNO-processed material are brought to the surface.
The treatment of the first dredge-up follows that of RV, except that we changed the numerical values slightly to incorporate the results of Sweigart et al. (1989, 1990).
The increase in the helium abundance, ΔY, is given by Sweigart et al. (1990). The following fits are based on their results:

$$
\begin{aligned}
\Delta Y &= -0.0170\, M_{in} + 0.0425 \quad M_{in} < 2,\ Y = 0.3 \\
&= -0.0068\, M_{in} + 0.0221 \quad 2 \leq M_{in} < 3.25,\ Y = 0.3 \\
&= -0.0220\, M_{in} + 0.0605 \quad M_{in} < 2.2,\ Y = 0.2 \\
&= -0.0078\, M_{in} + 0.0293 \quad 2.2 \leq M_{in} < 3.75,\ Y = 0.2 \\
&= 0 \quad \text{else}
\end{aligned}
\tag{26}
$$

The small dependence of ΔY on Z for a given Y is neglected. The change in hydrogen is opposite to the change in helium:

$$\Delta X = -\Delta Y \tag{27}$$

The change in ^{12}C and ^{14}N is calculated from:

$$
\begin{aligned}
g &= 0.64 - 0.05(M-3) \quad M < 3 \\
g &= 0.64 \quad M \geq 3 \\
\\
\Delta^{12}C &= {}^{12}C\,(g-1) \\
\Delta^{14}N &= -1.167\,\Delta^{12}C \\
\Delta^{16}O &= -0.01\,{}^{16}O
\end{aligned}
\tag{28}
$$

The number ratio $^{12}C/^{13}C$ after the first dredge-up does not vary much with mass or composition (Sweigart et al. 1989) and is set to 23.
It should be noted that observations indicate that some stars do not obey the standard model predictions. In particular, the $^{12}C/^{13}C$ ratio after the first dredge-up is often lower than predicted in stars of low mass, down to $^{12}C/^{13}C \approx 10$ (see e.g. the review by Lambert 1991). Rotationally induced mixing may play a role.

2.9.3 The second dredge-up

The second dredge-up is related to the formation of the electron-degenerate CO core in more massive ($M > M_{crit}$, Eq. 6) stars after central helium exhaustion. The base of the convective envelope moves inward through matter pushed outwards by the He-burning shell.
The treatment of the second dredge-up follows that of RV closely (see also IT and IR). The abundances after the second dredge-up can be obtained from the abundances prior to the second dredge-up and the abundances of the material that is dredged up using the relation:

$$X^{after} = aX^{prior} + bX^{du} \tag{29}$$

The coefficients a and b are as follows:

$$
\begin{aligned}
a &= \frac{M - M_c^B}{M - M_c^A} \\
b &= \frac{M_c^B - M_c^A}{M - M_c^A}
\end{aligned}
\tag{30}
$$

where M is the total mass and M_c^A and M_c^B are calculated from Eq. (2) and (4). The abundances prior to the second dredge-up are known, and the abundances of the dredged up material are given by RV and IT:

$$\begin{aligned} Y^{du} &= 1 - Z \\ {}^{14}N^{du} &= 14\,({}^{12}C/12 + {}^{13}C/13 + {}^{14}N/14 + {}^{16}O/16) \\ {}^{12}C^{du} &= {}^{13}C^{du} = {}^{16}O^{du} = 0 \end{aligned} \tag{31}$$

In the model, Eq. (29) was not used to calculate the hydrogen abundance after the second dredge-up, but was calculated from X = 1 − Y − Z, with Y and Z the helium and metal abundance after second dredge-up. This was done to ensure that X + Y + Z ≡ 1 at all times.

2.9.4 The third dredge-up

Although the third dredge-up is of crucial importance for the formation of carbon stars, it is still poorly understood. There is much debate whether or not material is dredged up at every pulse, and how much. It is also seems possible that the dredge-up process is turned off again when a star has become a carbon star (BS4, Lattanzio 1989a).

Another effect which has to be taken into account is the possible destruction of newly dredged up carbon at the base of the convective envelope in the CNO-cycle, a process referred to as Hot Bottom Burning (HBB), and extensively discussed in RV. This process is able to slow down or even prevent the formation of carbon stars. Since ^{12}C is processed into ^{13}C and ^{14}N, it also gives rise to the formation of ^{13}C-rich carbon stars (usually referred to as J-type carbon stars) and ^{14}N-rich objects. RV treated HBB in considerable detail as a function of the mixing length parameter (they considered α = 0, 1.0, 1.5, 2). Because the detailed envelope calculations performed by RV are beyond the scope of this paper and since RV found that the results are sensitive to the unknown mixing length parameter, we decided to include HBB in our model in an approximate way.

In our simple model to describe HBB four parameters are needed: (1) the (average) temperature at the base of the convective envelope, T_B, as a function of core and total mass, (2) the fraction (f_{HBB}) of newly dredged up matter exposed to the high temperatures at the bottom of the envelope, (3) the amount of matter in the envelope, relative to the total envelope mass, which is mixed down and processed at the bottom of the envelope (f_{bur}) and (4) the (average) exposure time, t_{HBB}, of matter in the zone of HBB.

The value of T_B can be derived from the data presented in RV. We implemented the algorithms used by RV to calculate AGB evolution in our code and found good agreement with RV in the case of no HBB for a small change in their quoted parameters. In the case of HBB we derived f_{bur}, f_{HBB} and t_{HBB} from fitting our model to the α = 2 case of RV. Details are given in Appendix A.

Let us now present the formulae used to describe the third dredge-up process in detail.

It is assumed that there is dredge-up only when the core mass is higher than a critical value M_c^{min}. The exact value of M_c^{min} is still a matter of debate. To make headway we initially assume the value of Lattanzio (1989c):

$$M_c^{min} = 0.62 + 0.7\,(Y - 0.20) \tag{32}$$

In Sect. 3 we will investigate if this value of M_c^{min} is compatible with the observed LF of carbon stars in the LMC.

The increase in core mass during the interpulse period is given by:

$$\Delta M_c = \int_o^{t_{ip}} \frac{dM_c}{dt} dt \tag{33}$$

A certain fraction of this amount is assumed to be dredged up:

$$\Delta M_{dredge} = \lambda \, \Delta M_c \tag{34}$$

The free parameter, λ, is as a first approach assumed to be constant and is of the order of 1/3 (see e.g. Lattanzio 1989c). Fitting their synthetic models to observations Bryan et al. (1990) found a best fit for $\lambda \approx 0.28$.
The composition of the material formed in the pocket after a TP is assumed to be (BS3): $X_{12} = 0.22$ (carbon), $X_{16} = 0.02$ (oxygen) and $X_4 = 0.76$ (helium). The carbon is formed trough incomplete helium burning in the triple α process and the oxygen in the $^{12}C(\alpha,\gamma)^{16}O$ reaction. Since HBB may be effective, this is not necessarily the composition of the material added to the envelope.
If f_{HBB} represents the fraction of the dredged up material processed in the CNO cycle at the bottom of the envelope (as defined above), the amount of material added to the envelope is:

$$\begin{aligned}
\Delta^4 He &= X_4 \, \Delta M_{dredge} \\
\Delta^{12} C &= \left((1 - f_{HBB}) \, X_{12} + \frac{f_{HBB}}{t_{HBB}} \int_0^{t_{HBB}} X_{12}^{HBB}(t) \, dt \right) \Delta M_{dredge} \\
\Delta^{13} C &= \left(\frac{f_{HBB}}{t_{HBB}} \int_0^{t_{HBB}} X_{13}^{HBB}(t) \, dt \right) \Delta M_{dredge} \\
\Delta^{14} N &= \left(\frac{f_{HBB}}{t_{HBB}} \int_0^{t_{HBB}} X_{14}^{HBB}(t) \, dt \right) \Delta M_{dredge} \\
\Delta^{16} O &= \left((1 - f_{HBB}) \, X_{16} + \frac{f_{HBB}}{t_{HBB}} \int_0^{t_{HBB}} X_{16}^{HBB}(t) \, dt \right) \Delta M_{dredge}
\end{aligned} \tag{35}$$

where t_{HBB} is the average time of exposure to the high temperatures at the base of the envelope. Details on how the time evolution of a species is calculated are given in Appendix A. The initial conditions to be used in the integrals in Eq. (35) are X_{12}^{HBB} (t=0) = X_{12} and similar for oxygen, while X_{13}^{HBB} (t=0) = X_{14}^{HBB} (t=0) = 0.
If we also allow for a fraction (f_{bur}) of the envelope mass to be mixed downwards and processed by HBB (as defined above), the abundance of a general species X, after a dredge-up period and HBB during the interpulse period can be calculated from:

$$X^{new} = \frac{X^{old} M_{env} \, (1 - f_{bur}) + \Delta X + \frac{f_{bur} M_{env}}{t_{HBB}} \int_0^{t_{HBB}} X(t) dt}{M_{env} + \Delta M_{dredge}} \tag{36}$$

where ΔX is given by Eq. (35). The initial condition in the integral appearing in Eq. (36) is X (t=0) = X^{old}. The case of no HBB can be recovered using $f_{bur} = 0$ and $f_{HBB} = 0$.

2.10 The numerical computations

We have developed two very similar computer programs, one to calculate the evolution of a single star and another program which calculates the evolution of a sample of stars distributed according to a preset distribution function.
In the former program we first specify the initial mass and the metallicity of the star and the free parameters (M_c^{min}, η_{EAGB}, η_{AGB}, λ and whether or not HBB is included). The program then calculates the effects of the first dredge-up on the abundances and the mass lost up to the first TP. The core mass and luminosity at the first TP are calculated and for stars experiencing the second dredge up, the abundances after the second dredge-up are derived. Subsequently the program enters the AGB subroutine.

At each new time step, the updated luminosity is calculated and the 'status' of the star is determined: carbon star (C/O $\geq$ 1.0), S-star (0.81 $\leq$ C/O $<$ 1.0; Smith & Lambert 1986), M-star (C/O $<$ 0.81), J-type or not (^{12}C/^{13}C $\gtrsim$10) and whether or not a certain mass loss rate, $\dot{M}_{IR}$, is exceeded (see Appendix C). The radius, mass loss rate and core growth rate are calculated. A new time step is determined from the condition that the core mass and the envelope mass may change by no more than a preset value (usually set at 0.001 $M_\odot$). with the additional provisos that the luminosity peak and the luminosity dip are covered by at least one time step and that the timestep does not exceed the interpulse period. Having determined the time step, all masses (total, core, envelope, core growth since the last pulse) are updated. If the total time since the last TP is less than the interpulse period a new time step is calculated. If it exceeds the interpulse period, the abundances are updated and a new interpulse period is determined. The evolution on the AGB is ended when the envelope mass is decreased below M_{end} or when the core mass exceeds the Chandrasekhar mass, so that the star ends as a supernova.

In the second code we calculate the evolution of a sample of AGB stars by selecting initial masses according to the probability that a star of initial mass M is on the AGB. Stars which are presently on the AGB must have been born an appropriate time ago, so that the distribution function may be written as:

$$N(M)dM \sim \int_0^{t_{AGB}(M)} \mathrm{IMF(M)}\ \mathrm{SFR}(\mathrm{T}_G - \mathrm{t_{pre}(M)} - x)\, dx$$

where IMF (in $M_\odot{}^{-1}$) is the Initial Mass Function ($\sim M^{-\alpha}$), SFR (in $M_\odot$/yr) is the Star Formation Rate, t_{AGB} the lifetime of a star on the AGB, T_G the age of the system and t_{pre} the pre-AGB lifetime of a star.

Realising that $t_{AGB} \ll t_{pre}$ for all M leads to:

$$N(M)dM \sim \mathrm{IMF(M)}\ \mathrm{SFR(M)}\ t_{AGB}(\mathrm{M}) \qquad M_{lower} < M < M_{upper} \qquad (37)$$

Estimates for t_{AGB} are derived in Appendix B.

In the program initial masses are randomly selected according to the distribution function Eq. (37). From a relation between the initial mass and the pre-AGB lifetimes, the SFR and metallicity at the time of birth are deduced. The number of stars N (usually 1000), M_{lower}, M_{upper}, the IMF, the SFR and the age-metallicity relation have to be specified. See Sect. 3 for details on the specific relations used for the LMC.

2.11 Limitations and uncertainties

We attempted to bring together in this model all knowledge provided by presently available evolutionary calculations for AGB stars. However, the mere fact that these calculations do not reproduce all observational quantities (e.g. the luminosity function of carbon stars in the LMC) implies that evolution theory still needs improvement.

Also within the framework of the adopted approximations there are some limitations. For example, the dredge-up parameter, λ (Eq. 34), is assumed to be constant. In all likelyhood it will depend, in a complex manner, on mass and composition. Secondly, a Reimers law was adopted to describe the mass loss rate on the AGB. Does this empirically derived law for Red Giants provide a good description of mass loss on the AGB? A third uncertainty lies in the initial abundances and the abundance changes prior to the AGB. Ideally one needs an age-metallicity relation for all important elements (He, C, N, O) separately. The few attempts to construct such relations for the Galaxy (Matteucci and François 1989, Rocca-Volmerange & Schaeffer 1990) give results which do not seem to agree with observations. For extragalactic systems age-metallicity relations

for individual elements do not exist.
A fourth uncertainty lies in the fact that we only consider single star evolution. It has been established e.g. that almost all CH- and BaII-stars and a significant fraction (~38%) of MS and S stars are binaries and that e.g. the R-stars show a normal binary frequency (McClure 1989, Smith & Lambert 1988, Brown et al. 1990). Iben and Tutukov (1989) estimate that ~15-20% of PN are expected to form in close binaries. Our calculations do not take into account close binary evolution and mergers.

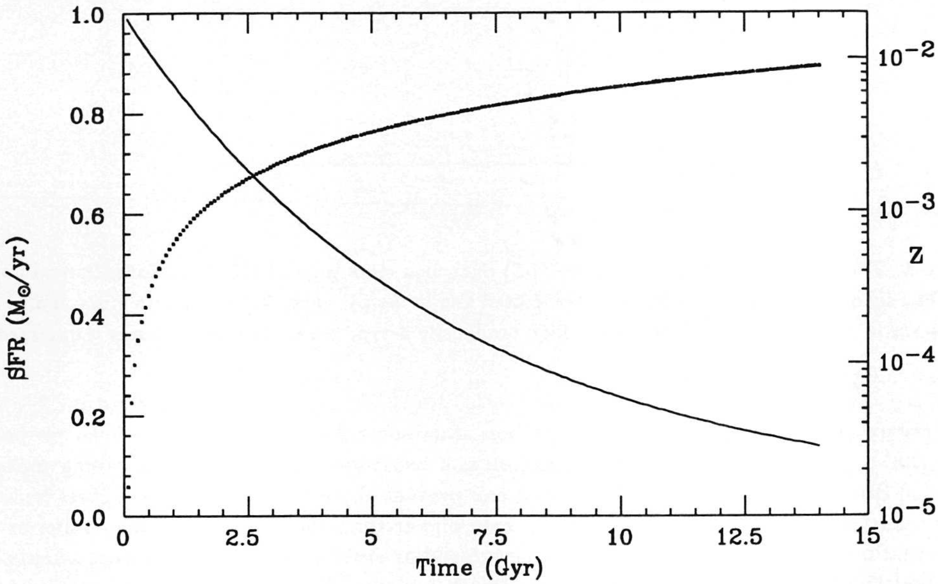

Figure 4: The age-metallicity relation (dotted curve, righthand scale) and Star Formation Rate (solid curve, lefthand scale) in the LMC adopted from Van den Hoek and de Jong (1992).

3 The carbon star luminosity function in the LMC

Iben (1981) published an article entitled "The carbon star mystery: why do the low mass ones become such and where are the high mass ones gone?" In this article Iben compared the theoretically predicted LF of carbon stars and the observed LF of carbon stars in the LMC which at the time was determined rather accurately for the first time from deep surveys (Blanco et al. 1980). The difference was striking: the observed carbon stars in the LMC had bolometric magnitudes from -3.5 to -6 while the predicted range was ~ -5 to -7.1, the maximum luminosity at the tip of the AGB.
As indicated by the title of Iben's work, subsequent work has focussed on the formation of low-luminosity carbon stars and suggestions an how to solve the problem of the high luminosity carbon stars.
With regard to the formation of low luminosity carbon stars we refer to the reviews of Iben (1988) and Lattanzio (1989b). It seems that carbon recombination at low temperatures, semi-convection, convective overshooting and the mixing length parameter α, play a role in the formation of low-luminosity carbon stars.

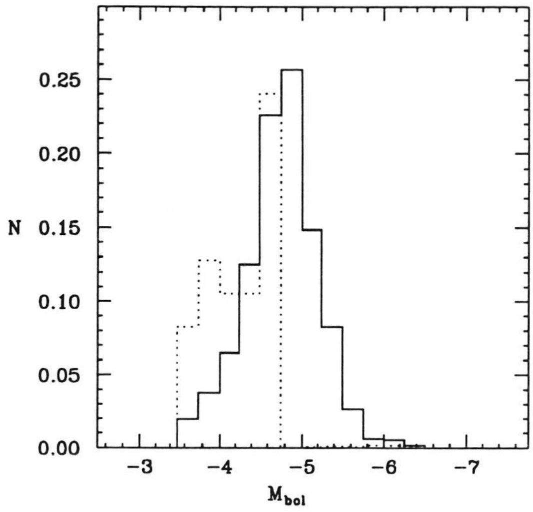

Figure 5: The observed luminosity function (LF) of carbon stars in the LMC for a distance modulus of 18.5. The solid line is the total LF, while the dotted line is the LF of the J-type carbon stars, multiplied by a factor of 5. Note the small number of high-luminosity J-type stars. The histogram is normalised to unity.

With regard to the the high-luminosity carbon stars several explanations have been proposed (Iben 1981): (1) a pause in the star formation and consequently an absence of young massive stars, (2) Hot Bottom Burning (HBB) which can prevent the formation of carbon stars because ^{12}C is transformed into ^{14}N, (3) a mass loss rate higher than the classical Reimers value or (4) the formation of stars enshrouded in thick circumstellar envelopes. The last two arguments are of course closely related. Only detailed calculations can show if enhanced mass loss on the AGB produces stars with thick circumstellar shells, which could have escaped detection from optical surveys. Finally, (5) Renzini et al. (1985) suggested that convective overshooting reduces M_{up}, the upper limit in initial mass of stars appearing on the AGB, from $\sim$8 $M_\odot$ to $\sim$5 $M_\odot$.
The first argument, a pause in the star formation rate, has been dismissed by Iben (1981) and Reid et al. (1990), because there exist many Cepheids in the Clouds which are the likely progenitors of the more massive AGB stars. The last argument, core overshooting, can not be the sole solution to the problem because even stars of 5 $M_\odot$ can reach high luminosities, as was noted by Reid et al. (1990). Hot Bottom Burning can prevent the formation of carbon stars (RV) but this implies that a star remains oxygen-rich for a longer time, thereby reaching higher luminosities. Although M-stars are known to exist with magnitudes in the interval $-6 \lesssim M_{bol} \lesssim -7$ (Wood et al. 1983) there seems to be a general scarcity of high-luminosity AGB stars. This would exclude HBB as the solution to the absence of the high luminosity carbon stars and leaves an enhanced mass loss rate as the most important cause for the absence of high luminosity carbon stars.
In the models described below we have used the following parameters, appropriate for the LMC. The IMF-slope, SFR and age-metallicity relation were adopted from van den Hoek & de Jong (1992), see Fig. 4. These relations were derived by simultaneously modeling the current gas fraction, current metallicity and age-metallicity relation for the LMC, constrained by the best available ages and metallicities of LMC clusters. Assuming a power-law IMF (IMF $\sim M^{-\alpha}$) and a density dependent SFR, the age-metallicity relation for the LMC was best modelled with α

= −2.72. The age of the LMC is taken as 11 Gyr, about equal to the age of the Galactic disk (Rocca-Volmerange & Schaeffer 1990). The pre-AGB lifetimes of Iben & Laughlin (1989) are used to relate the initial mass to the pre-AGB lifetimes[1]. From this relation it is also derived that stars down to $M_{lower} = 0.93\ M_\odot$ have lived long enough to have reached the AGB. If the mass loss rate on the RGB (and possibly the E-AGB) is high enough though, the stars with the lowest initial masses will not reach the AGB but will turn into white dwarfs on or after the RGB. From BI1 we derive $M_{upper} = 8.2\ M_\odot$ for typical LMC abundances. For the Chandrasekhar mass we assume $M_{Ch} = 1.2\ M_\odot$ (Hamada & Salpeter 1961).

To compare the model results to the observations we have combined the observed LMC carbon star LF of Cohen et al. (1981) with the data presented by Richer et al. (1979).

Blanco et al. (1980) surveyed three 0.12 square degree fields in the LMC, complete down to $M_{bol} \approx -2$. They found 186 carbon stars. Cohen et al. derived bolometric magnitudes for 165 of them. One carbon star brighter than $M_{bol} = -5.8$ was discovered. Westerlund et al. (1978), surveying 62.5 square degree down to $M_{bol} \approx -4.5$, discovered 302 carbon stars. Richer et al. presented R, I photometry for 112 of them. We transformed these into bolometric magnitudes using the bolometric corrections of Cohen et al.. In this sample, 28 have $M_{bol} < -5.8$.

Richer et al. (1979) and Richer (1981a) have investigated the relative importance of the J-type carbon stars, carbon stars enriched in ^{13}C, in both surveys. Richer found 3 J-type stars among the 23 he investigated in one of the Blanco et al. fields which contained a total of 70 carbon stars and Richer et al. found 7 among the 40 stars they investigated of the Westerlund et al. survey.

In Fig. 5 the observed LF of carbon stars in the LMC is presented, scaled to a distance modulus of the LMC of 18.5 (see Table 6 of Jacoby et al. 1990 for a compilation of distance determinations to the LMC. A recent determination with the HST for SN 1987A gave 18.50 ± 0.13 (Panagia et al. 1991)). The solid line is the total LF, while the dotted line is the contribution of the J-type carbon stars, blown up by a factor of 5. The observed number of J-type stars in each bin was scaled using the respective discovery rate in both fields and then the LF of both fields were weighted with the total discovery rate of carbon stars in the Blanco et al. and Westerlund et al. surveys. The LF of the J-type stars is uncertain due to the small numbers involved.

From Fig. 5 it is derived that carbon stars exist up to $M_{bol} \approx -6.5$ but that they are rare. Approximately 1% is brighter than $M_{bol} = -5.8$. The peak of the LF is at $M_{bol} = -4.875$ (center of bin). The distribution of the J-type stars is bimodal. There is a small fraction (~0.1%) of high luminosity J-type carbon stars, possibly connected to HBB and a more significant fraction (~10%) of low-luminosity J-type carbon stars. They dominate the lowest luminosity bins. The non-J-type carbon stars in the LMC are important for $M_{bol} < -4$. The origin of the low-luminosity J-type carbon stars is less clear. These stars might be descendents of, or related to, the R-type stars, which are observed in the Galactic bulge up to $M_{bol} \approx -2.8$ (Westerlund et al. 1991b). To allow for an observational error in the observed LF as well as for the depth of the LMC ($1\sigma = 0.04$ mag as quoted in Jacoby et al. 1990) and the intrinsic variability of stars on the AGB, all the theoretical calculated LFs shown below are convolved with a Gaussian of width $1\sigma = 0.20$ mag.

Besides the observed carbon star LF, the observed ratio of carbon-to-oxygen rich stars (C/M-ratio) in the LMC will be used as an additional constraint to the model.

For the carbon-to-oxygen rich star ratio a value of C/M ≈ 2 is often quoted but some care should be taken since this ratio strongly depends on spectral type of the M stars that are taken into account. Blanco & McCarthy (1983) give C/M2+ = 0.2 ± 0.1, C/M5+ = 0.80 ± 0.03, C/M6+ =

[1] In fact Iben & Laughlin presented a fit to the lifetimes needed to reach the white dwarf (WD) stage. Because the main sequence and RGB lifetimes dominate all other evolutionary phases, this is essentially equal to the pre-AGB lifetime.

2.2 ± 0.1 respectively. The question is therefore: what is the range in spectral type of oxygen-rich TP-AGB stars, and what is the contamination of e.g. E-AGB stars for a given spectral type? Hughes (1989) and Hughes & Wood (1990) have made a survey for LPV in the LMC and determined spectral types for many of them. The stars they found have luminosities which indicate that they are on the AGB, but it is not possible to discriminate conclusively between the E-AGB and the TP-AGB phase. In any case, they find that most LPV have spectral types M5 or later and that C/M = 0.63. It seems plausible that most stars in the LMC with spectral type M5 and later are on the TP-AGB. Based on the previous estimates we will assume a theoretically predicted C/M ratio of thermal pulsing AGB stars in the LMC of $0.6 < \mathrm{C/M} < 2.5$ as in agreement with observations.

3.1 The low-luminosity tail of the LF of carbon stars in the LMC

In this section the parameters which influence the low-luminosity tail of the carbon star LF will be discussed.

The standard model has the following parameters: pre-AGB mass loss rates of $\eta_{\mathrm{RGB}} = 0.86$ and $\eta_{\mathrm{EAGB}} = 3.0$, mass loss rate on the AGB $\eta_{\mathrm{AGB}} = 3.0$, minimum core mass for dredge-up according to Eq. (32), dredge-up parameter $\lambda = 1/3$, no convective overshooting, no HBB.

The fact that the luminosity during the first few pulses is below the core mass luminosity relation, and the fact that the luminosity is not constant during the flashcycle were long known, but never simultaneously included in any synthetic evolution model before. Iben (1981) approximately included the effects of the flashcycle in his calculations and Bedijn (1988) the effect of the first few pulses. The importance of taking both these effects into account is demonstrated in Fig. 6 were we plotted the LF of M-, S- and C-stars for the standard model for the following parameters (from left to right): not taking into account the variation during the flashcycle (no 'flashcycle') and the effect of the first few pulses (no 'first few pulses'), no 'flashcycle' but 'first few pulses' included, 'flashcycle' included but not the 'first few pulses', both 'flashcycle' and 'first few pulses' included.

The carbon star LF when neither the flashcycle and the effect of the first few pulses is included outlines the 'carbon star mystery' of about 10 years ago. Compared to the observed LF in Fig. 5 there are no low luminosity carbon stars and too many bright ones.

For the standard model, taking into account the effect of the 'first few pulses' has only effect on the M-star LF. The LF extents about 0.5 magnitudes to lower luminosities. This is indeed expected based on Fig. 2. The fact that the carbon star LF remains unchanged is simply because stars become carbon stars after the sixth TP, which is the timescale adopted to go from the first TP to full amplitude pulses.

The largest effect of the flashcycle is to lower the low-luminosity tail of the LF by about 0.8 magnitudes. This is expected based on the assumed properties of the flashcycle (Table 4).

It is obvious from comparing the left and rightmost LF in Fig. 6 that the effects of the flashcycle and the first few pulses are rather large and should not be neglected. Its also obvious by comparing the rightmost carbon star LF of Fig. 6 with the observed LF that these two effects alone are not sufficient to bring the observed LF in accord with the predicted one. The standard model including the 'flashcycle' and the 'first few pulses' still predicts too few low luminosity carbon stars and too many bright ones.

One could assume an even larger effect of the luminosity dip (one would need $\Delta \log \mathrm{L_{dip}} \approx -0.7$) but unless the evolutionary models are completely wrong, this seems not a viable option. Besides, this does not solve the discrepancy of the high-luminosity carbon stars and the wrong luminosity of the peak of the distribution. A more promising solution to the discrepancy at the low-luminosity end of the C-star LF is that the minimum core mass for dredge-up, $\mathrm{M}_c^{\mathrm{min}}$, is too

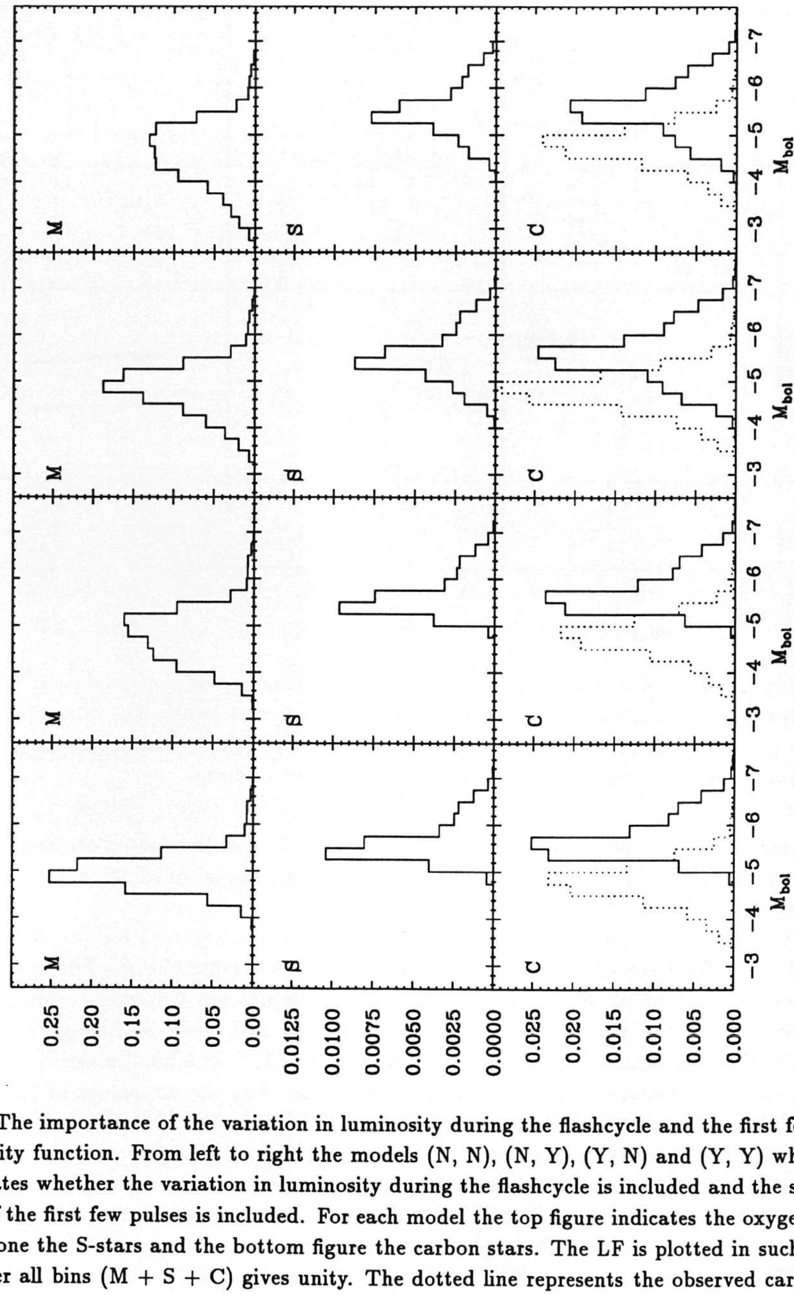

Figure 6: The importance of the variation in luminosity during the flashcycle and the first few pulses on the luminosity function. From left to right the models (N, N), (N, Y), (Y, N) and (Y, Y) where the first letter indicates whether the variation in luminosity during the flashcycle is included and the second one if the effect of the first few pulses is included. For each model the top figure indicates the oxygen-rich stars, the middle one the S-stars and the bottom figure the carbon stars. The LF is plotted in such a way that the sum over all bins (M + S + C) gives unity. The dotted line represents the observed carbon star LF of Fig. 5.

high in the standard model. An alternative solution, which will be investigated later, is that the amount of carbon dredged up at a TP is too low.
In evolutionary calculations M_c^{min} is determined by the adopted mixing length parameter, which is very uncertain. BS4 showed that by (suddenly) increasing α to 3 they could produce a carbon

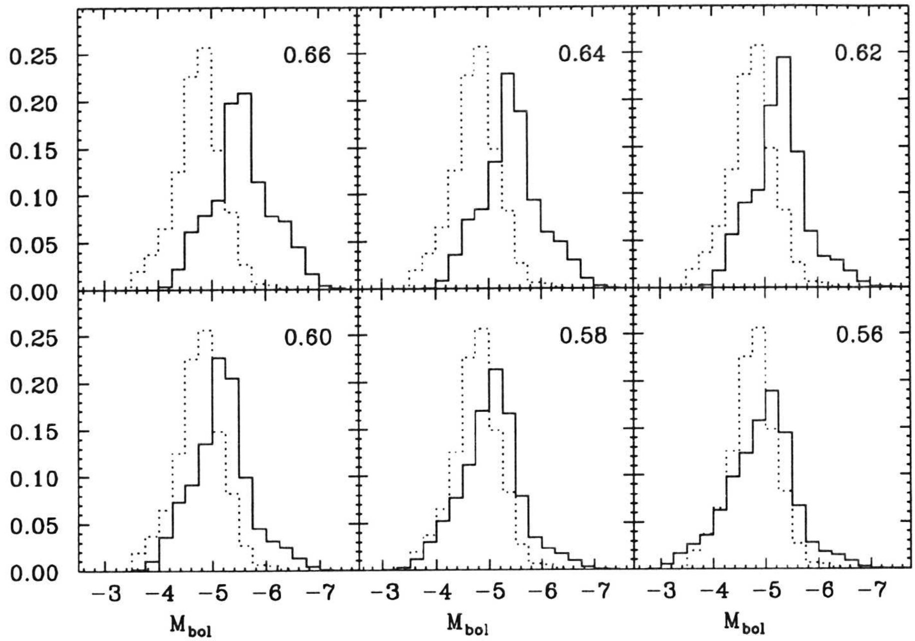

Figure 7: The influence of lowering the minimum mass for dredge-up on the carbon star LF. The LF is normalised to unity. The values of M_c^{min} (in $M_\odot$) are indicated in each panel. The value of C/M increases from 0.43 to 1.8 and the peak is shifted by 0.5 mag to lower luminosities. The dotted line represents the observed carbon star LF of Fig. 5. The histogram is normalised to unity.

star with a core mass of 0.566 from a star of initial mass 1.2 $M_\odot$. Dredge-up started immediately at a core mass of 0.566, far below the value in the standard model of $M_c^{min} \approx 0.66$ (Eq. 32 with $Y = 0.25$, appropriate for the LMC).

In Fig. 7 the carbon star LF is plotted (normalised to 1 in each panel) for the standard model but with $M_c^{min} = 0.66, 0.64, 0.62, 0.60, 0.58$ and 0.56. Decreasing the minimum core mass for dredge-up shifts the peak of the carbon star LF to lower values but this effect is small, about 0.5 mag. Decreasing M_c^{min} is not sufficient to let the predicted and observed LF agree. Because the observed LF starts at $M_{bol} \approx -3.5$ we can conclude that $M_c^{min} \geq 0.58$. Lowering the minimum value for dredge-up results in a longer carbon star phase. For the six values of M_c^{min} reported above, the C/M ratio increases from 0.11, 0.15, 0.25, 0.38, 0.59 to 0.74. The ratio of S-stars to carbon stars is almost constant: S/C = 0.31, 0.30, 0.29, 0.28, 0.27, 0.26.

Although we have established that the onset of the carbon star LF can be well explained with $M_c^{min} \approx 0.58$, the peak of the predicted LF is still at a luminosity which is too high. To steepen the carbon star LF we consider three possibilities: (1) a change in the distribution of stars on the AGB; (2) a decrease in the envelope mass of low-mass stars before the first TP and (3) an increase in the amount of carbon dredged up after each TP. The results are gathered in Fig. 8 and compared to the standard model with $M_c^{min} = 0.58$ (panel a).

Since the initial mass function is the dominant factor determining the distribution of stars on the AGB the slope of the IMF was changed from −2.72 to −3.5. This results in a relative increase of low-mass stars which should become carbon stars at lower luminosities. This is indeed found (panel b) but the change in the LF is small.

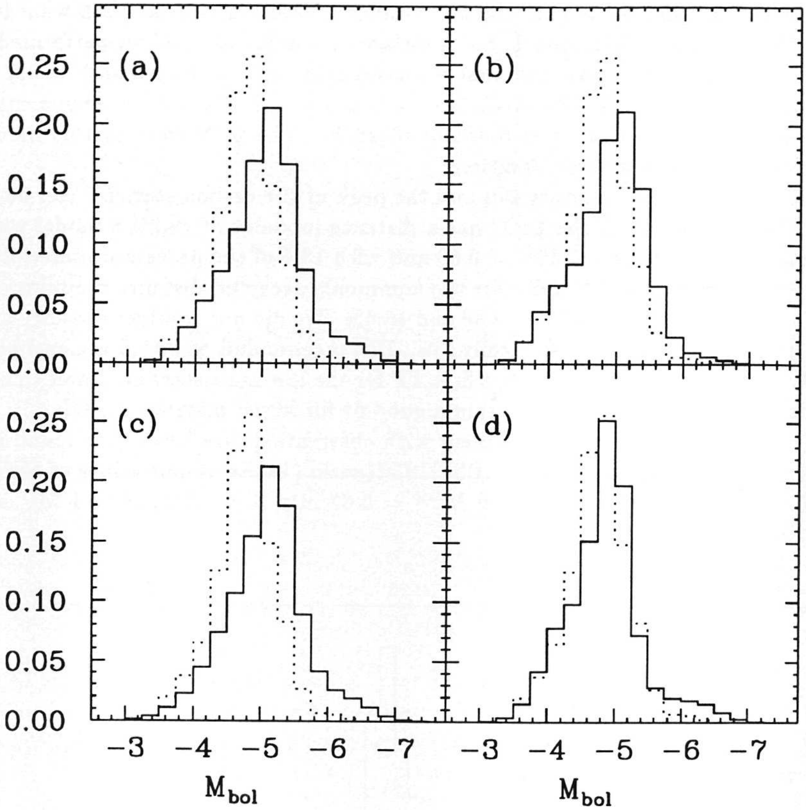

Figure 8: The normalised carbon star LF for the following models: (a) standard model with M_c^{min} = 0.58 $M_\odot$ ($\alpha = -2.72$, $\eta_{RGB} = 0.86$, $\lambda = 1/3$); (b) the slope of the IMF changed to $\alpha = -3.5$; (c) pre-AGB mass loss rate for the low-mass stars increased to $\eta_{RGB} = 2.5$; (d) the amount of carbon dredged-up at each TP increased from 7.3% to 16.5%. Only an increase in the amount of carbon dredged up at each TP is capable of bringing the observed and predicted carbon star LF in agreement. The dotted line represents the observed carbon star LF of Fig. 5.

Decreasing the envelope mass of the low-mass stars before the first TP, i.e. increasing η_{RGB}, has two opposite effects. There is less oxygen in the envelope so the star should become a carbon star at lower luminosities. On the other hand the lifetime is reduced, so the star experiences less thermal pulses resulting in less dredge up of carbon. From panel (c) we deduce that the latter effect wins. There is a small shift to higher luminosities.
The amount of carbon dredged up after each TP is determined by λ, the total amount of matter dredged up relative to the amount of matter processed between two successive thermal pulses and X_{12}, the abundance of carbon in the material that is dredged up. In the standard model 7.3% of all processed material is carbon ($\lambda = 1/3$, $X_{12} = 0.22$). In panel (d) this is increased to 16.5% ($\lambda = 0.75$, $X_{12} = 0.22$). The agreement with the observed LF is very good. The peak of the LF is now at the correct luminosity. The C/M-ratio is 1.4 in this model which is in good agreement with observations.
Although a distance modulus of 18.5 seems to be the most reliable one, we have considered distance moduli of 18.25 and 18.75. The latter value is incompatible with the observed carbon

star LF since it is not possible to shift the LF too much lower luminosities than what is achieved with the M_c^{min} =0.58, $\lambda = 0.75$ model. For a distance modulus of 18.25 we performed a similar analyses as described above. We find that a model with $M_c^{min} = 0.60$ and $\lambda = 0.6$ (i.e. 13% carbon dredged up after each TP) predicts a carbon star LF which is in agreement with the observed one if shifted to a distance modulus of 18.25. The C/M-ratio in this model is 0.69 which is still in agreement with observations.

We conclude that the low-luminosity tail and the peak of the carbon stars LF can be explained equally well by two models. If the LMC has a distance modulus of 18.25, a model with a minimum core mass for dredge-up of $M_c^{min} = 0.60$ and with 13% of the processed material in carbon fits the observed carbon star LF well. For the commonly accepted distance modulus of 18.5 the numbers of the best model are $M_c^{min} = 0.58$ and 16.5%. We did not consider distance moduli less then 18.25 because they are unrealistically low. Distance moduli of $\gtrsim$18.6 are excluded by our model. Only when the core masses at the first TP for the low-mass stars are lower than assumed in this model it might be possible to obtain a good fit for larger distance moduli.

The values of M_c^{min} found to be in agreement with observations are lower than found in existing models (except the one ad hoc model of BS4). Lattanzio (1989a) found values of M_c^{min} of 0.605 for a Z = 0.001 M = 1.5 $M_\odot$ model and M_c^{min} = 0.63 in a Z = 0.001, M = 1 $M_\odot$ and a Z = 0.01, M = 1.5 $M_\odot$ model.

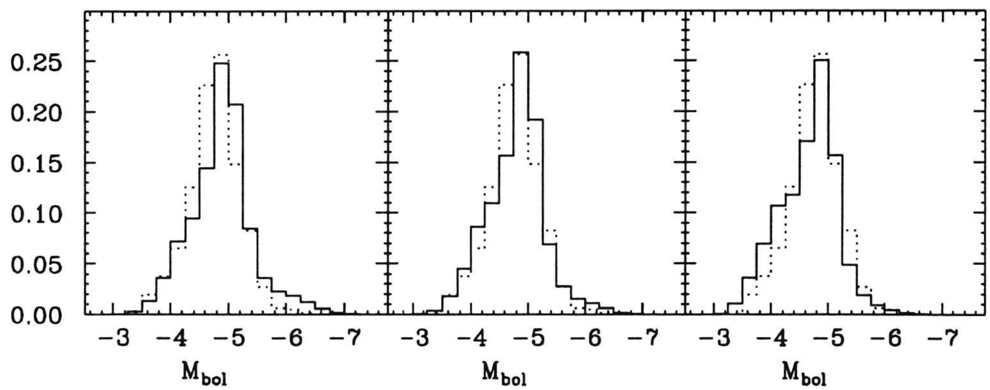

Figure 9: The effect of mass loss and obscuration on the optical carbon stars LF. From left to right models with $\eta_{AGB} = \eta_{EAGB}$ = 3, 5 and 8, respectively. The η_{AGB} = 8 model predicts too few high-luminosity and too many low-luminosity carbon stars. The dotted line represents the observed carbon star LF of Fig. 5. The histogram is normalised to unity

3.2 The high-luminosity tail of the LF of carbon stars in the LMC

As briefly pointed out earlier the high-luminosity tail of the carbon star LF could, in principle, depend on four factors: the mass loss rate, incompleteness of the optical surveys, HBB and/or convective overshooting. They will be discussed in that order.

We first consider the combination of the mass loss rate and optical obscuration. In Appendix C we derive that a maximum of 3% of all carbon stars brighter than $M_{bol} = -6$ could have been missed by the optical surveys. Based on radiative transfer calculations we derive in Appendix C the critical mass loss rate $\dot{M}_{IR}$ at which a carbon star in the LMC becomes invisible. The value of $\dot{M}_{IR}$ scales with the factor F_{IR} which depends on the assumed dust properties and the

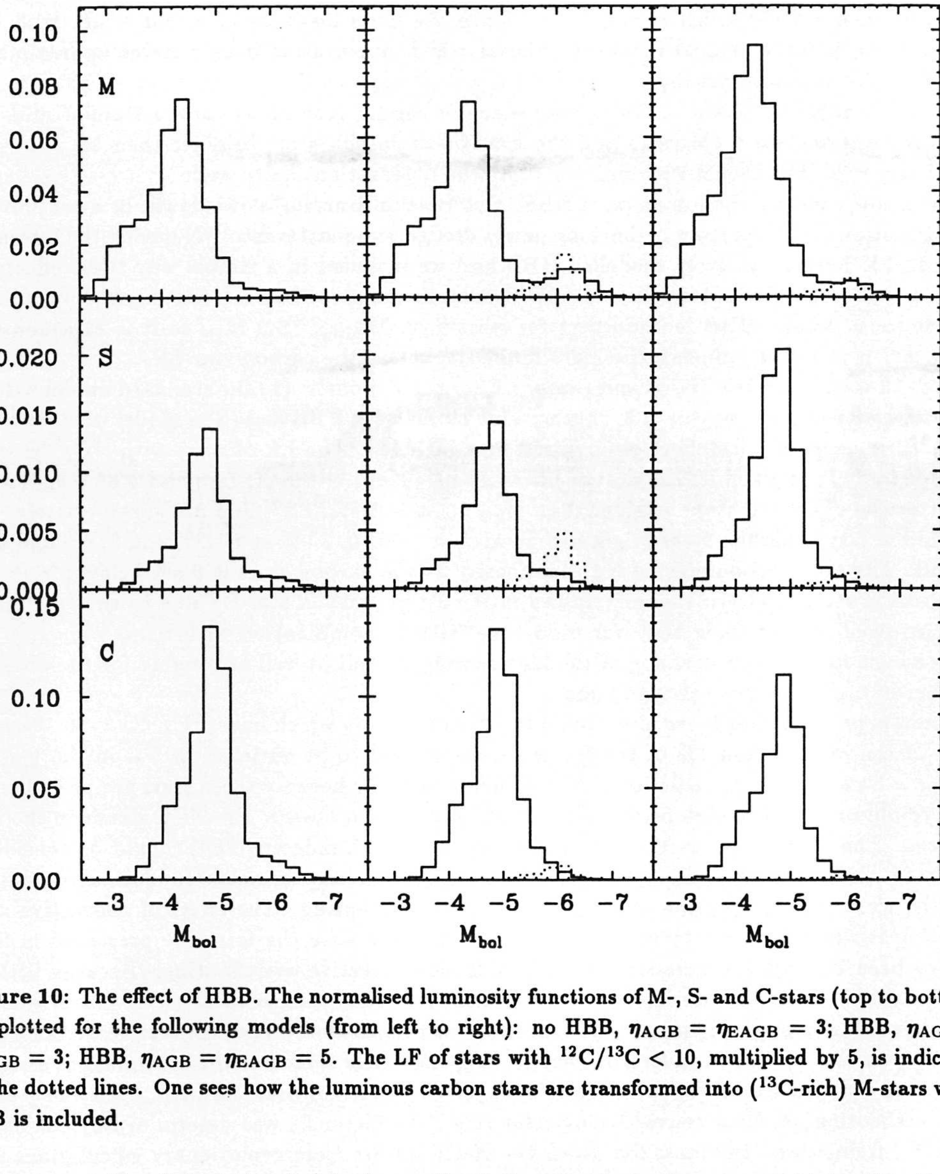

Figure 10: The effect of HBB. The normalised luminosity functions of M-, S- and C-stars (top to bottom) are plotted for the following models (from left to right): no HBB, $\eta_{\rm AGB} = \eta_{\rm EAGB} = 3$; HBB, $\eta_{\rm AGB} = \eta_{\rm EAGB} = 3$; HBB, $\eta_{\rm AGB} = \eta_{\rm EAGB} = 5$. The LF of stars with $^{12}C/^{13}C < 10$, multiplied by 5, is indicated by the dotted lines. One sees how the luminous carbon stars are transformed into (^{13}C-rich) M-stars when HBB is included.

dust-to-gas ratio. It is estimated in Appendix C that $F_{\rm IR}$ is in the range 0.04 to 100. In the calculations presented below $F_{\rm IR}$ was varied in such a way that 3% of all carbon stars brighter than $M_{\rm bol} = -6$ were obscured. The model then predicts the degree of obscuration at other luminosities. In Fig. 9 the optical carbon star LF is presented for $\eta_{\rm AGB} = \eta_{\rm EAGB} = 3, 5, 8$. The scale factor $F_{\rm IR}$ was found to be 10, 14 and 22, respectively. The overall C/M ratio is 1.44, 0.88 and 0.45, respectively. Of all carbon stars 3.8%, 1.8% and 0.7% are brighter than $M_{\rm bol} = -6$. The observed fraction is 1.3%. The overall fraction of obscured carbon stars is 0.12%, 0.07% and 0.03%, respectively. For the M- and S-stars the obscured fraction is even less.

We conclude that obscuration is not important. Even when the optical surveys have missed 3% of carbon stars brighter than $M_{\rm bol} = -6$ (which is in fact an upperlimit) the overall degree of obscuration is ~0.1% which is negligible. Since the mass loss rate of a star scales with L in Reimers law but the critical mass loss rate at which obscuration occurs scales approximately with $L^{0.5}$ this is not surprising.

A second conclusion, based on the overall shape of the LF (too many carbon stars at mid- and low-luminosities), the C/M ratio and the fraction of carbon stars brighter then $M_{bol} = -6$ is that $\eta_{AGB} < 8$. The model with $\eta_{AGB} = 5$ fits the observations quite well.

We will now consider the influence of HBB. Hot Bottom Burning slows down, or even prevents the formation of carbon stars by burning newly dredged-up matter into ^{14}N during the interpulse period. RV have extensively modelled HBB and we included in a simple way these effects for their $\alpha = 2$ case, which gives the most HBB. Details are given in Sect. 2.9.4 and Appendix A. For the $\alpha = 2$ case, HBB is important for stars with $M_{initial} \gtrsim 3.3\ M_\odot$, so it is expected that HBB can in principle influence the high-luminosity tail of the carbon star LF.

In Fig. 10 we present the M-, S- and C-star LF for three models: (1) the standard model without HBB and with $\eta_{AGB} = \eta_{EAGB} = 3$, (2) the same model with HBB and (3) a model with HBB and $\eta_{AGB} = \eta_{EAGB} = 5$. The effect of obscuration is included. The LF of stars with $^{12}C/^{13}C < 10$, multiplied by 5, is given by the dotted lines. The C/M ratio is 1.44, 1.28 and 0.85 respectively. The fraction of carbon stars brighter than $M_{bol} = -6$ is 3.8%, 1.2% and 0.7%, respectively. The fraction of J-type carbon stars brighter than $M_{bol} = -5$ is 0, 2.6% and 1.2% and 0, 0.9 and 0.4% overall. The observed number of high-luminosity J-type carbon stars is 0.5% below $M_{bol} = -5$ and ~0.1% overall. Given the uncertainty in the J-type carbon star LF due to the small numbers involved, we conclude that our model for HBB in combination with $\eta_{AGB} = \eta_{EAGB} = 5$ can account for the overall shape of the high-luminosity tail as well as roughly for the observed number of high-luminosity J-type stars.

Our model predicts that there also should be M- and S-stars which have $^{12}C/^{13}C < 10$. Roughly 0.8% of the M-stars and 1% of the S-stars are predicted to be enriched in ^{13}C in the $\eta_{AGB} = \eta_{EAGB} = 5$ model. This prediction will be difficult to verify because these stars are probably too faint to obtain the very high resolution spectra necessary to observe the ^{13}CO bands in the near infrared. The very luminous MS-stars (Wood et al. 1983, Lundgren 1988) should be considered first rate candidates for such an analysis when improved observational techniques allow this.

Finally, we briefly discuss the effect of convective overshooting. The effect of convective overshooting is rather difficult to estimate in our models, because the formulae presented in Sect. 2 have been derived from classical models without convective overshooting. Because little or no evolutionary calculations have been performed for AGB stars with convective overshooting models we have restricted ourselves to a zeroth order approximation of convective overshooting, based upon the fact that convective overshooting effectively increases the core mass of a star in such a way that a star of initial mass M behaves like a star of mass f_{os} M ($f_{os} > 1$, 'os' stands for overshooting) without convective overshooting. The factor f_{os} was determined by comparing the MS lifetimes and the mass for which the HeCF occurs from evolutionary calculations with and without convective overshooting. A factor $f_{os} \approx 1.2$-1.4 is appropriate for models with small convective overshooting (d = 0.25 H_p, Maeder & Meynet 1989), while for models with strong convective overshooting (d = 1 H_p, e.g. Chiosi et al. 1987) $f_{os} \approx 1.3$-1.6 seems appropriate. Convective overshooting is only important for stars with $M_{initial} \gtrsim 1.2\ M_\odot$, so f_{os} always equals 1 for stars below this limit. Selecting stars from the interval $M_{lower} \leq M \leq (M_{upper}/f_{os})$ we calculated the evolution as if the core mass was for a star of mass f_{os} M. The main changes relative to the non-convective overshooting models are threefold. Firstly, substantial mass loss on the RGB is restricted to stars with $M \lesssim 1.6\ M_\odot$, because stars above this limit will not experience the HeCF. Secondly, for a given initial mass the core mass at the first TP will be larger and thirdly, the envelope mass will be smaller.

A comparison of models (M_c^{min} = 0.58 $M_\odot$, λ = 0.75, $\eta_{AGB} = \eta_{EAGB}$ = 5, HBB included) calculated with and without convective overshooting (using f_{os} = 1.2) shows that the differences are small. The C/M ratio e.g. is reduced from 0.85 to 0.73. The shape of the carbon star LF remains virtually unchanged. The largest difference is in the initial-final mass relation. Because a star of mass M is supposed to evolve like a star of mass f_{os} M without overshooting, the final mass of a star will be higher than the final mass of the same star without overshooting. Stothers (1991) showed that all tests for the presence of convective overshooting are consistent with d/H_p = 0, and that the best tests place an upperlimit of d/H_p < 0.2. Convective overshooting will not affect the conclusions of this paper.

4 Discussion and conclusions

In Fig. 11 the M-, S- and C-star LF is plotted for the best model of the LMC. The parameters are M_c^{min} = 0.58 $M_\odot$, λ = 0.75, $\eta_{AGB} = \eta_{EAGB}$ = 5, η_{RGB} = 0.86, HBB included. We find that M, S and C stars occur in the ratio 0.501 : 0.077 : 0.422. The predicted (solid) and observed (dotted) carbon star LF agree very well. The predicted C/M ratio (0.85) lies within the observed range (0.6-2.5).

The chemical nature of AGB stars is based upon the C/O abundance ratio. We have assumed that the transition from M to S star occurs at C/O = 0.81 and from S to C star at C/O = 1.0. In particular the former value is uncertain. To illustrate this uncertainty we recalculated the LF for the final LMC model assuming that the M to S star transition occurs at C/O = 0.90. We find slightly different ratios of M, S and C stars, 0.539 : 0.039 : 0.422. The LF are virtually unchanged. The C/M ratio drops to 0.78, while the S/C ratio drops from 0.18 to 0.093. We conclude that the average lifetime of the S star phase approximately scales like $\sim (1 - \delta)$, where δ is the assumed C/O ratio of the M to S transition.

We can not distinguish between models with a high λ and a standard value of the carbon abundance after a TP (X_{12} = 0.22) or vice versa. All models with $\lambda X_{12} = 0.165$ fit the observations. Although a model with a higher X_{12} results in less helium being dredged up, and a model with higher λ results in lower final masses, these effects are too small to be used to determine if λ or X_{12} are different from the standard values (λ = 1/3, X_{12} = 0.22; $\lambda X_{12} = 0.073$).

The minimum core mass for dredge-up is lower and the dredge-up efficiency is higher than found in published evolutionary calculations ($M_c^{min} \gtrsim 0.60$ $M_\odot$, $\lambda \approx 1/3$). However these models do not predict carbon stars at the observed low luminosities. Only the model of BS4, when they arbitrarily increased the mixing-length parameter from 1 to 3, predicts the low luminosity carbon stars observed. Recently, Sackmann et al. (1990) and Sackmann & Boothroyd (1991) showed that with their code and for certain opacities (LAOL including molecular opacities) a mixing-length of α = 2.1 was required to obtain a standard solar model and to explain the observed position of the red giant branch. The value they used in their earlier AGB calculations was α = 1.0. Because an increase in the mixing-length parameter reduces the luminosity at which dredge-up begins, it is not surprising that the old BS models did not predict carbon stars at the observed low luminosities. We suggest that a systematic underestimate of the mixing-length parameter is the reason that evolutionary calculations could not produce carbon stars at the observed low luminosities.

Taking the SFR, IMF ($\alpha = -2.55$) and age-metallicity relation for the solar neighbourhood from a recent model (van den Hoek & de Jong 1992) and assuming that the AGB evolution parameters adopted for our final LMC model hold for the solar neighbourhood, the LF in Fig. 11 was calculated for the Galaxy. The shape of the carbon star LF is only slightly different from that in the LMC. This supports the assumption usually made by (e.g. Groenewegen et al. 1992) that

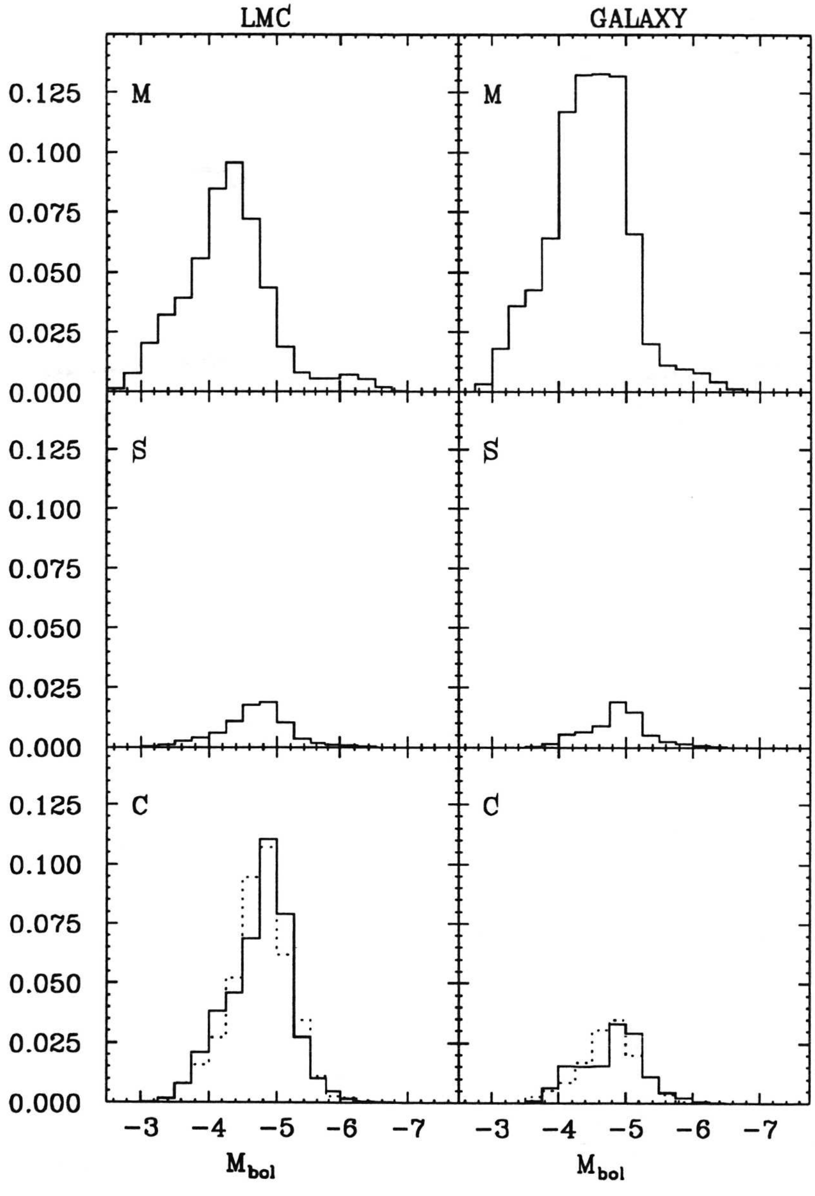

Figure 11: The normalised luminosity function of M-, S- and C-stars for the final LMC model with parameters $M_c^{min} = 0.58\ M_\odot$, $\lambda = 0.75$, $\eta_{AGB} = \eta_{EAGB} = 5$, HBB included. For the same set of parameters a Galactic model was calculated using the appropriate SFR, IMF and age-metallicity relation of Van den Hoek & de Jong (1992). The dotted curve is the observed LMC carbon star LF of Fig. 5.

the mean luminosity of Galactic carbon stars is about equal to LMC carbon stars. Compared to the LMC the C/M ratio is reduced from 0.85 to 0.17. The peak of the oxygen-rich AGB stars is increased from ~4400 $L_\odot$ in the LMC to ~5500 $L_\odot$ in the Galaxy.
In Fig. 12 the initial-final mass relation is presented for the LMC (crosses) and the Galac-

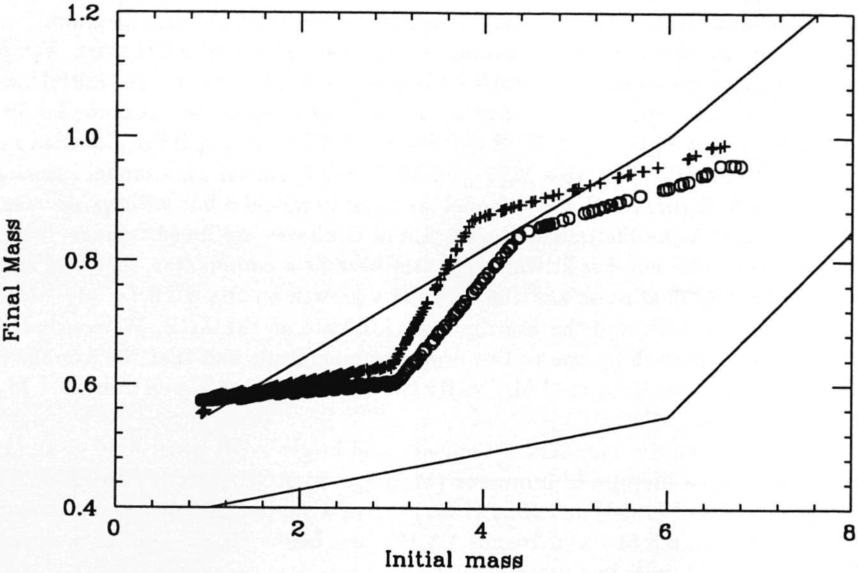

Figure 12: The initial-final mass relation for the LMC (crosses) and the Galactic model (circles). The two solid lines indicate the minimum and maximum final mass allowed for by the observations of white dwarfs in the solar neighbourhood.

tic model (circles) and compared to the observations. The observational data was taken from Weidemann & Koester (1983) and references therein and supplemented with new results from Koester & Weidemann (1985) and Reimers & Koester (1988, 1989). Instead of plotting individual points with their errors the two solid lines in Fig. 12 give the maximum and minimum final mass allowed for by the data for a given initial mass. In general there is good agreement for the low mass stars. For the Galactic model the final masses for the massive stars are in agreement with the observations. The discrepancy for the LMC model is probably not significant since the observations refer to WD in the solar neighbourhood and therefore should be compared to the solar neighbourhood model.

With our mass loss rates the difference between the final core mass and the core mass at the first TP is $\lesssim$0.03 $M_\odot$ (see Table 5). This means that the initial-final mass relation strongly reflects the initial-core mass at the first TP-relation (Eq. 1 and 4) which changes in slope near 3 $M_\odot$ (see Fig. 1). Figure 12 shows that it is difficult to obtain good agreement for the high mass stars. This is probably due to the fact that our algorithms for high mass stars are fitted to evolutionary calculations which neglected mass loss. This probably resulted in an overestimate of the core mass at the first TP.

We calculated the average final mass of the stars at the end of the AGB for the best model for the LMC and compared this to the average mass of the central stars of planetary nebulae. The mean value (M_f = 0.62 $M_\odot$) agrees well with the observed value of 0.60 $\pm$ 0.02 $M_\odot$ (Barlow 1989, Dopita & Meatheringham 1990, 1991, Clegg 1991). No selection effects are included in the theoretically predicted distribution. For example, the probability of observing a PN on the horizontal evolution track through the HR diagram is much higher for a low mass PN. On the other hand, some post-AGB objects of very low core mass (M_c $\lesssim$0.56 $M_\odot$) may evolve so slowly that they never become a PN, or are not recognised as such. This depends on the uncertain post-AGB mass loss rate, which determines the crossing time through the HR diagram.

We have so far concentrated on the global evolution of a distribution of AGB stars. For some combination of input parameters we have calculated the AGB evolution for selected initial masses. Some relevant quantities are collected in Table 5. We have considered the final model for the LMC ($\eta_{\rm RGB}$ = 0.86, $\eta_{\rm AGB}$ = $\eta_{\rm EAGB}$ = 5, $M_c^{\rm min}$ = 0.58, λ = 0.75, including HBB), labelled model 1, a model identical to model 1 but with $M_c^{\rm min}$ = 0.59, λ = 0.7 (model 2), a model identical to model 1 but with Z = 0.02 (model 3) and a model identical to model 3 but with $\eta_{\rm AGB}$ = $\eta_{\rm EAGB}$ = 7 (model 4). In Table 5 the lifetime of the M, S and C phases are listed together with the total AGB lifetime, the pulse number at which the star became a carbon star, the total number of pulses on the AGB, the final mass and the core mass growth on the AGB (= $M_f - M_c(1)$), the total mass lost on the AGB and the average mass loss rate on the AGB. We conclude that mass loss dominates core growth by one to two orders of magnitude and that the average mass loss rate on the AGB increases from 10^{-6} $M_\odot$/yr for the low mass stars to well over 10^{-5} $M_\odot$/yr for the most massive stars.

Based upon the observed relative numbers of Cepheids and bright AGB stars, Reid et al. (1990) concluded that the average lifetime of luminous ($M_{\rm bol} < -6$) AGB stars is "no more than 2 10^5 years". Hughes & Wood (1990) and Iben (1991) derive a similar lifetime. Our calculations confirm this. In our model, a 5 $M_\odot$ star spends 1.3 10^5 year below $M_{\rm bol} = -6$. This agreement supports our derived (high) mass loss rates.

Blanco & McCarthy (1983) have estimated the number of carbon stars in the LMC. They derived a number of ≈11000 over an area of ≈100 deg^2. The area they considered includes the outskirts of the LMC, and is much larger than that considered by others. Because we want to compare the number of AGB stars with the LPV census of Hughes (1989) in a future paper, we estimated the number of carbon stars in the area surveyed by Hughes for LPV (~55 deg^2), based on the isopleths of Blanco & McCarthy. This area includes all carbon stars within the 75 deg^{-2} isopleth (~ 7000 carbon stars) plus a large area within the 25 deg^{-2} isopleth. The total number of carbon stars within the area surveyed by Hughes for LPV is estimated to be 8250 ± 250. In Sect. 3 we estimated that 10% of all carbon stars are low-luminosity J-type stars which may not be on the AGB, but possibly related to the R-type carbon stars observed in the Galaxy. The number of carbon stars on the AGB is estimated to be 7500 ± 500. From Table 5 we find an average carbon star lifetime of (2.0 ± 0.5) 10^5 yr. We conclude that the birth rate of carbon stars on the AGB in the LMC equals $\frac{dN}{dt} \approx \frac{N}{T} = 0.038 \pm 0.010$ yr^{-1}.

For the oxygen-rich AGB stars a similar estimate can be made. The observed C/M ratio is between 0.4 and 2 depending on the spectral type included in counting M-stars (Blanco & McCarthy 1983). Assuming our model result of C/M = 0.85 with an error of 0.2 (based on a possibly spread of 0.02 in $M_c^{\rm min}$) we derive a number of 6700-12300 oxygen-rich AGB stars. With a mean lifetime of (1.6 ± 0.3) 10^5 yr (Table 5), we derive a birth rate of 0.058 yr^{-1} within a factor of 1.6 (i.e. 0.035 - 0.095 yr^{-1}).

An independent estimate can be made by realising that the carbon star birth rate equals the AGB death rate in the range ~ 1.2– ~ 3.5 $M_\odot$. Based on the adopted IMF and SFR we derive that the number of stars in the ~ 1.2– ~ 3.5 $M_\odot$ range is between 40 and 60% of all stars in the range ~ 0.93– ~ 8 $M_\odot$, depending on the exact values of the mass limits. Therefore we derive a birth rate of AGB stars of 0.076 yr^{-1} within a factor of 1.6 (i.e. 0.047 - 0.122 yr^{-1}). A birth rate of AGB stars of 0.07 ± 0.02 yr^{-1} is consistent with both estimates.

Payne-Gaposhkin (1971) identified 1111 Cepheids in a 55 deg^2 area in the LMC. This survey is incomplete, possibly upto a factor of 4 (Wright & Hodge 1971). Becker et al. (1977) derived a number of 2000 Cepheids. Assuming the LMC contains 2000 Cepheids within a factor of 2 and a mean lifetime of the Cepheid phase of 2-5 10^5 yr (Becker et al. 1977) we derive a birth rate of

Table 5: Results for some models

M	Model	Z	TM	TS	TC	TAGB	NC	N	MF	ΔM_c	ΔM_{AGB}	$\dot{M}_{AGB}$
0.93	1	0.0020	231	-	-	231	-	2	0.553	0.008	0.156	6.8 (−7)
1.00	1	0.0037	160	-	-	160	-	2	0.577	0.008	0.193	1.2 (−6)
1.16	1	0.0058	142	-	83	225	3	3	0.583	0.009	0.355	1.6 (−6)
1.20	1	0.0062	138	-	103	241	4	4	0.585	0.009	0.396	1.6 (−6)
1.50	1	0.0076	124	88	157	369	4	5	0.589	0.010	0.719	2.0 (−6)
2.50	1	0.0084	329	84	467	881	7	12	0.617	0.022	1.740	2.0 (−6)
3.00	1	0.0086	302	160	603	1065	8	16	0.627	0.025	2.093	2.0 (−6)
5.00	1	0.0087	152	3.3	14.8	170	47	51	0.918	0.016	2.228	1.3 (−5)
1.30	2	0.0068	288	-	-	288	-	4	0.592	0.016	0.498	1.7 (−6)
1.40	2	0.0072	299	-	28	327	5	5	0.594	0.016	0.605	1.9 (−6)
1.50	2	0.0076	206	88	68	362	5	5	0.595	0.016	0.713	2.0 (−6)
2.00	3	0.02	510	-	46	556	8	8	0.588	0.026	1.255	2.2 (−6)
2.50	3	0.02	602	89	162	853	10	11	0.597	0.035	1.752	2.0 (−6)
3.00	3	0.02	780	86	260	1126	12	15	0.599	0.037	2.121	1.9 (−6)
2.00	4	0.02	417	-	9.9	427	7	7	0.582	0.020	1.236	2.9 (−6)
2.50	4	0.02	602	-	44.2	646	9	9	0.589	0.027	1.703	2.6 (−6)
3.00	4	0.02	693	87	38.7	819	11	11	0.593	0.031	2.015	2.5 (−6)

Notes. Listed are the initial mass ($M_\odot$), the model number, the metallicity Z, the lifetime of the M, S, C and the total AGB phase in 10^3 years, the pulse number at which a star became a carbon star, the total number of pulses on the AGB, the final mass, the core growth on the AGB, the total mass lost on the AGB (all in $M_\odot$) and the average mass loss rate on the AGB (in $M_\odot$/yr).
Model 1: The final LMC model with $M_c^{min} = 0.58$ $M_\odot$, $\lambda = 0.75$, $\eta_{AGB} = \eta_{EAGB} = 5$ including HBB.
Model 2: As model 1 with $M_c^{min} = 0.59$ $M_\odot$, $\lambda = 0.70$.
Model 3: As model 1 but with Z = 0.02
Model 4: As model 3 and with $\eta_{AGB} = \eta_{EAGB} = 7$.

3-5 $M_\odot$ stars of 6.3 10^{-3} yr^{-1}. From the adopted IMF and SFR it is deduced that the number of stars in the range 0.93-8 $M_\odot$ to the number of 3-5 $M_\odot$ stars is between 12 and 22 depending on the exact value of the mass limits. Based on the number of Cepheids we estimate a birth rate of AGB stars of 0.10 yr^{-1} uncertain to a factor of 2.2 (i.e. 0.045 - 0.22 yr^{-1}).
Hardy et al. (1984) identified 2100 $\pm$ 210 clump stars in a 6' by 12' region in the NW part of the bar in the LMC. From Lattanzio (1991) we find a mean lifetime of (1.5 $\pm$ 0.5) 10^8 yr for the clump phase. Boldly extrapolating to the whole LMC (55 $\pm$ 5 deg^2) we estimate an evolution rate of clump stars of 0.11 $\pm$ 0.04 yr^{-1}.
Jacoby (1980) estimated the total number of PNe in the LMC to be 996 $\pm$ 253. A number of possible PNe included in Jacoby's calculation were subsequently shown not to be PNe (Boroson & Liebert 1989). Repeating Jacoby's analysis taking these new results into account (in particular $N_J = 25$, $f_1 = 2.19$ in Jacoby's formula) gives an improved number of 838 $\pm$ 212 PNe in the LMC. Using a mean lifetime of 2-5 10^4 yr results in a birth rate of PNe of 0.026 yr^{-1} uncertain to a factor of 2 (i.e. 0.013 - 0.052 yr^{-1}).
We conclude that the calculated lifetimes of AGB stars from our standard model, in combination with the observed number of carbon and oxygen-rich stars gives a birth rate of 0.07 $\pm$ 0.02 yr^{-1},

which is in good agreement with the AGB evolution rates estimated from the number of clump stars (0.11 ± 0.04 yr^{-1}) and Cepheids (0.10 yr^{-1} within a factor of 2.2). The estimated birth rate of PNe (0.026 yr^{-1} within a factor of 2) is well below this value which suggests that a fairly large number of low-mass stars ($M_{\rm initial} \lesssim 1.1$ $M_\odot$) either do not become PN (evolution probably too slow) or have simply not been detected yet.

Our model predicts that in the LMC stars more massive than 1.2 $M_\odot$ will pass through a carbon star phase and stars more massive than 1.5 $M_\odot$ pass through a S-star phase. If the transition from M to S star occurs at C/O = 0.90 instead of 0.81 the latter value would be ~1.7 $M_\odot$. These numbers depend on the minimum core mass for dredge-up and the dredge-up efficiency. For $M_c^{\rm min} = 0.59$ $M_\odot$ and $\lambda = 0.7$ only stars >1.4 $M_\odot$ pass trough the carbon star phase. We have compared our results with the observations of AGB stars in LMC clusters (Frogel et al. 1990, Westerlund et al. 1991a). They report that S-stars are observed in LMC clusters of SWB (Searle, Wilkinson & Bagnuolo 1980) type IV and V but not in type VI and VII. Carbon stars are predominately observed in clusters of type IV, V and VI with very few in type I - III. There is no known LMC cluster of type VII containing a carbon star. The oldest LMC clusters containing carbon stars (N1978, N2173) have ages between 2-3 Gyr (Sagar & Pandey 1989). Interpolating in the models of Sweigart et al. (1989) and Lattanzio (1991) this corresponds to stars that are on the AGB of initial mass between 1.3 and 1.6 $M_\odot$. This is in good agreement with our prediction. Our result that stars need to be somewhat more massive to go through a S-star phase is consistent with the fact that they are observed in clusters of earlier SWB type. The fact that there are few or no C and S stars in young clusters of SWB type I-III, corresponding to initial masses $\gtrsim 4$ $M_\odot$, is also in agreement with our predictions.

In comparing the solar metallicity models 3 and 4 with the LMC model 1, we note that the minimum mass for carbon star formation is raised to ≈ 2 $M_\odot$. For every initial mass the duration of the carbon star phase is shorter for the Z = 0.02 models than for the corresponding LMC models. This is of cource consistent with the fact the C/M ratio in the Galaxy is lower than in the LMC.

From a comparison of model 3 and 4 we stress the importance of the mass loss rate on the AGB in determining the lifetimes of AGB stars in general and the carbon stars in particular. For model 4, which may be indicative for the solar neighbourhood, we see that stars become carbon stars at the last TP on the AGB and that the carbon star phase last a few times 10^4 years. This number is in surprisingly good agreement with the lifetime estimate of the carbon star phase in the solar neighbourhood made by Groenewegen et al. (1992).

Acknowledgements. It is a pleasure to thank Bobby van den Hoek and Sander Slijkhuis for stimulating discussions and a critical reading of earlier versions of this paper.

Appendix A: Hot Bottom Burning

Hot Bottom Burning (HBB) has been described in detail by Sugimoto (1971), Uus (1973), Iben (1973), Scalo et al. (1975), RV and Sackmann & Boothroyd (1991). These authors do not agree on the exact extent of HBB. This is due to uncertainties in the temperature at the base of the convective envelope, T_B, which is quite sensitive to the core and total mass and to the mixing-length. In light of these uncertainties we restricted ourselves to a simple model for HBB, which reproduces the results of RV fairly well.

In order to make headway we have only considered the $\alpha = 2$ case of RV for three reasons. Firstly, RV gives information on T_B only for this case. Secondly, a mixing-length parameter of

2 seems more appropriate than the other values considered by RV (see e.g. Maeder & Meynet 1989) and thirdly, it will enable us to study the maximum effect of HBB on the results.

In our simple model to describe HBB four parameters are needed: (1) the (average) temperature at the base of the convective envelope, T_B, as a function of core and total mass, (2) the fraction (f_{HBB}) of newly dredged up matter exposed to the high temperatures at the bottom of the envelope, (3) the amount of matter in the envelope, relative to the total envelope mass, which is mixed down and processes at the bottom of the envelope (f_{bur}) and (4) the (average) exposure time, t_{HBB}, of matter in the zone of HBB.

The temperature at the base of the convective envelope is an important quantity since only for $T_B \gtrsim 30\ 10^6$ K significant HBB occurs (RV). When $T_B \lesssim 30\ 10^6$ K the lifetime of the species involved in the CNO-cycle against proton capture are too long.

The value of T_B, appropriate for the $\alpha = 2$ case of RV was derived from Figs. 4, 5, 6 of RV, where they list the values of T_B at different luminosities for different masses. Transforming the luminosities into core masses using the core mass-luminosity relation of RV, we have approximated T_B as a function of total and core mass. We find (temperatures in 10^6 K):

$$T_B = T_B^0 + 127.6\,(M_c - 0.8) \tag{A1}$$

where the zeropoint is initial mass dependent:

$$T_B^0 = -25.45 + 16.41\ M_{initial} \tag{A2}$$

Iben (1976) quotes $T_B = 44 + 100\ (M_c - 0.8)$ for a $M = 7\ M_\odot$ model derived with $\alpha_{\rm Iben} = 0.7$. The slopes of the two relations compare fairly well and the difference in the zeropoint is due to the difference in the mixing-length parameter.

Equation (A1) is valid until the envelope mass is reduced below a critical value, after which T_B drops significantly below the value given by Eq. (A1). The critical envelope mass is denoted by M_{env}^{HBB}.

Another important quantity is the total effective exposure time of matter to the high temperatures (t_{HBB}). If t_{ip} is the interpulse period and if a hump of matter spends a time t_1 in the HBB-zone due to the convective motion, and a time t_2 in the cooler outer parts of the envelope, this hump of matter will be mixed approximately $\frac{t_{ip}}{t_1+t_2}$ times through the HBB-zone during an interpulse period. Therefore the total time a hump of matter is exposed to the high temperatures during the interpulse period is roughly given by $t_{HBB} = \frac{t_1}{t_1+t_2}\ t_{ip}$. We have not made an effort to try to determine t_1 and t_2 from first principle, but rather determined the ratio $f = \frac{t_1}{t_1+t_2}$ by fitting our model to the results of RV. Since the region of high temperatures is small compared to the extent of the total envelope only $f \ll 1$ would be a physical meaningful result.

The fraction, f_{HBB}, of newly dredged-up material processed by HBB is expected to be close to 1. Since, the dredged-up material is forced through the bottom of the convective envelope, only a small fraction can escape HBB, trough the help of convective motion.

We implemented the algorithms used by RV and compared our model results with those of the RV model $\alpha = 2$ case ($Z = 0.02$, $Y = 0.28$, $\eta = 1/3$, case A) to determine the values of t_{HBB}, f_{HBB} and f_{bur}. We constructed a grid in these parameters and after some experimenting we found good results for combinations of parameters in the range: $0.0010\ t_{ip} \leq t_{HBB} \leq 0.0020\ t_{ip}$, $0.93 \leq f_{HBB} \leq 0.95$ and $2\ 10^{-4} \leq f_{bur} \leq 3\ 10^{-4}$. By comparing both lifetimes and yields, the most suitable parameters for the $\alpha = 2$ model of RV are: $t_{HBB} = 0.0014\ t_{ip}$, $f_{HBB} = 0.94$, $f_{bur} = 3\ 10^{-4}$. By comparing our model to the 'case B' model of RV we found that $M_{env}^{HBB} = 0.85\ M_{pn}$[2], gives very good results, except for $M = 3.3\ M_\odot$.

[2]The value of M_{pn} is given by RV's Eq. (33).

We are left with a discussion on the method to calculate the time evolution of the species involved in the CNO-cycle. We used the method presented in Clayton (1968). The basic assumption in his method is that the two reaction chains of the CNO-cycle, the CN-cycle,

$$^{12}C(p,\gamma)^{13}N(e^+,\nu)^{13}C(p,\gamma)^{14}N(p,\gamma)^{15}O(e^+,\nu)^{15}N(p,\alpha)^{12}C \tag{A3}$$

and the ON-cycle,

$$^{15}N(p,\gamma)^{16}O(p,\gamma)^{17}F(e^+,\nu)^{17}O(p,\alpha)^{14}N \tag{A4}$$

can be separated. This is due to the fact that the ^{15}N(p,γ) reaction occurs about once every 2800 ^{15}N(p,α) reactions.

After some simplifications (see Clayton) the evolution of the CN and ON-cycle is reduced to an eigenvalue problem in the (^{12}C, ^{13}C, ^{14}N) and (^{14}N, ^{16}O, ^{17}O) abundances respectively. The eigenvectors depend on the initial values of the abundances and the eigenvalues depend on the lifetimes of the species against proton captures. We used the reaction rates of Fowler et al. (1975) to calculate the reaction rates.

We verified the method of Clayton by comparing the results to the exact time dependent calculations of Caughlan (1965), using identical initial conditions and nuclear lifetimes. The differences in the abundances are less than 1%, which is similar to the accuracy claimed by Clayton.

In our model we do not need the abundances at a specific time but rather the averaged abundance $\frac{1}{t}\int_0^t X(t)dt$, see Eqs. (35) and (36). In the method of Clayton the evolution of a species X is of the simple form $X(t) = \sum_{i=1}^{3} U_i e^{\lambda_i t}$, so the average abundance can be calculated analytically.

Appendix B: AGB lifetimes

The distribution of stars on the AGB (Eq. 37) depends on the lifetime of stars on the AGB, t_{AGB}. We expect the AGB lifetimes to depend primarily on the mass loss rate on the AGB. We calculated t_{AGB} for a sequence of stars with η_{AGB} = 1, 5, 10 (solid, long dashed, dot-dashed in Fig. B1 respectively). For a given initial mass, the pre-AGB lifetimes of Iben & Laughlin (1989) were used to derive its age, and the age-metallicity relation of the LMC of van den Hoek & de Jong (1992) to derive Z. The helium abundance was calculated from Eq. (24). For other relevant parameters we used our standard model. The results are displayed in Fig. B1, where we normalised t_{AGB} to its value of the 3 $M_\odot$ model.

The shape of the t_{AGB} function is rather peculiar and deserves some further attention. It could be expected that t_{AGB} is an increasing function of initial mass, simply because there is more envelope mass available. Evidently this is not true. First of all, for stars of high enough mass, the AGB is terminated when the core mass reaches the Chandrasekhar mass. Therefore, the lifetime is determined by the time the core mass grows from $M_c(1)$ to M_{Ch}. This is (almost) independent of envelope mass and therefore constant (in absolute terms). Because the lifetime of the reference 3 $M_\odot$ model decreases with increasing η_{AGB}, the high mass points for η_{AGB} = 5 and 10 lie above the η_{AGB} = 1 curve. The value of η_{AGB} does determine however which stars live long enough to reach the Chandrasekhar mass. The transition from stars that end as white dwarfs and those who end as supernova is reflected in the peaks in the η_{AGB} = 1 (at M = 4.5 $M_\odot$) and η_{AGB} = 5 (at M = 7.5 $M_\odot$) curves.

For stars below 2 $M_\odot$, the mass loss on the RGB becomes increasingly important in determining the AGB lifetimes. For decreasing mass this means less envelope mass and lower lifetimes. For the lowest mass stars the lifetime increases suddenly. This is a metallicity effect as demonstrated in Fig. B1 where we plotted the results for η_{AGB} = 5 for a set of models following the age-metallicity relation (long dashed curve) and for a constant metallicity (short dashed). Down to

M $\approx$ 1.5 $M_\odot$ the two curves are identical. For stars below $\sim$1 $M_\odot$ the metallicity drops very fast with decreasing initial mass due to the age-metallicity relation. The mass loss on the RGB increases with decreasing mass but also decreases with decreasing metallicity (see Table 2). For the lowest mass stars the metallicity effect compensates the mass effect. There is (relative) more envelope mass available and the lifetime increases. When the calculations are extended to even lower initial masses, the AGB lifetimes increase a bit further and then drop to 0, for the star which has lost so much mass on the RGB that $M_{env} = 0$ at the start of the AGB.
From Fig. B1 we see that for stars with M $\lesssim$4 $M_\odot$ the influence of η_{AGB} on the relative AGB lifetimes is negligible and even for high mass stars the effect is small. Because some preliminary calculations indicated that $\eta_{AGB} > 1$ was needed to fit the observed carbon star LF in the LMC the following approximation to the curves in Fig. B1 was used:

$$\begin{array}{rcll} t_{AGB}(M)/t_{AGB}(3) & = & -2.061M + 2.197 & 0.93 < M < 1 \\ & = & 0.336M - 0.199 & 1 < M < 2 \\ & = & 0.528M - 0.584 & 2 < M < 3 \\ & = & -0.937M + 3.812 & 3 < M < 3.56 \\ & = & 0.48 & 3.56 < M < 8.2 \end{array}$$

This approximation is used in all calculations reported in this paper.

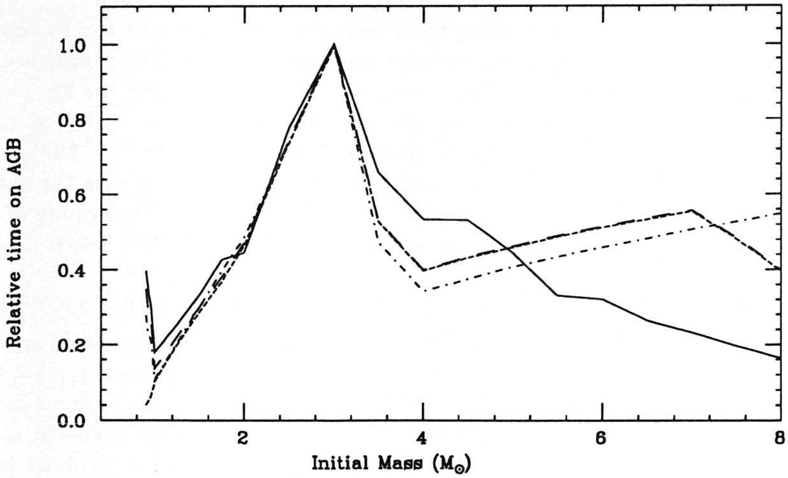

Figure B1: The relative lifetimes of stars on the AGB, for a mass loss parameter $\eta_{AGB} = 1$ (solid), 5 (long dashed), 10 (dotted). The upturn at the lowest masses is a metallicity effect. The shape of the curve at the highest masses is determined by the time to reach the Chandrasekhar mass. The short-dashed curve represents $\eta_{AGB} = 5$ with constant metallicity. Details are given in the text.

Appendix C: Obscuration of AGB stars

The carbon star LF (Fig. 5) which is used in this study is derived from optical surveys which are complete down to I $\approx$ 17. It is obvious that a star in the LMC which is losing mass at a considerable rate and is surrounded by a dust shell, could, in principle be weaker than I = 17. On the other hand, such a star may be detected by IRAS at 12 μm.

In this appendix we derive an upperlimit to the number of carbon stars missed by the optical surveys and show that it is possible that a carbon star which is fainter than I = 17 would *not* be detected by IRAS. We further discuss at which mass loss rate a star would become fainter than I = 17 in the LMC.
Would all carbon stars that are fainter than I = 17 be detected by IRAS? To answer this question some radiative transfer calculations were performed. The standard model was a star of T_{eff} = 3000 K, L = 20 000 $L_\odot$ ($M_{bol} \approx -6$) at a distance of 50.2 kpc surrounded by a dust shell. The shape of the spectrum is determined by the optical depth as a function of wavelength:

$$\tau_\lambda \sim \frac{\dot{M}\ \Psi\ Q_\lambda/a}{R_*\ r_{in}\ v_\infty\ \rho} \tag{C1}$$

where $\dot{M}$ is the mass loss rate,Ψ the dust-to-gas ratio, Q_λ the extinction coefficient, a the grain radius, R_* the stellar radius is solar units, r_{in} the inner radius of the dust shell in stellar radii, v_∞ the expansion velocity and ρ the grain density. Equation (C1) assumes a $1/r^2$ density law. The standard values are Ψ = 0.003, v_∞ = 15 km s^{-1}, ρ = 3.3 gr cm^{-3}. The inner radius is calculated selfconsistently by assuming a temperature at the inner radius (T_c) of 1500 K. For the grains we assume AC amorphous carbon (Bussoletti et al. 1987) with Q_λ/a = 213000 cm^{-1} at 0.8 μm[3]. We did not consider silicon carbide because it has become clear that this is a trace species ($\lesssim$10%) in the dust shells of Galactic carbon stars relative to amorphous carbon. In the LMC with its lower metallicity there should be even less silicon to form SiC.
We ran a series of models with increasing mass loss rate and calculated the I-magnitude and the IRAS flux at 12 μm (folded with the detector response of IRAS). The results are plotted in Fig. C1. Indicated are the curves for $M_{bol} = -4, -5, -6$ and -7. Along the $M_{bol} = -4$ curve the optical depth at 0.8 μm is indicated for the L = 20 000 $L_\odot$, T_{eff} = 3000 K model. For the standard parameters this corresponds to mass loss rates of 0, 2 10^{-7}, 5 10^{-7}, 1 10^{-6}, 1.5 10^{-6} and 3 10^{-6} $M_\odot$/yr. The mass loss rate does not scale exactly linear with the optical depth because of radiative transfer effects. For higher mass loss rates the backwarming of the grains becomes important so the assumed condensation temperature of 1500 K is reached at a greater distance.
For any point in the diagram the mass loss scales with $\sqrt{L/20\,000}/(T_{eff}/3000)^2$ due to the dependence of the optical depth on the stellar radius and approximately like $(T_{eff}/T_c)^{\frac{4+p}{2}}$ due to the dependence of the optical depth on the inner radius. The parameter p gives the overall wavelength dependence of the grains, $Q_\lambda \sim \lambda^{-p}$, and equals $\sim$1 for amorphous carbon. For example, from Fig. C1 we derive that a star of $M_{bol} = -4$ becomes invisible at I at $\tau \approx$ 3.3. If we assume a stellar temperature of 3500 K this corresponds to a mass loss rate of $\frac{3.3}{3.7}$ 1.0 10^{-6} $\sqrt{(3080/20\,000)\,(3500/3000)}$ = 3.7 10^{-7} $M_\odot$/yr.
Important to the synthetic evolution models is to know the mass loss rate at which a carbon star becomes optically invisible. We expect the flux in the optical to vary like:

$$\frac{c\ L}{4\ \pi\ D^2}\ e^{-\tau}\ =\ f_{lim}$$

where c is some constant, L the total luminosity, D the distance, τ the optical depth and f_{lim} the flux. This can be recast into:

$$M_{bol}\ =\ a\ -\ b\,\tau$$

[3]Actually we multiplied the value of Q_λ/a given by Bussoluetti et al. by a factor of 5 to let their results agree with those of Koike et al. 1980.

We have made a fit using the results of our radiative transfer models and found that a carbon star in the LMC becomes fainter than I = 17 at a mass loss rate:

$$\dot{M} \;=\; F_{IR}\,\frac{-1.49 - M_{bol}}{2.79\;10^6}\,\sqrt{L/20\;000}\,\sqrt{T_{eff}/3000} \tag{C2}$$

The change in the critical mass lose rate due to the luminosity effect alone is a factor of 4.6 going from $M_{bol} = -4$ to -6. The scale factor F_{IR} includes the uncertainties in v_∞, ρ, Q_λ/a, r_{in} and particularly the dust-to-gas ratio Ψ, which is poorly known in the LMC. Assuming a dust-to-gas ratio in the LMC between 1/700 and 1/1500 (Schwering 1988), terminal velocities which can be up to a factor of 3 lower than in the Galaxy (Wood 1987) and random errors in ρ, r_{in} and Q_λ/a of factors of 2, 2 and 5 respectively, an observational constraint of $0.04 < F_{IR} < 100$ can be set. Similar radiative transfer calculations were made for oxygen-rich stars. Astronomical silicate (Draine & Lee 1984 and unpublished work) was used with $Q_\lambda/a = 13230$ cm^{-1} at 9.5 μm, p = 2 and a condensation temperature of T_c = 1000 K. For the terminal velocity, the dust-to-gas ratio and the grain density the same values as for the carbon stars were used. We find that an oxygen-rich star becomes fainter than I = 17 in the LMC at a mass loss rate:

$$\dot{M} \;=\; F_{IR}\,\frac{-1.73 - M_{bol}}{2.19\;10^4}\,\sqrt{L/20\;000}\;\,(T_{eff}/3000) \tag{C3}$$

In the synthetic evolution models, Eq. (C2) was used for the carbon and S-stars and Eq. (C3) for the M-stars to determine at each timestep if a star was visible or obscured. The factor F_{IR} in Eqs. (C2) and (C3) were assumed to be equal.

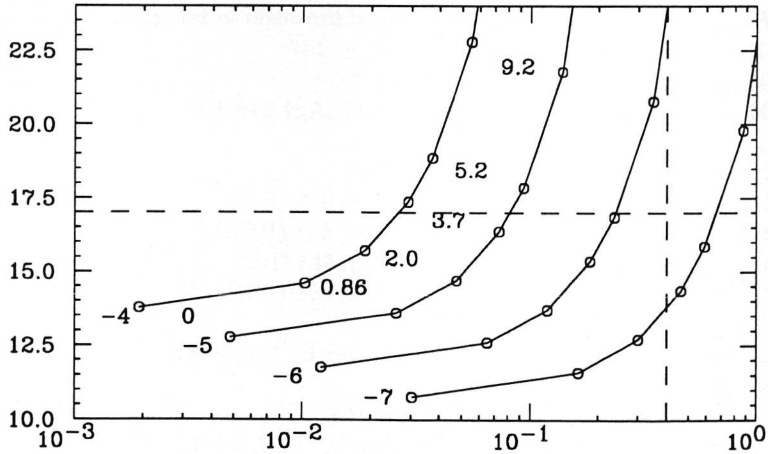

Figure C1: The I magnitude and IRAS 12 μm flux for stars in the LMC surrounded by a carbon-rich dust shell. Indicated are the curves for $M_{bol} = -4, -5, -6, -7$ and various optical depths at 0.8 μm. Numerical details are given in the text. From this diagram we conclude that it is possible that optically invisible carbon stars (I > 17) are not detected by IRAS (S_{12} < 0.4 Jy).

Reid et al. (1990) combined IRAS data (down to S_{12} = 0.1 Jy) with V and I plates of a 9.3 deg^2 area in the LMC. Out of a total of 156 IRAS detections 63 had the characteristics of a stellar photosphere or a circumstellar shell. After removing 17 foreground objects and 17 LMC

supergiants they were left with 13 AGB candidates and 16 IRAS sources with no obvious optical counterpart. The 13 AGB candidates have $11.1 < I < 15.7$ and therefore would have been found by the optical surveys. There remain 1.7 deg^{-2} sources with $S_{12} > 0.1$ Jy and $I > 17$.
The IRAS survey was essentially complete down to $S_{12} = 0.4$ Jy at 12 μm (*Explanatory Supplement* 1986, Chapter VIII). Of the 16 unidentified sources only 2 have $S_{12} > 0.4$ Jy ($\sim$0.2 deg^{-2}). From Fig. C1 we derive that IRAS could have missed obscured carbon stars with $S_{12} > 0.4$ Jy when $M_{bol} \gtrsim -6$. There are $\sim$7 deg^{-2} optical carbon stars brighter than $M_{bol} = -6$. If we assume that the unidentified sources are all carbon stars and all are brighter than $M_{bol} = -6$ we derive an upperlimit of $\sim$3% obscured carbon stars brighter than $M_{bol} = -6$.
In Sect. 3.3 where the influence of the mass loss rate and obscuration is investigated we proceeded in the following way. For a given mass loss rate η_{AGB}, Eqs. (C2) and (C3) were applied with the scale factor F_{IR} varied in such a way that 3% of the carbon stars brighter than $M_{bol} = -6$ were obscured. The model then provides information on the degree of obscuration at other luminosities.

References

Anders E., Grevesse N., 1989, Geochim. Cosmochim. Acta 53, 197

Barbuy B., Milone A., Spite M., Spite F., 1991, in: The Magellanic Clouds, eds. R. Hayes, D. Milne, Reidel Dordrecht, p. 370

Barlow M.J., 1989, in: Planetary Nebulae, ed. S. Torres-Peimbert, Kluwer, Dordrecht, p. 319

Becker S.A., Iben I., 1979, ApJ 232, 831 (BI1)

Becker S.A., Iben I., 1980, ApJ 237, 111 (BI2)

Becker S.A., Iben I., Tuggle R.S., 1977, ApJ 218, 633

Bedijn P., 1988, A&A 205, 105

Blanco V.M., McCarthy M.F., 1981, in: Physical processes in red giant stars, eds. I. Iben, A. Renzini, Kluwer, Dordrecht, p. 147

Blanco V.M., McCarthy M.F., 1983, AJ 88, 1442

Blanco V.M., McCarthy M.F., Blanco B.M., 1980, ApJ 242, 938

Blöcker T., Schönberner D., 1990, A&A 240, L11

Blöcker T., Schönberner D., 1991, A&A 244, L43

Boothroyd A. I., Sackmann I.-J., 1988a, ApJ 328, 632 (BS1)

Boothroyd A. I., Sackmann I.-J., 1988b, ApJ 328, 641 (BS2)

Boothroyd A. I., Sackmann I.-J., 1988c, ApJ 328, 653 (BS3)

Boothroyd A. I., Sackmann I.-J., 1988d, ApJ 328, 671 (BS4)

Boroson T.A., Liebert J., 1989, ApJ 339, 844

Brown J.A., Smith V.V., Lambert D.L., Dutchover E., Hinkle K.H., Johnson H.R., 1990, AJ 99, 1930

Bryan G.L., Volk K., Kwok S., 1990, ApJ 365, 301

Bussoletti E., Colangeli L., Borghesi A., Orofino V., 1987, A&AS 70, 257

Castellani V., Chiefi A., Straniero O., 1990, ApJS 74, 463

Caughlan G.R., 1965, ApJ 141, 688

Chiosi C., Bertelli G., Bressan A., 1987, in: Stellar evolution and dynamics of the outer halo of the Galaxy, eds. M. Azzopardi, F. Matteuci, ESO, Garching, p. 415

Clayton D., 1968, Principles of Stellar Evolution and Nucleosynthesis, McGraw-Hill, New York, p. 390

Clegg R.E.S., 1991, in: Evolution of Stars, IAU symposium 145, eds. G. Michaud, A. Tutukov, Reidel, Dordrecht, p. 387

Cohen J.G., Frogel J.A., Persson S.E., Elias J.H., 1981, ApJ 249, 481

Cox A.N., Steward J.N., 1970, ApJS 19, 243
Dopita M.A., Meatheringham S.J., 1990, ApJ 357, 140
Dopita M.A., Meatheringham S.J., 1991, ApJ 367, 115
Draine B.T., Lee H.M., 1984, ApJ 285, 89
Fowler W.A., Caughlan G.R., Zimmerman B.A., 1975, ARA&A 13, 69
Frantsman Yu.L., 1986, Afz 24, 131
Frogel J.A., Cohen J.G., Persson S.E., Elias J.H., 1981, in: Physical Processes in Red Giants Stars, eds. I. Iben, A. Renzini, Reidel, Dordrecht, p. 159
Frogel J.A., Mould J., Blanco V.M., 1990, ApJ 352, 96
Frogel J.A., Richer H.B., 1983, ApJ 275, 84
Grevesse N., 1991, in: The evolution of Stars, eds. G. Michaud, A. Tutokov, Reidel, Dordrecht, p. 63
Groenewegen M.A.T., de Jong T., Van der Bliek N.S., Slijkhuis S., Willems F.J., 1992, A&A 253, 150
Hamada T., Salpeter E.E., 1961, ApJ 134, 683
Hardy E., Buonanno R., Corsi C.E., Janes K.A., Schommer R.A., 1984, ApJ 278, 592
Hollowell D.E., 1987, in: Late Stages of Stellar Evolution, eds. S. Kwok, S. R. Pottasch, Reidel, Dordrecht, p. 239
Hollowell D.E., 1988, Ph. D. thesis, University of Illinois
Hughes S.M.G., 1989, AJ 97, 1634
Hughes S.M.G., Wood, P. R., 1990, AJ 99, 784
Iben I., 1973, ApJ 185, 209
Iben I., 1975, ApJ 196, 525
Iben I., 1976, ApJ 208, 165
Iben I., 1977, ApJ 217, 788
Iben I., 1981, ApJ 246, 278
Iben I., 1982, ApJ 260, 821
Iben I., 1985, QJRAS 26, 1
Iben I., 1988, in: Progress and Opportunities in Southern Hemisphere Optical Astronomy, eds. V.M. Blanco, M.M. Philips, PASPC 1, 220
Iben I., 1991, in: Evolution of stars, eds. G. Michaud, A. Tutukov, Kluwer, Dordrecht, p. 257
Iben I., Laughlin G., 1989, ApJ 341, 312
Iben I., Renzini A., 1983, ARA&A 21, 271 (IR)
Iben I., Truran J.W., 1978, ApJ 220, 980 (IT)
Iben I., Tutukov A.V., 1989, in: Planetary Nebulae, ed. S. Torres-Peimbert, Kluwer, Dordrecht, p. 505
Jacoby G.H., 1980, ApJS 42, 1
Jacoby G.H., Walker A.R., Ciardullo R., 1990, ApJ 365, 471
de Jong, T., 1990, in: From Miras to Planetary Nebulae, eds. M.O. Mennessier, A. Omont, Editions Frontieres, Gif-sur Yvette, p 289
Kippenhahn R., 1981, A&A 102, 293
Koester D., Weidemann V., 1985, A&A 153, 260
Koike C., Hasegawa H., Manabe A., 1980, Ap&SS 67, 495
Kudritzki R.P., Pauldrach A., Puls J., 1987, A&A 173, 293
Lambert D.L., 1991, preprint, 'Observational effects of Nucleosynthesis in Evolved Stars'
Lattanzio J.C., 1986, ApJ 311, 708
Lattanzio J.C., 1987a, ApJ 313, L15
Lattanzio J.C., 1987b, in: Late stages of stellar evolution, eds. S. Kwok, S. R. Pottasch,

Reidel, Dordrecht, p. 235
Lattanzio J.C., 1989a, ApJ 344, L25
Lattanzio J.C., 1989b, in: Evolution of Peculiar Red Giants Stars, eds. H. R. Johnson, B. Zuckerman, Cambridge UP, p. 161
Lattanzio J.C., 1989c, ApJ 347, 989
Lattanzio J.C., 1991, ApJS 76, 215
Lequeux J., 1990, in: From Miras to Planetary Nebulae, eds. M.O. Mennessier, A. Omont, Editions Frontieres, Gif-sur-Yvette, p. 271
Lundgren K., 1988, A&A 200, 85
Maeder A., Meynet G., 1989, A&A 210, 155
Matteucci F., François P., 1989, MNRAS 239, 885
Matteucci F., Franco J., François P., Treyer M.A., 1989, Rev. Mex. Astron. Astrofis. 18, 145
McClure R.D., 1989, in: Evolution of Peculiar Red Giant stars, eds. H. R. Johnson, B. Zuckerman, Cambridge UP, p. 196
Paczynski B., 1970, Acta Astron. 20, 47
Paczynski B., 1971, Acta Astron. 21, 417
Paczynski B., 1975, ApJ 202, 558
Pagel B.E.J., Terlevich R.J., Melnick J., 1986, PASP 98, 1005
Panagia N., Gilmozzi R., Macchetto F., Adorf H.-M., Kirshner R.P., 1991, ApJ 380, L23
Payne-Gaposchkin C.M., 1971, Smithson. Contrib. Astrophys. 13, 1
Refsdal S., Weigert A., 1970, A&A 6, 426
Reid N., Tinney C., Mould J., 1990, ApJ 348, 98
Reimers D., 1975, in: Problems in stellar atmospheres and envelopes, eds. B. Basheck et al., Springer, Berlin, p. 229
Reimers D., Koester D., 1988, A&A 202, 77
Reimers D., Koester D., 1989, A&A 218, 118
Renzini A., Bernazzani M., Buonanno R., Corsi C.E., 1985, ApJ 294, L7
Renzini A., Voli M., 1981, A&A 94, 175 (RV)
Richer H.B., 1981a, ApJ 243, 744
Richer H.B., 1981b, in: Physical Processes in Red Giants Stars, eds. I. Iben, A. Renzini, Reidel, Dordrecht, p. 153
Richer H.B., Olander N., Westerlund B.E., 1979, ApJ 230, 724
Rocca-Volmerange B., Schaeffer R., 1990, A&A 233, 427
Rood R.T., 1973, ApJ 184, 815
Russell S.C., Dopita M. A., 1990, ApJS 74, 93
Sackmann I.-J., 1980, ApJ 235, 554
Sackmann I.-J., Boothroyd B.S., 1991, ApJ 366, 529
Sackmann I.-J., Boothroyd B.S., Fowler W. A., 1990, ApJ 360, 727
Sagar R., Pandey K., 1989, A&AS 79, 407
Scalo J.M., Despain K.H., Ulrich R.K., 1975, ApJ 196, 805
Scalo J.M., Miller G.E., 1979, Ap J 233, 596
Schönberner D., 1983, ApJ 272, 708
Schönberner D., 1991, Workshop on probable post-AGB stars, Leuven 10-11 october 1991, in press
Schwering P.B.W., 1988, Ph. D. thesis, Leiden, p. 240
Searle L., Wilkinson A., Bagnuolo W.G., 1980, ApJ 239, 803
Smith V.V., Lambert D.L., 1986, ApJ 311, 843
Smith V.V., Lambert D.L., 1988, ApJ 333, 219

Spite F., Spite M., 1991a, in: The Magellanic Clouds, eds. R. Hayes, D. Milne, Reidel, Dordrecht, p. 243
Spite M., Spite F., 1991b, in: The Magellanic Clouds, eds. R. Hayes, D. Milne, Reidel, Dordrecht, p. 372
Steigman G., 1985, in: Nucleosynthesis: Challanges and New Developments, eds. W. Arnett, J. Truran, Chicago University press, p. 48
Steigman G., Gallagher J.S., Schramm D.N., 1989, Comm. Ap. 14, 97
Stothers R.B., 1991, ApJ 383, 820
Sugimoto D., 1971, Progr. Theor. Phys. 45, 761
Sweigart A.V., Greggio L., Renzini A., 1989, ApJS 69, 911
Sweigart A.V., Greggio L., Renzini A., 1990, ApJ 364, 527
Uus U., 1973, Nauch. Informatsii 26, 96
Van den Hoek L. B., de Jong T., 1993, A&A in preparation
Weidemann V., Koester D., 1983, A&A 121, 77
Westerlund B.E., Olander N., Richer H.B., Crabtree D.R., 1978, A&AS 31, 61
Westerlund B.E., Azzopardi M., Breysacher J., Rebeirot E., 1991a, A&AS 91, 425
Westerlund B.E., Lequeux J., Azzopardi M., Reiberot E., 1991b, A&A 244, 367
Wheeler J.C., Sneden W., Truran J.W., 1989, ARA&A 27, 279
Wood P.R., 1981, in: Physical processes in red gaints, eds. I. Iben, A. Renzini, Kluwer, Dordrecht, p. 135
Wood P.R., 1987, in: Late stages of stellar evolution, eds. S. Kwok, S.R. Pottasch, Kluwer, Dordrecht, p. 197
Wood P.R., 1990, in: From Miras to Planetary Nebulae, eds. M.O. Mennessier, A. Omont, Editions Frontieres, Gif-sur-Yvette, p. 67
Wood P.R., Bessell M.S., Fox, M. W., 1983, ApJ 272, 99
Wood P.R., Zarro D.M., 1981, ApJ 247, 247
Wright F.W., Hodge P.W., 1971, AJ 76, 1003

Chapter 9

Synthetic AGB evolution: II. The predicted abundances of planetary nebulae in the LMC

Abstract

In paper I of this series we presented a model to calculate in a synthetic way the evolution of AGB stars. The model was applied to the LMC and values were derived for the minimum core mass for third dredge-up, the dredge-up efficiency and the Reimers mass loss rate coefficient on the AGB. The observed carbon star luminosity function, the C/M-star ratio and the initial-final mass relation were used as constraints.
In this paper we compare the observed abundances of planetary nebulae (PNe) in the LMC to the values predicted by the final model of paper I. In general there is good agreement. The discrepancy between observations and predictions in the C/O-C/N diagram suggests that either the mass loss rate of the most massive stars is underestimated or that their is no dredge-up after hot-bottom burning ceases. From the N/O-N/H diagram we deduce that on the main sequence the ratio of the oxygen abundance to the total metallicity probably was higher in the past than it is now. This is consistent with observations of the oxygen abundance in the Galaxy as well as theoretical modelling of the chemical evolution for the LMC. The location of PNe in the N/O-He/H, C/O-He/H, C/O-C/N and N/O-N/H diagrams is a good indicator of its progenitor main sequence mass. Our model can explain the high He/H and N/O ratios observed in some planetary nebulae.

1 Introduction

Since planetary nebulae (PNe) have evolved from AGB stars one expects a relation between the abundances in the nebulae and in the photospheres of AGB stars. In this paper we compare the observed abundances of PNe in the LMC with the predictions of a synthetic AGB evolution code. Preliminary results of this work were presented by Groenewegen & de Jong (1993a).
We have developed a model to calculate the evolution of AGB stars in a synthetic way (Groenewegen & de Jong 1993b, paper I). This model is more realistic than previous synthetic evolution models in that more physics has been included. The variation of the luminosity during the interpulse period is taken into account as well as the fact that, initially, the first few pulses are not yet at full amplitude and that the luminosity is lower than given by the standard core mass-luminosity relation. Most of the relations used are metallicity dependent.
The model uses algorithms derived from recent evolutionary calculations for low and intermediate-mass stars. The main free parameters are the minimum core mass for (third) dredge-up M_c^{min}, the dredge-up efficiency λ and the Reimers mass loss coefficient on the AGB, η_{AGB}. By fitting the observed carbon star luminosity function (LF) in the LMC, the overall C/M-star ratio and the initial-final mass relation we showed in paper I that the best model has M_c^{min} = 0.58 $M_\odot$, λ = 0.75, η_{AGB} = 5. We also showed that hot-bottom burning (HBB) at the level of Renzini &

Voli's (1981; RV) $\alpha = 2$ case could well explain the observed number of high luminosity J-type carbon stars. This model will be referred to as the standard model.
A brief description of the model is given in Sect. 2. Based on the standard model we compare the predicted abundances in the ejecta of model stars with the observed abundances of PNe in Sect. 3. After discussing the discrepancies between observations and predictions an improved model is presented in Sect. 4. We conclude in Sect. 5.

2 Theoretical AGB evolution

The model is described in full detail in paper I. Some essential aspects, relevant to this paper, are briefly introduced here.
The observed population of AGB stars is modelled by randomly selecting stars from the distribution N dM $\sim$ IMF(M) SFR(M) t_{AGB}(M) dM for $M_{lower} < M < M_{upper}$ where t_{AGB} is the lifetime on the AGB, IMF is the Initial Mass Function and SFR is the Star Formation Rate. The masses $M_{lower} = 0.98\ M_\odot$ and $M_{upper} = 8.2\ M_\odot$ are the lowest and highest initial masses of stars on the AGB. The IMF-slope, SFR and age-metallicity relation for the LMC are adopted from van den Hoek & de Jong (1993). These relations were derived by simultaneously modeling the current gas fraction, current metallicity and age-metallicity relation for the LMC, constrained by the best available ages and metallicities of LMC clusters. Assuming a power-law IMF (IMF $\sim M^{-\alpha}$) and a density dependent SFR, the age-metallicity relation for the LMC was best modelled with $\alpha = -2.72$. The age of the LMC is taken as 11 Gyr, about equal to the age of the Galactic disk (Rocca-Volmerange & Schaeffer 1990). The pre-AGB lifetimes of Iben & Laughlin (1989) are used to relate the initial mass to the stellar lifetimes and initial metallicity. From this relation we find that stars down to $M_{lower} = 0.93\ M_\odot$ have lived long enough to have reached the AGB. From Becker & Iben (1979) we derive an upper limit to the initial mass of AGB stars of $M_{upper} = 8.2\ M_\odot$ for typical LMC abundances. A distance modulus to the LMC of 18.50 is adopted (Panagia et al. 1991).
Mass loss on the AGB is described by a Reimers (1975) law:

$$\dot{M} = \eta_{AGB}\, 4.0\ 10^{-13}\, \frac{L\,R}{M} \qquad M_\odot/yr \tag{1}$$

where L, R and M are in solar units. The luminosity L is not the quiescent luminosity but includes the effect of the luminosity variation during the flashcycle, so that the mass loss rate just after a TP is higher than during the H-burning phase or in the luminosity dip. In paper I we found that $\eta_{AGB} \gtrsim 3$ is needed to fit the initial-final mass relation for the low-mass stars and that $\eta_{AGB} = 5$ provides the best fit to the high-luminosity tail of the carbon star LF.
Tracks in the HR-diagram are calculated using the M_{bol}-T_{eff} relations of Wood (1990). The effects of first, second and third dredge-up are included. The algorithm to calculate the effects of the first dredge-up process is taken from RV but some of their numerical coefficients are updated using new results of Sweigart et al. (1989, 1990). The algorithm to calculate the effects of second dredge-up is taken from RV without change.
The third dredge-up process is described as follows. Dredge-up occurs only when the core mass is higher than a critical value M_c^{min}. In paper I we found that $M_c^{min} = 0.58\ M_\odot$ is needed to fit the low-luminosity tail of the carbon star LF. When there is dredge-up an amount of material

$$\Delta M_{dredge} = \lambda\, \Delta M_c \tag{2}$$

is added to the envelope, where ΔM_c is the core mass growth during the preceding interpulse period. The composition of the dredged up material is assumed to be (Boothroyd & Sackmann

1988): $X_{12} = 0.22$ (carbon), $X_{16} = 0.02$ (oxygen) and $X_4 = 0.76$ (helium). In paper I we found that $\lambda = 0.75$ is needed to fit the peak of the carbon star LF. Hot bottom burning (HBB) has been included at the level of the RV $\alpha = 2$ case (see Appendix A of paper I).

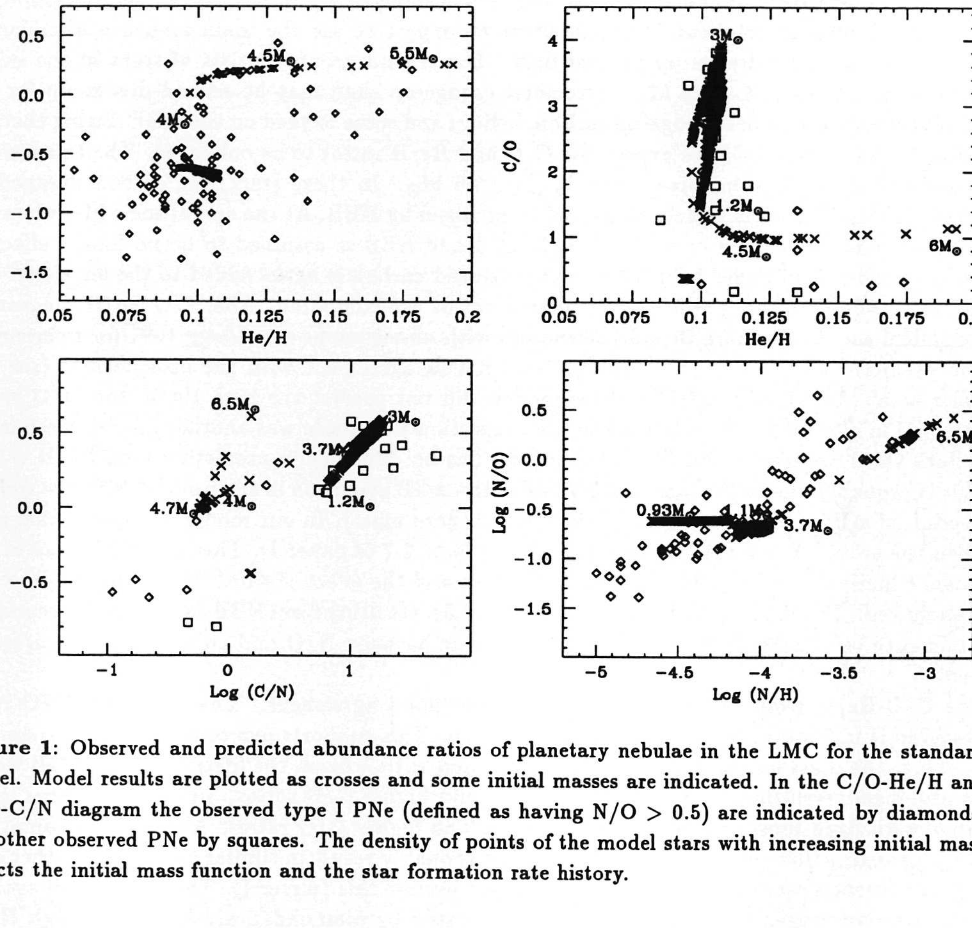

Figure 1: Observed and predicted abundance ratios of planetary nebulae in the LMC for the standard model. Model results are plotted as crosses and some initial masses are indicated. In the C/O-He/H and C/O-C/N diagram the observed type I PNe (defined as having N/O > 0.5) are indicated by diamonds, the other observed PNe by squares. The density of points of the model stars with increasing initial mass reflects the initial mass function and the star formation rate history.

3 The predicted abundances of PNe

In this section the observed abundances in LMC PNe are compared to the predicted abundances in the ejecta of our model stars for the standard model. The observed abundances are taken from Aller et al. (1987), Monk et al. (1988), Henry et al. (1989), Clegg (1991) and Dopita & Meatheringham (1991). The errors in the observed abundances are typically 0.015 in He/H and about 0.2 dex in all other ratios.

The abundances in the ejecta of the model stars are calculated by taking the average abundance in the material ejected during the final 5 10^4 yr on the AGB. This implies that a mean lifetime of the PNe phase of 5 10^4 yr is assumed (Zijlstra & Pottasch 1991). The predicted abundances do not change significantly if a value of 2 10^4 yr is used for the mean lifetime of a PN.

We emphasize that we do not claim all our model stars to actually become PNe. We calculate the average abundances in the ejecta of the AGB star. Whether these ejecta will be recognised

and classified as a PN is a different story. In fact, comparing the death rate of AGB stars and the birth rate of PNe in paper I, one finds that a fairly large number of low-mass stars will probably not become PNe or have so far not been identified as such.
We expect to find three distinct groups of stars. The first group consists of stars with $M_{\rm initial} \lesssim 1.2\ M_{\odot}$. These stars do not experience the second dredge-up and have core masses too low for the third dredge-up to occur. In these stars we expect to see the main sequence abundances changed by the first dredge-up process only. The second group consists of stars in the initial mass range $1.2\ M_{\odot} \lesssim M \lesssim 3.5\ M_{\odot}$. After first dredge-up (and may be second dredge-up for the massive ones) these stars dredge-up carbon, helium and some oxygen on the AGB during thermal pulses (third dredge-up). We expect the C/O and He/H ratios to be enhanced. The third group consists of stars more massive than $M_{\rm initial} \gtrsim 3.5\ M_{\odot}$. In these stars, the carbon dredged-up during thermal pulses is largely converted to nitrogen by HBB. At the end of their life, when the envelope mass is below a critical value ($M_{\rm env}^{\rm HBB}$) and HBB is assumed to be no longer effective (see Appendix A of paper I for details) unprocessed carbon is again added to the envelope.
In Fig. 1 observed and predicted abundance ratios are compared. The N/O-He/H diagram is a classical way to compare theoretical models with observations (see Clegg 1991 for references). The predictions of the RV models e.g. were not in agreement with the observations (see e.g. Kaler et al. 1990), in particular these models did not predict the high He/H and N/O ratios observed in some PNe. This has led to the suggestion that there was another mixing mechanism besides third dredge-up and HBB. Our model has no difficulty in predicting high He/H ratios. This is probably due to the fact that RV ended the AGB evolution in their model with the sudden ejection of a PNe (of 0.5 - 1.4 $M_{\odot}$ depending on core mass). In our model AGB evolution ends when the envelope mass is typically $10^{-3}\ M_{\odot}$ (Sect. 2.7 of paper I). Therefore, the stars in our model experience some additional thermal pulses and the effect of third dredge-up will be more pronounced. The type I PNe (defined as $N/O > 0.5$), resulting from HBB in our model, represent a sequence of increasing initial mass. The relation between N/O and core mass is discussed in Sect. 5.
The C/O-He/H panel in Fig. 1 shows a similar good agreement. The maximum C/O ratio observed is in good agreement with our prediction. This supports our combination of $\eta_{\rm AGB}$ and λ. If e.g. the mass loss rate would be much smaller, with λ fixed, the lifetime on the AGB would be prolonged, resulting in more thermal pulses and higher C/O ratios. Similarly, a higher value for λ, with fixed mass loss rate would also result in higher C/O ratios. Although combinations of higher $\eta_{\rm AGB}$ with lower λ or vice versa could probably result in similar C/O ratios, other constraints (carbon star LF, C/M ratio) would not permit this (paper I). The PNe which evolved from massive progenitors, the type I PNe (indicated by diamonds), are located at high He/H ratios. Note that they have C/O ratios between 0.8 and 1.2, while the observations indicate lower ratios.
The segregation of stars of different initial masses is most clearly demonstrated in the C/O-C/N diagram. The C/O ratio traces the third dredge-up process, while the C/N ratio is sensitive to the CNO-cycle. The observed type I PNe are indicated by diamonds, the other PNe by squares. The low-mass (model) stars are all located near $C/N \approx 1.5$, $C/O \approx 0.35$, the abundance ratios after the first dredge-up. Their observed counterparts are the two PNe near $C/N \approx 0.6$, $C/O \approx 0.16$. It is unclear if this discrepancy is real. An uncertainty is that the carbon abundance is difficult to determine and different methods do not agree (see e.g. Clegg 1991). Clearly, reliable carbon abundances must be determined for more (low-luminosity) PNe.
The intermediate mass stars are located at $C/O > 1.0$, $C/N > 5$. The observation and predictions agree perfectly. The massive stars experiencing HBB represent a sequence which neatly follows the observations up to $\sim 4.7\ M_{\odot}$, but then, apparently, carbon is added and the sequence

turns upwards and to the right. This is in contradiction with the observations which suggest that the C to N conversion is more active resulting in the PNe located at C/O $\approx$ 0.25, C/N $\approx$ 0.20.

The reason why carbon is added to the envelope of the most massive stars in our model at the end of their life is as follows. HBB is assumed to be effective until the envelope mass is below a critical value (M_{env}^{HBB}). This mimics the fact that only when the envelope is massive enough the high temperatures needed for HBB can be sustained. In our model, when HBB ceases, the third dredge-up process continues to be effective and adds carbon to the envelope. In paper I, M_{env}^{HBB} was determined by fitting our model to the models of RV. We found that M_{env}^{HBB} is in the range 0.4-0.8 $M_\odot$ for stars with core masses between 0.8-1.0 $M_\odot$. The most massive stars ($\lesssim$4.7 $M_\odot$) live long enough to experience thermal pulses which add carbon to the envelope, between the time that the envelope mass becomes less than M_{env}^{HBB} and the end of the AGB. This is not true for the less massive stars (3.5 - 4.7 $M_\odot$) due to the fact that M_{env}^{HBB} decreases (i.e. shorter lifetimes) with decreasing core mass (i.e. lower initial mass) and that the interpulse period increases with decreasing core mass. The comparison of the predicted and observed abundances of the massive stars suggest that the following (combination) of effects could be playing a role: (1) M_{env}^{HBB} is lower than assumed, (2) there is no dredge-up after HBB ceased ($\lambda = 0$), (3) the interpulse period has been underestimated for the massive stars (4) the mass loss has been underestimated for the massive stars. We do not favor the last two explanations since they imply selective effects only applying to the massive stars. There are no other indications that the interpulse period or the mass loss rate have been underestimated. In fact, in paper I we showed that a mass loss rate higher than $\eta_{AGB} = 5$ is in disagreement with the high-luminosity tail of the carbon stars LF, and predicts a C/M ratio which is lower than observed. In Sect. 4 we show that a model with $\lambda = 0$ after HBB ceases reproduces the observations well.

In the N/O-N/H diagram we see that the observations indicate a tight correlation between N/O and N/H. Our results confirm this relation for stars more massive than ~1.1 $M_\odot$. For stars of lower mass a decreasing mass results in lower N/H (because the initial Z is lower), but N/O remains constant, because of the original model assumption that the main sequence abundances of C, N and O relative to the total metallicity have solar values and the fact that the effects of the first dredge-up are not very mass dependent.

The comparison of observations and predictions suggest that the relative main sequence abundances of C, N and O change with Z and/or the effects of first dredge-up are mass dependent. These effects seem only to play a role below ~1.1 $M_\odot$ and therefore do not affect the conclusions of paper I about the formation and evolution of carbon stars, which occurs around or above ~1.2 $M_\odot$.

Can we distinguish between variations in the main sequence abundances and a mass dependent first dredge-up process? The observations indicate that for lower Z, N/O should be smaller. A lower nitrogen abundance seems unlikely since this would increase the discrepancy for the low-mass stars in the C/O-C/N diagram. A higher oxygen abundance would make this discrepancy smaller. This suggests main sequence rather than first dredge-up variations, since oxygen is hardly converted into nitrogen during the first dredge-up.

In the Galaxy the ratio of oxygen to all metals has been higher in the past (Wheeler et al. 1989). This is due to the fact that oxygen is mainly produced in massive stars. Based on the abundances of the PNe we conclude that a similar history of the oxygen abundance may apply to the LMC. Recently, Russell & Dopita (1992) by modelling the chemical evolution of the LMC showed that [O/Fe] was indeed higher in the past.

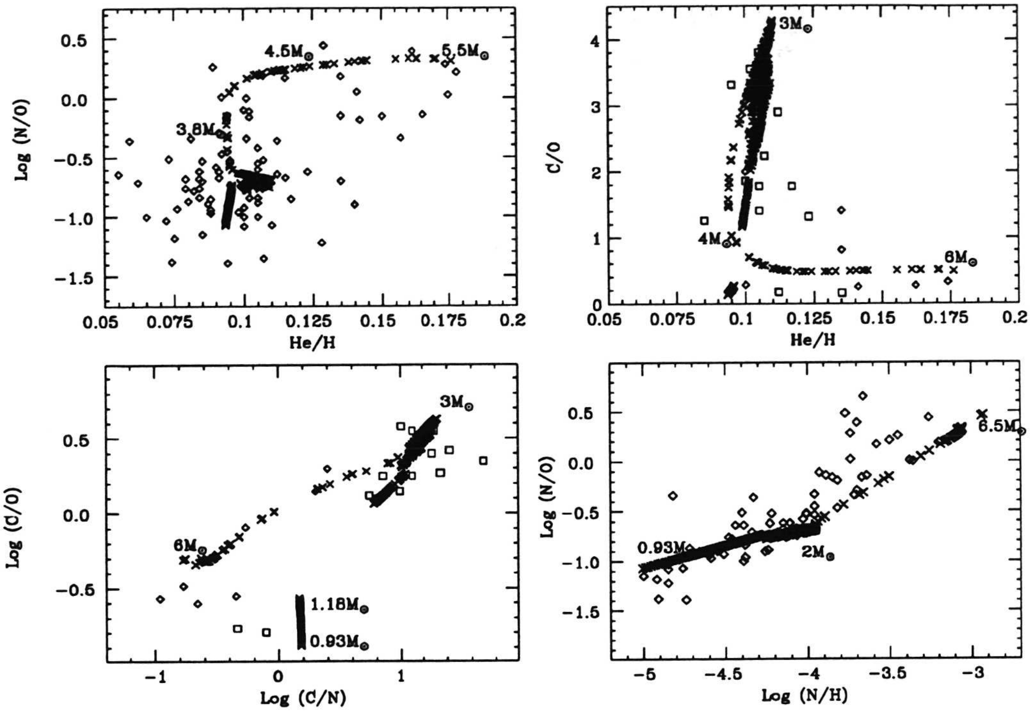

Figure 2: Observed and predicted abundance ratios of planetary nebulae for the final model. Model results are plotted as crosses and some initial masses are indicated. In the C/O-He/H and C/O-C/N diagram the observed type I PNe are indicated by diamonds, the other observed PNe by squares.

4 The final model

Based on the results of paper I and the discussion in the previous section our final model for the LMC has the following parameters: M_c^{min} = 0.58 $M_\odot$, λ = 0.75, η_{AGB} = 5.0, as before. HBB is still included but we now assume no dredge-up after HBB ceases. In addition, the relative main sequence oxygen abundance is given by $(O/Z) = 1/(1 + 0.838\ (Z/Z_0)^{0.7})$, where Z_0 is the present-day metallicity in the LMC. The Z for a given star is derived by the adopted age-metallicity relation (see paper I). The exponent in this empirical relation was determined by fitting the observations for log (N/H) < −4.2 in the N/O-N/H diagram. The present-day (O/Z) ratio is 1/(1 + 0.838) = 0.544, the ratio assumed in paper I (Sect. 2.9.1).
The predicted and observed abundances of PNe are compared in Fig. 2 for the final model. In the N/O-He/H diagram the main change with respect to Fig. 1 is the N/O ratio of the low-mass stars. Stars of ~0.9 $M_\odot$ are located at log (N/O) ≈ −1.1, stars of 1.2 $M_\odot$ at log (N/O) ≈ −0.7. In the C/O-He/H diagram the main change is in the C/O ratio of the massive stars due to the enhanced oxygen abundance. The C/O ratios are now ~0.5, in much better agreement with observations. In the C/O-C/N diagram the changes are twofold. The C/O ratio of the low-mass stars is lower and because dredge-up is assumed to stop when HBB ceases, the PNe of massive progenitors now evolve to log (C/O) ≈ −0.3, log (C/N) ≈ −0.8, in reasonable agreement with observations. The assumption that λ = 0 after HBB stops is rather ad-hoc. Lattanzio (1989) has found cases (for low-mass stars) where λ is 0 at some thermal pulses. That this process

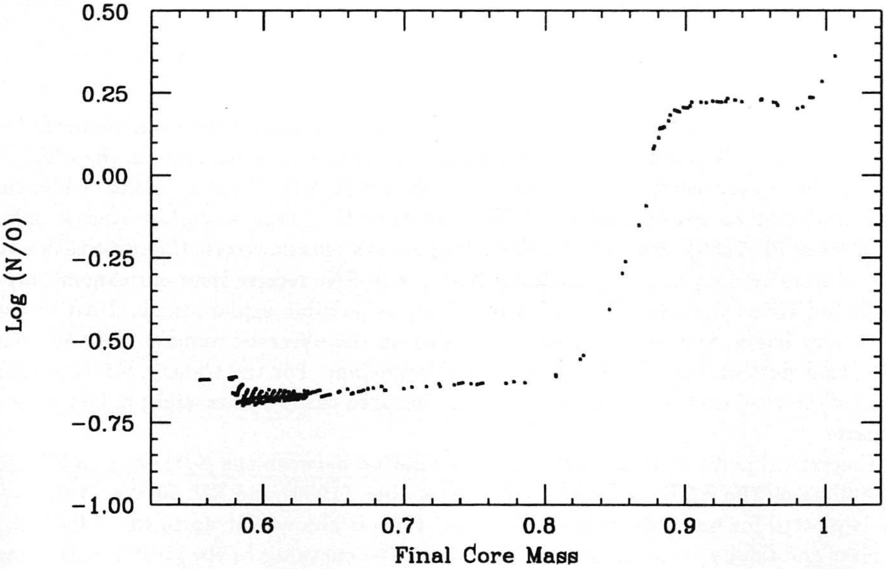

Figure 3: The theoretical relation between N/O in PNe and the final core mass on the AGB for the LMC model stars.

also occurs for massive stars after the end of HBB has yet to be demonstrated. An alternative hypothesis is that the mass loss rate of the most massive stars is underestimated. With a Reimers law, the mass loss rates of the massive stars can not be increased without violating the constraints used in paper I (C/M star ratio, C-star luminosity function). In a future publication (Groenewegen & de Jong 1993c) we investigate the influence of different mass loss rate laws (proposed by Vassiliadis & Wood 1992 and Blöcker & Schönberner 1993) and show that with a mass loss rate law with a steeper luminosity dependence than Reimers law the assumption $\lambda = 0$ after HBB stops is not necessary. In the N/O-N/H diagram the main change is in the N/O ratio for the low-mass stars. With our adopted variation of the main sequence oxygen abundance, the N/O-N/H diagram can be explained well for the low-mass stars.

The scatter of the observations around the model predictions in Fig. 2 is probably due to both observational uncertainties and uncertainties in the model assumptions. The former were already discussed and amount to about 0.015 in He/H and about 0.2 dex in the other abundance ratios. For the low-mass stars (M $\lesssim$1.2 $M_\odot$), which do not experience the third dredge-up, the predicted abundances are determined by the main sequence abundances and the first dredge-up process. We assumed an uniform age-metallicity relation and relative solar abundances for the CNO elements on the main sequence (except in Fig. 2, where the relative oxygen abundance was a function of metallicity). These two assumptions will probably not reflect the true chemical evolution history of different parts of the LMC for the different elements.

The largest uncertainty for the high-mass stars (M $\gtrsim$3.5 $M_\odot$) is probably the parameterization of HBB in our model. The RV $\alpha = 2$ case used in our model provides a good fit to the high-luminosity J-type carbon stars (paper I) and the PNe abundances of the massive stars. However, we are unable to explicitly test how e.g. the RV $\alpha = 1.5$ case would fit the observations since RV did not present the necessary data regarding the temperatures at the bottom of the convective envelope.

5 Discussion

Since PNe evolve from AGB stars it would be interesting to compare their abundances. Unfortunately, there are no CNO abundance determinations available for AGB stars in the LMC. For the Galaxy they have been compared by Smith & Lambert (1990). They note that while the C/O ratio in (disk-) PNe ranges up to about 4, the maximum C/O ratio in carbon stars is only about 1.4 (Lambert et al. 1986). Smith & Lambert suggest systematic errors, the obscuration of more carbon-rich stars by dust and the possibility that C-rich PNe receive their enrichment just before the superwind strips the AGB star of its envelope, as possible explanations. Dust obscuration seems not very likely. In paper I we showed, based on the observed number of IRAS sources in the LMC, that dust obscuration can not be very important. For the Galaxy, Groenewegen & de Jong (1993d) showed that in a sample of fourteen infrared carbon stars, eight in fact have optical counterparts.

From a theoretical point of view there is a clear relation between the N/O ratio in PNe and the final core mass on the AGB as shown by Becker & Iben (1980) and RV. In Fig. 3 the N/O-M_c-relation is plotted for our LMC model. The N/O ratio is almost flat up to $M_c = 0.84\ M_\odot$, then steeply rises and finally levels off around N/O $\approx$ 2. The curve up to the steep rise is determined by the initial abundances and the changes during first, second and third dredge-up. The location of the steep rise and the high core mass curve are determined by HBB.

From an observational point of view the hypothesis that type I PNe originate from massive progenitors has been tested by constructing a N/O versus core mass diagram (Kaler et al. 1990, Kaler & Jacoby 1990, Stasińska & Tylenda 1990). The N/O ratio is determined from an abundance analysis while the core mass of the PNe is inferred by plotting the star in a HR-diagram and comparing the position to the tracks of post-AGB stars, or a core mass-luminosity relation is used. Excluding some uncertain points Kaler et al. (1990) claim there is "a strong and convincing" relation between N/O and M_c. The same conclusion is reached by Stasińska & Tylenda (1990). Ratag et al. (1991) and Pottasch (1993) however, state there is no observational evidence for such a relation. Ratag et al. (1991) criticize Kaler et al. and Stasińska & Tylenda for making use of the Shklovskii method to derive distances which enter the luminosity determination. However, Kaler & Jacoby (1990) also find a relation between N/O and M_c for PNe in the LMC and SMC. Furthermore, the sudden increase in N/O at $M_c \approx 0.8\ M_\odot$ due to HBB is not expected in the sample of Galactic bulge PNe studied by Ratag et al.. Galactic bulge PNe (GBPNe) are thought to have evolved from stars of initial mass $<1.3 M_\odot$ (Ratag et al.). The core masses of GBPNe have been determined using different core mass-luminosity relations and different methods and are found to be $<0.68\ M_\odot$ (Ratag et al. 1991, Tylenda et al. 1991). For such low core masses HBB is probably not important and the scatter in the N/O versus core mass diagram is expected to be entirely due to initial abundance variations and the effect of first and third dredge-up.

There are several problems in determining the core mass of a PN from its position in the HR diagram. Firstly, the uncertain distances to Galactic PNe enter the luminosity determination. Secondly, a non-negligible amount of PNe may have evolved from He shell-burning AGB stars. From theory it is expected that ~30% of stars are He-burners when they leave the AGB (the duration of the luminosity dip relative to the interpulse period). Of the 22 AGB models recently calculated by Vassiliadis & Wood (1992), 6 left the AGB when burning Helium (= 27%). Since usually post-AGB tracks or core mass-luminosity relations for quiescent H shell-burning are used to determine the core mass, this underestimates M_c by ~0.05 $M_\odot$ for low core masses and by ~0.1 $M_\odot$ for stars with $M_c \approx 0.7\ M_\odot$ in 30% of the cases. Because it is exceedingly difficult to determine observationally if a PN has evolved from a H or a He shell-burning AGB star, this uncertainty may inhibit a detailed observational study into the role of HBB (and the distribution of the masses of PNe for that matter) even when the distances to PNe were known accurately.

References

Aller L.H., et al., 1987, ApJ 320, 159

Becker S.A., Iben I., 1979, ApJ 232, 831

Becker S.A., Iben I., 1980, ApJ 237, 111

Blöcker T., Schönberner D., 1993, in: IAU symposium 155 on Planetary Nebulae, eds. R. Weinberger, A. Acker, Reidel, Dordrecht, in press

Boothroyd A.I., Sackmann I.-J., 1988, ApJ 328, 653

Clegg R.E.S., 1991, in: Evolution of Stars, IAU symposium 145, eds. G. Michaud, A. Tutukov, Reidel, Dordrecht, p. 387

Dopita M.A., Meatheringham S.J., 1991, ApJ 377, 480

Groenewegen M.A.T., de Jong T., 1993a, in: IAU symposium 155 on Planetary Nebulae, eds. R. Weinberger, A. Acker, Reidel, Dordrecht, in press

Groenewegen M.A.T., de Jong T., 1993b, A&A 267, 410 (paper I, Chapter 8)

Groenewegen M.A.T., de Jong T., 1993c, A&A, in press (Chapter 10)

Groenewegen M.A.T., de Jong T., 1993d, A&AS, in press

Henry R.B.C., Liebert J., Boroson T.A., 1989, ApJ 339, 872

Iben I., Laughlin G., 1989, ApJ 341, 312

Kaler J.B., Jacoby G.H., 1990, ApJ 362, 491

Kaler J.B., Shaw R.A., Kwitter K.B., 1990, ApJ 359, 392

Lambert D.L., Gustafsson B., Eriksson K., Hinkle K., 1986, ApJS 62, 373

Lattanzio J.C., 1989, ApJ 344, L25

Monk D.J., Barlow M.J., Clegg R.E.S., 1988, MNRAS 234, 583

Panagia N., Gilmozzi R., Macchetto F., Adorf H.-M., Kirshner R.P., 1991, ApJ 380, L23

Pottasch S.R., 1993, in: IAU symposium 155 on Planetary Nebulae, eds. R. Weinberger, A. Acker, Reidel, Dordrecht, in press

Ratag M.A., 1991, Ph.D. thesis, Chapter 5, University of Groningen

Reimers D., 1975, in: Problems in stellar atmospheres and envelopes, eds. B. Basheck et al., Springer, Berlin, p. 229

Renzini A., Voli M., 1981, A&A 94, 175 (RV)

Rocca-Volmerange B., Schaeffer R., 1990, A&A 233, 427

Russell S.C., Dopita M.A., 1992, ApJ 384, 508

Smith V.V., Lambert D.L., 1990, ApJS 72, 387

Stasińska G., Tylenda R., 1990, A&A 240, 467

Sweigart A.V., Greggio L., Renzini A., 1989, ApJS 69, 911

Sweigart A.V., Greggio L., Renzini A., 1990, ApJ 364, 527

Tylenda R., Stasińska G., Acker A., Stenholm B., 1991, A&A 246, 221

Van den Hoek L.B., de Jong T., 1993, in preparation

Vassiliadis E., Wood P.R., 1992, preprint (VW)

Wheeler J.C., Sneden W., Truran J.W., 1989, ARA&A 27, 279

Wood P.R., 1990, in: From Miras to Planetary Nebulae, eds. M.O. Mennessier, A. Omont, Editions Frontieres, Gif-sur-Yvette, p. 67

Zijlstra A.A., Pottasch S.R., 1991, A&A 243, 478

Chapter 10

Synthetic AGB evolution: III. The influence of different mass loss laws

Abstract

In paper I of this series we presented a model to calculate in a synthetic way the evolution of thermal-pulsing AGB stars. The model was applied to the LMC and values were derived for the minimum core mass for third dredge-up and the dredge-up efficiency. In paper I mass loss on the AGB was parameterized with a Reimers mass loss law with a best-fit value for the coefficient $\eta_{\rm AGB}$ of 5. In paper II we showed that the best fitting model of paper I could also reproduce the observed abundance patterns in planetary nebulae (PNe) in the LMC, under the assumption that there is no dredge-up after hot bottom burning (HBB) ceases.
To investigate the sensitivity of the results in papers I and II to the adopted mass loss law we repeat in this paper the analysis of papers I and II for two recently proposed mass loss laws, viz. that of Vassiliadis & Wood (1992, VW) and that of Blöcker & Schönberner (1993, BS).
We find that the BS-law with a scaling factor $\eta_{\rm BS} = 0.1$ fits all observational constraints equally well as the Reimers law. With a BS mass loss law there is no need to curtail dredge-up after HBB ceases. For the VW-law no combination of parameters could be found that fits all constraints simultaneously. This is probably due to the extreme luminosity dependence ($\dot{\rm M} \sim {\rm L}^{\alpha}, \alpha = 6$) implied by the VW-law. We conclude that synthetic AGB models with mass loss laws that are moderately luminosity dependent ($1 < \alpha \lesssim 4$) can be made to fit all presently available observational constraints.

1 Introduction

We have developed a model to calculate the evolution of thermal-pulsing AGB stars in a synthetic way (Groenewegen & de Jong 1993a, paper I). This model is more realistic than previous (e.g. Renzini & Voli 1981) synthetic evolution models in that more details on the evolution have been included. The variation of the luminosity during the interpulse period is taken into account as well as the fact that, initially, the first few pulses are not yet at full amplitude and that the luminosity is lower than given by the standard core mass-luminosity relation. Most of the relations used are metallicity dependent.
The model uses algorithms derived from recent evolutionary calculations for low- and intermediate-mass stars. The main free parameters are the minimum core mass for (third) dredge-up $\rm M_c^{min}$ and the dredge-up efficiency λ as well as the parameterization of the mass loss process. In paper I we assumed a Reimers mass loss law with coefficient $\eta_{\rm AGB}$ (defined in Eq. 2).
In paper I we determined the minimum core mass ($\rm M_c^{min}$), the efficiency (λ) for third dredge-up and the scaling coefficient $\eta_{\rm AGB}$. We achieved this by fitting the carbon star luminosity function (LF), the ratio of the number of C/M stars on the AGB in the LMC, and the initial-final mass relation. We found a best-fitting model with $\rm M_c^{min} = 0.58\ M_{\odot}$, $\lambda = 0.75$ and $\eta_{\rm AGB} = 5$. We

also showed that hot-bottom burning (HBB) at the level of Renzini & Voli's (1981; RV) $\alpha = 2$ case explains the observed number of high luminosity J-type carbon stars well. We furthermore showed that the best-fitting model predicts that carbon stars are formed from stars of initial masses between $\sim$1.2 and $\sim$4 $M_{\odot}$, in agreement with observations in LMC clusters. In addition we showed (Groenewegen & de Jong 1993b, paper II) that the best-fitting model of paper I also reproduces the observed abundance patterns of planetary nebulae (PNe) in the LMC, if we make the additional assumption that there is no dredge-up after HBB ceases.
One of the most uncertain aspects of the model is the parameterization of the mass loss rate. In paper I we adopted a Reimers (1975) law which is an empirical relation derived for red giants. Since mass loss on the AGB seems to be related to pulsation, a mass loss law related to pulsations may be more physical. Recently, two such mass loss rate laws were presented; that of Vassiliadis & Wood (1992, VW) and that of Blöcker & Schönberner (1993, BS). In this paper we repeat the analyses of papers I and II for these two different mass loss laws.

2 The mass loss laws

The model is described in full detail in paper I. Here we only discuss the aspects related to the mass loss process.
Prior to the AGB stars lose mass on the main-sequence, the RGB (important mainly for stars below $\sim$2.2 $M_{\odot}$ which experience the helium core flash) and on the Early-AGB (E-AGB; important for massive stars). The total mass lost by stars with initial masses $\lesssim$2.2 $M_{\odot}$ preceding the AGB is taken from the models of Sweigart et al. (1990) scaled in such a way to give a mass loss of 0.22 $M_{\odot}$ for a 0.85 $M_{\odot}$ star ($\eta_{\rm RGB}$ = 0.86 in the nomenclature of Sect. 2.6.1 of paper I). In addition all stars lose mass on the E-AGB parameterized as (cf. Paper I, M in $M_{\odot}$):

$$\Delta M_{EAGB} = \eta_{EAGB}\ 0.056\ (M/3)^{3.7} \qquad M_{\odot} \tag{1}$$

In paper I mass loss on the AGB is described by a Reimers (1975) law:

$$\dot{M} = \eta_{AGB}\ 4.0\ 10^{-13}\ \frac{L\,R}{M} \qquad M_{\odot}/yr \tag{2}$$

with L and R in solar units. In paper I we assumed $\eta_{\rm EAGB} = \eta_{\rm AGB}$ and found that $\eta_{\rm AGB} \gtrsim 3$ is needed to fit the initial-final mass relation for the low mass stars and that $\eta_{\rm AGB} = 5$ provides the best fit to the high-luminosity tail of the carbon star LF. In paper II we showed that with $\eta_{\rm AGB} = 5$ the observed abundance patterns of PNe are also reproduced quite well.
We now consider alternative mass loss rate laws. The mass loss rate law proposed by BS is:

$$\dot{M} = \eta_{BS}\ \left(4.8\,10^{-9}\ \frac{L^{2.7}}{M^{2.1}}\right)\ \left(4.0\,10^{-13}\ \frac{L\,R}{M}\right) \qquad M_{\odot}/yr \tag{3}$$

i.e. a Reimers law with an additional $(L^{2.7}/M^{2.1})$ dependence. We include a scaling factor $\eta_{\rm BS}$. BS derived this law by fitting the mass loss rates listed by Bowen (1988) for his standard model based on dynamical calculations for long-period variables. Direct comparison of Eqs. (2) and (3) shows that the mass loss rate adopted by BS is equivalent to high Reimers coefficients. For representative values of L = 3000 $L_{\odot}$, M = 1 $M_{\odot}$ or L = 20 000 $L_{\odot}$, M = 5 $M_{\odot}$ the equivalent value of $\eta_{\rm AGB}$ are 12 and 67, respectively.
The mass loss law proposed by VW is:

$$\dot{M} = \eta_{VW}\ \mathrm{minimum}\left(\frac{L}{v_{exp}\,c},\ 10^{-11.4+0.0125[P-y\,100\,(M-2.5)]}\right) \qquad M_{\odot}/yr \tag{4}$$

where $y = 1$ for M larger than 2.5 $M_\odot$ and $y = 0$ for smaller masses. The expansion velocity v_{exp} and the fundamental mode pulsation period (P, in days) are calculated using the relations in VW. We include a scaling factor η_{VW}.
The luminosity L in Eqs. 2-4 is not the quiescent luminosity but includes the effect of luminosity variation during the flashcycle; the mass loss rate just after a thermal pulse (TP) is higher than during the quiescent H-burning phase or in the luminosity dip.
We implemented the BS and VW mass loss laws in our code. BS only consider stars of 3 and 5 $M_\odot$ for which mass loss on the RGB is not important. In our calculations mass loss preceding the AGB is treated as in paper I (see above). From BS we derive $\eta_{EAGB} = 0.5$. VW neglect any mass loss prior to the AGB for stars above 1 $M_\odot$. Using our model with the mass loss laws of BS and VW we determine η_{BS} and η_{VW} needed to reproduce the TP-AGB lifetimes reported by BS and VW for their models (with Z = 0.021 and Y = 0.24 for BS and Z = 0.008 and Y = 0.25 for VW). We find $\eta_{BS} = 0.35$ and $\eta_{VW} = 0.6$. That η_{BS} and η_{VW} are not unity is most likely due to differences in the effective temperature of the AGB tracks in the HR-diagram between our code and the calculations of BS and VW. Additionally, small differences between the algorithms adopted in paper I for the core mass-luminosity relation and other relations and the evolutionary calculations of BS and VW may play a role.

3 The constraints

In this section we briefly discuss the constraints to the models.
The first constraint is the observed carbon star luminosity function (LF) in the LMC as derived from the survey results of Blanco et al. (1980) and Westerlund et al. (1978) (see paper I). In paper I we showed that the predicted low-luminosity tail of the LF is sensitive to the value of M_c^{min} and that the peak of the LF is sensitive to the dredge-up efficiency λ. The high-luminosity tail is sensitive to the mass loss rates.
The second constraint is the ratio of C/M stars on the AGB in the LMC. The observed value is between 0.2 and 2 (Blanco & McCarthy 1983) depending on the spectral type of the M-stars included. For our best model we found a value of C/M = 0.85 in paper I.
The third constraint is the initial-final mass relation based on stars in the solar neighbourhood (for detailed references see paper I).
The fourth constraint is provided by observations of AGB stars in LMC clusters (Frogel et al. 1990, Westerlund et al. 1991) which show that stars between ~1.3 $M_\odot$ and ~4 $M_\odot$ become carbon stars and that S-stars originate from slightly more massive stars.
The fifth constraint is the birth rate of AGB stars. Based on the death rate of horizontal branch (clump) stars and cepheids in the LMC we derived in paper I a birthrate of AGB stars between 0.05 and 0.15 yr^{-1}.
The sixth constraint is the set of abundance ratios of PNe in the LMC, discussed in paper II. The abundances in the ejecta of the model stars are calculated by taking the average abundance in the material ejected during the final 5 10^4 yr on the AGB. This should be representative of the abundances observed in PNe. We emphasize again that we do not claim all our model stars to actually become PNe. We calculate the average abundances in the ejecta of the AGB star. Whether these ejecta will be recognised and classified as a PN is a different story.

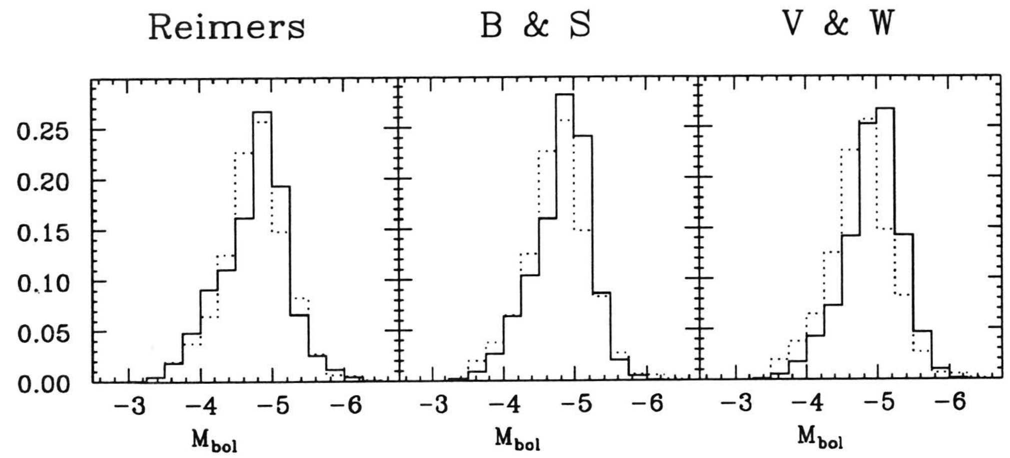

Figure 1: The carbon star luminosity function for the Reimers law with $\eta_{AGB} = 5$ (from paper I), a BS-law with $\eta_{BS} = 0.1$ and a VW-law with $\eta_{VW} = 3$. The dotted curve is the observed LMC carbon star luminosity function (from paper I).

4 Model results

We determined M_c^{min}, λ and η_{BS} (c.q. η_{VW}) in the following way. The C-star LF is largely determined by M_c^{min} and λ, the maximum C/O ratio observed in PNe is largely determined by η. Fine tuning by comparison to the other constraints yields the final choice of parameters: for the BS model $M_c^{min} = 0.58\ M_\odot$, $\lambda = 0.75$ and $\eta_{BS} = 0.1$, for the VW model $M_c^{min} = 0.58\ M_\odot$, $\lambda = 0.75$ and $\eta_{VW} = 3$.

We first discuss the BS-law model. The carbon star LF is shown in the middle panel of Fig. 1. It fits the observed distribution about equally well as using the Reimers law (paper I, left panel). The ratio of C/M stars on the AGB is 0.93, compared to 0.85 for the Reimers-law model. The observed value is between 0.2 and 2. The initial-final mass relation is equally well fitted as with a Reimers law (Fig. 2). The predicted PNe abundances are shown in Fig. 3. The differences are small when compared to the model for a Reimers law (taken from paper II)[1]. The maximum C/O ratio is in good agreement with observations. The BS-law model does not predict the high He/H ratios observed in some PNe. In the C/O-C/N diagram the sequence that is determined by HBB lies at lower C/O ratios (for a given C/N) than the Reimers model. Note that in the BS-law model we did not have to assume that λ drops to zero when HBB stops. The fact that there is no dredge-up after HBB ceases is due to the higher mass loss rate which causes the AGB to terminate before any fresh carbon can be added to the envelope.

The results for BS-law models for individual model stars are listed in Table 1, including the results for the best fitting Reimers-law model (taken from Table 5 of paper I) for comparison. The differences are generally small. The model predicts carbon star formation for stars between ~1.2 and ~4 $M_\odot$, similar to the results of paper I and in agreement with observations. The death rate of AGB stars is ~0.05 yr^{-1}, compared to ~0.07 yr^{-1} with a Reimers law and an observed

[1]The Reimers model with the standard parameters of paper I does not fit the observations in the C/O-C/N and N/O-N/H panel. In paper II we showed that with the additional assumptions that $\lambda = 0$ after HBB ceases and with an oxygen-to-metallicity ratio which is higher in the past, the discrepancy can be explained. These additional assumptions are not made for the BS and the VW model.

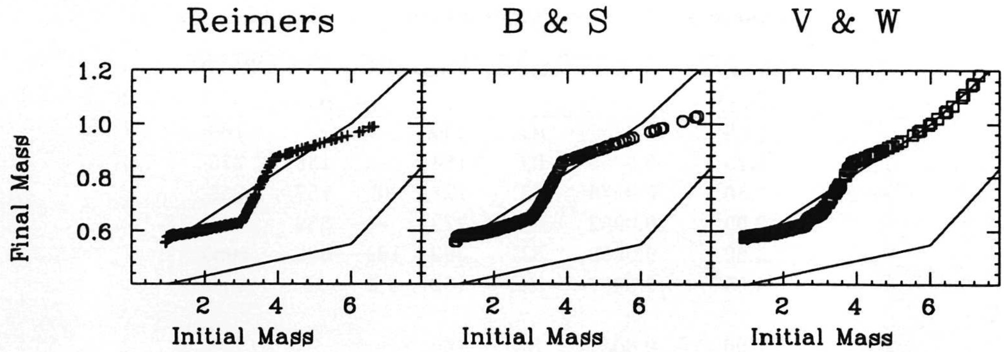

Figure 2: The initial-final mass relation for the Reimers-law (+, from paper I), the BS-law with η_{BS} = 0.1 (o) and the VW-law with η_{VW} = 3 (□). The values allowed by the observations lie between the two solid lines.

value between 0.05 yr^{-1} and 0.15 yr^{-1} (paper I).
We tried lower values for η_{BS}. This results in higher C/M star ratios and higher than observed C/O ratios in PNe. We tried to compensate this by increasing M_c^{min} or decreasing λ. This results in a shift of the C-star LF to higher luminosities, in disagreement with observations.
We next discuss the VW-model. The C-star LF is presented in Fig. 1 (right panel). The C/M star ratio is 0.73. The initial-final mass relation is shown in Fig. 2. The PNe abundances are compared in Fig. 3 and the results for some models are in Table 1. Carbon stars are predicted at somewhat lower initial masses than observed. The carbon star LF peaks at higher luminosities than observed. The predicted abundances are not in good agreement with observations. The model predicts higher than observed C/O and N/O ratios. We could not find parameters that simultaneously fitted all constraints, e.g. the high C/O ratio in some PNe suggests either an increase in η_{VW}, an increase in M_c^{min} or a decrease in λ. These choices would reduce the C/M star ratio close to the minimum value allowed by the observations. Such a change in M_c^{min} or λ would make the C-star LF peak at even higher luminosities. A higher M_c^{min} would increase the minimum mass from which carbon stars are formed.

5 Discussion

The reproduction of the BS models for Galactic stars requires η_{BS} = 0.35 (Sect. 2) while the observations for the LMC require η_{BS} = 0.1. This suggests that the mass loss rate in the LMC is about a factor of 3 lower than in the Galaxy. This could imply that the mass loss rate depends on metallicity like $Z^{1.5}$, compared to a $Z^{0.5}$ dependence found for O-stars (Kudritzki et al. 1987). We consider such a conclusion premature however, firstly because the adopted mass loss rate by BS for Galactic stars may be incorrect and secondly because of the uncertainty in the mass loss rates derived by Bowen (1988) (on which BS based Eq. 3). Uncertainties in the dust properties and other quantities (see Table 9 of Bowen 1988) make Bowen's estimates for the mass loss rate uncertain by a factor of about 5.
The main differences between the three mass loss laws considered here is in their dependence on luminosity ($\dot{M} \sim L^{\alpha}$). The Reimers-law and the BS-law have α = 1 and 3.7, respectively. Using the period-luminosity relation for LPVs in the LMC (Hughes & Wood 1990) we derive that the $\dot{M}-P$ relation of VW implies $\alpha \approx 6.1$, at least for P $\lesssim$ 600.

Table 1: Model results for different mass loss laws

initial mass ($M_\odot$)	Z	model	TM	TS	TC	TAGB
					10^3 years	
1.00	0.0037	RE	160	-	-	160
1.25	0.0066	RE	134	-	136	270
1.50	0.0076	RE	124	88	157	369
2.00	0.0082	RE	272	-	339	611
3.00	0.0086	RE	302	160	603	1065
5.00	0.0087	RE	152	3.3	15	170
1.00	0.0037	BS	165	-	-	165
1.25	0.0066	BS	134	94	36	264
1.50	0.0076	BS	212	-	140	352
2.00	0.0082	BS	272	87	328	687
3.00	0.0086	BS	380	87	1260	1722
5.00	0.0087	BS	87	-	-	87
1.00	0.0037	VW	290	-	3	293
1.25	0.0066	VW	229	-	56	285
1.50	0.0076	VW	212	92	19	323
2.00	0.0082	VW	272	87	261	620
3.00	0.0086	VW	380	162	1839	2381
5.00	0.0087	VW	195	-	-	195

Note. RE, BS and VW refer to the different mass loss laws (see text). TM, TS, TC, TAGB refer to the lifetime of the M, S, C and the total AGB phase.

VW use an observed $\dot{M}$–P relation (Wood 1990). Their plot contains little date below P = 350 days, where most of the LPVs are located (Hughes & Wood 1990). Schild (1989) and Whitelock (1990) derived $\dot{M}$–P relations containing data points at lower periods. The latter two relations agree very well with each-other and have a much shallower dependence of $\dot{M}$ on P than Wood's relation.

Since the VW-law can be excluded, while a Reimers- and BS-law fit the constraints in the LMC about equally well, we infer that probably all models with a mass loss luminosity dependence of $1 < \alpha \lesssim 4$ will fit the constraints discussed in Sect. 3. For Schild's $\dot{M}$–P relation we derive $\alpha \approx 2$ in the range P = 200-600 days, in between the value for the Reimers- and the BS-law.

An additional constraint on the dependence of the mass loss law on stellar parameters may come from the observation that some Galactic M-, S- and C-stars describe a loop in the IRAS color-color diagram (Willems & de Jong 1988, Zijlstra et al. 1992). Derivation of the mass loss rate in the different phases of the pulse cycle for the well studied case S Sct (Groenewegen & de Jong 1993c) shows that the ratio of the mass loss rate in the thermal pulse phase to that in the quiescent H-burning phase is about 20 and that the ratio of the mass loss rate in the thermal pulse phase to that in the luminosity dip is about 700. Since the corresponding changes in luminosity are about 1.8 and 3.5, respectively, this implies $\alpha \approx 5$. This value is somewhat larger than derived previously. Perhaps S Sct is a special case. An analysis of the mass loss rate history in other carbon stars with double-peaked CO line profiles would be interesting. Perhaps the luminosity dependence of the mass loss rate is steeper in the Galaxy than in the LMC. Perhaps the mass loss rate in AGB stars does not primarily depend on luminosity but also depends in some unknown manner on chemical composition. The carbon stars seem to describe larger loops in the IRAS color-color-diagram than the M- and S-stars, implying that the drop in the mass loss rate between the thermal-pulse phase and the luminosity-dip is larger for the carbon stars. This may be related to their particular chemical composition.

References

Blanco V.M., McCarthy M.F., Blanco B.M., 1980, ApJ 242, 938

Blanco V.M., McCarthy M.F., 1983, AJ 88, 1442

Blöcker T., Schönberner D., 1993, in: IAU symposium 155 on Planetary Nebulae, eds. R. Weinberger, A. Acker, Reidel, Dordrecht, in press (BS)

Bowen G.H., 1988, ApJ 329, 299

Frogel J.A., Mould J., Blanco V.M., 1990, ApJ 352, 96

Groenewegen M.A.T., de Jong T., 1993a, A&A 267, 410 (paper I, Chapter 8)

Groenewegen M.A.T., de Jong T., 1993b, A&A in press (paper II, Chapter 9)

Groenewegen M.A.T., de Jong T., 1993c, A&A in press (Chapter 6)

Hughes S.M.G., Wood P.R., 1990, AJ 99, 784

Kudritzki R.P., Pauldrach A., Puls J., 1987, A&A 173, 293

Reimers D., 1975, in: Problems in stellar atmospheres and envelopes, eds. B. Basheck et al., Springer, Berlin, p. 229

Renzini A., Voli M., 1981, A&A 94, 175 (RV)

Schild H., 1989, MNRAS 240, 63

Sweigart A.V., Greggio L., Renzini A., 1990, ApJ 364, 527

Vassiliadis E., Wood P.R., 1992, preprint (VW)

Westerlund B.E., Olander N., Richer H.B., Crabtree D.R., 1978, A&AS 31, 61

Westerlund B.E., Azzopardi M., Breysacher J., Reiberot E., 1991, A&AS 91, 425

Whitelock P.A., 1990, PASPC 11, 365

Willems F.J., de Jong, 1988, A&A 196, 173

Wood P.R., 1990, in: From Miras to Planetary Nebulae, eds. M.O. Mennessier, A. Omont, Editions Frontieres, Gif-sur-Yvette, p. 67

Zijlstra A.A., Loup C., Waters L.B.F.M., de Jong T., 1992, A&A 265, L5

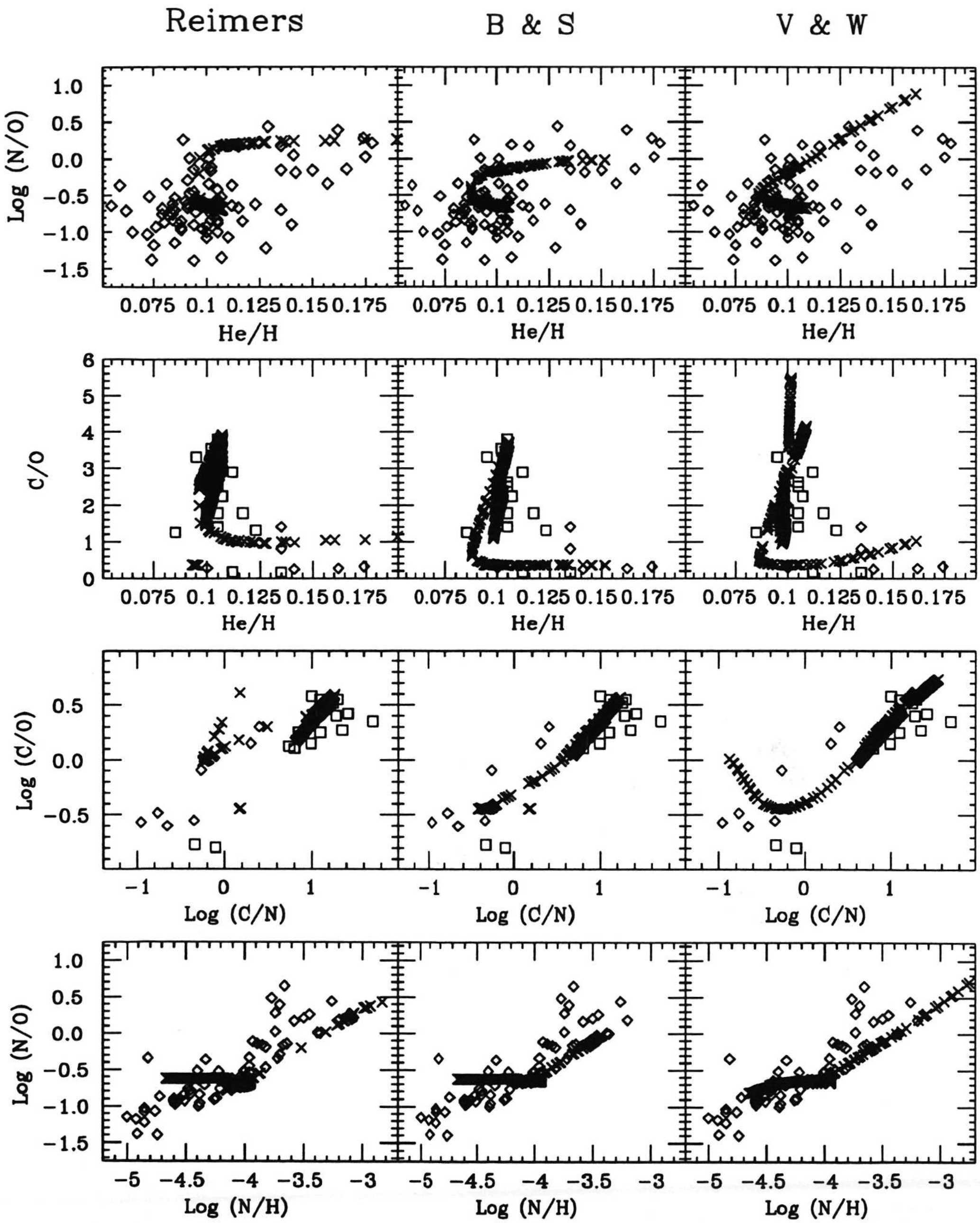

Figure 3: Observed and predicted abundance ratios of planetary nebulae in the LMC for the Reimers model (taken from paper II), the BS-law with $\eta_{BS} = 0.1$ and the VW-law with $\eta_{VW} = 3$. Model results are plotted as crosses. In the C/O-He/H and C/O-C/N diagram the observed type I PN (defined as having N/O > 0.5) are indicated by diamonds, the other observed PN by squares.

Chapter 11

Synthetic AGB evolution: IV. LPVs in the LMC

Abstract

We present a simple model to explain the observed properties of long-period variables (LPVs) in the LMC. It is assumed that pulsation only occurs in an instability strip in the HR-diagram. The instability strip is characterised by three parameters: the temperature at some reference luminosity, the width of the instability strip and the slope $\frac{dT_{eff}}{dM_{bol}}$. The first two are free parameters in the model. Based on observations we use $\frac{dT_{eff}}{dM_{bol}}$ = 275 K mag^{-1} for $M_{bol} > -5$ and 100 K mag^{-1} for $M_{bol} < -5$. An additional complication is that the pulsation period depends rather sensitively on the effective temperature scale. The location of the AGB tracks in the HR-diagram (the zero point of the effective temperature scale) is the third free parameter.
From observations we derive that the ratio of the number of C-rich LPVs to the total number of carbon stars is ~0.05 and that the ratio of the number of oxygen-rich LPVs to the total number of oxygen-rich AGB stars is between 0.05 and 0.10.
Both a model with a Reimers mass loss law inside and outside the instability strip, and a model with the mass loss in the instability strip given by a scaled version of the Blöcker & Schönberner (1992) mass loss law, fit the observational constraints equally well.
We conclude that first harmonic pulsation can be excluded unless the canonical relation between (J–K) color and effective temperature (based on lunar occultation observations) gives temperatures which are too high by ~20%, much larger than the estimated uncertainty of ~8% or possible systematic effects ($\lesssim$10%). Fundamental mode pulsation is therefore probably the dominant pulsation mode among LPVs in the LMC.
A second conclusion is that for most stars the instability strip is not the final phase of AGB evolution. Based on our calculations for individual stars we find that the AGB is terminated in the instability strip only for stars with initial masses $\lesssim$1.14 $M_{\odot}$. More massive stars spend a considerable amount of time in the phase between the end of pulsation and the end of the AGB. We propose an alternative explanation for (some of) the non-variable OH/IR stars in the Galaxy.

1 Introduction

Many AGB stars are observed to pulsate. However, the details how the evolution of AGB stars of different masses is related to the different classes of variable stars (Miras, Semi-regulars (SRs) and Irregulars) and to the evolution of the pulsation period remain uncertain. Recent studies (Jura & Kleinmann 1992a, b, Kerschbaum & Hron 1992) indicate that Miras and SRs with periods between 300 and 400 days have a scale height of about 250 pc, while Miras with periods between 100 and 300 days and SRs with periods between 200 and 300 days have a scale height of about 500 pc and thus have evolved from less massive progenitors. The situation for SRs with periods less than 200 days and the Irregulars is less clear.
Hughes (1989) and Hughes & Wood (1990) have performed a deep and extensive search for long-

period variables (LPVs) in the LMC. They found close to 1100 LPVs, about 470 showing large amplitude variations ($\Delta I \geq 0.9$, called Miras by them) and about 570 having smaller amplitudes (called SRs by them). Follow-on spectroscopy and near-infrared photometry has provided an indication of the C to M star ratio among the LPVs. The survey was complete down to $I \approx 18$, equal to the completeness limit reached in optical surveys for AGB stars. For obvious reasons their survey is most sensitive to large amplitude variables. From their figures we deduce that the detection probability for a variable with an amplitude $\Delta I = 1.2$ was close to 100%, but for a star with an amplitude of $\Delta I = 0.6$ only ~50%. Thus the presently known LPVs in the LMC contain essentially all Miras and SRs with large amplitudes. By using this well defined population of LPVs, for which luminosity, period and chemical type are relatively well known, we will in this paper attempt to place the LPVs in the general context of AGB evolution.
After a brief summary of our synthetic AGB evolution model (Sect. 2), the average duration of the LPV phase is derived from observations in Sect. 3. In Sect. 4 the observed period distribution of oxygen-rich and carbon-rich LPVs is fitted. We conclude in Sect. 5.

2 Synthetic AGB evolution

We have developed a model to calculate the evolution of AGB stars in a synthetic way (Groenewegen & de Jong 1993, paper I). This model is more realistic than previous synthetic evolution models in that more details on the evolution both prior to and on the AGB have been included. The variation of luminosity during the interpulse period was taken into account as well as the fact that, initially, the first few pulses are not yet at full amplitude and that the luminosity is lower than given by the standard core mass-luminosity relation. Most of the relations used are metallicity dependent. The model uses algorithms derived from recent evolutionary calculations for low- and intermediate-mass stars. The model is described in full detail in paper I. Some essential aspects, relevant to this paper, are briefly introduced here.
In the model stars are selected according to their probability to be on the AGB, which depends on the star formation rate, the initial mass function and the lifetime on the AGB (see paper I). With such an approach we can calculate for a population of stars distributions of relevant quantities like the luminosity function, or, in this paper, the period distribution.
The main free parameters of the model are the minimum core mass M_c^{min} for (third) dredge-up to occur, the dredge-up efficiency λ and the Reimers mass loss coefficient η_{AGB}.
In paper I, mass loss on the AGB was described by a Reimers (1975) law:

$$\dot{M}_R = \eta_{AGB}\, 4.0\, 10^{-13}\, \frac{L\, R}{M} \qquad M_\odot/yr \tag{1}$$

In this paper we also consider the mass loss law derived by Blöcker & Schönberner (1992) based on the results of the dynamical modelling of LPVs by Bowen (1988):

$$\dot{M}_{BS} = \eta_{LPV}\, 4.8\, 10^{-9}\, \frac{L^{2.7}}{M^{2.1}}\, \dot{M}_R \qquad M_\odot/yr \tag{2}$$

where η_{LPV} is a scaling factor, which is unity in Blöcker & Schönberner. The luminosity L is not the quiescent luminosity but includes the effect of the luminosity variation during the flashcycle, i.e. the mass loss rate just after a TP is higher than during quiescence H-burning or in the luminosity dip. In paper I we found that $\eta_{AGB} \gtrsim 3$ is needed to fit the initial-final mass relation for the low mass stars and that $\eta_{AGB} = 5$ provides the best fit to the high-luminosity tail of the carbon star luminosity function (LF). AGB evolution is ended when the envelope mass is

reduced to $\sim 10^{-3}$ $M_\odot$.
The third dredge-up process is described as follows. Dredge-up operates only when the core mass is above a critical value M_c^{min}. In paper I we found that $M_c^{min} = 0.58$ $M_\odot$ is needed to reproduce the low-luminosity tail of the carbon star LF. During dredge-up an amount of material

$$\Delta M_{dredge} = \lambda \, \Delta M_c \tag{3}$$

is added to the envelope, where ΔM_c is the core mass growth during the preceding interpulse period. The composition of the dredged up material is assumed to be (Boothroyd & Sackmann 1988): $X_{12} = 0.22$ (Carbon), $X_{16} = 0.02$ (Oxygen) and $X_4 = 0.76$ (Helium). In paper I we found that $\lambda = 0.75$ is needed to fit the peak of the carbon star LF. Hot bottom burning (HBB) has been included at the level of the RV $\alpha = 2$ case (see Appendix A of paper I).
The effective temperature is calculated using the relations of Wood (1990) for AGB tracks in the HR-diagram:

$$\begin{aligned} \log T_{eff} &= (M_{bol} + 2.65 \log M)/15.7 - 0.12 \, \log(Z/0.02) + \Delta + 3.764 \quad (M \leq 1.5 M_\odot) \\ &= (M_{bol} + 4.00 \log M)/20.0 - 0.10 \, \log(Z/0.02) + 3.705 \qquad (M \geq 2.5 M_\odot) \end{aligned} \tag{4}$$

where $M_{bol} = -2.5 \log L + 4.72$ and Δ is a correction term which accounts for the fact that the effective temperature increases at the end of the AGB phase when the envelope mass becomes small. The Δ-term is calculated from Wood (1990):

$$\begin{aligned} \Delta &= 0 && x \geq 0.8 \\ &= 0.07 \, (0.8 - x)^{2.54} && x < 0.8 \\ x &= M_{bol} + 7.0 - 1.2/M^{1.7} \end{aligned} \tag{5}$$

For stars with masses between 1.5 and 2.5 $M_\odot$ we interpolate in log T_{eff} using the mass M as variable. The zero point of these relations was determined by Wood from the assumption that the star o Ceti (Mira) with a period of 330 days, $Z = Z_\odot$ and $M_{bol} = -4.32$, has a mass of 1 $M_\odot$ and is pulsating in the fundamental mode.
Fundamental mode and first harmonic pulsation periods are calculated as follows. The fundamental period (in days) is calculated following Wood (1990):

$$\begin{aligned} P_0 &= 0.00851 \, R^{1.94} \, M^{-0.90} \quad M \leq 1.5 M_\odot \\ &= 0.00363 \, R^{2.09} \, M^{-0.77} \quad M \geq 2.5 M_\odot \end{aligned} \tag{6}$$

Wood found this relation to be reasonably independent of metallicity. For stars with masses between 1.5 and 2.5 $M_\odot$ we interpolate linearly in P_0 using M as variable. The formalism to calculate the first overtone period is adopted from Wood et al. (1983):

$$P_1 = Q \, R^{1.5} \, M^{-0.5} \tag{7}$$

with

$$\begin{aligned} Q &= 0.038 + 5.5\,10^{-5} (P_1 - 100) && M \leq 0.85 \text{ and } P_1 \geq 100 \\ &= 0.038 + 4.5\,10^{-5} (P_1 - 150) && 0.85 < M \leq 1.5 \text{ and } P_1 \geq 150 \\ &= 0.038 + 2.5\,10^{-5} (P_1 - 300) && 1.5 < M \leq 2.5 \text{ and } P_1 \geq 300 \\ &= 0.038 && \text{all other cases} \end{aligned} \tag{8}$$

Equations (4-8) have been derived for oxygen-rich stars. Lacking any better estimate we will also use them for carbon stars. This assumption is discussed in Sect. 5.

In Sect. 4 we need to derive effective temperatures from observations. The effective temperatures for both oxygen-rich and carbon-rich stars are derived from (Bessell et al. 1983):

$$T_{eff} = \frac{7070}{(J-K)+0.88} \tag{9}$$

where the (J–K) color is in the Johnson system. This relation has been calibrated using effective temperature determinations from the lunar occultation observations of Ridgway et al. (1980a, 1980b). The accuracy of Eq. (9) is about 250 K. It is possible however that Eq. (9) gives too low effective temperatures for the carbon stars or that there is a systematic effect in applying this empirical equation, derived from stars in the solar neighbourhood, to LMC stars.

3 The duration of the LPV phase

In their study of LPVs in the LMC, Hughes (1989) and Hughes & Wood (1990) identified 594 definite and 449 probable LPVs in an 53 deg^2 area. Of the definite LPVs, 247 showed large amplitude variations in their lightcurves ($\Delta I \geq 0.9$, called Miras) and 347 showed smaller variations ($\Delta I < 0.9$, called Semi-Regulars). Of the 449 probable LPVs, 224 showed Mira-like behaviour and 225 SR-like behaviour.

About 500 stars were classified as carbon- or oxygen-rich based on low resolution spectra or (J–K) color. Of 307 Miras, 119 were classified as carbon stars (38.8%), of 181 SRs investigated, 69 were classified as carbon stars (38.1%). Extrapolating to the total number of 1043 LPVs we derive an estimated number of 401 carbon-rich and 642 oxygen-rich LPVs. The same area in the LMC contains about 7500 carbon stars and between 6700 and 12000 oxygen-rich AGB stars (paper I).

The ratio of LPVs to the number of AGB stars is 0.053 for the carbon-rich and between 0.054-0.096 for the oxygen-rich AGB stars. Using the average lifetimes of the AGB phase (from paper I), this corresponds to a mean lifetime of the carbon-LPV and oxygen-LPV phase of $\sim$1.1 10^4 and 0.7-1.8 10^4 yrs respectively. Based on the observed C/M ratio of 0.63 in the LPV phase an independent estimated lifetime for the oxygen-rich LPV phase of 1.8 10^4 yrs is derived. Hughes & Wood derived a value of $\sim$1.5 10^4 yrs for the total LPV phase based on the number of definite LPVs only. Adding the probable LPVs, the lifetime of Hughes & Wood ($\sim$2.6 10^4 yrs) is in good agreement with our estimate (2.9 10^4 yrs).

4 Fitting the period distribution of LPVs

In Fig. 1 the observed LF and period distribution of the carbon and oxygen-rich Miras (the solid line) and SRs (the dotted line) are plotted. The oxygen-rich SRs are concentrated towards lower luminosities and lower pulsation periods. For the carbon-rich LPVs the difference between Miras and SRs is much smaller. In the remainder of this section we will not distinguish between Miras and SRs and added the observed period distribution (weighted by number) to obtain the observed period distribution of LPVs in the LMC.

We first calculated the fundamental and first harmonic pulsation period distribution for the standard model of paper I according to Eq. (6-8), under the assumption that stars pulsate everywhere on the AGB. The resulting period distribution is compared to the observed one in Fig. 2. There is strong disagreement. Both the fundamental and the first harmonic period distributions are too broad, i.e. the model predicts pulsation at both too low and too high periods. This is true for both oxygen-rich and carbon stars.

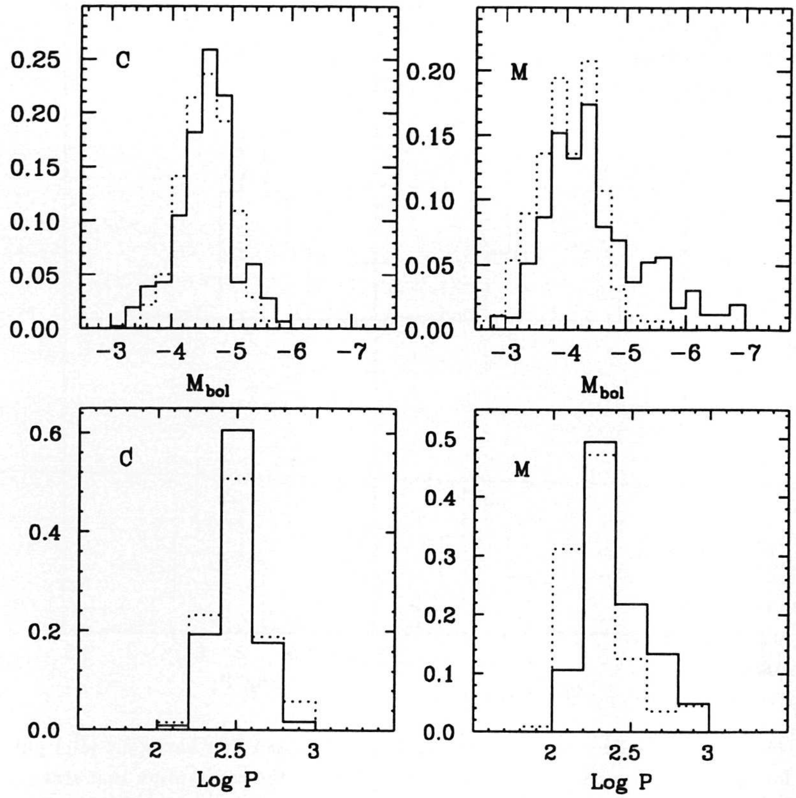

Figure 1: The luminosity function and period distribution of carbon and oxygen-rich 'Miras' and 'Semi Regulars' (SRs) variables (as defined by Hughes 1989) in the LMC from the data of Hughes (1989) and Hughes & Wood (1990). The Miras are represented by the solid lines, the SRs by the dotted line. There is a tendency (in particular for the oxygen-rich stars) for the SRs to have lower luminosities and lower periods than the Miras. All histograms are normalised to unity.

In Fig. 3 we show the evolution of two stars of 1.25 $M_\odot$ (O) and 5 $M_\odot$ (X) in the period-luminosity (P-L) diagram. The variation of the luminosity during the flashcycle is represented by a block profile (paper I). This is reflected in Fig. 3 where stars jump from one phase to another: the luminosity dip, quiescent H-burning and the shell flash. The assumption that pulsation occurs everywhere on the AGB results in periods which are both lower and higher than observed (the strip bounded by the two full lines in Fig. 3). This is true for both low and high initial masses. A similar conclusion is derived by Vassiliadis & Wood (1992).

The naive assumption that AGB stars always pulsate is incorrect. The LPV phase is, on average, a brief one (~6% of the total AGB phase). Thus, either all AGB stars go through a brief LPV phase, or, only a small fraction of AGB stars is LPV during their entire AGB life. There are several arguments to favor the first hypothesis, i.e. a majority of AGB stars going through a brief LPV phase rather than a minority having a prolonged LPV phase. Firstly, as shown in Fig. 2 and 3, any prolonged LPV phase results in period distributions which are too broad. Secondly, LPVs are observed over a wide range of masses, from low mass stars in Galactic globular clusters (Menzies & Whitelock 1985) to the more massive OH/IR stars. If most intermediate mass stars

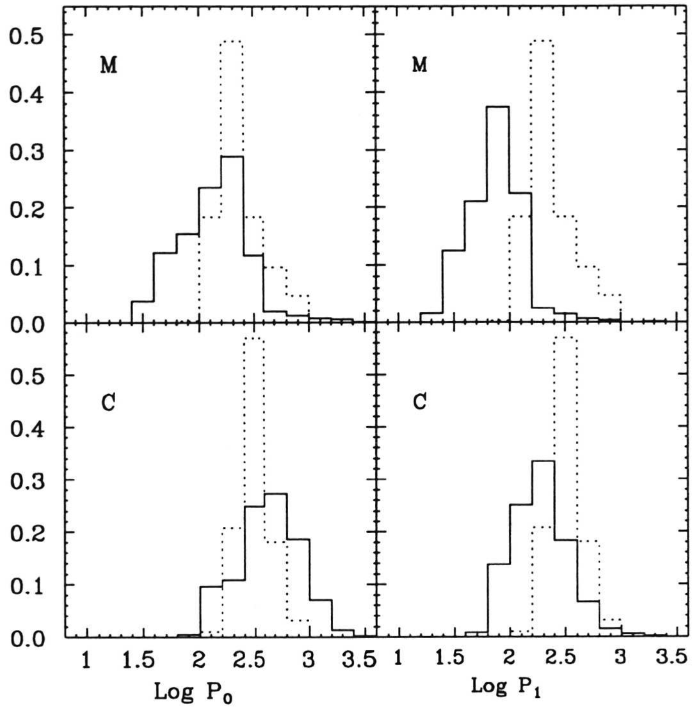

Figure 2: The predicted (solid lines) fundamental mode (P_0) and first harmonic (P_1) pulsation period distribution for the standard model of paper I calculated under the assumption that stars pulsate during their entire AGB life. The dotted line represents the observed period distribution. All histograms are normalised to unity.

can become a LPV then each star can only be a LPV for a short time interval.
We consider an instability strip of the form:

$$\begin{aligned} T_l &= T_l^0 + \frac{dT_{eff}}{dM_{bol}}(M_{bol} + 5) \\ T_h &= T_h^0 + \frac{dT_{eff}}{dM_{bol}}(M_{bol} + 5) \end{aligned} \tag{10}$$

where T_l and T_h are the low and high end effective temperatures of the instability strip. The width of the instability strip ($T_h - T_l$) determines the overall duration of the LPV phase, while the position of the instability strip in the HR-diagram determines the C/M ratio in the instability strip. The free parameters are T_l^0 and T_h^0. The third free parameter is the location of the AGB tracks in the HR-diagram (the zeropoint of the effective temperature scale; Eq. 4). This complication is necessary since the pulsation periods are sensitive to the stellar radius (Eqs. 6-8) and hence the effective temperature. The value of η_{AGB} has to be modified when the zero point of the effective temperature scale is changed to give identical evolutionary behaviour on the AGB ($\dot{M} \sim \eta_{AGB}$ R $\sim \eta_{AGB}$ T_{eff}^{-2}).
The slope $\frac{dT_{eff}}{dM_{bol}}$ can be determined from observations. Feast et al. (1989) have derived a relation between (J–K) color, averaged over the lightcurve, and log P for Miras in the LMC. Combining Eq. (9) with the mean P-L-relation of Hughes & Wood (1990) we derive $\frac{dT_{eff}}{dM_{bol}} \approx 275$ K mag^{-1}

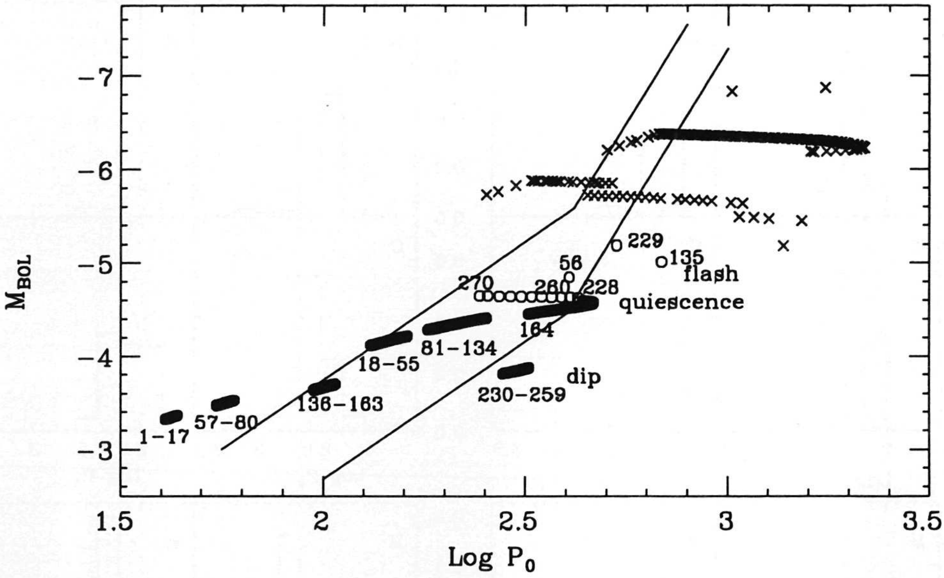

Figure 3: The (fundamental) Period-Luminosity relation for stars of 1.25 $M_\odot$ (O) and 5 $M_\odot$ (X) for the standard model of paper I calculated under the assumption that pulsations occurs during the entire AGB. The P_1-L relation is qualitatively similar. The observed period range for a given luminosity is given by the two full lines. The time evolution of the 1.25 $M_\odot$ model is indicated (lifetimes in 10^3 yrs). The interval between points plotted is 1000 years. The evolution of the 5 $M_\odot$ model is similar. Because the luminosity variation during the interpulse period was assumed to be a block profile, stars jump from the luminosity dip to the quiescent H-burning phase to the thermal flash.

for $M_{\rm bol} > -5$ and $\approx$100 K mag^{-1} for $M_{\rm bol} < -5$.

The constraints to the model are the duration of the LPV phase relative to the total AGB phase for both oxygen-rich and carbon-rich stars, the observed pulsation period distribution for both oxygen-rich and carbon-rich stars, and the observed effective temperatures of Miras in the LMC (Feast et al. 1989). Later on we will also discuss the ability of the models to reproduce the observed $\dot{M}$−P relation for galactic stars. Based on the results of Sect. 3, a duration of the C-star LPV phase relative to the carbon star AGB phase of 0.053 and a C/M ratio in the instability strip of 0.63 are used as constraints.

It should be emphasized that when we refer to the effective temperature of LPVs, we implicitly assume the effective temperature of a non-pulsating star. The pulsation will trigger variations in the effective temperature resulting in real LPVs to have effective temperatures which may be outside the instability strip.

The fitting procedure is as follows. We consider four zero points of the effective temperature scale: the original zero point of paper I (Eq. 4) and zero points lower by 0.02 dex, 0.05 dex and 0.10 dex. The value of $\eta_{\rm AGB}$ has to be modified when the zero point of the effective temperature scale is changed, as discussed before, in particular, $\eta_{\rm AGB}$ = 5.0, 4.6 4.0, 3.15 are used respectively. For the moment $\eta_{\rm AGB}$ is assumed to be equal inside and outside the instability strip. In the program, pulsation periods are calculated for stars in the instability strip, i.e. $T_l \leq T_{\rm eff} \leq T_h$. The temperatures T_l^0 and T_h^0 are determined to fit the assumed duration of the carbon star LPV phase and the C/M ratio in the instability strip. The predicted period distribution for both

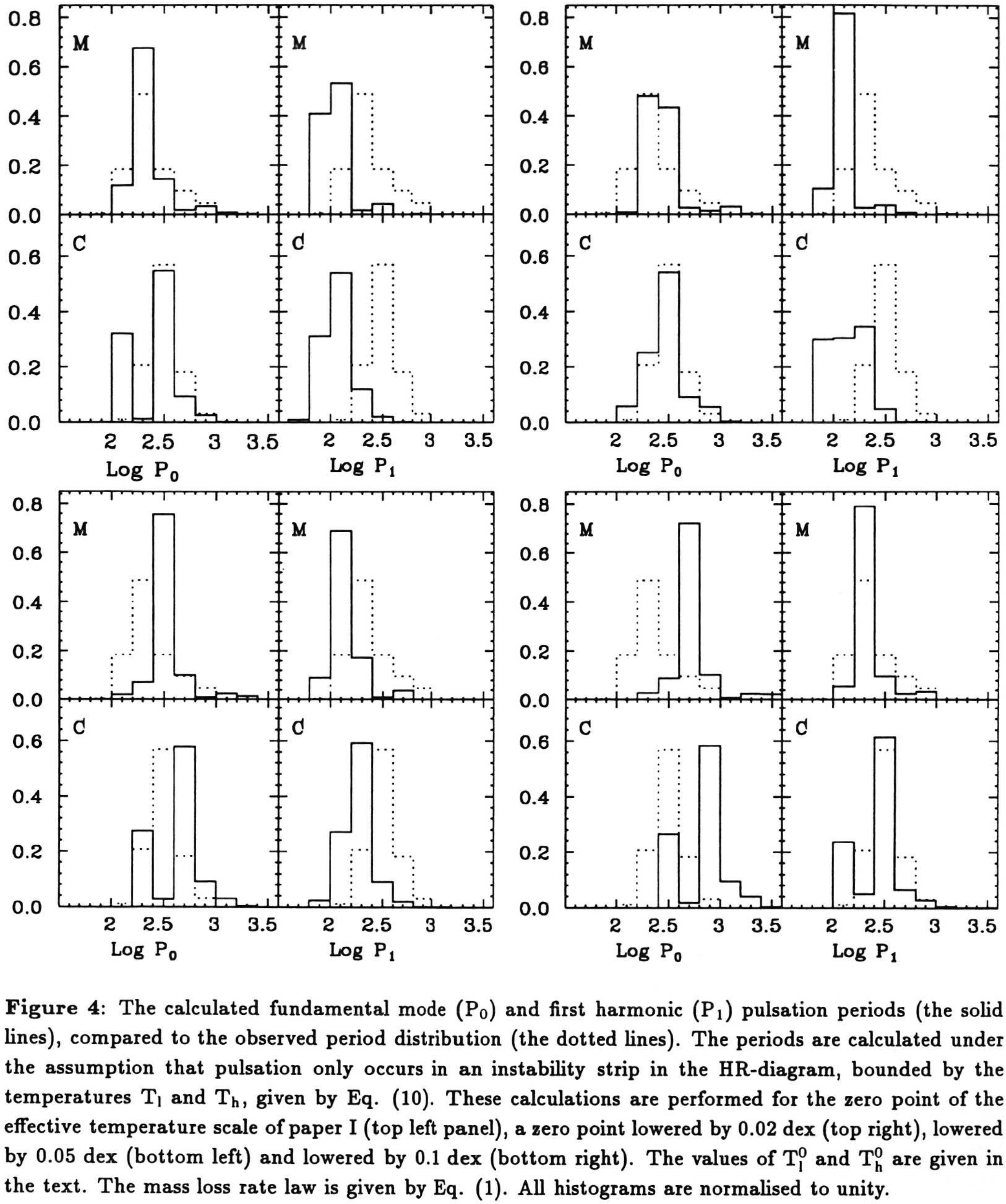

Figure 4: The calculated fundamental mode (P_0) and first harmonic (P_1) pulsation periods (the solid lines), compared to the observed period distribution (the dotted lines). The periods are calculated under the assumption that pulsation only occurs in an instability strip in the HR-diagram, bounded by the temperatures T_l and T_h, given by Eq. (10). These calculations are performed for the zero point of the effective temperature scale of paper I (top left panel), a zero point lowered by 0.02 dex (top right), lowered by 0.05 dex (bottom left) and lowered by 0.1 dex (bottom right). The values of T_l^0 and T_h^0 are given in the text. The mass loss rate law is given by Eq. (1). All histograms are normalised to unity.

M- and C-stars is then compared to the observed period distribution.
The results of the calculations are shown in Fig. 4. For $\Delta \log T_{\rm eff} = 0, -0.02, -0.05, -0.10$ relative to the zero point adopted in paper I, we find $T_l^0 = 3330, 3180, 2970, 2640$ K and $T_h^0 = 3380, 3227, 3014, 2682$ K respectively. The $\Delta \log T_{\rm eff} = -0.02$ model for fundamental mode pulsation provides the best overall fit. The predicted effective temperatures of LPVs at $M_{\rm bol} = -5$ ($T_{\rm eff} \approx 3200$ K) is in agreement with the observed value ($T_{\rm eff} = 3180$ K) derived from the data in

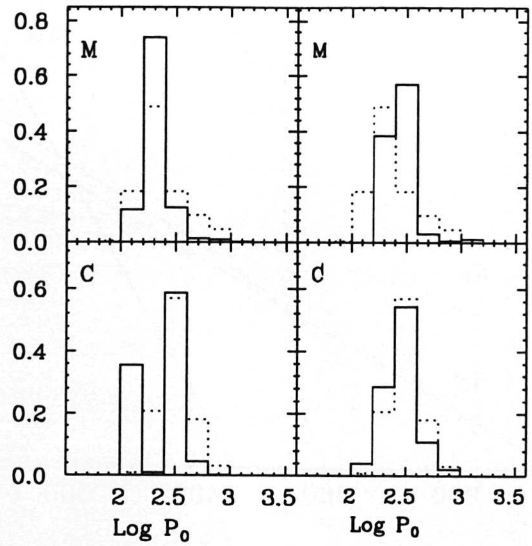

Figure 5: The calculated fundamental mode (P_0) pulsation period distribution (the solid lines), compared to the observed period distribution (the dotted lines). The periods are calculated under the assumption that pulsation only occurs in an instability strip in the HR-diagram, bounded by the temperatures T_l and T_h, given by Eq. (10). The zero point of the effective temperature scale is equal to (left part) and 0.02 dex lower than the scale used in Paper I (right part). The mass loss scaling parameter outside the instability strip, $\eta_{\rm AGB}$, is 5.15 (left side) and 4.7 (right side). The mass loss scaling parameter inside the instability strip, η_{LPV}, is 0.055 (left side) and 0.05 (right side). All histograms are normalised to unity.

Feast et al. (1989). At other luminosities the agreement is equally good since the slope $\frac{dT_{eff}}{dM_{bol}}$ is not a free parameter but determined by observations. When the period distribution for M- and C-stars are considered separately a $\Delta \log T_{\rm eff} \approx -0.01$ model would best fit the M-star period distribution while a $\Delta \log T_{\rm eff} \approx -0.03$ model would best fit the carbon star period distribution. The small remaining discrepancy between the observed and the predicted period distributions may be due to uncertainties in the pulsation constants or a difference in pulsation constants between carbon- and oxygen-rich stars.

Extrapolating our results we estimate that a reasonable fit to the observed period distributions could also be achieved for the first harmonic pulsation mode if $\Delta \log T_{\rm eff} \approx -0.12$. The predicted effective temperature at $M_{\rm bol} = -5$ would be $\sim$2550 K. This would imply that Eq. (9) gives temperatures too high by $\sim$20%, much larger than the uncertainty quoted for Eq. (9) which is $\sim$8%. Based on these arguments we favor fundamental mode pulsation as the (dominant) mode of pulsation in LPVs in the LMC.

In our calculations we adopted a Reimers law in the instability strip. There is observational evidence that in LPVs pulsation and mass loss are related (De Giola-Eastwood et al. 1981, Schild 1989, Wood 1990, Whitelock 1990). We therefore also consider a mass loss rate in the instability strip which is based on Blöcker & Schönberner's (1992) fit to the modelling of LPVs by Bowen (1988). Outside the instability strip we keep Eq. (1). We performed some test calculations to determine η_{LPV} (cf. Eq. 2) since the absolute values of the mass loss rates derived by Bowen are uncertain due to uncertainties in his model. Furthermore, the mass loss rates and effective temperatures in the LMC and in the Galaxy may be different. We proceeded as follows. A value

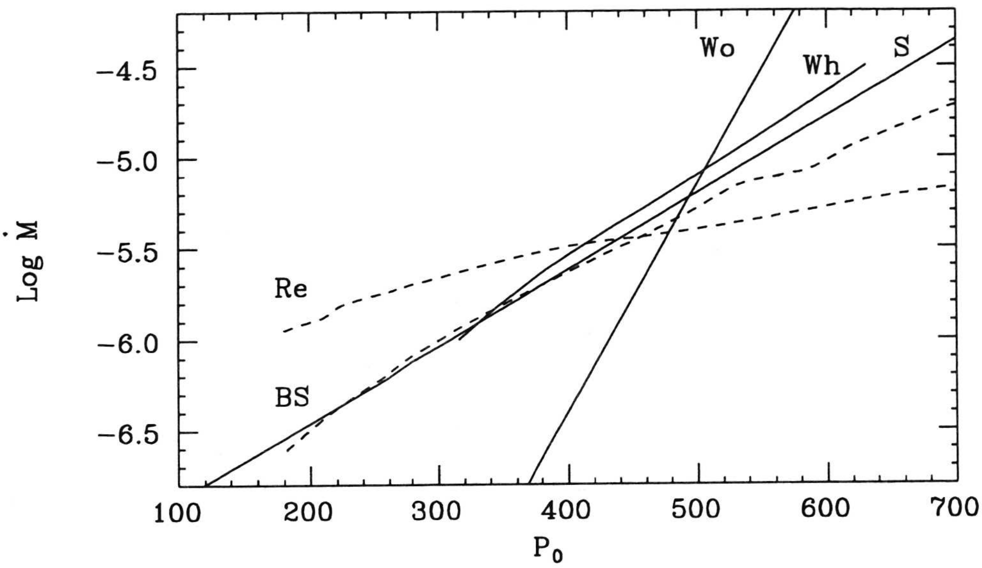

Figure 6: The relation between $\dot{M}$ and fundamental mode pulsation period P_0 for the model with a Reimers law in and outside the instability strip ($\Delta \log T_{eff}$ = -0.02 dex, η_{AGB} = 4.6) indicated by 'Re' and the model with the BS law in the instability strip ($\Delta \log T_{eff}$ = -0.02 dex, η_{AGB} = 4.7, η_{LPV} = 0.05) indicated by 'BS'. Also shown are the observed relations in the Galactic bulge (Whitelock 1990, 'Wh') and the solar neighbourhood (Schild 1989, 'S', and Wood 1990, 'Wo').

for η_{LPV} was assumed. We first determined the value of the mass loss scaling parameter outside the instability strip (η_{AGB}) by considering the carbon star luminosity function and the C/M ratio of AGB stars (see paper I). As before, we then optimised the fit to the period distribution by modifying the zero point of the effective temperature scale. We calculated the $\dot{M}-P$ relation for some stars and guessed a new value for η_{LPV}. The model which best fits the period distribution of the M-stars has the following parameters: $\Delta \log T_{eff} = 0.0$, $\eta_{LPV} = 0.055$, $\eta_{AGB} = 5.15$, $T_l^0 = 3350$ K, $T_h^0 = 3390$ K. The model which best fits the period distribution of the C-stars has the following parameters: $\Delta \log T_{eff} = -0.02$, $\eta_{LPV} = 0.05$, $\eta_{AGB} = 4.7$, $T_l^0 = 3175$ K, $T_h^0 = 3210$ K. The (fundamental) period distributions for both models are shown in Fig. 5. They fit the observed distribution equally well as the simpler model where the mass loss is equal in and outside the instability strip.

The $\dot{M}-P$ relation is shown for the Reimers and for the BS model (both with $\Delta \log T_{eff} = -0.02$) in Fig. 6. For comparison we show the observed relations in the Galactic bulge (Whitelock 1990) and the solar neighbourhood (Schild 1989 and Wood 1990). The error in the observed relations is about 0.2-0.5 dex in $\dot{M}$ for a given P. The relation of Wood is in disagreement with that of Schild and Whitelock, which suggests that the AGB lifetimes of the low mass stars derived by Vassiliadis & Wood (1992) have been overestimated. The slope in the $\dot{M}-P$ relation is well fitted for the BS mass loss law in the instability strip. This is due to the $L^{3.7}$ dependence of the mass loss rate. With a Reimers law ($\sim$L) the slope in the $\dot{M}-P$ relation can not be reproduced as well.

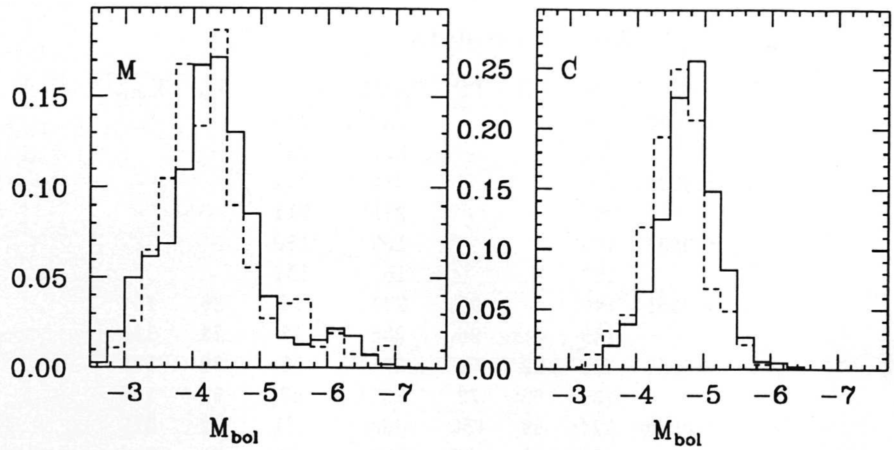

Figure 7: In the left panel the theoretically predicted luminosity function (LF) of oxygen-rich AGB stars (solid line) is compared to the observed LF of oxygen-rich LPVs (dotted line). In the right-hand panel the observed LF of carbon stars on the AGB (solid line) is compared to the observed LF of carbon-rich LPVs (dotted line). The histograms are normalised to unity.

5 Discussion and conclusions

Our exploratory quantitative study into the pulsational properties of LPVs in the LMC leads to two conclusions: (1) fundamental mode pulsation is the (dominant) pulsation mode of LPVs in the LMC, and (2) for most AGB stars the instability strip where (large amplitude) pulsation occurs is not the final phase of AGB evolution.

The mode of pulsation of LPVs has long been a point of controversy. Recently, a consensus seems to have been reached in favor of fundamental mode pulsation (Hill & Willson 1979, Bowen 1988, Wood 1990). Our results support this. Based on our model we exclude first harmonic pulsation unless Eq. (9) overestimates the temperatures by $\sim$20%, which is much larger than the quoted uncertainty of $\sim$8%. Equation (9) was derived for Galactic stars but has traditionally been used for the LMC as well. Based on Eq. (4) we estimate that for fixed mass and luminosity a star in the LMC has a 8-10% lower effective temperature than a corresponding star in the Galaxy. This possible systematic effect does not affect the conclusion about the fundamental mode being the dominant mode of pulsation in LPVs in the LMC.

We implicitly assumed that all LPVs found by Hughes are (thermal pulsing-) AGB stars and not e.g. early-AGB stars. For the carbon stars this assumption is of course valid but for the oxygen-rich stars this may not be the case. When the observed LF of oxygen-rich LPVs is compared to the (predicted) LF of oxygen-rich AGB stars (Fig. 7) one sees that the two LF almost overlap. If the LPV population would contain a significant number of low-luminosity early-AGB (E-AGB) stars one would expect that the LF of LPVs would be more concentrated towards low luminosities, especially since the E-AGB phase lasts much longer than the TP-AGB phase. We conclude that most LPVs found in the Hughes survey are indeed (TP-) AGB stars.

Independent of the exact assumptions on the shape of the instability strip and the mass loss rate in and outside the instability strip, AGB evolution does not end in the instability strip for most stars. This is emphasized in Table 1 where some characteristic lifetimes have been listed for individual stars for the models with $\eta_{\rm AGB}$ = 4.6, η_{LPV} = 0 and $\eta_{\rm AGB}$ = 4.7, η_{LPV} = 0.05 (in both cases $\Delta \log T_{\rm eff} = -0.02$). Only stars between 0.98 and 1.14 $M_\odot$ end the AGB in the

Table 1: Results for some masses

M	Z	TM	TS	TC	TAGB	T_{before}	T_{in}	T_{after}
0.93	0.0020	230	-	-	230	230	-	-
		227	-	-	227	227	-	-
0.96	0.0028	214	-	-	214	214	-	-
		211	-	-	211	211	-	-
1.00	0.0037	159	-	-	159	159	-	-
		157	-	-	157	157	-	-
1.18	0.0061	140	-	91	231	64	36	131
		139	-	96	235	77	23	136
1.30	0.0068	131	92	62	285	75	32	179
		131	92	72	295	89	51	156
1.50	0.0076	124	88	156	368	111	42	215
		124	88	161	373	123	36	214
2.00	0.0082	272	-	338	610	255	44	310
		272	-	347	619	269	35	315
2.50	0.0084	329	84	469	882	465	56	362
		329	84	487	900	477	64	360
3.00	0.0086	380	82	618	1080	658	37	385
		302	160	626	1088	662	55	370
3.50	0.0086	142	55	226	423	212	19	192
		142	37	230	409	213	9	187
4.00	0.0087	219	48	-	267	108	21	138
		208	38	-	246	108	8	130
5.00	0.0087	189	-	-	189	60	16	113
		167	-	-	167	59	5	104

Notes. Listed are the initial mass ($M_\odot$), the metallicity Z, the lifetime of the M, S, C and the total AGB phase, the lifetime before, in and after the instability strip (in 10^3 years). The first line is for the model with $\eta_{AGB} = 4.6$, $\eta_{LPV} = 0.0$, the second line for $\eta_{AGB} = 4.7$, $\eta_{LPV} = 0.05$. In both cases is $\Delta \log T_{eff} = -0.02$.

instability strip. More massive stars spend a considerable amount of time to the right (in the HR-diagram) of the instability strip and stars below 0.98 $M_\odot$ do not reach the instability strip. Although this is contrary to the widespread belief that AGB evolution ends when the star is an LPV, all observations of LPVs in the LMC point to a different conclusion.

In the Galaxy there is the class of the non-variable OH/IR stars (Habing et al. 1987). If a similar scenario holds for the Galaxy as we derive for the LMC, the non-variable OH/IR stars can be interpreted as massive stars ($M_{initial} \gtrsim 3.5\ M_\odot$) which are now in the phase between the end of the instability strip and the end of the AGB. This is an alternative explanation to the one proposed by Habing et al. (1987). Based on the fact that the spectrum of (some) non-variable OH/IR stars is redder than normal OH/IR stars, suggesting that the inner radius of the dust shell has moved away from the star (due to a lower present-day mass loss) Habing et al. suggested that the non-variable OH/IR stars are in the process of moving from the AGB to the post-AGB phase. In our scenario the drop in the mass loss rate is due to the transition from the high-mass-loss instability strip to the lower-mass-loss final AGB phase.

Van der Veen (1989) showed that stars in region IV and V of the IRAS color-color diagram with energy distributions similar to the non-variable OH/IR stars originate from ~4 $M_\odot$ stars and have present-day mass loss rates of 10^{-6} - 10^{-5} $M_\odot$/yr, surprisingly high for post-AGB mass loss which is typically only 10^{-8} - 10^{-6} $M_\odot$/yr.
The transition from the AGB to the post-AGB phase is a brief one (~10^3 years, see e.g. Slijkhuis 1992). The Habing et al. scenario cannot explain why so many of the OH/IR stars are non-variable (van Langevelde 1992 finds that ~20% of OH/IR stars in the Galactic center are non-variable). In our scenario the non-variable OH/IR phase lasts about 10^4-10^5 years relative to a total AGB phase of 1 - 5 10^5 years (see Table 1). If these lifetimes also apply to the Galaxy we predict about 10 - 20% non-variable OH/IR stars, in reasonable agreement with observations.

References

Bessell M.S., Wood P.R., Lloyd Evans T., 1983, MNRAS 202, 59
Blöcker T., Schönberner D., 1992, in: IAU symposium 155 on Planetary Nebulae, eds. R. Weinberger, A. Acker, Reidel, Dordrecht, in press
Boothroyd A. I., Sackmann I.-J., 1988, ApJ 328, 653
Bowen G.H., 1988, ApJ 329, 299
De Giola-Eastwood K., Hackwell J.A., Grasdalen G.L., Gehrz R.D., 1981, ApJ 245, L75
Feast M.W., Glass I.S., Whitelock P.A., Catchpole R.M., 1989, MNRAS 241, 375
Groenewegen M.A.T., de Jong T., 1993, A&A 267, 410 (paper I, Chapter 8)
Habing H.J., van der Veen W.E.C.J., Geballe T., 1987, in: Late stages of stellar evolution, eds. S. Kwok and S.R. Pottasch, Reidel, Dordrecht, p. 91
Hill S.J., Willson L.A., 1979, ApJ 229, 1029
Hughes S.M.G., 1989, AJ 97, 1634
Hughes S.M.G., Wood, P. R., 1990, AJ 99, 784
Jura M., Kleinmann S.G., 1992a, ApJS 79, 105
Jura M., Kleinmann S.G., 1992b, ApJS 83, 329
Kerschbaum F., Hron J., 1992, A&A 263, 87
Menzies J.W., Whitelock P.A., 1985, MNRAS 212, 783
Reimers D., 1975, in: Problems in stellar atmospheres and envelopes, eds. B. Basheck et al., Springer, Berlin, p. 229
Ridgway S.T., Jacoby G.H., Joyce R.R., Wells D.C., 1980a, AJ 85, 1496
Ridgway S.T., Joyce R.R., White N.M., Wing R.F., 1980b, ApJ 235, 126
Schild H., 1989, MNRAS 240, 63
Slijkhuis S., 1992, Ph. D. thesis, University of Amsterdam
Van der Veen W.E.C.J., 1989, A&A 226, 108
Van Langevelde H.J., 1992, Ph. D. thesis, chapter 7, Leiden University
Vassiliadis E., Wood P.R., 1992, preprint
Whitelock P.A., 1990, PASPC 11, 365
Wood P.R., 1990, in: From Miras to Planetary Nebulae, eds. M.O. Mennessier, A. Omont, Editions Frontieres, Gif-sur-Yvette, p. 67
Wood P.R., Bessell M.S., Fox M.W., 1983, ApJ 272, 99

Chapter 12

The evolution of Galactic carbon stars

Abstract

We use literature data for carbon stars in binaries and open clusters, and for C/O ratios in carbon stars, combined with new synthetic AGB evolution calculations, to propose an evolutionary scenario for carbon stars.

We find that the lowest initial mass from which carbon stars form is close to 1.5 $M_\odot$. This constraint combined with four other constraints (the observed initial-final mass relation, the birth rate of carbon stars, the observed abundance ratios in planetary nebulae (PNe) and the number ratios C/M and S/C of AGB stars) are used to derive the following parameters for the synthetic AGB evolution model. Third dredge-up occurs for core masses above 0.58 $M_\odot$ and the dredge-up efficiency is $\lambda = 0.75$. We consider a Reimers mass loss law (with a scaling factor $\eta_{\rm AGB}$) and the mass loss rate law recently proposed by Blöcker & Schönberner (1993; with a scaling factor $\eta_{\rm BS}$). We find $\eta_{\rm AGB} = 4$ and $\eta_{\rm BS} = 0.08$. Both models fit the observations equally well.

The model predicts that stars in the range 1.5 $M_\odot \lesssim M \lesssim 1.6$ $M_\odot$ become carbon stars at their last thermal pulse (TP) on the AGB and live only a few 10^4 yrs as carbon stars. More massive stars experience additional TPs as carbon stars (up to 23 for a 3 $M_\odot$ star) and live up to 10^6 yrs. For M $\lesssim 2$ $M_\odot$, M-stars skip the S-star phase when they become carbon stars. The average lifetime of the carbon star phase is ~ 3 10^5 yrs.

The carbon stars for which C/O ratios have been derived in the literature (with values $\lesssim 1.5$) are predominantly optical carbon stars with a 60 μm excess. Yet, PNe are known with C/O ratios up to about 4. We predict that carbon stars with C/O ratios $\gtrsim 1.5$ are to be found among the infrared carbon stars. The probability that a carbon star has C/O $\gtrsim 1.5$ is about 30%, in reasonable agreement with the observed ratio of the surface density in the galactic plane of infrared carbon stars to all carbon stars. The infrared carbon stars are predicted to be (on average) more massive than the optical carbon stars.

The geometrically thin detached shells around some optical carbon stars are thought to originate from the brief period of high luminosity corresponding to the TP itself when the mass loss rate is considerably higher than in the phase of quiescent H-burning prior to the TP (Olofsson et al. 1990). The fact that carbon stars with C/O $\gtrsim 1.5$ apparently never reach the optical carbon star (with detached shell) phase suggests that the mass loss rate history in these stars is different. The qualitative explanation is as follows. If infrared carbon stars are on average more massive (i.e. have larger core masses) than the optical carbon stars then the interpulse period is shorter, and the increase in luminosity during the TP is smaller (due to the larger envelope mass). Both effects will decrease the likelihood of a detached shell to occur. We predict that two-thirds of all detached shells around optical carbon stars are oxygen-rich.

1 Introduction

The study of carbon stars has gained significant momentum by studying their infrared properties. It was realised that a large number of carbon stars radiate predominantly in the near- and far-infrared and that there are even carbon stars (the infrared carbon stars) with no or very faint optical counterparts.

Different samples of carbon stars, selected on the basis of infrared properties, were studied by Claussen et al. (1987), Thronson et al. (1987), Willems (1988a, b), Jura et al. (1989), Jura & Kleinmann (1989) and Groenewegen et al. (1992). It was recognised that many optical carbon stars have an excess at 60 μm (Willems 1988a). This raised questions on the evolution of carbon stars in general, and that in the IRAS color-color diagram in particular.

Willems & de Jong (1988) proposed a scenario for carbon star evolution related to the occurrence of thermal pulses. In this scenario, the oxygen-to-carbon transition causes the mass loss to drop and the oxygen-rich circumstellar shell to expand and dilute. This gives rise to the characteristic excess at 60 μm observed in many optical carbon stars. Willems & de Jong (1988), Chan & Kwok (1988) and Egan & Leung (1991) modelled the evolution in the IRAS color-color diagram of a carbon star with a detached shell. They assumed the detached shell to be geometrically thick, i.e. they assumed the detached shell to correspond to the mass loss in the phase of quiescent H-burning prior to the thermal pulse that turned the star into a carbon star. It has become clear that this picture needs revision. By mapping the circumstellar shell of S Sct (a carbon star with a 60 μm excess) in CO (Olofsson et al. 1992, Yamamura et al. 1993) and fitting the spectral energy distribution (Groenewegen & de Jong 1993e) it has been shown that this detached shell is geometrically thin. Double-peaked CO line profiles have been observed in two additional carbon stars with a 60 μm excess (Olofsson et al. 1990). Although photodissociation may also play a role, the width of the shells are consistent with the scenario that they correspond to the brief (on the order of 10^3 yrs) period of high mass loss corresponding to the actual thermal pulse. This suggests that the phenomenon of detached shells is not confined to the thermal pulse where the oxygen-to-carbon star transition occurs but is related to thermal pulses in general. This has been confirmed recently by Zijlstra et al. (1992) who showed that there are also M- and S-stars with an excess at 60 μm.

Based on their models, Willems & de Jong and Chan & Kwok estimated that the timescale to make a loop through the IRAS color-color diagram is about 2 10^4 yrs. Assuming a geometrically thin shell and taking into account the limited beam-size of the IRAS detectors, Groenewegen & de Jong (1993e) showed for S Sct that this timescale is probably overestimated by about 30%.

Groenewegen et al. (1992) extended the evolutionary scenario of Willems & de Jong to the infrared carbon stars. They derived space densities and lifetimes under the assumption that the sequence of optical carbon stars to infrared carbon stars is an evolutionary sequence and that carbon stars only make one loop through the IRAS color-color-diagram. A total carbon star lifetime of ~26 000 yrs was estimated.

The validity of this short carbon star lifetime has been questioned by Zuckerman and co-workers who also argued that the detached shell around optical carbon stars should be carbon-rich rather than oxygen-rich (Claussen et al. 1987, Jura 1988, Zuckerman & Maddalena 1989, Zuckerman 1993, but see de Jong 1989).

In this paper we want to address several questions regarding the evolution of carbon stars on the AGB: (1) is the detached shell around optical carbon stars oxygen-rich or carbon-rich, (2) how many thermal pulses does a carbon star make and does this result in as many loops through the IRAS color-color diagram, (3) what is the lifetime of the carbon star phase and (4) is the distribution of carbon stars in the IRAS color-color-diagram a sequence in time or in initial mass?

To answer these questions we combine existing literature data with new synthetic AGB calculations, which already proved to be successful in explaining the properties of carbon stars and the abundance ratios in planetary nebulae (PNe) in the LMC (Groenewegen & de Jong 1993a, b, c). In Sect. 2 the synthetic AGB evolution model is introduced and the constraints are discussed in Sect. 3. In Sect. 4 the results of the calculations are presented. In Sect. 5 the evolutionary scenario is presented and discussed.

2 The synthetic AGB evolution model

The synthetic evolution model is explained in detail in Groenewegen & de Jong (1993a, paper I). It is based on recent evolutionary calculations for low- and intermediate-mass stars. Here only the most important features are outlined and some improvements to the previous model are discussed. The calculations in the present paper supersede the preliminary calculations for the Galaxy presented in Table 5 of paper I.

In the model a population of stars is selected according to the probability that they presently are on the AGB. This probability depends on the initial mass function, the star formation rate and the duration of the AGB phase, as outlined in paper I. With such an approach, average population properties (e.g. a luminosity function) can be calculated, using as input the evolution of individual stars.

AGB evolution starts at the first thermal pulse and ends when the envelope mass of the AGB star is reduced to $\sim 10^{-3}$ $M_{\odot}$. The changes in the abundances due to the first and second dredge-up, prior to the AGB phase, are taken into account. On the AGB, third dredge-up is assumed to occur for core masses above M_c^{min}. For the LMC we derived M_c^{min} = 0.58 $M_{\odot}$ (paper I). At each thermal pulse an amount $\Delta M_{dredge} = \lambda\ \Delta M_c$ is added to the envelope, where ΔM_c is the core mass growth during the preceding interpulse period and λ is the dredge-up efficiency. For the LMC we derived $\lambda = 0.75$ (paper I). The composition of the material dredged-up is: carbon (22%), oxygen (2%) and helium (76%).

Prior to the AGB, stars lose mass on the main sequence, on the Red Giant Branch (RGB; only important for stars below $\sim$2.2 $M_{\odot}$ which experience the helium core flash) and on the Early-AGB (E-AGB; important for massive stars). The total mass lost by stars with initial masses $\lesssim$2.2 $M_{\odot}$ preceding the AGB is taken from the models of Sweigart et al. (1990) scaled in such a way to give a mass loss of 0.22 $M_{\odot}$ for a 0.85 $M_{\odot}$ star (η_{RGB} = 0.86 in the nomenclature of Sect. 2.6.1 of paper I). In paper I we used the evolutionary tracks of Maeder & Meynet (1989) to estimate the mass loss rate prior to the AGB for massive stars. With the new tracks of Schaller et al. (1992) and Schaerer et al. (1993) it is possible to include a metallicity dependence. Equation 21 in paper I is replaced by:

$$\Delta M_{EAGB} = \eta_{EAGB}\ 0.116 \left(\frac{Z}{0.008}\right)^{0.61} \left(\frac{M}{7}\right)^{1.97\left(\frac{Z}{0.008}\right)^{0.35}} \qquad M_{\odot}. \tag{1}$$

Schaller et al. (1992) find a mass loss rate at the start of the thermal-pulsing AGB of 6.1 10^{-8} and 3.1 10^{-7} $M_{\odot}$/yr for a 3 and a 5 $M_{\odot}$ solar metallicity star. In order to let the mass loss rate prior to the AGB be in better agreement with that predicted by us at the start of the AGB we adopt η_{EAGB} = 3. This choice does not affect any of our results since ΔM_{EAGB} is always much smaller than the envelope mass at the start of the TP-AGB. Unfortunately, observationally determined mass loss rates of massive E-AGB stars are unavailable to estimate η_{EAGB}.

In paper I mass loss on the AGB was described by a Reimers (1975) law with a scaling factor η_{AGB}. For the LMC we derived η_{AGB} = 5 in paper I. In paper III (Groenewegen & de Jong 1993c) we showed that with the mass loss rate law proposed by Blöcker & Schönberner (1993;

BS) an equally good fit to the observational constraints in the LMC can be obtained. In paper IV (Groenewegen & de Jong 1993d) we showed that with the latter mass loss rate the slope in the observed relation between the mass loss rate and pulsation period is reproduced. In the present paper both mass loss laws are considered. The Reimers mass loss law is:

$$\dot{M} = \eta_{AGB}\, 4.0\; 10^{-13}\, \frac{L\,R}{M} \qquad M_\odot/yr. \tag{2}$$

with L, R and M in solar units. The mass loss rate law proposed by BS is:

$$\dot{M} = \eta_{BS} \left(4.8\, 10^{-9}\, \frac{L^{2.7}}{M^{2.1}}\right) \left(4.0\, 10^{-13}\, \frac{L\,R}{M}\right) \quad M_\odot/yr \tag{3}$$

i.e. a Reimers law with an additional ($L^{2.7}/M^{2.1}$) dependence. We include a scaling factor η_{BS}. BS derived this law by fitting the mass loss rates listed by Bowen (1988) for his standard model based on dynamical calculations for long-period variables. Direct comparison of Eqs. (2) and (3) shows that the mass loss rate adopted by BS is equivalent to high Reimers coefficients. For representative values of L = 3000 $L_\odot$, M = 1 $M_\odot$ or L = 20 000 $L_\odot$, M = 5 $M_\odot$ the equivalent value of η_{AGB} are 12 and 67, respectively. Repeating the analysis of papers I and II (Groenewegen & de Jong 1993b) we found that all constraints in the LMC can be fitted with $\eta_{BS} = 0.1$ (paper III).

A major improvement to the model are the estimates of the main sequence abundances. In paper I (Sect. 2.9.1) we estimated the main sequence helium abundance from the primordial helium value and a simple $\Delta Y/\Delta Z = 2.5$ scaling law and assumed that the decomposition of Z (the sum of all metals) in carbon, oxygen and nitrogen is constant in time and equal to the solar value. In the present paper we use separate age-metallicity relations for Z, He, C, N and O derived for the solar neighbourhood by van den Hoek et al. (1993). The star formation rate and slope of the initial mass function are also taken from this paper (see Fig. 1).

The tracks of Schaller et al. (1992) have been used to calculate the total lifetime prior to the AGB. This lifetime is needed to estimate the metallicity of a star on the main sequence from the adopted age-metallicity relation and the star formation rate at the time of birth of a star. The new pre-AGB lifetimes are longer than those used in paper I (that were based on a fit by Iben & Laughlin 1989). The age of the Galaxy is taken as 14 Gyr, indicating that the lower mass limit of stars that can reach the AGB is $M_{lower} = 0.966\ M_\odot$ (from Schaller et al. 1992). The upper mass limit is taken as $M_{upper} = 8\ M_\odot$. More massive stars are assumed to evolve into supernovae.

3 The constraints

In this section we discuss five constraints to the synthetic evolution model. Four of these, the abundances of PNe, the birth rate of carbon stars, the number ratio of M-, S- and C-stars on the AGB, and the initial-final mass relation, are similar to those used for the LMC in paper I, and are briefly discussed in Sect. 3.2. The last constraint, the mass range from which carbon and S-stars form, is discussed in detail below.

3.1 The mass range from which carbon stars and S-stars form

The most reliable information on the mass of C-stars (and S-stars) can be obtained from stars in binaries and open clusters. In a classical paper Gordon (1968) listed 10 candidates for binaries containing a carbon star and a less evolved star. Later work includes Barbaro & Dallaporta (1974), Olson & Richer (1975) who added some new candidates, Reimers & Grootte (1983) and

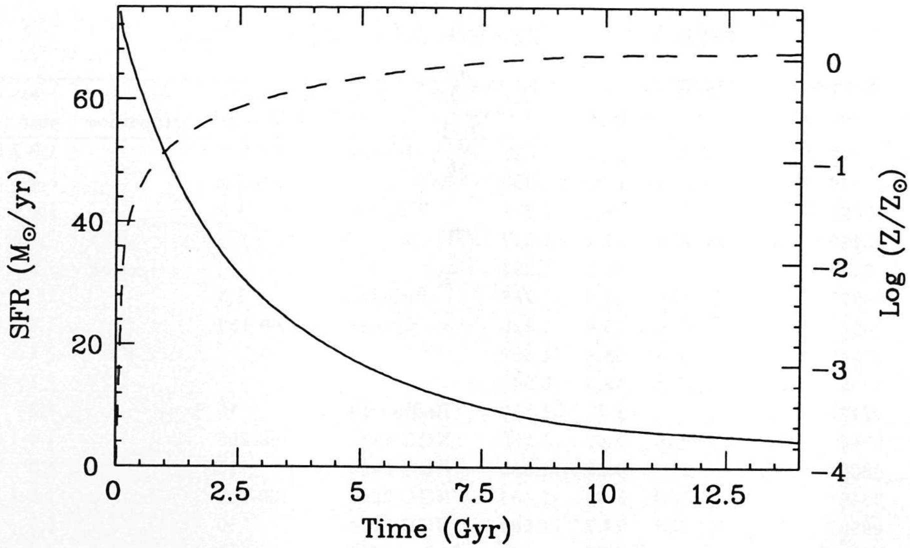

Figure 1: The star formation rate (solid line; left-hand scale) and age-metallicity relation (dashed line, right-hand scale) adopted in this study for the solar neighbourhood (van den Hoek et al. 1993).

Le Bertre (1990). Carbon stars in clusters are discussed by Gordon (1968), Barbaro & Dallaporta (1974), Bouchet & Thé (1983), Jørgensen (1988) and most recently by Eggen & Iben (1991).
In Table 1 all suspected binaries containing a carbon star with spectral type N (indicating the star is cool and therefore on the AGB) and a main sequence companion, and all N-type carbon stars which may be in open clusters are collected. Possible carbon stars with giant companions or companions of which the luminosity class is unknown or uncertain are not considered since no reliable masses can be estimated in these cases. In Table 1 the number in the Stephenson's catalog (1989), the IRAS-name[1], the variable star name, the 12 μm flux-density, the C_{21} color (defined as 2.5 $\log(S_{25}/S_{12})$), the cluster name, the age of the cluster, the spectral type of the companion and the estimated main sequence mass of the carbon star are listed. The spectral type of the companion is transformed into a mass using the spectral type-mass conversion of Straižys & Kuriliene (1981) and Schmidt-Kaler (1982). This is a lower limit to the main sequence mass of the carbon star. An uncertainty of one spectral sub-class corresponds to an uncertainty of $\sim$0.06 $M_{\odot}$ at spectral type F2V, and of $\sim$2 $M_{\odot}$ at B2V. For the carbon stars in clusters the mass of the carbon star is estimated using the turn-off age and the tracks of Schaller et al. (1992). From Table 1 we derive that carbon stars are formed from stars above 1.8 $M_{\odot}$ (from the cluster data), although the data on carbon stars in binaries allows masses of $\gtrsim$1.2 $M_{\odot}$ for carbon star formation. The upper mass limit is more uncertain but is at least 5 $M_{\odot}$ and may be higher.
The information on S-stars in binaries and clusters is scarce (see Scalo & Miller 1979). An additional complication is that S-stars are observed with and without the radioactive s-process element technetium (Tc). Only S-stars with Tc are believed to be on the AGB (see Chapter 4). The S-stars with Tc in binaries are π Gru and the lithium-rich star T Sgr. The former has a G0V companion implying an initial mass for π Gru of $\gtrsim$1.1 $M_{\odot}$. On the other hand, π Gru is normally associated with the Hyades implying a mass of 1.9-2.5 $M_{\odot}$ (see Table 1). The star T Sgr has an F3IV companion implying an initial mass of $\gtrsim$1.5 $M_{\odot}$. S-stars possibly in clusters

[1]All stars turned out to be detected by IRAS. This was not a selection criterion.

Table 1: Carbon stars in binaries and open clusters

C	IRAS-name	GCVS	S_{12} (Jy)	C_{21}	cluster name	age cluster (10^7 yrs)	Sp. type companion	mass C-star ($M_\odot$)
471	03112−5730	TW Hor	94.0	-1.028	Hyades	60-150		1.9-2.5
789	04476+4335	HN Aur	2.78	-1.390	NGC 1664	1.0-3.2		3.5-5.1
853	05028+0106	W Ori	184.	-1.377	Pleiades	1.3		15
911	05185+3227	UV Aur	69.4	-1.317			B9V	$\gtrsim$3.5
1263	06217−2702		20.5	-1.293			A5V	$\gtrsim$2.2
1264	06225+1445	BL Ori	44.5	-1.258	Pleiades	1.3		15
1478	06528−4218	NP Pup	35.9	-1.120	Hyades	60-150		1.9-2.5
1549	07045−0728	RY Mon	58.8	-1.352			F3IV	$\gtrsim$1.5
1565	07057−1150	W CMa	39.0	-0.941			B2V	$\gtrsim$10.4
1859	07427−2816		1.47	-1.310	Haffner 14	16		4.3
1910	07487−3839	QT Pup	3.61	-1.280	NGC 2447	160-200		1.8-1.9
2063	08050−2939		4.61	-1.383	NGC 2533	16		4.3
2315	08408−4701	GV Vel	3.36	-1.183	NGC 2660	160-200		1.8-1.9
2685	09582−5958	SZ Car	24.7	-1.087	NGC 3114	10		5.1
3526	14417−6129		4.73	-1.411	Loden 1409	16		4.3
3875	17419−1836	SZ Sgr	18.6	-0.674			A7V	$\gtrsim$1.8
4111	18448+0523	DR Ser	16.0	-0.948			A6IV	$\gtrsim$2.1
4653	20028+2030	X Sge	16.8	-1.144			F2V	$\gtrsim$1.5
4716	20085+3547	RY Cyg	9.1	-1.325	NGC 6883	3.2-6.5		6.1-8.6
5570	22036+3315	RZ Peg	15.8	-0.874			F9V	$\gtrsim$1.2
5987	00020+4316	SU And	10.4	-1.219			F0V	$\gtrsim$1.7

are the lithium-rich star TT9 (in N 3372, M $\gtrsim$10 $M_\odot$, no data on Tc), TT10 (in N 3372, M $\gtrsim$10 $M_\odot$, no data on Tc), TT12 (in N 3572b, M $\gtrsim$10 $M_\odot$, no data on Tc) and R And (in the Wolf 630 group, M $\approx$ 1.7 $M_\odot$, contains Tc).

Additional information about the typical mass of S-stars and C-stars comes from kinematical data and from some binaries containing a White Dwarf (WD). Dean (1976) finds that the majority of carbon stars kinematically behave like F5 stars, although his figure 4 suggest that the spectral type is closer to F3, corresponding to a mass of about 1.5 $M_\odot$.

The S-stars without technetium, the barium-stars and the CH-stars are in binary systems which consist of a WD and a star with enhanced (relative to normal giants) s-process elements and C/O ratio. These chemical peculiarities are believed to be due to a previous phase of mass transfer when the WD was on the AGB (see Chapter 1). The presence of such systems places a lower limit to the mass at which third dredge-up occurs.

The mass function ($Q \equiv M_{WD}^3/\ (M + M_{WD})^2$) of the barium- and the S(no-Tc) stars is Q = 0.04-0.05 (Jorissen & Mayor 1992). Since the WD must have a core mass high enough for third dredge-up to have occurred on the AGB ($M_{WD} \geq M_c^{min}$) and experienced some core-growth during its AGB evolution, this implies a lower limit to the current mass of the secondary of 1.4 $M_\odot$ (for Q = 0.05 and M_{WD} = 0.57 $M_\odot$) and a probable mass of 1.5 $M_\odot$ (for Q = 0.044 and M_{WD} = 0.58 $M_\odot$). Since the secondary is probably on the RGB now, its main sequence mass may have been a little higher (by a few 10^{-2} $M_\odot$) due to mass loss on the RGB. On the other hand, if mass transfer from the former AGB star was very effective (due to Roche-lobe overflow) the secondary may now be more massive than on the main sequence. Jorissen & Boffin (1992) argue, however, that a wind accretion model can explain the observed chemical peculiarities of

Ba-stars.
Considering all observational evidence we conclude that the lowest initial mass at which third dredge-up produces S-stars and C-stars occurs close to 1.5 $M_\odot$ (within 0.1 $M_\odot$).

3.2 The other constraints

The second constraint is the observed ratio of the number of carbon-, S- and M-stars on the AGB. This number is taken from Herman (1988) and Jura & Kleinmann (1992a, b). Herman (1988) finds a ratio C/M = 0.18 and S/C = 0.28. Jura & Kleinmann (1992a, b) investigate the number densities and scaleheights of M-, S- and C-rich Miras and semi-regulars (SRs). Although it is unclear if AGB stars are LPVs (long period variables) during their entire AGB life (in the LMC this is not the case, see e.g. paper IV and references therein), the C/M-ratio of LPVs may be indicative for the AGB as a whole. The C-stars, S-stars and the oxygen-rich Miras with periods between 300-400 days and the SR's with periods between 100-150 and 300-400 days all have about the same scaleheight and therefore presumably evolved from the same population. For this data set the ratios of stars are C/M = 0.21 and S/C = 0.30, in good agreement with the earlier estimate.
The third constraint is the observed abundance ratios in planetary nebulae (PNe). In paper II we showed that these can constrain the duration of the AGB phase. The abundances are taken from a variety of sources but mainly from Aller & Cryzack (1983), Zuckerman & Aller (1986), Aller & Keyes (1987) and Kaler et al. (1990). The few Halo PNe are not included, since the present calculations concentrate on the galactic disk. The errors in the observed abundances are typically 0.015 in He/H and about 0.2 dex in all other ratios. In the model the abundances of PNe are estimated by averaging the abundances in the ejecta over the final 5 10^4 yrs on the AGB. This should be representative of the abundances determined in PNe. The predicted abundances do not change significantly if a lifetime of 2 10^4 is adopted. We do not claim that all our model stars will become PNe. Some stars may evolve so slowly in the post-AGB phase that the material ejected during the AGB phase is dispersed before the central star is hot enough to ionize the material.
The fourth constraint is the observed initial-final mass relation based on WDs in the solar neighbourhood (for detailed references see paper I).
The fifth constraint is the birth rate of PNe and the death rate of main sequence stars. Pottasch (1992) quotes a birth rate of PNe of 0.5-2 yr^{-1} in the Galaxy. The fraction of carbon-rich PNe (in the solar neighbourhood) is $\sim$0.6 (Zuckerman & Aller 1986). Extrapolating to the Galaxy gives a birth rate of C-rich PNe of 0.3-1.2 yr^{-1}.
From the SFR model of van den Hoek et al. (1993) for the Galaxy we derive a (present-day) birth rate of carbon stars (initial mass range 1.5-8 $M_\odot$) of 0.36 yr^{-1}, calculated from the death rate of main sequence stars a pre-AGB lifetime ago. For masses above 1.5 $M_\odot$ (lifetimes $\lesssim$3 Gyr) the SFR is nearly constant (cf. Fig. 1) and the main uncertainty (less than a factor of 2) in the derived birthrate is the observed present-day SFR.

4 Results of the synthetic evolution model calculations

The parameter space in M_c^{min}, λ and η_{AGB} (c.q. η_{BS}) is investigated. The models that best fit all constraints simultaneously have the following parameters: $M_c^{min} = 0.58$ $M_\odot$, $\lambda = 0.75$ (as derived for the LMC in paper I) and $\eta_{AGB} = 4$, c.q. $\eta_{BS} = 0.08$.
For the Reimers mass loss, there is only a small range in the parameters which can fulfill the constraints. Values for η_{AGB} smaller than 4 are not possible since then the initial-final mass

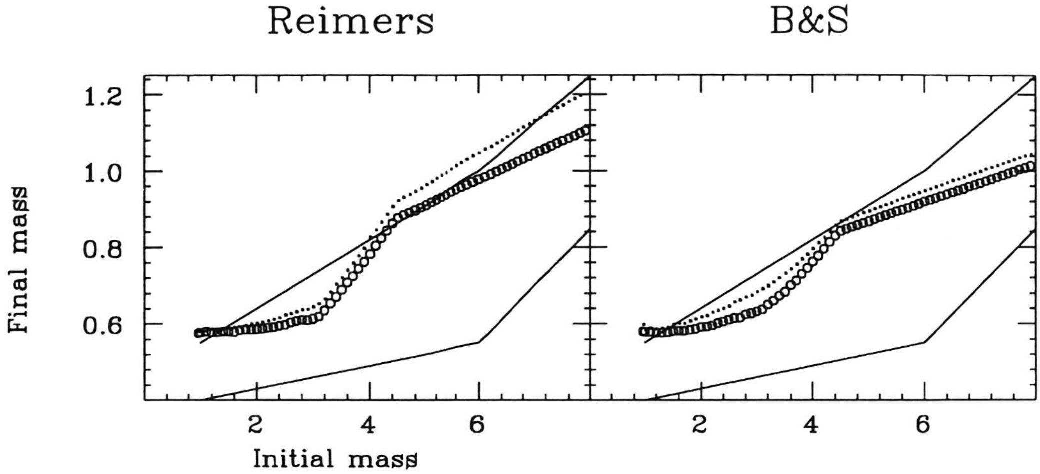

Figure 2: The initial-final mass relation for Reimers and the BS mass loss. The best-fitting models are represented by the circles, while the minimum and maximum mass allowed for by the observations are indicated by the two lines. For the Reimers law a model with M_c^{min} = 0.58 $M_\odot$, λ = 0.75 and η_{AGB} = 2 is also shown (dots); for the BS law a model with M_c^{min} = 0.59 $M_\odot$, λ = 0.65 and η_{BS} = 0.03 is also shown (dots).

constraint is no longer fulfilled (see Fig. 2). Larger values for η_{AGB} result in the formation of fewer carbon stars and lower values of the maximum predicted C/O ratio in PNe. In principle, this can be compensated for by decreasing M_c^{min} or increasing λ. However, values of M_c^{min} below 0.57 $M_\odot$ can be excluded since then nearly all stars go through a carbon star phase, for any reasonable choice of the other parameters. This violates the observed lower limit of $\sim$1.5 $M_\odot$ for carbon star formation. For M_c^{min} = 0.575 $M_\odot$ and λ = 0.90, a model with η_{AGB} = 5 fits the constraints about equally well as the best-fitting model. Models with $\eta_{AGB} \geq 7$ can be excluded since then e.g. the maximum predicted C/O ratio in PNe is only $\sim$3 instead of the observed value of 4 (see Fig. 3) and the ratio of C/M stars is only 0.11.

The BS mass loss law, allows for a wider range of possible parameters. The value of η_{BS} can be as low as 0.03 and still fulfill the observed initial-final mass relation (Fig. 2). A model with η_{BS} = 0.03, M_c^{min} = 0.59 $M_\odot$, λ = 0.65 can fulfill most constraints. However, the average lifetime of the carbon star phase then becomes so long (35% longer then for the best-fitting model) that the constraint on the birth rate of carbon stars is not fulfilled.

For M_c^{min} = 0.573 $M_\odot$ and λ = 0.90, a model with η_{BS} = 0.16 can fit all constraints. However, for λ = 0.90 the increase in the C/O ratio at every thermal pulse is so large that the C/O ratio of $\sim$1.5 $M_\odot$ stars when they turn into carbon stars is larger than 2. However, the largest C/O ratio observed in optical carbon stars is $\sim$1.8 and most have a C/O ratio near 1.2 (Lambert et al. 1986, see the discussion in Sect. 5.2). The best constraint to determine M_c^{min} and λ is the observed luminosity function of carbon stars (paper I), which unfortunately is not available in the Galaxy due to the lack of reliable distances. The sensitivity of the M-, S- and C-star LFs to M_c^{min} and λ is illustrated in Fig. 4.

The best-fitting Reimers and BS model are now discussed in detail. In Fig. 2 the predicted and observed initial-final mass relation are compared for the Reimers and the BS law. Both fit the observations about equally well. Because the BS mass loss law has a stronger luminosity dependence, the mass loss rate for the massive stars is larger than for the Reimers case and vice

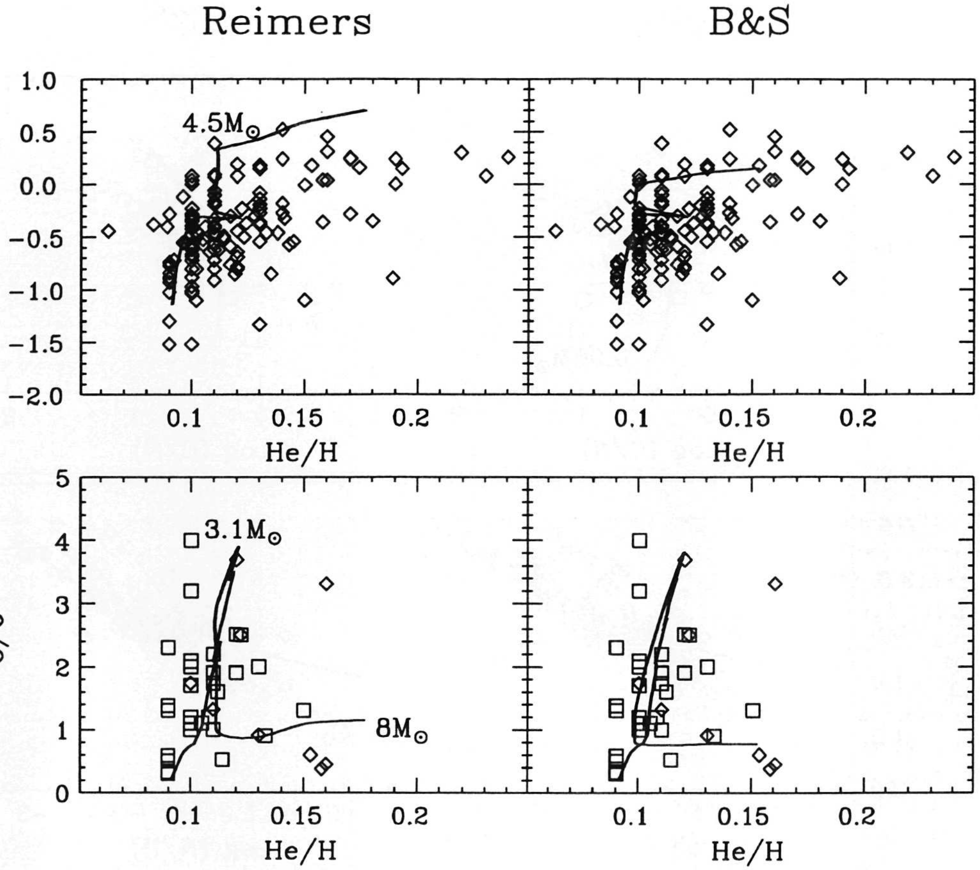

Figure 3: The predicted (the solid line) and observed abundance ratios in galactic planetary nebulae (PNe). In the C/O-He/H diagram the observed type I PNe (with N/O>0.5) are indicated by a ◇ and the non-type I PNe by a □. Some initial masses are indicated.

versa for the low mass stars. That is the reason why the final masses for the massive stars in the BS model are lower than in the Reimers model and vice versa for the low mass stars.
The predicted average mass of the central stars of PNe (CSPNe), c.q. WDs, is 0.578 $M_\odot$ for both the Reimers and the BS mass loss law. This is in good agreement with observations. From Bergeron (1992) we calculate for 112 WDs with masses between 0.45 and 1 $M_\odot$ (the WDs with lower masses are thought to have originated from binary evolution) that the average mass is 0.583 $M_\odot$. The mass estimate of CSPNe is hampered by uncertainties in the determination of effective temperature and luminosity but generally most CSPNe have masses between 0.55 and 0.6 $M_\odot$ (Weidemann 1990).
In Fig. 3 the observed and predicted abundances in PNe for the two best models are compared. We expect to find three distinct groups of stars. The first group consists of stars with initial masses less than about 1.5 $M_\odot$. These stars do not experience the second dredge-up and have core masses too low for the third dredge-up to occur. In these stars we expect to see the main sequence abundances changed by the first dredge-up process only. The second group consists of stars in the initial mass range 1.5 $M_\odot \lesssim M \lesssim 4$ $M_\odot$. After the first dredge-up (and maybe

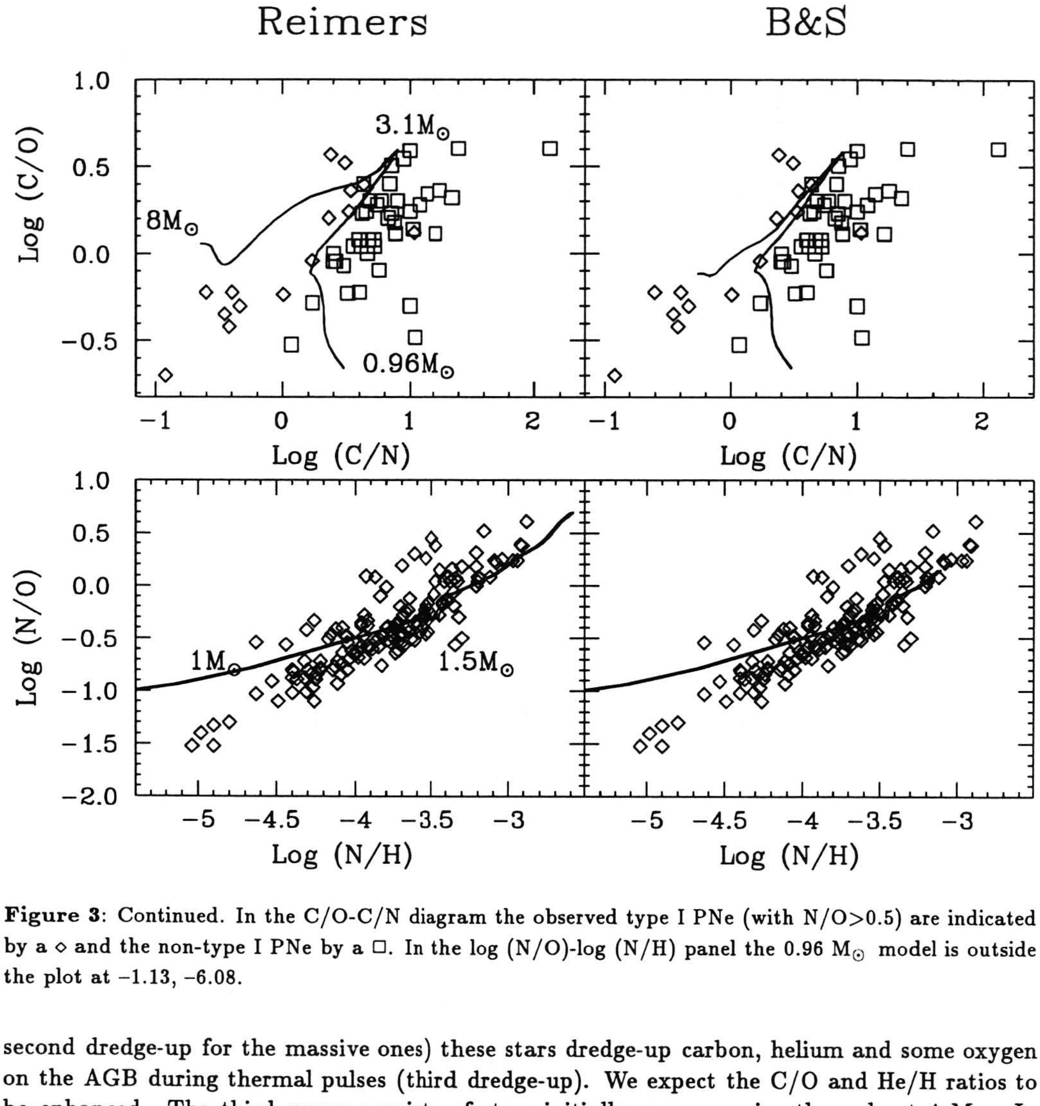

Figure 3: Continued. In the C/O-C/N diagram the observed type I PNe (with N/O>0.5) are indicated by a ◇ and the non-type I PNe by a □. In the log (N/O)-log (N/H) panel the 0.96 $M_{\odot}$ model is outside the plot at −1.13, −6.08.

second dredge-up for the massive ones) these stars dredge-up carbon, helium and some oxygen on the AGB during thermal pulses (third dredge-up). We expect the C/O and He/H ratios to be enhanced. The third group consists of stars initially more massive than about 4 $M_{\odot}$. In these stars, the carbon dredged-up during thermal pulses is largely converted to nitrogen by hot bottom burning (HBB; see paper I).

In the N/O-He/H panel the main difference between the Reimers and the BS model is in the predicted N/O ratio for masses above 4.5 $M_{\odot}$. Both models fail to predict He/H ratios larger than 0.2. This may be due to the adopted parameterization of HBB. In the C/O-He/H panel the main difference is in the C/O ratio of the most massive stars. The Reimers model predicts C/O $\gtrsim$1 while the few observations (the ◇'s near He/H = 0.16) seem to favor the BS model. In the C/O-C/N panel the differences are small. Both models predict too small C/N ratios for a given C/O ratio in the mass range 1.5-3 $M_{\odot}$. In the N/O-N/H panel differences are small. Most interestingly, for M $\lesssim$1.5 $M_{\odot}$ the relation between N/O and N/H is determined by the age-metallicity relation of N and O for main sequence stars. Stars in this mass range do not experience a third dredge-up and the effects of the first dredge-up are not very mass dependent.

Table 2: Results for individual stars

M ($M_\odot$)	Z	P (%)	model	TM	TS	TC	TAGB	N_c	N_{tot}	$\dot{M}_{AGB}$ (10^{-6} $M_\odot$/yr)	C/O [1]	$^{12}C/^{13}C$ [1]	C/O [2]	$^{12}C/^{13}C$ [2]
					(10^3 yrs)									
0.97	0.0008	0	Re	486	0	0	486	-	3	0.43	-	-	0.23	23
			BS	544	0	0	544	-	3	0.43	-	-	0.23	23
1.0	0.0033	29.2	Re	206	0	0	206	-	3	0.91	-	-	0.35	23
			BS	232	0	0	232	-	3	0.80	-	-	0.35	23
1.2	0.0107	74.2	Re	281	0	0	281	-	4	1.38	-	-	0.67	23
			BS	264	0	0	264	-	4	1.47	-	-	0.67	23
1.4	0.0171	85.5	Re	358	0	0	358	-	5	1.70	-	-	0.78	23
			BS	324	0	0	324	-	5	1.88	-	-	0.78	23
1.45	0.0178	87.0	Re	359	0	28	386	6	6	1.73	5.02	219	5.02	219
			BS	338	0	0	338	-	5	1.97	-	-	0.79	23
1.5	0.0181	88.2	Re	356	0	52	407	6	6	1.77	2.38	80	2.38	80
			BS	351	0	0	351	-	5	2.06	-	-	0.80	23
1.55	0.0182	89.2	BS	355	0	37	392	6	6	1.99	1.59	50	1.59	50
1.6	0.0182	90.1	Re	354	0	106	460	6	7	1.82	1.47	45	7.47	433
			BS	354	0	62	416	6	6	2.01	1.27	39	1.27	39
1.75	0.0183	92.5	Re	354	0	204	558	6	8	1.80	1.16	35	7.81	480
			BS	354	0	173	527	6	7	1.90	1.07	32	1.47	46
2.0	0.0185	95.3	Re	352	91	310	753	7	10	1.71	1.28	40	6.50	341
			BS	352	91	367	810	7	10	1.59	1.18	36	2.08	70
2.5	0.0188	97.5	Re	351	91	773	1214	7	15	1.52	1.03	33	4.08	171
			BS	351	91	1166	1607	7	20	1.15	1.00	32	3.26	126
3.0	0.0189	98.6	Re	437	185	1001	1623	9	21	1.43	1.08	36	4.33	194
			BS	437	185	1667	2289	9	31	1.00	1.04	35	3.54	147
3.5	0.0191	99.2	Re	106	119	746	971	8	28	2.80	1.05	34	6.12	332
			BS	106	119	640	865	8	25	3.15	1.04	34	3.00	119
4.0	0.0191	99.6	Re	55	83	537	675	11	48	4.56	1.01	33	3.69	155
			BS	55	83	183	321	11	22	9.66	1.01	33	1.57	55
5.0	0.0191	99.9	Re	391	161	0	552	-	129	6.97	-	-	0.86	16
			BS	140	0	0	140	-	29	27.9	-	-	0.75	20
7.0	0.0192	99.9	Re	181	281	113	575	326	444	9.32	1.00	15	1.13	13
			BS	99	0	0	140	-	55	54.9	-	-	0.77	20

Notes. (1) the C/O ratio and the $^{12}C/^{13}C$ ratio at the thermal pulse when the star becomes a carbon star, (2) the C/O ratio and the $^{12}C/^{13}C$ ratio at the end of the AGB.

Listed are the initial mass, the initial metallicity, the cumulative probability to find a star on the AGB with a mass between M_{lower} and M, the type of model (Re = Reimers, BS = Blöcker & Schönberner), the lifetime of the M, S, C and the total AGB phase, the pulse number at which the star becomes a carbon star, the total number of thermal pulses on the AGB and the average mass loss rate on the AGB.

The predicted position of the 0.96 $M_\odot$ model is off the plot at log (N/O) = −1.13, log (N/H) = −6.08. The lowest observed log (N/H) ratio is −5.0. There are several explanations for this discrepancy: (1) The age-metallicity relation for N and/or O for M $\lesssim$1 $M_\odot$ ($\gtrsim$10 Gyr) is incorrect, (2) stars below $\lesssim$0.98 $M_\odot$ do not reach the AGB either because mass loss prior to the AGB has ended their life prematurely or because the age of the Galaxy (c.q. the Galactic disk) is less than 14 Gyr ($M_{lower} \approx 0.98\ M_\odot$ instead of $0.96\ M_\odot$). Alternatively, (3) stars do reach the AGB but do not form a PN (evolution too slow), or (4) have so far not been observed (due to their expected low surface brightnesses). A combination of the last two arguments seems the most plausible.

The predicted ratio of stars for both mass loss models is C/M = 0.15 and S/C = 0.13. Both ratios are somewhat below the observed values. The C/M ratio is sensitive to the SFR during the first 10 Gyr. A lower SFR during this time will result in a higher C/M ratio. The S/C ratio is sensitive to the adopted C/O ratio where the M to S transition occurs.

In Table 2 the results for individual masses are listed for the two best models. With the BS law carbon stars are predicted above $1.55\ M_\odot$, for the Reimers law this is $1.45\ M_\odot$. This is in good agreement with observations. The model predicts that stars in the range $1.5\ M_\odot \lesssim M \lesssim 1.6\ M_\odot$ become carbon stars at their last thermal pulse (TP) on the AGB and live only a few 10^4 yrs as carbon stars. More massive stars experience additional TPs as carbon stars and live up to 10^6 yrs. For both mass loss models S-stars originate from slightly more massive stars ($M \gtrsim 2\ M_\odot$). A similar results was found for the LMC (paper I) in agreement with observations of S-stars in LMC clusters. For the Galaxy one might argue (Sect. 2) that S- and C-stars originate from roughly the same population. If future observations would confirm this, this could mean that λ increases with core- and/or initial mass. For smaller λ the increase in the C/O ratio at every thermal pulse is less, increasing the probability that the star will go through an S-star phase.

The mean carbon star lifetime, averaged over the probability to find a star of a given mass in the carbon star phase, is $3.0\ 10^5$ yrs for the Reimers mass loss law and $4.4\ 10^5$ yrs for the BS law. The carbon star lifetime we derive is much longer than the estimate in Groenewegen et al. (1992). This is due the assumption in Groenewegen et al. (1992) that the thermal pulse that forms the carbon star is also the last thermal pulse on the AGB. We now show that carbon stars can have additional thermal pulses.

The observed surface density in the galactic plane of carbon stars in the solar neighbourhood depends on the assumed mean luminosity. For a value of $7050\ L_\odot$ the local surface density is 85 kpc^{-2} (Groenewegen et al. 1992). The main contribution to the surface density comes from optical carbon stars with a 60 μm excess (Groenewegen et al. 1992). As the lifetime of the detached shell causing the 60 μm excess is $\lesssim 2\ 10^4$ yrs, these stars could well have a luminosity below the mean, since they still could be in the luminosity dip of the thermal pulse cycle. If the luminosity of the optical carbon stars with a 60 μm excess were $5000\ L_\odot$ then the total surface density of carbon stars would be 130 kpc^{-2} (Groenewegen et al. 1992). Thronson et al. (1987) and Jura et al. (1989) found no gradient of carbon stars along the galactocentric axis on a scale of at least 4 kpc. If the surface density of carbon stars is constant throughout the Galaxy we estimate a total number of $9\ 10^4$ carbon stars in the Galaxy (if $\sigma = 130\ kpc^{-2}$). Using the mean lifetime derived above, we estimate a birth rate of carbon stars of 0.31 and 0.21 carbon stars yr^{-1} in the Galaxy for the Reimers and the BS law, respectively. Both values agree with the observed rate (0.3-1.2 yr^{-1}) considering the uncertainty in both the predictions and observations (see Sect. 3.2).

5 Discussion

5.1 The predicted luminosity function of AGB stars

In Fig. 4 the predicted luminosity functions (LFs) of M-, S- and C-stars are given for the two best-fitting models (solid lines) and some additional models (dotted and dashed lines). There are no major differences between using the BS and the Reimers mass loss law. The peak of the carbon star LF occurs at the same luminosity as in the LMC (see paper I), providing support

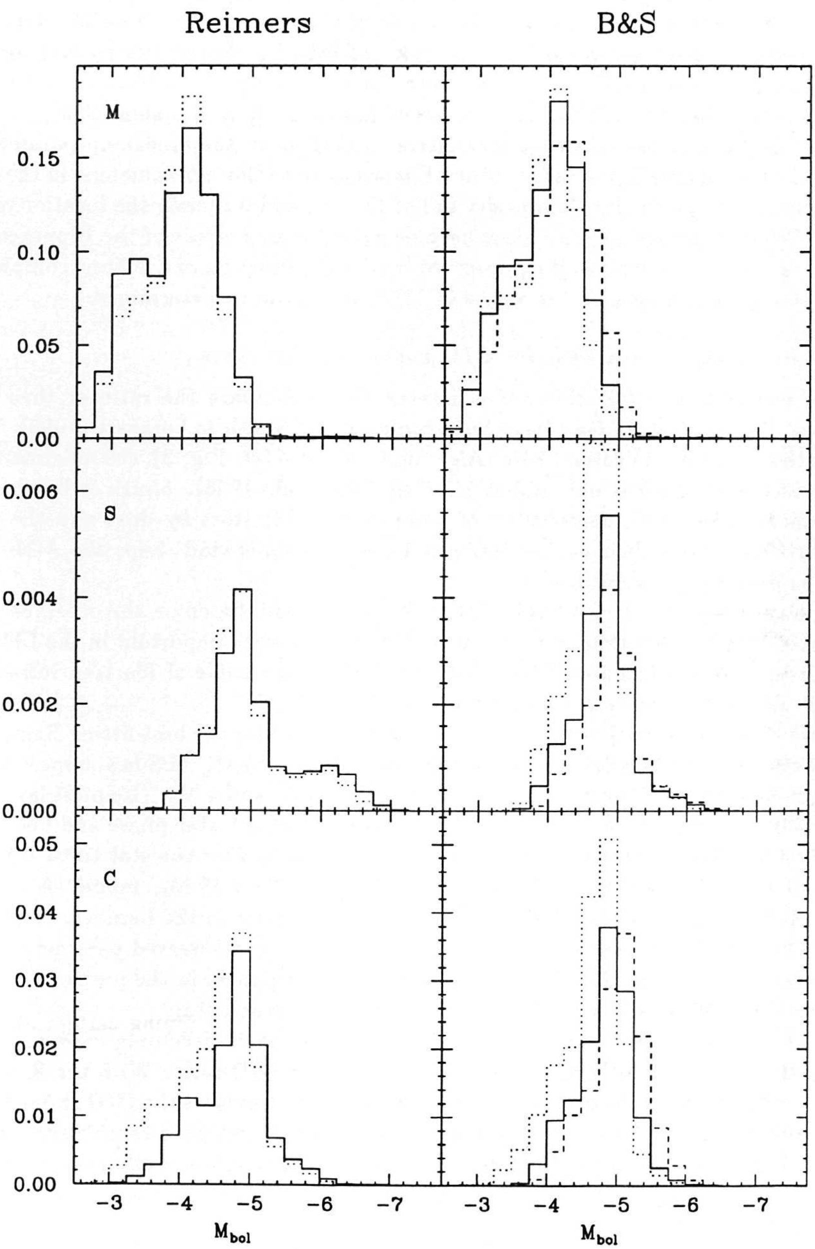

Figure 4: The predicted luminosity functions of M-, S- and C-stars for the best-fitting BS and Reimers mass loss models (solid lines). For the Reimers law a model with M_c^{min} = 0.575 $M_\odot$, λ = 0.90 and η_{AGB} = 5 is also shown (dotted line); for the BS law, models with M_c^{min} = 0.573 $M_\odot$, λ = 0.90 and η_{BS} = 0.16 (dotted line) and M_c^{min} = 0.59 $M_\odot$, λ = 0.65 and η_{BS} = 0.03 (dashed line) are also shown. The sum over all bins is unity.

for the assumption in Groenewegen et al. (1992) and Groenewegen (1993) of a mean luminosity of 7050 $L_\odot$ for Galactic carbon stars. The peak of the oxygen-rich TP-AGB stars occurs at 3400 $L_\odot$. This is in good agreement with the value of 4000 $L_\odot$ determined by Habing (1988) by modelling the space distribution of AGB stars. The luminosity of a typical Galactic AGB star is in any case less than the 10^4 $L_\odot$ often assumed (e.g. Jura & Kleinmann 1989).
The M- and S-star LFs are relatively insensitive to changes in the dredge-up parameters M_c^{min} and λ. As shown in paper I, the carbon star LF is sensitive to those parameters, in the sense that M_c^{min} mainly influences the low-luminosity tail of the LF, and λ mainly the location of the peak of the LF. When distances to AGB stars become available as a result of the Hipparcos mission, the predicted LFs can be tested. If an observed luminosity function of a volume complete sample of carbon stars is available then the values of M_c^{min} and λ can be determined.

5.2 The evolution in time of the C/O ratio in AGB stars

Since PNe evolve from AGB stars, it is interesting to compare the ratio of their C and O abundances. For the Galaxy they have been compared by Smith & Lambert (1990). They note that while the C/O ratio in (disk-) PNe ranges up to about 4 (cf. Fig. 3), the maximum observed C/O ratio in carbon stars is only about 1.5 (Lambert et al. 1986). Smith & Lambert suggest that systematic errors, the obscuration of more carbon-rich stars by dust and the possibility that C-rich PNe receive their enrichment just before the superwind strips the AGB star of its envelope, as possible explanations.
Dust obscuration seems not very likely. In paper I we showed, based on the observed number of IRAS sources in the LMC, that dust obscuration cannot be very important in the LMC. For the Galaxy, Groenewegen & de Jong (1993f) showed that in a sample of fourteen infrared carbon stars, eight in fact have optical counterparts.
In Fig. 5 we show the evolution of the C/O ratio on the AGB for the best-fitting Reimers and BS models for stars of 1.5 $M_\odot$ (Reimers law, upper left panel), 1.55 $M_\odot$ (BS law, upper right panel), 2 $M_\odot$ (Reimers law, middle left; BS law, middle right panel) and 4 $M_\odot$ (Reimers law, lower left; BS law, lower right panel). The 1.5 and 1.55 $M_\odot$ star skip the S-star phase and become carbon stars at their last thermal pulse on the AGB. The C/O ratio after the star turns into a carbon stars is 2.4 for the Reimers 1.5 $M_\odot$ model and 1.6 for the BS 1.55 $M_\odot$ model. A C/O ratio of 2.4 is in disagreement with observations. The largest C/O ratio in the Lambert et al. sample is 1.76. The BS 1.55 $M_\odot$ model represents the upper range of the observed parameter space. If λ would be smaller than 0.75 at small core masses (see the argument in the previous section) then the C/O ratio would be smaller when the star becomes a carbon star.
The 2 $M_\odot$ model stars evolve through the S-star phase before becoming carbon stars. They experience three additional thermal pulses increasing their C/O ratio. With the Reimers law it experiences a late thermal pulse at low envelope mass which increases the C/O ratio significantly. This shows that the suggestion by Smith & Lambert that C-rich PNe receive their enrichment at the very end of the AGB can play a role in some cases. The 4 $M_\odot$ models behave in a similar way as the 2 $M_\odot$ models except that the interpulse period is shorter and therefore the stars experience a larger number of pulses.
A comparison of the observed range in the C/O (1.0–1.76) and $^{12}C/^{13}C$ ratio (20-100; excluding the J-type stars) in the Lambert et al. sample with the predicted C/O and $^{12}C/^{13}C$ ratios in Table 2 suggest that only carbon stars during their firstly few pulses (depending on initial mass) are represented in the Lambert et al. sample.
Willems & de Jong (1988) and Groenewegen et al. (1992) have classified carbon stars in groups II to V. Group II C-stars have a 60 μm excess indicating a phase of high mass loss in the past, group III stars have a moderate present-day mass loss and groups IV and V are infrared carbon

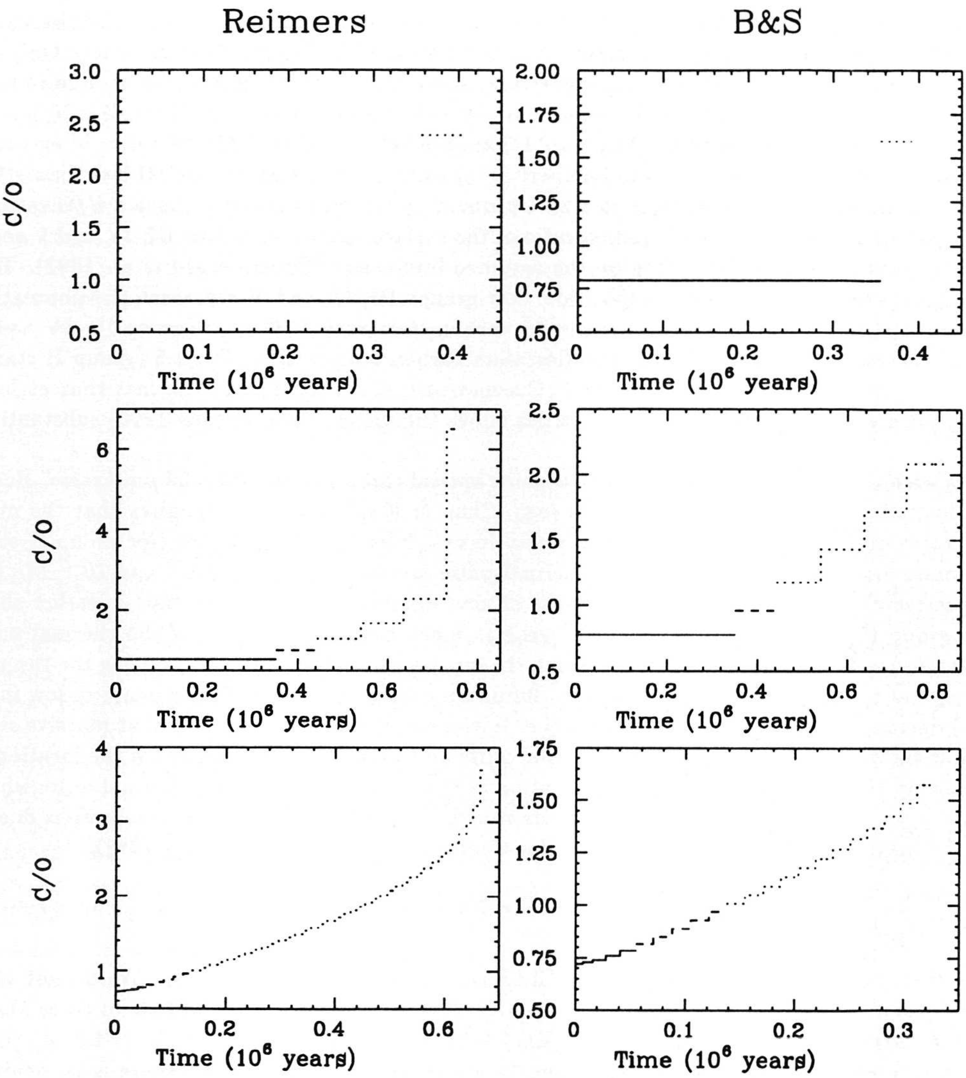

Figure 5: The predicted evolution of the C/O ratio for the best-fitting BS and Reimers mass loss models. Indicated are the evolution of a 1.5 (upper left), 1.55 (upper right), 2 $M_{\odot}$ (middle panels) and 4 $M_{\odot}$ models (lower panels). The M-, S- and C-star phase are represented by the solid, dashed and dotted line respectively.

stars with a high present-day mass loss rate. Group I consists of carbon stars with a peculiar evolutionary history (e.g. Barnbaum et al. 1991). Groenewegen et al. (1992) assumed that most Galactic carbon stars have a similar initial mass, loop only once in the IRAS color-color diagram, and that groups II-V represent an evolutionary sequence. This working hypothesis needs refinement.

Of the 30 stars with a C/O ratio determined by Lambert et al., 90% belong to group II and the remaining 10% to group III. Yet, PNe are known with C/O ratios up to about 4. This implies first that carbon stars with C/O $\gtrsim$1.5 are to be found among groups III, IV and V, and secondly that stars with C/O $\gtrsim$1.5 do not make loops through the IRAS color-color diagram. Only for one infrared carbon star is a C/O ratio determined. For IRC 10216 (a group IV star) a ratio C/O $\approx$ 2.5 has been inferred based on its molecular emission lines (Morris 1975, Mitchell & Robinson 1980). The carbon stars with C/O ratios $\gtrsim$1.5 are predicted to show $^{12}C/^{13}C$ ratios in excess of the 30-80 which are observed in the Lambert et al. sample for C-stars with C/O less than $\sim$1.5. From our model we find that there is a 29% probability for carbon stars to have a C/O ratio of $\gtrsim$1.5 (based on Table 2). The observed ratio of the surface density of groups III, IV and V to all carbon stars is 14-21%, depending on the assumed luminosity (Groenewegen et al. 1992). This is roughly consistent with the proposition that groups III, IV and V represent the population of carbon stars with C/O $\gtrsim$1.5. On average, carbon stars with C/O $\gtrsim$1.5 (group III, IV and V stars) represent a more massive population than carbon stars with C/O $\lesssim$1.5 (group II stars). The scale height of the different groups (Groenewegen et al. 1992) and the fact that at least some infrared carbon stars have luminosities above the mean (Groenewegen 1993) substantiate this.

Stars with C/O $\gtrsim$1.5 apparently do not become optical carbon stars with a 60 μm excess. Based on theoretical radiative transfer models (e.g. Chan & Kwok 1988) this requires that the mass loss rates during and after the thermal pulse do not differ by a large factor (for group II stars the mass loss rate during and after a thermal pulse are on the order of 10^{-5} and 10^{-7} $M_\odot$/yr, respectively) and that the time for a phase of new significant mass loss to start is rather short (for group II stars this is about 1-2 10^4 years). Since both the duration of the thermal pulse (identified with the phase of high mass loss), the increase in surface luminosity during the thermal pulse, and the duration of the subsequent luminosity dip (identified with the phase of low mass loss) decrease with increasing core mass (i.e. initial mass) it may be possible that massive stars do not show significant loops after a thermal pulse and would therefore not reach the location of the group II stars. Alternatively, the variation in the mass loss rate at the thermal pulse where the oxygen- to carbon-star transition occurs may be larger than at other thermal pulses due to the dramatic change in opacity in the stellar atmosphere (Willems & de Jong 1988).

5.3 The location of the carbon stars with known masses in the IRAS color-color diagram

The stars in Table 1 are plotted in the IRAS color-color diagram in Fig. 6. We do not wish to comment on some of the high masses (W Ori, BL Ori) and divide the sample in three about equally large subgroups ($M < 1.9$ $M_\odot$ (X), 1.9 $M_\odot \leq M \lesssim 4.2$ $M_\odot$ (*) and $M \geq 4.3$ $M_\odot$ (O)). Stars without high-quality 60 μm flux-density are plotted at $C_{32} = -2.4$. There is no obvious relation between mass and infrared colors. Of the 13 stars with reliable flux-densities in all three bands, 8 have an excess at 60 μm. Figure 6 shows that probably carbon stars of all masses go through a phase of 60 μm excess and an optical carbon star phase at least once.

Of the stars in Table 1 three (W Ori, BL Ori and W CMa) are in the sample of Lambert et al.. All three are massive, even above the classical upperlimit of 8 $M_\odot$ for AGB stars if the mass estimates in Table 1 are to be believed, and have C/O ratios of 1.16, 1.04 and 1.05 respectively. This shows that massive carbon stars are only to be found in the optical carbon star phase when their C/O ratio is relatively small.

5.4 Are the detached shells around carbon stars carbon-rich ?

The chemical composition of the shells around the carbon stars with 60 μm excess is an open question. We have suggested that sub-mm observations may resolve the question whether the shells are carbon-rich or oxygen-rich (Groenewegen & de Jong 1993e). In a recent paper, Zuck-

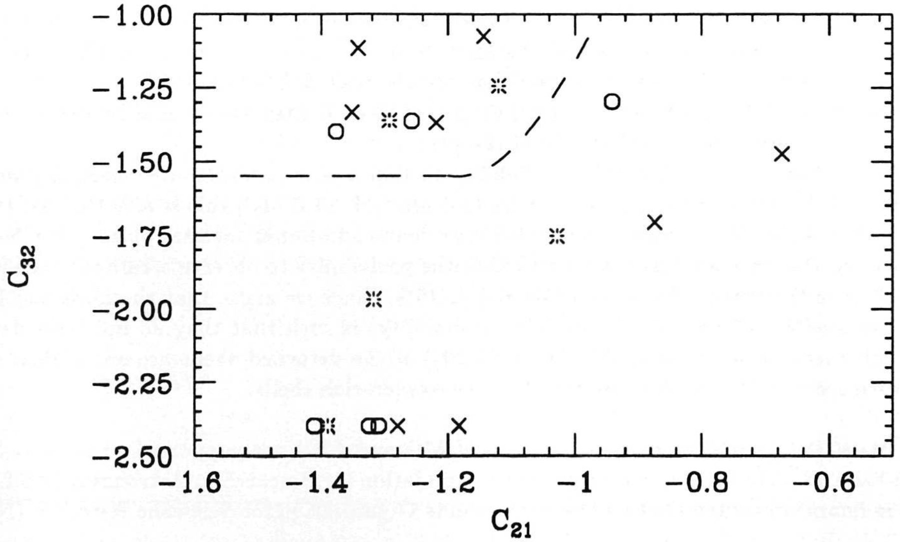

Figure 6: The IRAS color-color diagram for carbon stars with main sequence companions and carbon stars in clusters ($C_{21} = 2.5\log(S_{25}/S_{12})$ and $C_{32} = 2.5\log(S_{60}/S_{25})$). Stars without 60 μm flux-density are plotted at $C_{32} = -2.4$. The stars are divided in $M < 1.9 M_\odot$ (X), $1.9\ M_\odot \leq M \lesssim 4.2\ M_\odot$ (*) and $M \geq 4.3\ M_\odot$ (O). Stars in the upperleft part (to the left of the dashed line) have a 60 μm excess. The blackbody point of stellar photospheres is located at $C_{21} = -1.56$, $C_{32} = -1.88$.

erman (1993) has claimed that the detection of HCN around some carbon stars with 60 μm excess indicates that the detached shells are carbon-rich. This argument is flawed. From the calculations of Olofsson et al. (1990), and of Bergman et al. (1993) for S Sct, it follows that HCN is destroyed at radii corresponding to time scales of $\lesssim 10^3$ yrs. The inner radii of the dust shells which cause the 60 μm excesses are located at distances corresponding to timescales of $\sim 10^4$ yrs. The presence of HCN in these stars is due to present-day carbon-rich mass loss and not related to the detached shell.

Zuckerman continues to point out that the Willems & de Jong (1988) scenario predicts that when the 12 and 25 μm fluxes are entirely photospheric, the 60/25 ratio decreases as the dust shell moves further out. This is true. However, this is also the case if the detached dust shell were carbon-rich, as is Zuckerman's preferred model. The fact that the double-peaked CO line profiles are found in a few stars with moderate 60/25 ratios, but not in carbon stars with lower 60/25 ratios, therefore is not an indication of the incorrectness of the Willems & de Jong model, as claimed by Zuckerman, but must be due to some mechanism which prevents the occurrence of double-peaked CO profiles in stars with moderate 60/25 ratios, independent of the chemical composition of the detached shell.

This mechanism is photodissociation. The calculations of Bergman et al. (1993) for S Sct show that the detached CO shell will survive for only another few thousand years. As the evolution towards lower 60/25 ratios is very slow, it is not clear that stars with a small 60 μm excess should still show a double-peaked CO line profile. The time scale a detached CO shell can avoid photodissociation depends on the product of the mass loss rate in, and the duration of the phase of high mass loss rate, and on the interstellar radiation field. For S Sct, an UV field twice the standard value reduces the lifetime of the CO shell from $\sim 1.2\ 10^4$ to $< 10^4$ yrs (Bergman et al.

1993). As the mass loss rate that caused the detached shell in S Sct is probably higher than in other carbon stars with 60 μm excess, the lifetime of the CO shell in most carbon stars will be shorter than that of S Sct. We conclude that double-peaked CO line profiles are very unlikely in carbon stars with a moderate or small 60 μm excess. If they ever would be discovered this would imply a very high mass loss rate in the past.

From Table 2 one can estimate the probability to find a star just after the thermal pulse that turned the star carbon-rich. For some stars (1.5 $M_\odot \lesssim M \lesssim 1.6$ $M_\odot$) this is also the last thermal pulse on the AGB. More massive stars will experience additional thermal pulses. For both the Reimers and the BS mass loss law we find that the probability to observe a carbon star after the thermal pulse that made the star carbon-rich is 45%. Since we argue that the mass loss history of the stars with C/O ratios $\gtrsim$1.5 (a 29% probability) is such that they do not have detached shells this means that at least 63% (45/(100-29)) of the detached shells around optical carbon stars with a 60 μm excess are expected to have oxygen-rich shells.

Acknowledgements. The research of MG and LBH are supported under grants 782-373-030 and 782-373-028 by the Netherlands Foundation for Research in Astronomy (ASTRON), which is financially supported by the Netherlands Organisation for Scientific Research (NWO).

References

Aller L.H., Cryzak S.J., 1983, ApJS 51, 211
Aller L.H., Keyes C.D., 1987, ApJS 65, 405
Barbaro G., Dallaporta N., 1974, A&A 33, 21
Barnbaum C., Morris M., Likkel L., Kastner J.H., 1991, A&A 251, 79
Bergeron P., Schaffer R.A., Liebert J., 1992, ApJ 394, 228
Bergman P., Carlström U., Olofsson H., 1993, A&A 268, 685
Blöcker T., Schönberner D., 1993, in: IAU symposium 155 on Planetary Nebulae, eds. R. Weinberger, A. Acker, Reidel, Dordrecht, in press (BS)
Bouchet R., Thé P.S., 1983, PASP 95, 474
Bowen G.H., 1988, ApJ 329, 299
Chan S.J., Kwok S., 1988, ApJ 334, 362
Claussen M.J., Kleinmann S.C., Joyce R.R., Jura M., 1987, ApJS 65, 385
Dean C.A., 1976, AJ 81, 364
de Jong T., 1989, A&A 223, L23
Egan M.P., Leung C.M., 1991, ApJ 383, 314
Eggen O.J., Iben I., 1991, AJ 101, 1377
Gordon C.P., 1968, PASP 80, 597
Groenewegen M.A.T., de Jong T., van der Bliek N.S., Slijkhuis S., Willems F.J., 1992, A&A 253, 150
Groenewegen M.A.T., de Jong T., 1993a, A&A 267, 410 (paper I; Chapter 8)
Groenewegen M.A.T., de Jong T., 1993b, A&A in press (paper II; Chapter 9)
Groenewegen M.A.T., de Jong T., 1993c, A&A submitted (paper III; Chapter 10)
Groenewegen M.A.T., de Jong T., 1993d, A&A to be submitted (paper IV; Chapter 11)
Groenewegen M.A.T., de Jong T., 1993e, A&A submitted (Chapter 6)
Groenewegen M.A.T., de Jong T., 1993f, A&AS, in press
Groenewegen M.A.T., 1993, A&A to be submitted (Chapter 7)
Habing H.J., 1988, A&A 200, 40
Herman J., 1988, A&AS 74, 133

Iben I., Laughlin G., 1989, ApJ 341,312
Jørgensen U.G., Westerlund B.E., 1988, A&AS 72, 193
Jorissen A., Mayor M., 1992, A&A 260, 115
Jorissen A., Boffin H., 1992, ESO preprint 832
Jura M., 1988, ApJS 66, 33
Jura M., Joyce R.R., Kleinmann S.G., 1989, ApJ 336, 924
Jura M., Kleinmann S.G., 1989, ApJ 341, 359
Jura M., Kleinmann S.G., 1992a, ApJS 79, 105
Jura M., Kleinmann S.G., 1992b, ApJS 83, 329
Kaler J.B., Shaw R.A., Kwitter K.A, 1990, ApJ 359, 392
Lambert D.L., Gustafsson B., Eriksson K., Hinkle K.H., 1986, ApJS 62, 373
Le Bertre T., 1990, A&A 236, 472
Maeder A., Meynet G., 1989, A&A 210, 155
Mitchell R.M., Robinson G., 1980, MNRAS 190, 669
Morris M., 1975, ApJ 197, 603
Olofsson H., Carlström U., Eriksson K., Gustafsson B., Willson L.A., 1990, A&A 230, L13
Olofsson H., Carlström U., Eriksson K., Gustafsson B., 1992, A&A 253, L17
Olson B.I., Richer H.B., 1975, ApJ 200, 88
Pottasch S.R., 1992, A&AR 4, 215
Reimers D., 1975, in: Problems in stellar atmospheres and envelopes, eds. B. Basheck et al., Springer, Berlin, p. 229
Reimers D., Grootte D., 1983, A&A 123, 257
Scalo J.M., Miller G.E., 1979, ApJ 233, 596
Schaerer D., Meynet G., Maeder A., Schaller G., 1993, A&AS 98, 523
Schaller G., Schaerer D., Meynet G., Maeder A., 1992, A&AS 96, 269
Schmidt-Kaler Th., 1982, in: Landolt-Bornstein, eds. K. Schaiffers, H.H. Voigt, Springer, Berlin
Smith V.V., Lambert D.L., 1990, ApJS 72, 387
Stephenson C.B., 1989, Publ. Warner and Swasey Obs., Vol. 3, 55
Straižys V., Kuriliene G., 1981, A&SS 80, 353
Sweigart A.V., Greggio L., Renzini A., 1990, ApJ 364, 527
Thronson H.A., Latter W.B., Black J.H., Bally J., Hacking P., 1987, ApJ 322, 770
Van den Hoek L.B., Groenewegen M.A.T., Nomoto K., de Jong T., 1993, in preparation
Weidemann V., 1990, ARA&A 28, 103
Willems F.J., 1988a, A&A 203, 51
Willems F.J., 1988b, A&A 203, 65
Willems F.J., de Jong T., 1988, A&A 196, 173
Yamamura I., Onaka T., Kamijo F., Izumiura H., Deguchi S., 1993, PASJ, in press
Zijlstra A.A., Loup C., Waters L.B.F.M., de Jong T., 1992, A&A 265, L5
Zuckerman B., Aller L.H., 1986, ApJ 301, 772
Zuckerman B., Maddalena R.J., 1989, A&A 223, L20
Zuckerman B., 1993, preprint

Chapter 13

Nederlandse Samenvatting

Dit proefschrift heeft tot onderwerp de evolutie en eigenschappen van AGB sterren. AGB staat voor Asymptotic Giant Branch, oftewel Asymptotische Reuzen Tak. Deze naam heeft betrekking op de groep van sterren die in het Hertzsprung-Russell diagram (waarin de hoeveelheid licht die een ster uitstraalt uitstaat tegen de oppervlakte temperatuur van de ster) dicht bij de groep van rode reuzen gelegen is. De AGB is het laatste evolutiestadium van sterren met een massa tussen de 1 en 8 zonsmassa's.
In dit hoofdstuk geef ik een beschrijving van de evolutie van AGB sterren en een samenvatting van de inhoud van dit proefschrift.

1 De evolutie van AGB sterren

Alleen sterren met een massa die bij het ontstaan tussen de circa 1 en 8 zonsmassa's ligt, blijken uiteindelijk door een AGB fase heen te gaan. Lichtere sterren evolueren zo langzaam dat ze op dit moment in de ontwikkeling van het heelal de AGB fase nog niet hebben bereikt. Zwaardere sterren eindigen hun leven met een supernova explosie en gaan ook niet door een AGB fase.
De essentie van de evolutie van sterren bestaat uit het fuseren van lichtere elementen tot zwaardere. Dit kernfusieproces levert de energie om de ster te behoeden voor het ineenvallen onder zijn eigen gewicht. Kernfusie kan optreden in het centrum van de ster of in een schil rond het centrum. Zo zal een ster de volgende processen doorlopen: kernfusie van waterstof tot helium in het centrum (in deze fase bevindt zich de Zon op het ogenblik), fusie van waterstof tot helium in een schil, fusie van helium tot koolstof in het centrum en vervolgens fusie van helium in een schil. Als een ster dit laatste stadium heeft doorlopen volgt een belangrijke scheiding. Sterren die bij de geboorte zwaarder waren dan circa 8 zonsmassa's zullen in het centrum koolstof gaan verbranden. In lichtere sterren is de temperatuur daarvoor niet hoog genoeg en zal er kernfusie optreden in een *tweede* schil. Het proces van dubbele-schil verbranding is kenmerkend voor AGB sterren.
Op de AGB zal gedurende de meeste tijd waterstof in helium worden omgezet in de buitenste schil. Dit nieuw geproduceerde helium komt terecht in de binnenste schil. Na verloop van tijd zullen de temperatuur en de dichtheid zo hoog zijn dat het helium op explosieve wijze tot koolstof wordt verbrand. Dit proces heet een thermische puls (TP) of een helium schil flits. De tijd tussen twee opeenvolgende thermische pulsen heet de interpuls periode. Tijdens en na een TP zal de lichtkracht van de ster ongeveer 2 maal de waarde hebben van net voor de TP en dat gedurende circa 1% van de interpuls periode. Bij een TP wordt de energie die vrijkomt met name gebruikt om de ster uit te doen zetten en daardoor wordt de temperatuur in de twee verbrandingsschillen zo laag dat er weinig kernfusie meer optreedt. De lichtkracht van de ster zakt in tot circa de helft van de waarde net voor de TP (de 'luminosity dip') en blijft laag gedurende 20-40% van de interpuls periode. Vervolgens bereikt de ster weer in z'n oorspronkelijke grootte en komt de waterstof schil verbranding opnieuw op gang (de rest van de interpuls periode). De lichtkracht zal aan het einde van een thermische puls cyclus iets hoger zijn dan net voordat de TP afging.

Dit proces kan zich vele malen herhalen al naar gelang de massa van de ster.
Normaal gesproken hebben de kern van de ster (deze bevat circa 0.6 zonsmassa's) en het gedeelte buiten de kern (de mantel van de ster met een massa die kan variëren van een paar honderdste tot maximaal zo'n 5 zonsmassa's in een bol met een straal die een paar honderd keer groter is dan de Zon) geen weet van elkaar. Echter, na een TP kan er contact zijn tussen de kern en de mantel. Daarbij wordt een bepaalde fractie van de koolstof die is gemaakt tijdens de TP toegevoegd aan de al aanwezige koolstof in de mantel. Dit proces heet 'dredge-up' (in het Nederlands vertaald 'op-dreggen'). Door dit proces zal in de buitenlagen van de ster de C/O verhouding, de verhouding van het aantal koolstof atomen t.o.v. het aantal zuurstof atomen, stijgen. Normaal gesproken is deze verhouding ongeveer 0.5. Sterren waarbij de C/O verhouding kleiner is dan circa 0.8 worden als M-sterren waargenomen, sterren waarbij de C/O verhouding tussen de circa 0.8 en de 1 ligt hebben een S-ster spectrum en sterren met een C/O verhouding boven de 1 zijn C-sterren of koolstofsterren. Dit proefschrift gaat grotendeels over deze koolstofsterren.

AGB sterren verliezen massa, en wel in een zodanig tempo dat de levensduur van deze sterren hierdoor wordt bepaald. Eén zonsmassa in de mantel wordt er in 10 000 tot 1 miljoen jaar afgepeld. In de Zon is het massaverlies heel gering en wordt de levensduur bepaald door de snelheid waarmee zich de kernfusieprocessen in het centrum afspelen. AGB sterren zijn relatief koel met temperaturen van minder dan 3000 °C (de Zon heeft een oppervlakte temperatuur van circa 5500 °C). De combinatie van een groot massaverlies en lage temperaturen geeft aanleiding tot de vorming van moleculen en stofdeeltjes rond de ster, in de zgn. circumstellaire schil. Welke moleculen en stofdeeltjes zich vormen hangt af van de C/O verhouding. Koolmonoxide (CO) is een zeer stabiel molecuul. In een M-ster zal al het beschikbare koolstof eerst CO vormen. De zuurstof atomen die dan nog beschikbaar zijn, zullen dan andere moleculen vormen, bv. water (H_2O) en silicium oxide (SiO), of stofdeeltjes, met name allerhande silicaten. In een C-ster is het net andersom. Hier zullen alle zuurstofatomen in koolmonoxide gaan zitten en vormt het overschot aan koolstofatomen moleculen als HCN, of stofdeeltjes als silicium carbide (SiC) en amorf koolstof. Bij S-sterren kunnen allerlei mengvormen optreden. De moleculen en stofdeeltjes kunnen we waarnemen. Bij moleculen gebeurt dit veelal door de overgangen te bestuderen bij radiofrequenties (typisch 100 GHz). De studie van stof heeft een grote impuls gekregen met de lancering van IRAS (Infrarood Astronomische Sateliet) in 1983. Aan boord bevond zich o.a. het in Nederland gebouwde LRS instrument (Lage Resolutie Spectrograaf) dat van een paar duizend bronnen goede spectra heeft genomen in het gebied tussen de 8 en 23 micrometer. In dit golflengte gebied hebben de hierboven genoemde silicaten en siliciumcarbide stofdeeltjes karakteristieke emissiebanden. Door bestudering van LRS spectra kunnen we iets zeggen over de chemische samenstelling in de circumstellaire schil en over het massaverlies van de onderliggende AGB ster.

2 Samenvatting van dit proefschrift

Hoofdstuk 2 en 3 gaan over de CO emissie in een klasse van M-sterren die een heel groot massaverlies hebben, de zgn. OH/IR sterren. Enkele jaren geleden bleek dat in sommige van deze OH/IR sterren minder CO werd waargenomen dan men op grond van het uit infrarode waarnemingen bepaalde massaverlies mocht verwachten. Er werden destijds een tweetal suggesties gedaan: of het model waarmee de CO waarnemingen werden geïnterpreteerd was incorrect, of het massaverlies was lager in het verleden. Dit laatste argument is gebaseerd op het feit dat het heetste stof dichter bij de ster zit dan de CO schil en dus recenter gevormd is. Ik heb een model ontwikkeld om de emissie van moleculen in een circumstellaire schil te berekenen (Hoofdstuk 2) en toegepast op twee OH/IR sterren (Hoofdstuk 3). Voor de OH/IR ster met het kleinste massaverlies vind ik dat het massaverlies bepaald op grond van de infrarode en CO waarnemingen in goede overeenstemming met elkaar zijn. Voor de OH/IR ster met het grootste massaverlies vind ik dat met een constant massaverlies de waarnemingen niet verklaard kunnen worden. Met een massaverlies dat lager is geweest in het verleden lukt dat wel.

Hoofdstuk 4 behandelt een aspect van S-sterren. Er blijken S-sterren met en zonder het element technetium (Tc) te zijn. Technetium is radioactief en vervalt met een halfwaarde tijd van circa 200 000 jaar. Het is een element dat na een thermische puls wordt gevormd en wordt gemengd in de mantel van de ster. De afwezigheid van Tc duidt er dus op dat er in de laatste 1 miljoen jaar geen 'dredge-up' heeft plaatsgevonden.
Tot nu toe zijn we er van uitgegaan dat onze AGB ster alleen door het leven gaat. Het blijkt echter dat de meeste sterren zich in dubbelster (of meervoudige) systemen bevinden. De zwaarste van de twee sterren zal het snelst evolueren. Als deze ster een massa tussen de 1 en de 8 zonsmassa's heeft en de afstand tussen de twee sterren is groot genoeg, zal deze een AGB ster worden. Het interessante aspect is dat een deel van de massa die de AGB ster uitstoot kan worden opgevangen door de tweede ster, die in de meeste gevallen nog op de hoofdreeks zit. Hierdoor kan de hoofdreeksster de chemische eigenaardigheden van een echte AGB ster vertonen, in het bijzonder de toename in de C/O verhouding. De oorspronkelijk zwaarste ster zal na de AGB fase in helderheid afnemen en een witte dwerg worden. Het radioactive Tc in de minst zware ster zal vervallen. Er is op het ogenblik een aantal klassen van systemen bekend die bestaan uit een witte dwerg en een ster met sommige chemische eigenschappen van AGB sterren. Eén daarvan is de S-sterren zonder Tc. In Hoofdstuk 4 bespreek ik een methode om de S-sterren met en zonder Tc van elkaar te onderscheiden *zonder* dat men de hoeveelheid Tc in de atmosfeer hoeft te meten. Het blijkt dat de twee klassen van S-sterren heel verschillende infrarode eigenschappen hebben. De S-sterren met Tc zijn echte AGB sterren en hebben dus een geprononceerde circumstellaire schil, de S-sterren zonder Tc zijn minder geëvolueerd hebben dus nauwelijks een circumstellaire schil.

Hoofdstukken 5-7 hebben betrekking op de stofschillen rond C-sterren. In Hoofdstuk 5 presenteer ik een model om de emissie van een stofschil rond een AGB ster te berekenen. In Hoofdstuk 6 wordt de ster S Sct bekeken. Dit is de enige koolstofster met een koele stofschil die ook in detail in CO is bekeken. Uit de CO waarnemingen blijkt dat de (CO) schil geometrisch dun is en ongeveer 9000 jaar geleden uitgestoten te zijn. De spectrale energie verdeling is hiermee consistent.
In Hoofdstuk 7 worden de stofschillen rond 21 infrarode koolstofsterren geanalyseerd. Parameters die afgeleid worden zijn het massaverlies, de temperatuur van het heetste stof en de verhouding van silicium carbide tot amorf koolstof stof. Vergeleken met de waarnemingen voorspelt het standaard model met een constant massaverlies te veel flux op 60 en 100 micrometer. Dit verschil wordt groter naarmate de ster meer in het infrarood gaat stralen. Ik bespreek twee mogelijke oplossingen: of het massaverlies was lager in het verleden of de golflengte afhankelijkheid van de stof absorptie is anders. Deze laatste mogelijkheid wordt echter van de hand gewezen. Ik argumenteer dat de reeks van steeds toenemende roodheid van koolstofsterren in statistische zin een reeks van toenemende begin massa is. Echter, voor elke individuele ster worden de infrarode eigenschappen bij lange golflengten sterk bepaald door de tijdsafhankelijkheid van het massaverlies.

Hoofdstukken 8-11 hebben betrekking op een zgn. synthetisch AGB evolutie model. Bij synthetische evolutie berekeningen maakt men geen gebruik van een echt stermodel om de evolutie uit te rekenen maar van vereenvoudigde relaties tussen de belangrijkste grootheden. Het voordeel hiervan is dat deze methode snel is en dat men op een gemakkelijke manier bepaalde effecten kan testen.

Hoofdstuk 8 beschrijft een synthetisch model om de evolutie van AGB sterren uit te rekenen en past dit toe op koolstofsterren in de Grote Magellaanse Wolk (GMW; een nabij gelegen melkwegstelsel). In Hoofdstuk 9 vergelijken wij de voorspelde abundanties in Planetaire Nevels (PNs; de evolutie fase na de AGB) in de GMW met de voorspellingen op basis van het beste model van Hoofdstuk 8 en vinden een goede overeenkomst. In Hoofdstuk 8 (en 9) gebruiken wij een bepaalde parameterisering van het massaverlies, een zgn. Reimers-wet. In Hoofdstuk 10 herhalen wij de analyse van Hoofdstukken 8 en 9 voor twee andere massaverlieswetten en tonen aan dat waarschijnlijk alleen massaverlieswetten met een lichtkracht afhankelijkheid ($\dot{M} \sim L^{\alpha}$), $1 \lesssim \alpha \lesssim 4$ de waargenomen eigenschappen van AGB sterren en abundanties in PNs in de GMW kunnen verklaren. In Hoofdstuk 11 proberen wij de eigenschappen van lang-periodiek variabelen (LPV) in de GMW te verklaren. Het blijkt dat AGB sterren slechts gedurende een korte tijd op de AGB ook LPV zijn. De meeste sterren eindigen hun leven op de AGB niet als LPV.

Tenslotte wordt in Hoofdstuk 12 een scenario gegeven over de evolutie van koolstof sterren in de zonsomgeving. Alleen sterren met een massa zwaarder dan 1.5 maal de zon zullen koolstofster worden. De gemiddelde levensduur van de koolstofsterfase bedraagt 300 000 jaar.

Publication List

Groenewegen M.A.T., Lamers H.J.G.L.M., 1989, A&AS 79, 359, "The winds of O-stars: I An analysis of the UV line profiles using the SEI method"

Groenewegen M.A.T., Lamers H.J.G.L.M., Pauldrach A.W.A., 1989, A&A 221, 78, "The winds of O-stars: II The terminal velocities of stellar winds of O-type stars"

Lamers H.J.G.L.M., Groenewegen M.A.T., 1990, PASPC 7, 189, "Winds of O-stars: Velocities and ionization "

Groenewegen M.A.T., Lamers H.J.G.L.M., 1991, A&A 243, 429, "The winds of O-stars: III A comparison between the observed and predicted degrees of ionization in the winds of O-stars "

Groenewegen M.A.T., de Jong T., 1991, ESO Messenger 66, 40, "Multi-wavelength observations of infrared-bright carbon stars"

Groenewegen M.A.T., de Jong T., van der Bliek N.S., Slijkhuis S., Willems F.J., 1992, A&A 253, 150, "A flux-limited sample of galactic carbon stars"

Van Driel W., Augarde R., Bottinelli L., Gouguenheim L., Hamabe M., Maehara M., Baan W.A., Goudfrooij P., Groenewegen M.A.T., 1992, A&A 259, 71, "A study of the NGC 7448 group of galaxies"

Slijkhuis S., Groenewegen M.A.T., 1992, Chapter 6 in the Ph.D. thesis of Slijkhuis, University of Amsterdam (to be published in A&A), "Radiative transfer modelling of dust-shells around post-AGB stars"

Groenewegen M.A.T., de Jong T., 1993, A&A 267, 410, "Synthetic AGB evolution I: A new model" (Chapter 8)

Groenewegen M.A.T., 1993, A&A 271, 180, "On the infrared properties of S-stars with and without Technetium" (Chapter 4)

van den Hoek L.B., Groenewegen M.A.T., Nomoto K., 1993, in: The feedback of chemical evolution on the stellar content of galaxies, eds. D. Alloin, G. Stasinska, l'Observatoire de Paris, "New theoretical yields for intermediate and massive stars: the chemical evolution of the Galaxy and the Magellanic clouds", p. 69

Groenewegen M.A.T., de Jong T., 1993, A&A in press, "The circumstellar envelope of S Sct" (Chapter 6)

Groenewegen M.A.T., de Jong T., 1993, A&A in press, "Synthetic AGB evolution II: The predicted abundances of PNe in the LMC" (Chapter 9)

Groenewegen M.A.T., de Jong T., 1993, A&AS in press, "Optical photometry of carbon stars"

Groenewegen M.A.T., de Jong T., Baas F., 1993, A&AS in press, "Near-infrared and submillimeter photometry of carbon stars"

Groenewegen M.A.T., de Jong T., 1993, in: Mass loss on the AGB and beyond, ed. H. Schwarz, in press, "Synthetic AGB evolution applied to the carbon stars in the LMC"

Groenewegen M.A.T., de Jong T., 1993, in: IAU symposium 155 on planetary nebulae, eds. R. Weinberger, A. Acker, in press, "Synthetic evolution: The abundances of Planetary Nebulae in the LMC"

Groenewegen M.A.T., de Jong T., 1993, submitted to A&A, "Synthetic AGB evolution III: The influence of different mass loss laws" (Chapter 10)

Groenewegen M.A.T., 1993, to be submitted to A&A, "A revised model for circumstellar molecular emission" (Chapter 2)

Groenewegen M.A.T., 1993, to be submitted to A&A, "The mass loss rates of OH/IR 32.8–0.3 and OH/IR 44.8–2.3 (Chapter 3)

Groenewegen M.A.T., de Jong T., Geballe T.R., 1993, to be submitted to A&A, "The 3 μm spectra of candidate carbon stars"

Groenewegen M.A.T., 1993, to be submitted to A&A, "Dust shells around infrared-carbon stars" (Chapter 7)

Groenewegen M.A.T., de Jong T., 1993, to submitted to A&A, "Synthetic AGB evolution IV: LPVs in the LMC" (Chapter 11)

Groenewegen M.A.T., van den Hoek L.B., de Jong T.,, 1993, to be submitted to A&A, "The evolution of Galactic carbon stars" (Chapter 12)

Curriculum Vitae

Mijn leven nam een aanvang op 8 juli 1964. Het beroep van mijn vader bracht frequente verhuizingen met zich mee; ik heb gewoond in Ede, Selsingen (Dld), Wageningen,'s-Heerenberg en Rheden. Het ouderlijk domicile bevindt zich op dit moment in Bakkeveen.
Na het doorlopen van de lagere school bezocht ik de Gemeenschappelijke Scholen Gemeenschap Doetinchem (GSGD) alwaar ik in 1982 het diploma 'ongedeeld VWO' behaalde. In september van dat jaar begon ik mijn studie sterrenkunde aan de Rijksuniversitiet Utrecht. Een jaar later werd het propedeutisch examen behaald. De laatste twee jaar van mijn studie deed ik onderzoek aan de sterrenwinden rond O-sterren o.l.v. Prof. Henny Lamers op de SRON afdeling van Utrecht. Eind augustus 1988 studeerde ik af in de algemene sterrenkunde met als extra keuzevakken sterrenkunde (!) en wiskunde en theoretische natuurkunde. Ik behaalde het diploma met het judicium cum laude.
Van 1-7-1989 tot 30-6-1993 was ik in dienst van NWO/ASTRON als onderzoeker-in-opleiding met als standplaats het sterrenkundig instituut van de Universiteit van Amsterdam. Een deel van het verrichtte onderzoek is in dit proefschrift weergegeven. Vanaf 1 november 1993 zal ik voor 2 jaar verbonden zijn aan het Institut d'Astrophysique de Paris (IAP).

Dankwoord/Acknowledgements

Mijn dank zou in de eerste plaats uit moeten gaan naar mijn natuurkunde leraar op de middelbare school, Dhr. Otten. Op mijn vraag of hij me geschikt achtte om natuurkunde c.q. sterrenkunde te gaan studeren, antwoordde deze, na een doodse stilte van een paar seconden, met een JA. Was het een nee geweest dan was ik waarschijnlijk economie gaan studeren.

Vervolgens wil ik mijn ouders hartelijk bedanken. Zij hebben mijn keuzes altijd gerespecteerd en mij volledig ondersteund.

De laatste vier jaar was ik verbonden aan het sterrenkundig instituut van de Universiteit van Amsterdam. Een aantal mensen heeft direct en indirect bijgedragen aan de totstandkoming van dit proefschrift. In de eerste plaats mijn promotor, Teije de Jong. Al hebben we minder en onregelmatiger overleg gevoerd dan ik soms had gewild, ik heb de meeste besprekingen en discussies altijd als nuttig ervaren en verhelderend gevonden.

Dit proefschrift is voor een groot deel gebaseerd op IRAS data. Het beschikbaar hebben van de IRAS data producten was essentieel. Sander Slijkhuis heeft de LRS-atlas van de Cyber naar de Vax overgehaald (een klein wonder). Wim Peters heeft het GRAPHIC pakket van de Universiteit van Grenoble geïnstalleerd, waarmee ik toegang had tot de Point Source Catalog en het CLASS reductiepakket.

Voor dit proefschrift is heel veel gerekend. Mijn excuses aan de 'owners' van de batch-queue's en mede computer gebruikers voor het ongemak.

A non-negligible part of the past four years was spent on observations. I would like to thank the staff of the ESO telescopes in Chile, the IRAM telescope in Grenada, Spain and the UKIRT and JCMT in Hawaii, for their support, in particular Tom Geballe (UKIRT) and Fred Baas (JCMT).

Mijn dank aan ASTRON voor het financieren van project 782-373-030 dat aan dit onderzoek ten grondslag ligt en aan NWO/ASTRON en het LKBF voor het financieren van sommige waarneemreizen en conferentiebezoeken.

Ich möchte Josef Hron danken für den herzlichen Empfang und die Unterstützung während meines Aufenthaltes an die Sternwarte Wien.

Speciale dank aan Sander Slijkhuis, Bobby van den Hoek en René Oudmaijer, met wie ik niet alleen samen artikelen heb geschreven maar ook veel heb gelachen.